Insights into the Regulation of the Mitochondrial Apoptotic Pore

Dissertation

der Mathematisch-Naturwissenschaftlichen Fakultät

der Eberhard Karls Universität Tübingen

zur Erlangung des Grades eines

Doktors der Naturwissenschaften

(Dr. rer. nat.)

vorgelegt von

Andreas Felix Jenner

aus Pforzheim

Tübingen

2026

Gedruckt mit Genehmigung der Mathematisch-Naturwissenschaftlichen Fakultät der Eberhard Karls Universität Tübingen.

Tag der mündlichen Qualifikation:	15.04.2026
Dekan:	Prof. Dr. Thilo Stehle
1. Berichterstatterin:	Prof. Dr. Ana J. García-Sáez
2. Berichterstatter:	Prof. Dr. Ralf Jansen
2. Berichterstatter:	Prof. Dr. Atan Gross

Für meine Mutter,
die immer an mich geglaubt hat.
Danke für alles, was du mir mitgegeben hast.

Table of Contents

Abstract

Apoptotic pore formation by the BCL-2 executioners BAX and BAK at the mitochondrial outer membrane represents the decisive step of intrinsic apoptosis. This process is accompanied by extensive mitochondrial fragmentation mediated by the dynamin-like protein DRP1, which colocalizes with BAX on mitochondria during apoptosis. Following outer membrane permeabilization, mitochondrial inner membrane extrusion and permeabilization allows the release of mitochondrial DNA into the cytosol, which can trigger inflammatory signaling. However, the mechanism by which BAX and BAK assemble to form apoptotic pores, the molecular basis and functional consequences of the apoptotic interplay of BAX and DRP1, as well as the processes underlying mitochondrial inner membrane extrusion and permeabilization, remain obscure.

Here, we reveal a direct physical interaction between BAX and DRP1 that is enhanced during apoptosis. Complex formation between BAX and DRP1 occurs specifically in the membrane environment, requires the N-terminal region of BAX, and promotes the membrane-remodeling activity of both proteins. Forced dimerization of BAX and DRP1 is sufficient to trigger their activation and mitochondrial translocation, inducing mitochondrial fragmentation and permeabilization in the absence of canonical apoptotic triggers. These findings identify DRP1 as a noncanonical, direct activator of BAX through physical engagement with its N-terminal region.

We further uncover that BAX and BAK exhibit distinct properties of apoptotic pore formation. BAK oligomerizes with faster kinetics into smaller structures than BAX, and nucleates and accelerates BAX assembly into oligomers that continue to grow during apoptosis. Both proteins co-assemble into the same apoptotic pores, where their relative abundance determines pore growth rates and the relative kinetics of mitochondrial content release, specifically of the mitochondrial DNA. This cooperative mechanism modulates the activation of the cGAS/STING pathway, linking apoptotic pore formation to inflammatory signaling.

In addition, we developed a multimodal super-resolution approach, termed CorreLative Oligomerization STED Electron (CLOSE) microscopy, which enables the correlative

assessment of the stoichiometry of individual protein complexes and their nanoscale structural assembly, as well as alterations in the underlying membrane ultrastructure. Using CLOSE, we characterize the oligomeric state and nanoscale structural organization of BAK within individual apoptotic pores in relation to the mitochondrial membrane ultrastructure. We find that the geometry of the outer membrane opening defines the spatial arrangement of BAK assemblies and that mechanical forces drive inner membrane extrusion through the apoptotic pore. Conversely, the inner membrane exerts forces on the outer membrane, promoting further pore expansion. These results demonstrate mechanical coupling between mitochondrial membranes that governs apoptotic pore growth and provide a biophysical framework for inner membrane extrusion, defining the structural organization of the apoptotic pore.

Together, our findings identify DRP1 as a noncanonical activator of BAX and uncover fundamental mechanistic principles of apoptotic pore formation by BAX and BAK. We propose a multimodal model in which cooperative BAX/BAK oligomerization nucleates pore opening and expansion through an oligomerization-dependent process. Once the apoptotic pore reaches a critical diameter, inner membrane extrusion and membrane mechanics drive further pore growth, thereby coupling outer and inner membrane permeabilization and modulating downstream immune signaling.

Zusammenfassung

Die Bildung apoptotischer Poren durch die BCL-2-Exekutorproteine BAX und BAK in der äußeren Mitochondrienmembran stellt den zentralen Regulationsschritt der intrinsischen Apoptose dar. Dieser Prozess geht mit einer ausgeprägten Fragmentierung des mitochondrialen Netzwerks einher, die durch die dynamin-ähnliche GTPase DRP1 vermittelt wird. Im Verlauf der Apoptose werden sowohl BAX als auch DRP1 zu den Mitochondrien rekrutiert, wo beide Proteine in sogenannten apoptotischen Foci kolokalisieren. Nachdem die äußere Mitochondrienmembran durch die Bildung apoptotischer Poren permeabilisiert wurde, ermöglicht die Ausstülpung und anschließende Permeabilisierung der inneren Mitochondrienmembran die Freisetzung von mitochondrialer DNA in das Zytosol, wodurch Entzündungssignalwege aktiviert werden können. Trotz der signifikanten Bedeutung dieser Prozesse während der Apoptose sind der molekulare Mechanismus der Porenbildung durch BAX und BAK, die funktionellen Folgen der Wechselwirkung von BAX mit DRP1 sowie die mechanistische Grundlage der Ausstülpung und Permeabilisierung der inneren Mitochondrienmembran noch weitgehend unverstanden.

In dieser Arbeit zeigen wir, dass BAX eine direkte molekulare Interaktion mit DRP1 eingeht, die während der Apoptose verstärkt wird. Diese Interaktion ist membranabhängig und erfordert die N-terminale Region von BAX. Eine erzwungene Dimerisierung beider Proteine reicht aus, um deren Aktivierung und mitochondriale Translokation auszulösen. Dies führt zu einer Fragmentierung und Permeabilisierung der Mitochondrien, wodurch auch in Abwesenheit kanonischer Apoptoseauslöser Apoptose induziert wird. Auf Grundlage dieser Ergebnisse identifizieren wir DRP1 als einen nichtkanonischen, direkten Aktivator von BAX durch eine direkte, molekulare Interaktion mit dessen N-terminaler Region.

Diese Arbeit enthüllt darüber hinaus, dass sich BAX und BAK in der Art und Weise, wie sie Poren bilden, grundlegend unterscheiden. BAK oligomerisiert schneller und bildet kleinere Strukturen als BAX. Zudem initiiert und beschleunigt BAK die Bildung von BAX-Oligomeren, die während der Apoptose stetig weiterwachsen. Beide Proteine reichern sich gemeinsam in denselben apoptotischen Poren an, wobei ihr relatives

Verhältnis sowohl die Wachstumsrate der Poren als auch die Kinetik der Freisetzung des mitochondrialen Inhalts, insbesondere der mitochondrialen DNA, bestimmt. Dieser kooperative Regulationsmechanismus moduliert die Aktivierung des cGAS/STING-Signalwegs und verbindet damit die Bildung apoptotischer Poren funktionell mit zellulären Entzündungsreaktionen.

Im Rahmen dieser Arbeit wurde zudem die CLOSE-Mikroskopie entwickelt: ein multimodales, hochauflösendes mikroskopisches Verfahren zur Charakterisierung des oligomeren Zustands von BAK und seiner nanoskaligen strukturellen Organisation innerhalb einzelner apoptotischer Poren. Mithilfe dieses Verfahrens konnte festgestellt werden, dass die Geometrie der Öffnung der äußeren Mitochondrienmembran die räumliche Anordnung von BAK bestimmt. Darüber hinaus konnte demonstriert werden, dass mechanische Kräfte den Austritt der inneren Mitochondrienmembran durch die apoptotische Pore antreiben, während die sich auswölbende innere Membran wiederum Kräfte auf die äußere Membran ausübt, die das weitere Porenwachstum fördern. Diese Daten belegen eine mechanische Kopplung zwischen der inneren und äußeren mitochondrialen Membran, die die Dynamik des Porenwachstums maßgeblich steuert. Ergänzend wird ein biophysikalisches Modell der Ausstülpung der inneren Membran vorgestellt, das die strukturelle Organisation apoptotischer Poren erklärt.

Zusammenfassend identifiziert diese Arbeit DRP1 als nichtkanonischen Aktivator von BAX und erweitert das mechanistische Verständnis der Porenbildung durch BAX und BAK während der intrinsischen Apoptose. Auf Basis der Ergebnisse wird ein multimodales Modell der Regulation apoptotischer Poren vorgeschlagen: Die kooperative Oligomerisierung von BAX und BAK initiiert zunächst die Öffnung der Pore in der mitochondrialen Außenmembran und treibt deren allmähliche Ausdehnung voran. Sobald die Pore einen kritischen Durchmesser erreicht hat, bestimmt die Ausstülpung der inneren Membran durch mechanische Rückkopplung das weitere Wachstum der Pore. Auf diese Weise sind die Permeabilisierung beider Membranen und die nachgeschaltete Immunantwort funktionell gekoppelt.

List of Publications and Manuscripts included in this study

Published Articles

1. **"DRP1 interacts directly with BAX to induce its activation and apoptosis"**

   Authors:

   Andreas Jenner, Aida Peña-Blanco*, Raquel Salvador-Gallego*, Begoña Ugarte-Uribe*, Cristiana Zollo*, Tariq Ganief, Jan Bierlmeier, Markus Mund, Jason E Lee, Jonas Ries, Dirk Schwarzer, Boris Macek, and Ana J Garcia-Saez
   *equal contribution

   Published in:

   The EMBO Journal, Vol. 41, No. 8, on April 19, 2022,
   Published online on Jan. 13, 2022, https://doi.org/10.15252/embj.2021108587

   Attached in Appendix section 1.1

2. **"The interplay between BAX and BAK tunes apoptotic pore growth to control mitochondrial-DNA-mediated inflammation"**

   Authors:

   Katia Cosentino*, Vanessa Hertlein*, **Andreas Jenner***, Timo Dellmann, Milos Gojkovic, Aida Peña-Blanco, Shashank Dadsena, Noel Wajngarten, John S.H. Danial, Jervis V. Thevathasan, Markus Mund, Jonas Ries, and Ana J. Garcia-Saez
   *equal contribution

   Published in:

   Molecular Cell, Vol. 82, Issue 5, on March 03, 2022,
   Published online on Feb. 03, 2022, https://doi.org/10.1016/j.molcel.2022.01.008

   Attached in Appendix section 1.2

Submitted Manuscripts

1. **“Mechanical forces drive mitochondrial matrix extrusion and apoptotic pore growth”**

   Authors:

   Andreas Jenner, Timo Dellmann, Hyuntae Kim, David Gomez, Cristiana Zollo, Jürgen Köfinger, Katrin Seidel, Felix Gaedke, Astrid Schauss, Gerhard Hummer, Ana J. Garcia-Saez

   Submitted to:

   Nature on May 12, 2025

   Published on BioRxiv on May, 13, 2025,

   https://doi.org/10.1101/2025.05.12.653510

   Attached in Appendix section 2.1

Statement on Author Contributions

Published Articles

1. **“DRP1 interacts directly with BAX to induce its activation and apoptosis”**
   In this accepted publication, the candidate is the first author out of 13.
   He contributed about 10 percent to the study's scientific conceptual development. His primary contributions were to experimental implementation, accounting for approximately half of the data generation. These contributions included methodological development, execution of key experiments, visualization, and formal data analysis. He contributed about 45% to the analysis and interpretation of the data and played a central role in the mechanistic evaluation of the results. He was involved in the critical revision and scientific editing of the manuscript (approximately 5%).
   His contributions were essential to the experimental validation and mechanistic characterization of the direct molecular interaction between DRP1 and BAX, as well as to establishing its functional relevance in apoptosis.

2. **“The interplay between BAX and BAK tunes apoptotic pore growth to control mitochondrial-DNA-mediated inflammation”**
   In this accepted publication, the candidate is shared first author among 13 authors.
   He contributed about 20% to the study's scientific conceptual framework and participated in designing the research strategy. His experimental contribution amounted to about 30% of the generated data. This included substantial methodological development, cellular stoichiometry experiments, recruitment assays, STING pathway analyses, and STED microscopy. The candidate contributed about 30% to the analysis and interpretation of the data, especially by integrating structural and functional datasets into a coherent mechanistic model. He contributed about 10% to writing the manuscript, including co-authoring key sections and critically revising it.

His work was especially significant in cellular stoichiometry analysis and in establishing the functional relationships among apoptotic pore growth, mitochondrial DNA release, and activation of the cGAS/STING inflammatory signaling pathway.

Submitted Manuscripts

1. **“Mechanical forces drive mitochondrial matrix extrusion and apoptotic pore growth”**

   In this study, the candidate is the first author among eleven authors.

   He contributed approximately 40% to the project's scientific conceptual development. He played a central role in developing the core hypothesis and the mechanistic framework underlying the study. His main contribution was extensive experimental and methodological work, which accounted for about 70% of the generated data. This work included developing and implementing CLOSE microscopy, executing experiments, quantitatively analyzing stoichiometry and structural data, and integrating multiscale imaging data. The candidate contributed approximately 70% to the analysis and interpretation of the data. He played a leading role in developing the membrane mechanical model that explains pore growth and mitochondrial matrix extrusion. He contributed approximately 50% to the preparation of the manuscript, including drafting.

   His contributions were essential to the nanoscale structural characterization of BAK assemblies and to the development of the biophysical framework describing mechanically driven apoptotic pore expansion.

Introduction

Apoptosis – a form of regulated cell death

Apoptosis is a fundamental and highly conserved form of regulated cell death essential for embryonic development, tissue homeostasis, and removal of damaged or dysfunctional cells. It was first recognized by Kerr, Wyllie, and Currie in 1972 as a morphologically and mechanistically 'programmed' process, characterized by controlled cellular self-destruction and distinct from lytic types of cell death, such as accidental or regulated necrosis (Elmore, 2007; Kerr et al., 1972). Morphologically, apoptotic cells undergo characteristic changes including cell shrinkage, chromatin condensation (pyknosis), nuclear fragmentation (karyorrhexis), membrane blebbing, and fragmentation into membrane-bound apoptotic bodies, which are rapidly engulfed by phagocytes, thereby preventing the leakage of intracellular contents (Kerr et al., 1972; Taylor et al., 2008). Biochemically, apoptosis is driven by the activation of caspases, a family of cysteine-aspartyl proteases. Based on their functional role, caspases are categorized into initiator and executioner caspases. Initiator caspases such as caspases-2, -8, and -9 are apical in the apoptosis pathway, where they function to detect and integrate upstream death signals. Upon activation, they activate executioner caspases, including caspases-3, -6, and -7, which catalyze the systemic dismantling of cellular components, including DNA fragmentation and breakdown of key structural proteins, causing the characteristic phenotypic changes of apoptosis (Galluzzi et al., 2018; Nicholson, 1999; Tait and Green, 2010).

Evolutionary studies have revealed that the core regulatory components and signaling events of apoptosis are conserved across metazoans, from nematodes and flies to mammals, underscoring its ancient evolutionary origin as a cell-fate program. Genetic disposition for orthologues of mammalian apoptosis regulators is found, for example, in both *C. elegans* and *D. melanogaster*, underscoring the high degree of conservation of the pathway (Bender et al., 2012; Fuchs and Steller, 2011; Krasovec et al., 2024; Lee et al., 2011; Metzstein et al., 1998).

Functionally, apoptosis is indispensable during embryogenesis for morphogenetic processes such as digit separation, neural tube closure, and sculpting of organ structures (Fuchs and Steller, 2011; Jacobson et al., 1997; Lindsten et al., 2000). In adult tissues, apoptosis is crucial for maintaining equilibrium in cell numbers within proliferative systems, such as the hematopoietic and epithelial compartments, and for immune homeostasis by depleting autoreactive lymphocytes and attenuating immune responses (Elmore, 2007; Nagata and Tanaka, 2017). Apoptosis acts as a quality-control mechanism, selectively removing cells with irreparable genomic damage, oncogenic transformation, or intracellular infection to preserve tissue integrity and organismal health (Elmore, 2007; Galluzzi et al., 2018; Reed, 1999).

The initiation of apoptosis can be triggered by diverse intracellular or extracellular cues, transduced via either the extrinsic (death receptor) or intrinsic (mitochondrial, see Mitochondrial apoptosis) pathways. These distinct but interconnected signaling pathways converge on the activation of executioner caspases to ensure the controlled dismantling of the cell (Galluzzi et al., 2018; Lossi, 2022). Tight regulation is essential, as insufficient apoptosis allows genetically unstable or autoreactive cells to survive, promoting tumorigenesis or autoimmune disease. Conversely, excessive or inappropriate apoptosis contributes to degenerative, ischemic, and certain infectious diseases. Thus, the balance, timing, and localization of apoptosis are crucial determinants of tissue homeostasis and pathology, making its core machinery a focal point of therapeutic exploration in cancer, neurodegeneration, autoimmunity, and beyond (Adams and Cory, 2007; Mattson, 2000; Moujalled et al., 2021; Singh et al., 2019)

The role of Mitochondria

In mammalian cells, mitochondria serve as dual-function organelles that sustain cellular life through oxidative phosphorylation, intermediate biosynthetic metabolism, and the regulation of calcium homeostasis and redox balance (Duchen, 2004). At the same time, they actively govern cell death decisions as critical signaling hubs for intrinsic apoptosis, acting as both sensors and executioners of intracellular stress signals (Bock and Tait, 2019; Tait and Green, 2010). Their involvement reflects an

evolutionary origin as endosymbiotic α-proteobacteria that established a mutualistic relationship within ancestral eukaryotic cells more than 1.5 billion years ago (Dyall et al., 2004; Gray, 2012; Roger et al., 2017; Sagan, 1967; Sicheritz-Pontén et al., 1998). Mitochondria are double-membrane organelles composed of the mitochondrial outer membrane (MOM) and the highly folded mitochondrial inner membrane (MIM), both characterized by specific lipid compositions and permeabilities. The MOM acts as a semi-permeable barrier to the cytosol, mediates inter- and intraorganellar communication via membrane contact sites, and facilitates the exchange of proteins, metabolites, lipids, and ions with the cytosol and other cellular compartments (Chandel, 2014; Eisenberg-Bord and Schuldiner, 2017a, 2017b; Gellerich et al., 2000; Marchi et al., 2017). The MIM possesses highly restricted permeability and is critical for maintaining the proton gradient that gives rise to the mitochondrial transmembrane potential, required for oxidative phosphorylation, and for phospholipid biosynthesis (Frey et al., 2002; Kühlbrandt, 2015; Tatsuta and Langer, 2017; Zhao et al., 2019). While the MOM is mainly rich in phosphatidylcholine, phosphatidylethanolamine, and phosphatidylinositol, the MIM is enriched in non-bilayer-forming lipids such as cardiolipin (CL), due to the bacterial ancestry (Ardail et al., 1990; Colbeau et al., 1971; De Kroon et al., 1997; Hovius et al., 1993). Structurally, the MIM contains highly folded invaginations, named *cristae*, which harbor the mitochondrial oxidative phosphorylation system (Frey et al., 2002; Kühlbrandt, 2015; Palade, 1953; Sjöstrand, 1953). The mitochondrial matrix fulfills essential functions, including the assembly of iron-sulfur clusters and the tricarboxylic acid (TCA) cycle (Cardenas-Rodriguez et al., 2018; Lill and Lill, 2020; Mailloux et al., 2007; Martínez-Reyes and Chandel, 2020). It also contains the mitochondrial DNA (mtDNA) and the transcriptional and translational machinery required for mitochondrial gene expression. During the symbiotic evolution of mitochondria and eukaryotic cells, the vast majority of the proto-mitochondrial genome was transferred to the host nucleus, while the retained mtDNA only encodes for a subset of essential oxidative phosphorylation components (Mazunin et al., 2015). Consequently, nuclear-encoded mitochondrial proteins are imported into the individual mitochondrial compartments by specialized, well-regulated translocase complexes in the mitochondrial membranes (Wiedemann and Pfanner, 2017).

In mammalian cells, mitochondria have evolved into a highly dynamic network. The dynamics of this network are mediated by constant fusion and fission of the organelle and are essential for proper mitochondrial function, the proper segregation and transmission of mtDNA, and adaptation to cellular cues, such as alterations in metabolic state (Cantó, 2018; Giacomello et al., 2020; Joaquim and Escobar-Henriques, 2020; Sabouny and Shutt, 2021; Tábara et al., 2024; Wai and Langer, 2016; Youle and Van Der Bliek, 2012). Mitochondrial dynamics are regulated by a finely tuned machinery of dynamin-related large GTPases, including dynamin-related protein 1 (DRP1), which is responsible for mitochondrial fission, mitofusin 1 and 2 (MFN1/2), which mediate fusion of the MOM, and optic atrophy 1 (OPA1), which is responsible for MIM fusion and involved in regulating *cristae* ultrastructure (Tábara et al., 2024). This machinery is further modulated by post-translational modifications, including ubiquitylation, phosphorylation, sumoylation, and proteolytic processing in response to cellular triggers (Escobar-Henriques and Langer, 2014; Hofer and Wenz, 2014; MacVicar and Langer, 2016; Mishra and Chan, 2016). Mitochondrial plasticity is closely associated with mitochondrial biogenesis, degradation, and apoptosis regulation, and is therefore critical for cellular health, while its dysregulation is strongly linked to disease (Chan, 2020).

Despite their intricate functional integration, mitochondria have retained structural, biochemical, and signaling characteristics from their bacterial origins, such as the CL-rich MIM, which have been repurposed in apoptosis regulation, among other functions. Their bacterial evolutionary heritage and subsequent symbiotic integration have provided the molecular framework that enables mitochondria to function as platforms for apoptotic regulation and to tightly couple mitochondrial function to eukaryotic cell fate decisions.

Mitochondrial apoptosis and MOMP

Two distinct molecular signaling pathways mediate the execution of apoptosis (Lossi, 2022): the ‘extrinsic’ or ‘death receptor’ pathway and the ‘intrinsic’ or ‘mitochondrial’ pathway. Extrinsic apoptosis is triggered by external factors via death receptors at the plasma membrane, such as Fas (also known as CD95), tumor necrosis factor (TNF),

and TNF-related apoptosis-inducing ligand (TRAIL) receptors. Upon binding their corresponding ligands, these receptors form a death-inducing signaling complex (DISC), which triggers the activation of initiator caspases, such as caspase-8, followed by the activation of effector caspases-3 and -7. Unlike the extrinsic pathway of apoptosis, the intrinsic apoptotic pathway is initiated by a variety of intracellular stress stimuli, including irreparable DNA damage, oncogene activation, cytoskeletal disruption, oxidative stress, and growth factor deprivation (Galluzzi et al., 2018; Lossi, 2022). Such stress cues converge on mitochondria, specifically the MOM, where they trigger MOM permeabilization (MOMP), facilitated via the formation of the so-called apoptotic pore by pro-apoptotic effectors of the B-cell lymphoma-2 (BCL-2) protein family (Chipuk et al., 2006; Czabotar and Garcia-Saez, 2023; Peña-Blanco and García-Sáez, 2018; Youle and Strasser, 2008), see The BCL-2 protein interactome). Apoptotic pore formation represents a decisive, rate-limiting step in apoptosis, as it physically breaches the outer membrane and allows the release of mitochondrial content such as cytochrome *c* (cyt *c*) into the cytosol, triggering downstream apoptosis execution. Cytosolic cyt *c* binds to apoptosis protease-activating factor-1 (APAF-1) in a dATP/ATP-dependent manner, inducing the oligomerization of APAF-1 into the ~1.4 MDa heptameric apoptosome, which recruits and activates initiator caspase-9 (Kim et al., 2005; Li et al., 1997; Riedl and Salvesen, 2007; Zou et al., 1997). Active caspase-9 subsequently cleaves and activates downstream executioner caspases-3 and -7, triggering downstream apoptosis execution. Apoptotic pores in the MOM additionally allow the release of other intermembrane space factors such second mitochondria-derived activator of caspase (SMAC, also known as DIABLO) or the serine protease HtrA2 (also referred to as OMI) which bind to and antagonize inhibitor of apoptosis proteins (IAPs), thereby allowing rapid and efficient activation of caspases (Du et al., 2000; Hao and Mak, 2010; Suzuki et al., 2001; Verhagen et al., 2000). Additional proteins released from mitochondria during MOMP, such as apoptosis-inducing factor (AIF) and endonuclease G, may propagate caspase-independent death pathways, particularly in contexts where caspase activation is inhibited (Joza et al., 2001; Van Loo et al., 2001). Recent findings revealed that, in addition to classical apoptogenic proteins, the mtDNA can be released into the

cytosol through apoptotic pores (McArthur et al., 2018; Riley et al., 2018). Cytosolic mtDNA acts as a ligand for the cyclic GMP–AMP synthase (cGAS), triggering activation of the cGAS-stimulator of interferon genes (STING) signaling, which promotes an innate immune response characterized by the production of type I interferons. This inflammatory signaling is normally restrained by caspases, which cleave key components of pro-inflammatory pathways to suppress immune activation (Rongvaux et al., 2014; White et al., 2014). However, when caspase activity is reduced or inhibited, MOMP facilitates the activation of pro-inflammatory signaling responses.

This underscores the pivotal role of mitochondrial apoptotic pore formation and MOMP, as well as subsequent mitochondrial alterations, in determining cell fate: cells that undergo MOMP inevitable die, even when caspase activation is inhibited, via alternative death mechanisms (Tait and Green, 2010, 2008). Accordingly, current models propose that caspases primarily function to limit MOMP-driven inflammation and accelerate the removal of dying cells, rather than to drive cell death execution (Rongvaux et al., 2014; White et al., 2014).

The BCL-2 protein interactome

The mitochondrial pathway of apoptosis and the execution of MOMP are tightly regulated by the BCL-2 proteins, a family of proteins evolutionarily and functionally conserved throughout a broad spectrum of metazoans (Aouacheria et al., 2013). This family is comprised of about 20 canonical members with specific pro- and anti-apoptotic functions, which form a complex regulatory network termed the ‘BCL-2 interactome’, that enables the integration of internal cellular stress signals to trigger rapid life or death decisions ((Galluzzi et al., 2018), reviewed in (Czabotar and Garcia-Saez, 2023; Jenner and Garcia-Saez, 2024)). Due to their pivotal role at this critical checkpoint, BCL-2 proteins are indispensable for developmental and cellular homeostasis and implicated in a broad spectrum of pathological conditions when dysregulated, including cancer, autoimmunity, and degenerative diseases (Czabotar and Garcia-Saez, 2023; Singh et al., 2019). The BCL-2 proteins are characterized by the presence of up to four BCL-2 homology (BH) domains, which mediate protein folding and interaction with other BCL-2 proteins (Lee et al., 2011; Popgeorgiev et al., 2020). Based on their

domain organization, structure, and functional role in the BCL-2 interactome, they are categorized into three groups. The ‘executioner’ BCL-2 proteins BCL-2-associated X protein (BAX) and BCL-2 homologous antagonist/killer (BAK) are the executors of apoptotic pore formation and thus direct mediators of MOMP. Executioners contain the BH-domains 1-3 and structurally adopt the so-called BCL-2 fold (see below). The pore-forming family member BCL-2-related ovarian killer protein (BOK) is also classified as an executioner, yet remains considerably less understood than BAX and BAK, particularly with regard to its interactome and regulation (Shalaby et al., 2020). ‘Initiator’ BCL-2 proteins, including BH3-interacting domain death agonist (BID), BCL-2-associated agonist of cell death (BAD), BCL-2-interacting mediator of cell death (BIM), p53 upregulated modulator of apoptosis (PUMA), and phorbol-12-myristate-13-acetate-induced protein 1 (NOXA), are also referred to as BH3-only proteins as the majority of them contain only BH domain 3 and, except for their BH3 domain, are largely unstructured. The functional role of initiators is to sense cellular stresses and trigger executioner activation either directly (‘direct activators’) or indirectly by inhibiting the pro-survival role of guardian BCL-2 proteins (‘sensitizers’) (Dai et al., 2011; Hockings et al., 2015; Kim et al., 2009; Kuwana et al., 2005; Letai et al., 2002; Wei et al., 2000). BID is unusual among the initiator group as it also contains a BH4 domain, adopts the classical BCL-2 fold, and was recently shown to exhibit direct executioner function in addition to its role as initiator (Chou et al., 1999; Flores-Romero et al., 2022; Kvansakul et al., 2008). The ‘guardian’ BCL-2 proteins, including BCL-2, B-cell lymphoma-extra large (BCL-XL), BCL-2-like protein 2 (BCL-W), induced myeloid leukemia cell differentiation protein (MCL-1), and BCL2A1, contain all four BH domains and adopt the BCL-2 fold. Functionally, they promote cell survival by sequestering both initiator and executioner BCL-2 proteins into inhibitory complexes and by promoting the retro-translocation of executioners form the membrane to the cytosol (Billen et al., 2008; Czabotar and Garcia-Saez, 2023; Edlich et al., 2011; Jenner and Garcia-Saez, 2024).

The dynamic and competitive network of homo- and heterotypic interactions among members of these three BCL-2 protein groups (i.e., the BCL-2 interactome) constitutes the central regulatory component of mitochondrial apoptosis. These interactions occur both in the cytosol and in the membrane-embedded context, particularly at the MOM,

where the local membrane environment, like lipid composition and curvature, modulates the binding hierarchy between family members (Bleicken et al., 2017; Czabotar and Garcia-Saez, 2023; García-Sáez et al., 2009). Central to this dynamic regulation is the globular, α-helical BCL-2 fold exhibited by all multi-domain BCL-2 proteins in solution (Chou et al., 1999; Denisov et al., 2003; McDonnell et al., 1999; Muchmore et al., 1996; Petros et al., 2004, 2001; Suzuki et al., 2000). It is composed of two central, predominantly hydrophobic α-helices shielded by six to seven surrounding amphipathic α-helices of varying length and bears an intrinsic conformational instability, which allows for structural rearrangements associated with the activation of the BCL-2 proteins. This provides the perquisite for three main regulatory features: i) the central amphipathic region (α-helices 5 and 6), which, when exposed, can directly interact with membrane lipids and is essential for pore-forming activity, ii) a hydrophobic surface groove within the BCL-2 fold that can be occupied by a C-terminal membrane anchor (α-helix 9), which regulates the localization to lipid membranes, including the MOM, and iii) the BH3 domain located in α-helix 2, which is critical in mediating interaction between BCL-2 family members by binding to the hydrophobic surface groove.

Upon cellular stress triggers, initiator BCL-2 proteins act as ‘BH3 donors’ to trigger the activation of apoptotic executioners and neutralize the anti-apoptotic role of guardians. Executioner activation involves opening the intrinsically unstable BCL-2 fold, initiated by the binding of an initiator BH3 domain to the executioner's hydrophobic groove. This interaction displaces the executioner's C-terminal membrane anchor, a process termed ‘unlocking’, thereby enabling its insertion into the MOM (Czabotar & Garcia-Saez, 2023). Unlocking further destabilizes the BCL-2 fold, leading to dissociation and unfolding of the N-terminal α-helix 1, exposure of the BH3 domain, and homo-dimerization of the executioners via symmetric BH3-into-groove interactions. This stabilizes the open, active conformation and exposes the hydrophobic pore-forming region of the executioner, thereby promoting higher-order oligomerization and pore formation. Once activated, executioners can also serve as BH3 donors, driving the activation of additional executioners in a manner analogous to initiator-driven

activation. Guardian BCL-2 proteins act as ‘BH3 sinks’ as they bind BH3 domains of initiators or executioners but lack the ability to form pores (Billen et al., 2008)

Differences in binding affinities among subsets of initiators, guardians, and executioners, together with distinct interaction hierarchies of complexes in solution compared to the membrane, give rise to a highly complex BCL-2 protein interaction network (Bleicken et al., 2017). Consequently, the function of BCL-2 proteins in apoptotic pore formation should be understood as the outcome of an integrated regulatory system, rather than attributed to individual proteins (reviewed in (Czabotar and Garcia-Saez, 2023)).

Apoptotic pore formation by BAX and BAK

The BCL-2 proteins BAX and BAK are considered the key executors of mitochondrial apoptosis as they directly mediate the formation of apoptotic pores. In healthy cells, BAX is predominantly cytosolic, whereas BAK is anchored to MOM via its C-terminal transmembrane domain, where it is maintained in its inactive conformation by binding to voltage-dependent anion-selective channel protein 2 (VDAC2) (Cheng et al., 2003; Lazarou et al., 2010; Suzuki et al., 2000). The cytosolic localization of BAX is explained by the accommodation of its transmembrane domain within its own hydrophobic surface groove, as well as its continuous removal from mitochondria through retrotranslocation, which is mediated by interactions with the guardian BCL-xL (Edlich et al., 2011; Garner et al., 2016; Robin et al., 2018; Suzuki et al., 2000). Upon activation, both BAX and BAK undergo a series major conformational rearrangements, including dissociation and unfolding of α-helix 1, exposure of the BH3 domain (α-helix 2), and detachment of the core region (α-helices 2–5) from the latch region (α-helices 6–8), a process termed ‘unlatching’ (Alsop et al., 2015; Bleicken et al., 2014; Cuconati et al., 2002; Czabotar et al., 2013; Dewson et al., 2008; Griffiths et al., 1999; Sandow et al., 2021; Weber et al., 2013). Consequently, the exposed BH3 domain engages neighboring executioners to form homo- or heterotypic dimers of BAX and BAK, and opening of the core region exposes hydrophobic surface patches (α-helices 4–5) and the pore-forming α-helices 5 and 6, resulting in direct interaction of BAX and BAK with MOM lipids (Czabotar et al., 2013; Dewson et al., 2012, 2008). Membrane insertion

and dimerization provide the molecular basis for higher-order oligomerization, which is tightly correlated with apoptotic pore formation (Birkinshaw et al., 2021; Cowan et al., 2020; Subburaj et al., 2015)

The toroidal nature of apoptotic pores

The pores formed by BAX and BAK are toroidal, or protein-lipid pores (Basanez et al., 1999; Basañez et al., 2002; García-Sáez et al., 2006; Qian et al., 2008; Terrones et al., 2004). In such pores, both proteins and lipids line the lumen, with the two membrane leaflets bending to form a highly curved, continuous surface at the pore edge. Consequently, the properties of toroidal pores are defined not only by the proteins involved but also by the biophysical characteristics of the membrane bilayer. Consistent with models of toroidal pore formation by α-helical proteins, estimations from experiments in model membranes suggest that the membrane insertion of BAX and BAK leads to local membrane thinning and an associated increase in membrane tension (Bleicken et al., 2018; Stephanie Bleicken et al., 2013; Cowan et al., 2020; Flores-Romero et al., 2020; García-Sáez et al., 2005; García-Sáez et al., 2006; Lee et al., 2004). In these models, pore opening is predicted to occur once this tension exceeds a critical threshold. The resulting high curvature at the pore rim would generate energetically highly unfavorable lipid-packing defects, creating line tension that favors pore closure. BAX and BAK are thought to counteract this effect, presumably by superficially inserting α-helices into the lipid headgroup region to reduce the line tension and stabilize open pores (Bleicken et al., 2018, 2014; Stephaniel Bleicken et al., 2013; García-Sáez et al., 2007; Lee et al., 2004; Unsay et al., 2017). Importantly, these models are largely based on experiments in simplified membrane systems. Direct quantitative measurements of the relevant biophysical parameters in native mitochondrial membranes are still lacking. Consequently, the precise *in situ* mechanism of pore formation by BAX and BAK remain to be fully elucidated.

Although the precise structural determinants remain unresolved, models have been proposed to explain how BAX and BAK dimers arrange at the pore edge. The ‘clamp model’ suggests a symmetric arrangement of dimers across the bilayer, with their transmembrane domains inserted anti-parallel from opposite sides of the membrane,

whereas the ‘asymmetric model’ proposes that both transmembrane domains of a dimer insert in parallel from the outer leaflet (Bleicken et al., 2014; Mandal et al., 2016). However, the pronounced conformational flexibility of activated BAX and BAK has so far precluded discrimination between these models (Bleicken et al., 2018, 2014).

After initial pore opening, further pore expansion involves higher-order oligomerization of BAX and BAK, which has been proposed to involve direct protein-protein interaction, membrane-mediated interactions, and linkage of dimers through lipid acyl chains (Cowan et al., 2020; Dewson et al., 2009; Reynwar et al., 2007; Uren et al., 2017). Notably, BAX and BAK oligomers lack a defined stoichiometry but assemble into multiple coexisting structures composed of dimer units (Dewson et al., 2008; Subburaj et al., 2015). At the supramolecular level, BAX has been shown to form complexes of varying size and geometry in the MOM, including line-, arc-, and ring-shaped assemblies, of which arcs and rings have been shown to form membrane pores (Salvador-Gallego et al., 2016). In line with their toroidal nature, apoptotic pores are highly tunable in size. While small apoptotic pores are sufficient to release mitochondrial apoptotic factors into the cytosol, they expand with the progressive insertion of BAX and BAK into the membrane (Bleicken et al., 2018; Riley et al., 2018), reaching diameters of several hundred nanometers (Salvador-Gallego et al., 2016; Schweighofer et al., 2024).

Mitochondrial alterations in apoptosis

In addition to and associated with apoptotic pore formation and MOMP, mitochondria undergo severe structural and functional alterations that modulate the efficiency and outcome of cell death (reviewed in (Cosentino and García-Sáez, 2014)). These include the transfer of lipids between mitochondria and other organelles, such as the endoplasmic reticulum (ER) (Hoppins and Nunnari, 2012), and between the MIM and MOM (Kagan et al., 2005). Of special importance is the enrichment of CL at the MOM, which has been linked to alterations in membrane curvature, the interaction with BCL-2 proteins, and the release of apoptotic factors, thus further promoting apoptosis progression (Garcia Fernandez et al., 2002; Gonzalvez et al., 2005; Kagan et al., 2005; Lutter et al., 2001; Unsay et al., 2013). In addition, apoptotic pore formation and its

downstream consequences inevitably result in the loss of essential mitochondrial functions, including the regulation of calcium homeostasis and maintenance of the transmembrane potential necessary for oxidative phosphorylation, which is associated with swelling of the mitochondrial matrix (Green and Kroemer, 2004; Ricci et al., 2004; Scorrano et al., 2003; Vander Heiden et al., 1999; Wang, 2001). Furthermore, proteolytic processing and disruption of mitochondrial fusion GTPase optic atrophy 1 (OPA1) oligomers during apoptosis destabilize the characteristic MIM *cristae* ultrastructure, a process termed *cristae* remodeling, causing the *cristae* junctions to open and the MIM to unfold. Apoptotic *cristae* remodeling also facilitates the complete release of cyt *c*, which is typically confined within the *cristae* folds (Cipolat et al., 2006; Frezza et al., 2006; Scorrano et al., 2002). Recent studies report an additional striking alteration of the mitochondrial ultrastructure, which is the permeabilization and extrusion of the MIM through apoptotic macropores formed by BAX and BAK in the MOM. MIM permeabilization (MIMP) enables the release of mitochondrial matrix macromolecules, such as mtDNA, into the cytosol (McArthur et al., 2018; Riley et al., 2018), where they function as immunogenic triggers. Consequently, MIM extrusion and MIMP following MOMP can shift the generally immunologically silent consequences of apoptosis execution to inflammatory responses under conditions of low caspase activity (Rongvaux et al., 2014; White et al., 2014). This modulation directly affects the surrounding cellular microenvironment, which has critical implications for various disease pathologies (Heilig et al., 2023; Victorelli et al., 2023). However, the regulatory basis of apoptotic macropore formation at the molecular and structural levels, the mechanisms of MIM extrusion and MIMP, and the potential contributions of additional factors, such as mitochondrial membranes and interacting proteins, remain incompletely understood.

The link between mitochondrial apoptosis and mitochondrial fission

Another striking characteristic of apoptosis is the extensive fragmentation of the mitochondrial network. This phenomenon is a conserved feature of apoptotic cell death, even in species that do not involve MOMP, yet its mechanistic contribution to cell death remains poorly understood (Arnoult, 2007; Youle and Karbowski, 2005).

In healthy cells, mitochondrial fission is initiated by the recruitment of DRP1 to the MOM via adaptor proteins, including mitochondrial fission factor (MFF), the mitochondrial dynamics proteins of 49 and 51 kDa (MID49/MID51), and the mitochondrial fission 1 protein (FIS1) (Losó n et al., 2013; Osellame et al., 2016; Palmer et al., 2013). DRP1 oligomerizes into helical structures at mitochondria-ER contact sites (MERCs), which are associated with mtDNA replication and pre-constriction of mitochondria mediated by actin nucleation (Friedman et al., 2011; Fröhlich et al., 2013; Kalia et al., 2018; Korobova et al., 2013). Following DRP1 recruitment and constriction, the final step of mitochondrial division is governed by mitochondrial membrane tension and may involve other factors, such as dynamin 2 (Lee et al., 2016; Mahecic et al., 2021).

During apoptosis, DRP1 mediates mitochondrial fragmentation and participates in *cristae* remodeling to facilitate cyt *c* release (Frank et al., 2001; Otera et al., 2016). Upon BAX and BAK activation, DRP1 is SUMOylated by the mitochondrial-anchored RING-finger containing protein MAPL, which stabilizes its oligomeric form at mitochondria. This, in turn, functionally stabilizes MERCs, which act as hotspots for mitochondrial fission, calcium flux, *cristae* remodeling, and cyt *c* release (Prudent et al., 2015). DRP1 colocalizes with BAX at apoptotic pores in the MOM, supporting the assumption of a functional interplay between the two proteins (Karbowski et al., 2002). Indeed, DRP1 has been shown to enhance BAX oligomerization by promoting negative membrane curvature in reconstituted systems *in vitro* (Montessuit et al., 2010). Despite these findings, the role of DRP1 in apoptosis remains controversial as mitochondrial fission and cyt *c* release can be uncoupled, and DRP1-deficient cells also undergo apoptosis, albeit with altered kinetics (Parone et al., 2006; Sheridan et al., 2008). Thus, although DRP1 clearly interfaces with apoptotic regulators such as BAX, the molecular mechanisms and functional significance of DRP1 in apoptosis execution remain unclear.

Closing remarks

Despite major advances in elucidating the regulatory principles of mitochondrial apoptosis, key mechanistic questions remain unresolved. While BAX and BAK are well established as the executioners of MOMP through the formation of toroidal apoptotic

pores, the mechanisms governing their activation, oligomerization, and pore growth at the MOM are increasingly recognized as multifactorial and tightly integrated with mitochondrial membrane dynamics. Recent findings show that apoptotic pores can expand to form large macropores that permit extrusion of the MIM, leading to MIMP and the release of matrix macromolecules, including mtDNA, thereby reshaping the immunological consequences of apoptosis. Yet, how these macropores evolve from initial BAX and BAK oligomers, the structural and biophysical determinants that govern pore expansion, and the spatial and temporal regulation of these processes remain incompletely understood.

Further complexity arises from the interplay between mitochondrial dynamics and apoptosis. The fission GTPase DRP1 has emerged as a potential co-regulator of apoptotic pore formation, as it colocalizes with BAX and modulates membrane curvature, suggesting roles beyond mitochondrial division. However, the molecular requirements, regulatory control, and functional consequences of the BAX-DRP1 interplay at mitochondria remain unresolved and highly controversial.

In this study, we address these outstanding questions by dissecting the structural, molecular, and mechanistic basis of BAX- and BAK-mediated apoptotic pore formation, with a particular focus on the functional interplay between BAX and DRP1 and the mechanistic regulation governing apoptotic macropore formation and MIM extrusion.

Aims of the Study

The overarching goal of this study is to elucidate the regulatory aspects and molecular determinants of mitochondrial apoptotic pore formation.

First, we investigate the mechanistic interplay between the fission GTPase DRP1 and the executioner protein BAX, focusing on defining the molecular requirements, temporal regulation, and functional relevance of their interaction during apoptosis. By identifying how DRP1 influences BAX activation, we aim to clarify the contribution of mitochondrial dynamics machinery to mitochondrial apoptotic pore formation.

Second, we characterize the cooperative behavior of the executioner proteins BAX and BAK to determine whether their functional redundancy masks distinct molecular regulatory differences. We assess their oligomerization kinetics, supramolecular assembly, and structural organization into apoptotic pore complexes at the single-molecule level to identify a potential co-regulatory mechanism.

Third, this study examines the kinetics of apoptotic pore growth and how the rate of pore expansion governs differential permeability to mitochondrial effector molecules. By linking pore growth dynamics to downstream signaling events, we aim to decipher how pore formation influences the immunological outcome of apoptosis, including inflammatory signaling driven by mitochondrial content release.

Finally, we explore the consequences of apoptotic pore formation for mitochondrial architecture and membrane ultrastructure. This includes assessing how the biophysical properties of both the MIM and the MOM influence pore expansion, facilitate MIM extrusion, and ultimately determine cell fate.

Together, these aims seek to provide a mechanistic and structural framework for understanding how BAX- and BAK-mediated apoptotic pore formation is regulated, how DRP1 contributes to apoptotic execution, and how the pore architecture dictates the downstream cellular and immunological consequences of apoptosis.

Summary of Results and Discussion

1. The functional interplay between BAX and DRP1 in apoptosis

Although extensive mitochondrial fragmentation mediated by DRP1 is a striking feature of apoptosis, and a connection between BAX and DRP1 was proposed based on their colocalization at apoptotic foci, the molecular basis and functional relevance of their interplay remain controversial. Previous studies failed to detect direct contacts between the two proteins and instead suggested that DRP1 influences BAX activity indirectly through its role in membrane remodeling (Montessuit et al., 2010). However, in this model, the possibility of a direct physical interaction between BAX and DRP1, as well as its implications for apoptosis execution, remains open to debate. (Estaquier and Arnoult, 2007; Karbowski et al., 2002; Parone et al., 2006; Sheridan et al., 2008). Using multiple complementary approaches *in vitro* and in cells, we now provide evidence that challenges this conception and demonstrate that BAX and DRP1 physically interact under several experimental conditions.

1.1 BAX and DRP1 interact directly with each other in the membrane environment

To gain detailed insights into the spatial organization of BAX and DRP1 during apoptosis, we used single-molecule localization microscopy (SMLM) to visualize both proteins in apoptotic cells. Our results demonstrate that BAX and DRP1 not only colocalize but are part of the same protein complex in mitochondria of apoptotic cells. Quantification of the distance between individual BAX and DRP1 molecules in these complexes revealed that they are less than 30 nm apart (Appendix 1.1 Figure 1A-B, D), which is the limit of resolution of this technique. The measured distance between BAX and DRP1 is comparable to the distance observed between individual DRP1 molecules in an oligomeric DRP1 complex (Appendix 1.1 Figure 1C). Considering that both BAX and DRP1 are known to form large structures at the supra-molecular level (Fröhlich et al., 2013; Große et al., 2016; Salvador-Gallego et al., 2016), these results indicate that BAX and DRP1 may interact directly with each other. To validate this hypothesis, we utilized the dimerization-dependent fluorescent protein (ddFP) technique, a methodology that allows for the detection of direct protein interactions by the appearance of a fluorescent emission signal if the two tested components are less than

10 nm apart. Interestingly, the ddFP signal of BAX and DRP1 was negligible in healthy cells but became apparent as discrete mitochondrial foci upon apoptosis induction (Appendix 1.1 Figure 1E-G). These results were consistent across different cell types and apoptotic triggers (Appendix 1.1 Figure EV1) and demonstrate that BAX and DRP1 physically interact directly with each other, and that this interaction is strongly enhanced during apoptosis. Additionally, we measured the temporal evolution of the interaction of BAX and DRP1 by ddFP signal during apoptosis and found that it is tightly correlated with MOMP, as indicated by the release of fluorescently labeled SMAC into the cytosol (Appendix 1.1 Figure 2A-B). This interaction is independent of downstream caspase activation and persists until cell death (Appendix 1.1 Figure 2B-C), suggesting that it temporally correlates with the regulatory event of apoptotic pore formation.

These findings establish the association of BAX and DRP1 within the physiological cellular environment, particularly during apoptosis. However, they do not provide evidence to clarify whether this interaction is facilitated by direct binding between the two proteins or mediated through additional cellular factors. Thus, we employed fluorescence cross-correlation spectroscopy (FCCS) in a minimal reconstituted system to determine the individual molecular requirements for the interaction of BAX and DRP1. Notably, positive cross-correlation, and consequently the interaction between BAX and DRP1, was only detectable in the membrane of CL-containing giant unilamellar vesicles (GUVs) but not in solution (Appendix 1.1 Figures 3A-C and EV2A-B). This interaction was outcompeted by the addition of the activated BCL-2 initiator tBID, which interacts with BAX, demonstrating the specificity of the BAX-DRP1 interaction (Appendix 1.1 Figures 3C and EV2C). Our FCCS measurements additionally indicate a high binding affinity between BAX and DRP1, as we observed considerable complex formation at low membrane densities of both proteins (Appendix 1.1 Figure 3A-B). Our results demonstrating that BAX peptides interact with DRP1 in GUVs and cross-linking of BAX and DRP1 in large unilamellar vesicles (LUVs), followed by mass spectrometry (see below), provide additional evidence for BAX-DRP1 interaction specifically in the membrane environment *in vitro*. These results demonstrate that BAX and DRP1 interact directly *in vitro* and that the membrane environment is the sole additional requirement for their interaction.

The observation that the interaction between BAX and DRP1 depends on the membrane has important mechanistic implications. Both proteins adopt distinct oligomeric states and membrane-bound structural conformations compared to their soluble forms in the cytosol. Our results suggest that specifically the membrane-bound conformations of BAX and DRP1 provide the structural requirement necessary for their interaction. While DRP1 has been shown to assemble into helical oligomers on constricted lipid nanotubes (Fröhlich et al., 2013), the membrane-bound conformation of BAX remains poorly understood. It has been proposed that membrane insertion of BAX involves stable BAX dimers that further oligomerize into higher-order oligomeric complexes to mediate apoptotic pore formation (Czabotar et al., 2013; Hauseman et al., 2020; Lv et al., 2021; Salvador-Gallego et al., 2016; Subburaj et al., 2015). A recent study by cryo-electron microscopy provides structural insights into the conformational arrangement of BAX oligomers (Zhang et al., 2025). This study proposes that BAX oligomers are composed of repeating units consisting of four BAX protomers arranged as dimers of asymmetric dimers. In this model, the α1 helix of BAX becomes disordered, while the core region (α2–α5) mediates protomer interaction via the classically described BH3-in-groove interface. The C-terminal region (α6–α9) adopts distinct conformations in the two protomer types, and the α9 helices drive end-to-end association of the repeating units, enabling the formation of line-, arc-, and ring-shaped assemblies. Importantly, these structural data were obtained in the absence of a membrane environment. Consequently, the resolved conformations may not fully reflect the native architecture of membrane-bound BAX oligomers. Due to the limitation of incomplete or low-resolution data, the membrane-bound structure of BAX remains debated. Although technically challenging, further structural investigation of the membrane-associated complexes of both BAX and DRP1 will be necessary to uncover the structural details of their association.

1.2. The N-terminal region of BAX is required for the interaction with DRP1

To decipher the interaction surfaces of BAX involved in interaction with DRP1, we used a BAX peptide array and quantified the ability of individual BAX peptides immobilized on GUVs to recruit fluorescently labeled DRP1 (Appendix 1.1 Figure 4A-B). We found that peptides derived from α-helices 2, 5, 7, and 9 of BAX can recruit DRP1 to the GUV

membrane (Appendix 1.1 Figure 4C-D). Additionally, crosslinking of BAX-DRP1 complexes in LUVs, followed by mass spectrometry, revealed crosslinking sites in α-helices 2 and 5 of BAX (Appendix 1.1 Figures 4E-F and EV3). To validate the relevance of these interaction surfaces for the interaction of BAX and DRP1 in cells during apoptosis, we applied the ddFP system with α-helix deletion and point mutation variants of BAX (Appendix 1.1 Figure 5A) and quantified their interaction with DRP1. Importantly, we found that deletion of the N-terminal region of BAX, specifically the residues 19-37 located in α-helix 1 and the loop between α-helices 1 and 2 of BAX, completely abolished the interaction with DRP1. While we observed reduced interaction, the deletion of α-helices 4 or 5 and the C-terminal region of BAX, which we identified in the peptide array, is not sufficient to disrupt the interaction with DRP1 in cells (Appendix 1.1 Figure 5B-D). As the BH3 domain of BAX (located in α-helix 2) plays a critical role in BAX activation and its interaction with the BCL-2 proteins (Czabotar et al., 2013; Gavathiotis et al., 2010; Wang et al., 1998; Westphal et al., 2014), we tested whether it is also involved in the interaction with DRP1. However, except for the L63E point mutation, deletions or mutations in the BH3 domain of BAX did not cause significant changes in the interaction with DPR1 (Appendix 1.1 Figure 5B-E). This indicates that the BH3 domain of BAX is not required for its interaction with DRP1. Together, these results suggest that, although the interaction with DRP1 engages multiple BAX surfaces, it does not involve canonical interaction via the BH3 domain but instead requires the N-terminal region of BAX. This finding aligns with the structural model of BAX oligomers, in which the α1 helix does not contribute to the formation of the core dimer interface, suggesting that the N-terminal region remains accessible for interaction with DRP1.

1.3 The functional consequences of BAX-DRP1 interaction

The direct interaction of BAX and DRP1 in membranes in *vitro* and their association at apoptotic foci in cells raises the question of whether they contribute to each other's membrane recruitment or exert mutual functional influence. To address this, we examined how their interaction affects the membrane-remodeling activities of both proteins. The pore-forming activity of BAX, assessed by calcein release from LUVs and the influx of larger molecules such as cyt *c* (12.5 kDa) and the 104 kDa protein APC

into GUVs, was enhanced in the presence of DRP1 (Appendix 1.1 Figures 3D-E and EV2D). While the catalytic GTPase activity of DRP1 remained unaffected (Appendix 1.1 Figure EV2E), its membrane tethering activity, quantified by changes in the shape index of LUVs, increased in a concentration-dependent manner in the presence of BAX (Appendix 1.1 Figure 3F-G). These findings suggest that the interaction between BAX and DRP1 enhances the biochemical activities of both proteins, consistent with their functional roles in apoptosis. Beyond the previously proposed effects of both proteins on membrane remodeling (Montessuit et al., 2010), the involvement of the C-terminal membrane anchor of BAX in its association with DRP1 raises the possibility that DRP1 directly modulates the pore-forming activity of BAX, potentially influencing the architecture or stability of apoptotic pores. Conversely, the impact of BAX on the membrane remodeling activity of DRP1 aligns with the role of DRP1 in driving mitochondrial fragmentation during apoptosis and may depend on membrane-inserted regions of BAX that engage DRP1.

To test whether BAX and DRP1 recruit each other to apoptotic foci, we visualized the kinetics of the accumulation of fluorescently labeled BAX and DRP1 in mitochondria upon apoptotic triggers. Despite the technical difficulty of detecting small, initial complexes due to limited sensitivity in detecting the dim signal, DRP1 complexes consistently appeared in mitochondria prior to BAX accumulation in the same foci (Appendix 1.1 Figure 6A). To assess the potential role of DRP1 in recruiting BAX to the mitochondrial membrane, we tested several functional DRP1 mutants for their interaction with BAX using the ddFP system. These included the catalytic dominant-negative K38A, D221A, which inhibits higher-order oligomerization, R376E, which blocks DRP1 binding to MFF, and the monomeric K642E variant of DRP1, which we expressed in DRP1 KO cells. Interestingly, while these mutations caused alterations in mitochondrial morphology, none inhibited the interaction with BAX (Appendix 1.1 Figure 5F-H). Except for the K38A mutant version of DRP1, these mutations caused a delay in the appearance of the ddFP signal. In line with the observation that the GTPase activity of DRP1 is not influenced by BAX, this suggests that membrane insertion, which is altered in these variants, and not the catalytic activity of DRP1, is the main requirement for BAX/DRP1 interaction.

Previous studies demonstrated that DRP1 is SUMOylated by MAPL to stabilize its oligomeric form at mitochondria during apoptosis (Prudent et al., 2015). We therefore tested whether MAPL-dependent SUMOylation is required for the interplay of BAX and DRP1. However, neither depletion of MAPL nor the SUMO-dead K557/560/569/571R mutant of DRP1 altered its interaction with BAX, as measured by the ddFP signal (Appendix 1.1 Figures 5F-H and EV4E-G). These findings indicate that the BAX-DRP1 interaction occurs independently of DRP1 SUMOylation, suggesting that SUMOylation may instead occur downstream of their association. Notably, BAX accumulation in apoptotic complexes is independent of DRP1, as BAX forms complexes without DRP1, and its mitochondrial accumulation remains unchanged when DRP1 is depleted (Appendix 1.1 Figure 6B). Collectively, these findings suggest that DRP1 is recruited to mitochondrial apoptotic foci upstream of BAX, where the two proteins interact in the same complex, but DRP1 is not required for the translocation of BAX to mitochondria.

Our findings clearly demonstrate that the interaction between BAX and DRP1 modulates the membrane activity of both proteins *in vitro*. However, determining the functional relevance of this interaction during apoptosis has proven difficult. One key challenge is disentangling the direct influence of DRP1 on BAX activity from secondary effects, such as changes in mitochondrial morphology and homeostasis. Genetic manipulation of DRP1 inevitably perturbs mitochondrial dynamics, thereby affecting apoptotic sensitivity. The complexity is further amplified by the redundancy of the BCL-2 family in regulating apoptosis, particularly among BH3-only proteins, which provide multiple alternative paths for BAX activation. To overcome these limitations, we implemented a chemically inducible protein dimerization system to artificially dimerize BAX and DRP1 in cells. Remarkably, induced dimerization of BAX and DRP1 in living cells triggered both proteins to translocate to mitochondrial oligomeric complexes resembling apoptotic foci (Appendix 1.1 Figures 6C and EV5A, F). This translocation was associated with profound remodeling of the mitochondrial network, including fragmentation and perinuclear collapse of mitochondria, and induced MOMP, as indicated by mitochondrial depolarization (Appendix 1.1 Figure 6D-F). Additionally, this process is accompanied by characteristic apoptotic hallmarks, including BAX activation, cyt *c* release, activation of executioner caspases, PARP cleavage, and cell

death (Appendix 1.1 Figure EV5G-K). Strikingly, BAX and DRP1 dimerization also triggered mitochondrial translocation, mitochondrial network remodeling, and mitochondrial depolarization in cells lacking all canonical BCL-2 initiator (BH3-only) proteins (Appendix 1.1 Figure 6J-K). In contrast, induced dimerization of DRP1 or BAX with itself, or the artificial targeting of BAX to the MOM by dimerization with TOM20, failed to cause the apoptotic hallmarks observed with dimerized BAX and DRP1, indicating that this effect is specific to the interaction of BAX and DRP1 (Appendix 1.1 Figures 6G-I and EV5B-D). Collectively, these results demonstrate that forcing the interaction of BAX and DRP1 is sufficient to induce mitochondrial apoptosis in the complete absence of apoptotic triggers. This reveals an activating role for the interaction of DRP1 with BAX and raises the possibility that DRP1, despite lacking a BH3 domain, may substitute for or modulate the canonical BH3-dependent activation of BAX.

1.4 The role of DPR1 as a non-canonical BAX activator

Our findings demonstrate that the N-terminal region of BAX is essential for its interaction with DRP1, thereby providing a potential mechanism by which DRP1 may facilitate BAX activation. This region is proximal to the so-called “rear” site of BAX, located on the opposite side of the canonical hydrophobic groove, which engages BH3 domains of pro-apoptotic BCl-2 family initiators (Appendix 1.1 Figure EV4D). In addition to this canonical activation, previous work has established that binding at the rear site in soluble BAX can also trigger its activation (Gavathiotis et al., 2008). This non-canonical activation is attributed to the intrinsic conformational instability of the BCL-2 fold, which is partially stabilized by the N-terminal region acting as a ‘lock’ to maintain the inactive conformation. Consistently, systematic functional dissection of the N-terminal region of BAX and BAK demonstrated that antibodies or small molecules targeting the loop between α-helices 1 and 2 destabilize the fold and induce conformational rearrangements that trigger BAX activation (Alsop et al., 2015; Gitego et al., 2023; Iyer et al., 2016; Westphal et al., 2014). In line with these observations, our data suggest a previously unrecognized mechanism in which DRP1 engages the N-terminal region of membrane-associated BAX, thereby promoting conformational rearrangements that facilitate BAX activation and subsequent oligomerization

(Appendix 1.1 Figure EV6). This mechanism is consistent with the exclusive occurrence of BAX and DRP1 interaction in the membrane environment and with its independence from the catalytic activity of DRP1. Although it is not required for the interaction in cells, binding of DRP1 to other regions of BAX, particularly the α-helices 2, 5, and 9, as identified in the peptide array, may provide additional regulatory control during apoptosis. The α-helix 2 of BAX contains the BH3 domain, which mediates canonical regulatory interactions with other BCL-2 family members and drives symmetric BH3-into-groove dimerization during apoptotic pore formation. The α-helix 5 forms part of the central hydrophobic pore-forming region, whereas α-helix 9 serves as the C-terminal transmembrane controlling BAX insertion into the MOM. Engagement of these structural elements by DRP1 could provide additional means to modulate apoptotic pore formation.

In summary, we demonstrate that BAX and DRP1 directly interact at mitochondrial apoptotic foci, where their association contributes to apoptotic progression. We identify several BAX regions involved in this interaction, including the pore-forming hairpin, the C-terminal transmembrane anchor, and the N-terminal region. Functionally, our data reveal that DRP1 promotes BAX activation, thereby inducing MOMP and apoptotic cell death. Together, these findings establish a pro-death role for the BAX-DRP1 interplay and support a model in which DRP1 acts as a previously unrecognized, non-canonical activator of BAX.

Looking ahead, it will be important to resolve the structural details of the interplay of BAX and DRP1 within their macromolecular assemblies at mitochondria and to clarify how this association influences apoptotic pore modulation, particularly in relation to the biophysical properties of the membrane. Furthermore, systematic dissection of the BCL-2 regulatory network to distinguish redundant or compensatory mechanisms of BAX activation from the specific contribution of DRP1 will be critical to define the physiological and pathological relevance of DRP1 in apoptotic cell death across different cellular contexts.

2. The cooperative action of BAX, BAK, and mitochondrial membranes in apoptotic pore formation

BAX and BAK are the key executioner BCL-2 proteins that mediate MOMP by forming apoptotic pores in the MOM in response to apoptotic triggers. Their high degree of sequence and structural homology, together with their functional redundancy in executing MOMP, has long supported the assumption that they act through identical and fully overlapping molecular mechanisms. Despite this overlap, there are relevant differences between BAX and BAK, including the cytosolic localization of BAX versus the constitutive mitochondrial localization of BAK in healthy conditions, distinct binding affinities within the BCL-2 family, particularly toward BH3-only initiators, and different cellular expression levels of both proteins ((Kale et al., 2018; Sarosiek et al., 2013; Singh et al., 2019), (https://www.proteomicsdb.org/proteomicsdb; BAX ID Q07812, BAK ID Q16611)). The complexity of the co-dependent regulatory network of BCL-2 proteins, combined with the apparent functional redundancy of BAX and BAK, has so far prevented a clear determination of whether these differences translate into distinct contributions to apoptotic pore formation.

Using a combination of super-resolution fluorescence and atomic force microscopy (AFM) to investigate the supra-molecular structural organization of apoptotic pores formed by BAX and BAK, together with single-molecule stoichiometry quantification of their oligomerization kinetics in apoptotic cells, we now reveal mechanistic differences between both proteins with important functional implications for apoptosis execution and its immunological consequences. In addition, using correlative super-resolution light-electron microscopy (superCLEM) in combination with stoichiometry quantification of individual apoptotic pore assemblies, we investigate the relationship between protein oligomeric state and pore size at the single-molecule level and reveal a mechanistic role for mitochondrial mechanics in the regulation of apoptotic pores.

2.1 The supra-molecular structure of apoptotic pores

Using SMLM and AFM, previous work demonstrated that BAX assembles into heterogeneous line, arc, and ring structures in apoptotic mitochondria to mediate MOMP, with arcs and rings forming membrane pores (Salvador-Gallego et al., 2016).

To compare these features with BAK, we analyzed the nanoscale structural organization of monomeric enhanced GFP (mEGFP)-BAK expressed in BAX/BAK double knock-out (DKO) cells using SMLM. In healthy conditions, BAK displayed a homogenous distribution across the mitochondrial network. Upon apoptosis induction, it relocalized into discrete, structured mitochondrial complexes in temporal correlation with MOMP, as indicated by the release of fluorescently labeled SMAC into the cytosol (Appendix 1.2 Figure 1). Structural analysis of these complexes revealed that BAK, like BAX, assembled into line, arc, and ring structures in apoptotic mitochondria. Unexpectedly, BAK assemblies were more uniform in size and, on average, 50 % smaller than those formed by BAX (Appendix 1.2 Figures 2A-F and S1, (Salvador-Gallego et al., 2016)). Assessing the temporal evolution of these structures during apoptosis progression, we observed a small decrease in line structures, accompanied by a slight increase in rings (Appendix 1.2 Figures 2G and S2), suggesting a potential progression from lines to arcs (as intermediate structures) to rings over time. However, the structures formed by BAK remained stable soon after MOMP, and the persistence of a large fraction of lines and arcs suggests that these represent stable, discrete entities rather than obligate structural intermediates of ring formation.

To determine the functional relevance of these structures in pore formation, we performed AFM imaging of activated, recombinant full-length BAK (Appendix 1.2 Figure S3A-D) in supported lipid bilayers (SLBs) prepared from proteoliposomes as described previously (Salvador-Gallego et al., 2016; Subburaj et al., 2015). We demonstrate that, like BAX, BAK arcs and rings were associated with membrane pores (Appendix 1.2 Figure 3A-E). However, consistent with our observations by SMLM in apoptotic mitochondria, BAK structures were smaller and more uniform in size than those described for BAX (Appendix 1.2 Figure S3E-F). Complementary experiments in GUVs confirmed these differences in pore size between BAX and BAK, as BAK pores permitted the influx of cyt *c* (12.5 kDa) in a concentration-dependent manner but excluded the 104 kDa protein APC (Appendix 1.2 Figure 3F-G), indicating a pore size at or below this range. In contrast, BAX pores allow the passage of both cyt *c* and APC *in vitro* (Appendix 1.1 Figure 3E), reinforcing the notion of intrinsic pore-size differences between BAX and BAK.

As BAX and BAK dynamically oligomerize in mitochondria during apoptosis, we hypothesized that their oligomeric state might define the morphology and size of apoptotic nanoassemblies. To test this, we developed a multimodal imaging approach termed CorreLative Oligomerization STED and Electron (CLOSE) microscopy, which allows the correlative assessment of the protein stoichiometry of single particles using photon-counting confocal microscopy and their nanoscale organization based on STED microscopy, as well as the cellular context information provided by an additional correlative step with electron tomography. We applied CLOSE microscopy to correlate BAK molecularity and supra-molecular structural organization of individual apoptotic pores with structural alterations of the mitochondrial membranes (Appendix 2.1 Figure 1). For this, we endogenously expressed HALO-tagged BAK (HALO-BAK) in U2OS cells (Appendix 2.1 Figure S1A-C) grown on carbon-coated, coordinate-gridded dishes to enable tracking of individual cells throughout all imaging steps. We labeled HALO-BAK with Janelia Fluor X 650 (JFX650) HALO-tag ligand, and stained mitochondria with MitoTracker. The cells were fixed one hour after apoptosis induction, which we defined as the time point at which MOMP occurred in the majority of cells, as determined by loss of TMRE signal (Appendix 2.1 Figure S1D-F). To quantify BAK stoichiometry, we performed photon-counting confocal microscopy on individual cells located via the coordinate system, followed by single-particle ratiometric stoichiometry quantification. As a fluorescence calibration standard, we used U2OS cells endogenously expressing HALO-tagged NUP96 (NUP96-HALO), a 32-mer component of the nuclear pore complex, labeled with JFX650. Using the theoretical brightness of a single fluorescent emitter, calculated with NUP96-HALO, we converted the measured brightness of apoptotic BAK assemblies into BAK molecularity (Appendix 2.1 Figure S2A-B). The same cells and regions of interest were subsequently imaged by STED microscopy to resolve the nanoscale structural organization of BAK assemblies. After fluorescence imaging, the samples were resin-embedded, serially sectioned, and contrast-stained for electron tomography to visualize mitochondrial ultrastructure. The coordinate grid enabled the re-identification of previously imaged cells for electron microscopy (EM). We aligned the fluorescence and EM datasets using the MitoTracker

signal as a fiducial marker, enabling precise multi-correlative analysis (Appendix 2.1 Figure 1).

Using CLOSE, we quantified the copy number of BAK molecules within individual apoptotic BAK assemblies and correlated it with their nanoscale structural organization (Appendix 2.1 Figure 2). Strikingly, BAK exhibited a broad oligomeric distribution, ranging from 50 to over 500 BAK molecules per individual apoptotic pore assembly (Appendix 2.1 Figure S2C-G). Contrary to our expectation, we did not detect significant differences in BAK stoichiometry between line, arc, and ring structures (Appendix 2.1 Figure 2A-B), suggesting that the oligomeric state of BAK does not define the morphology of its assemblies. In addition, we analyzed the sizes of individual line, arc, and ring assemblies relative to the number of BAK molecules. Consistent with our SMLM data, BAK structures varied widely in size, with lines slightly smaller than arcs and arcs smaller than rings. However, we failed to detect a significant correlation between the number of BAK molecules and the size of the assemblies (Appendix 2.1 Figure 2C-J). The lack of correlation between BAK stoichiometry and the shape or size of the nanoscale assemblies indicates that the oligomeric state of BAK is not the primary factor in determining the morphology or dimensions of apoptotic BAK pores, suggesting that additional factors contribute to shaping its supramolecular organization. Given the toroidal nature of apoptotic pores, with both proteins and lipids lining the pore lumen, which is specifically evident for the pores formed by arc structures observed *in vitro* ((Salvador-Gallego et al., 2016), Appendix 1.2 Figure 3D and S3E), we reasoned that the local membrane environment might influence the size and shape of apoptotic pore assemblies. To test this, we correlated the shape of supramolecular apoptotic BAK assemblies with the mitochondrial environment using CLOSE microscopy. Quantitation of BAK pores according to their location at mitochondria revealed that the majority of pores formed at the mitochondrial tip, some of which were associated with extrusion of the MIM through the MOM pore, whereas a minority of pores formed along the longitudinal side (Appendix 2.1 Figure 3). Notably, the shape of BAK assemblies strongly correlated with the position of MOM openings they caused, with the majority of MOM pores located at mitochondrial tips, suggesting a preferential site for apoptotic pore formation.

Together, these findings provide direct structural evidence that BAK, like BAX, assembles into heterogeneous line, arc, and ring structures in the membrane and that these assemblies are directly associated with pore formation both *in vitro* and in mitochondria of apoptotic cells. Notably, these observations provide direct evidence for the toroidal nature of apoptotic pores *in situ*, as both lipids and protein line the pore rim, a feature especially evident for pores formed by arc structures. In line with this, our data indicate that BAK oligomers delineate MOM openings. Together with the lack of correlation between BAK stoichiometry and the size or shape of the supramolecular assemblies, this suggests that the membrane opening contributes to defining the spatial organization of apoptotic BAK assemblies. This observation highlights the significance of the biophysical properties of the MOM in the formation of apoptotic pores and offers a potential explanation for the heterogeneity in the size and morphology of apoptotic BAX and BAK nanoassemblies. Although the structural similarities between BAX and BAK assemblies suggest a shared mechanism of membrane permeabilization, the formation of consistently smaller, more homogeneous pores by BAK, both in mitochondria and in membranes in vitro, points to intrinsic structural differences that may reflect distinct modes of action in apoptosis.

2.2 Assembly mechanism of BAX and BAK apoptotic pores

Given the structural differences we observed for BAX and BAK complexes in membranes, and the fact that both proteins relocalize to mitochondrial complexes upon apoptotic triggers, we hypothesized that these differences could arise from distinct modes of assembly. To test this, we quantified the oligomerization kinetics of both proteins during apoptosis using single-molecule photon-counting confocal microscopy combined with ratiometric stoichiometry analysis ((Finan et al., 2015; Jenner et al., 2020; Verdaasdonk et al., 2014), (Appendix 1.2 Figure S5). We expressed mEGFP-BAX or -BAK in BAX/BAK DKO cells and monitored the growth of individual apoptotic foci relative to the time point of MOMP, indicated by SMAC-release (Appendix 1.2 Figure 4A). Similar to what we observed for the oligomeric states of BAK by CLOSE microscopy, BAX assemblies showed a broad stoichiometry distribution, ranging from a few molecules to several hundred per complex. However, assessment of the kinetic oligomerization demonstrated that the stoichiometry of BAX increased steadily over the

course of the measurement time. In contrast, BAK complexes reached a stable oligomeric distribution within approximately 10 minutes after MOMP, and displayed a more uniform oligomer distribution than BAX (Appendix 1.2 Figure 4B-E and G-J). This difference in the stoichiometry of BAX or BAK oligomers is in good agreement with the structural data from SMLM and CLOSE microscopy experiments and highlights clear differences in the assembly properties of both proteins. BAK assembles faster into smaller, stable oligomeric complexes, while BAX assembles more slowly but continues to grow steadily into large oligomers. To address whether these differences were simply a consequence of the steady-state localization and molecular availability, we considered the distinct subcellular distribution of both proteins in healthy conditions. BAK is constitutively localized in the MOM, while BAX is cytosolic and requires conformational rearrangements for membrane insertion. This could enable BAK to participate earlier in pore formation but limit its abundance, whereas BAX, despite delayed membrane integration, may grow into larger assemblies due to its higher cytosolic availability. To test this hypothesis, we analyzed a constitutively membrane-anchored BAX mutant, BAX(S184V), which retains full activity (Kuwana et al., 2020; Nechushtan et al., 1999). Remarkably, BAX(S184V) oligomerized slightly faster than wild-type BAX but slower than BAK and, like wild-type BAX, continued to grow steadily over time (Appendix 1.2 Figure 4B-C, F-G, and J). These results indicate that the faster assembly kinetics of BAK are only partially explained by its localization and that the saturation of BAK oligomer stoichiometry is not a consequence of its molecular availability. Together, these results demonstrate that, despite their high degree of homology and functional redundancy, BAX and BAK assemble into apoptotic pores with intrinsically different assembly properties.

Because BAX and BAK colocalize in apoptotic foci (Zhou and Chang, 2008), we next asked whether they assemble into the same higher-order structures. To address this, we implemented live-cell dual-color STED microscopy to visualize BAX and BAK with high spatial resolution in mitochondria of apoptotic cells. We identified line, arc, and ring structures formed by both proteins, demonstrating that BAX and BAK co-assemble into the same supra-molecular apoptotic pore structures (Appendix 1.2 Figures 6A-B and S7A). These findings are consistent with recent reports (Schweighofer et al., 2024)

and provide direct visualization of apoptotic pores formed in mitochondria of living cells. To confirm these results, we employed a set of complementary approaches, including *in situ* proximity labeling using the engineered ascorbate peroxidase 2 (APEX2), ddFP measurements of BAX and BAK (as described above), and co-immunoprecipitation of lipid/protein nanoparticles, generated from mitochondria using styrene maleic anhydrate (SMA) co-polymers (Appendix 1.2 Figures 6C-G and S7B). These assays confirmed that BAX and BAK are localized in close proximity (within 10 nm) within apoptotic mitochondrial complexes, but not in healthy mitochondria, and that they co-assemble into the same apoptotic pore complexes.

Considering the differences in the assembly kinetics and size of apoptotic pore structures we observed between BAX and BAK, we wondered whether these differences influence the co-assembly of the two proteins. To address this, we quantified the oligomerization kinetics of BAX or BAK in single knock-out cells (Appendix 1.2 Figure S8A), i.e., in the presence of either endogenous BAX or BAK, in comparison to our results in DKO cells. While both proteins maintained their characteristic assembly behavior in the single KO context, BAX oligomerized faster and BAK slower in the presence of the respective other protein (Appendix 1.2 Figures 5A-H and S6). Moreover, comparative assessment of the size of supra-molecular BAK assemblies showed that BAK assemblies were significantly larger when BAX was present (Appendix 1.2 Figure 5I-M). These findings indicate reciprocal contributions of BAX and BAK during apoptotic pore formation: BAX increases the size of BAK pore structures, whereas BAK accelerates the oligomerization of BAX.

The observation that BAK oligomerizes faster and accelerates the assembly of BAX suggests that BAK oligomers might act as nucleation sites for recruiting cytosolic BAX and triggering its activation during apoptosis. This hypothesis aligns well with the observation that fluorescently labeled BAK appeared in mitochondrial clusters before BAX (Appendix 1.2 Figure 6H). To test this directly, we developed an optogenetic tool for light-induced BAK oligomerization in living cells. Remarkably, induced oligomerization of BAK led to its redistribution into apoptotic foci, the recruitment of cytosolic BAX to the same sites, and the initiation of apoptosis in the absence of

apoptotic stimuli (Appendix 1.2 Figure 6I). We confirmed this observation *in vitro* using recombinant BAX and BAK in GUVs, where membrane-bound, activated BAK successfully recruited inactive, soluble BAX to the GUV membrane (Appendix 1.2 Figure 6J-K). Although BAK is not required for BAX activation in the cellular context (Chen et al., 2015; Chin et al., 2018; Ma et al., 2014), these results suggest that BAK not only accelerates the growth of BAX assemblies, but that it can directly recruit and activate cytosolic BAX, thereby driving cooperative apoptotic pore formation.

This cooperative mechanism is in line with previous studies proposing a non-canonical activation pathway in which the exposed BH3 domain of activated BAX or BAK can further trigger the activation of additional executioner molecules, complementing the canonical activation mechanism by BH3-only initiators (Czabotar et al., 2013; Iyer et al., 2020; Singh et al., 2022). At the molecular level, the faster assembly kinetics and the initially higher density of BAK assemblies at the MOM may reflect more efficient intra-dimer interactions of BAK compared to BAX. In support of this view, BAK has been shown to possess a greater capacity than BAX to activate additional BAX or BAK molecules (Iyer et al., 2020). Other contributing factors may include increased accessibility of BAK to the BH3 domains, or distinct interaction dynamics with mitochondrial binding partners such as other BCL-2 family members or VDAC2 (Cheng et al., 2003; Chin et al., 2018; Ma et al., 2014; van Delft et al., 2019).

2.3 The role of mitochondrial membrane mechanics in apoptotic pore formation

Using our CLOSE microscopy approach, we examined the mitochondrial membrane ultrastructure at the sites of individual apoptotic pores and found that the vast majority of pores formed at mitochondrial tips. Interestingly, a substantial fraction of these pores was associated with the extrusion of the MIM through the MOM opening (Appendix 2.1 Figure 3B). To systematically assess the prevalence of MIM extrusion, we established a fluorescent imaging-based assay combining MOM and mitochondrial matrix markers with HALO-BAK in apoptotic cells. Confocal and STED microscopy revealed that although approximately 40% of mitochondria retained an apparently intact MOM (small pores in the MOM are not detectable due to the limited spatial resolution of this technique), 39% of mitochondria with MOM openings showed MIM extrusion, whereas

only 21% displayed MOM openings without extrusion (Appendix 2.1 Figure 4A-D). These findings demonstrate that MIM extrusion is a frequent consequence of MOM pore formation. Notably, BAK localized predominantly to either one or both sides of the MOM opening at the pore rim but was absent from the extruding MIM (Appendix 2.1 Figure 4B).

Given the lack of correlation between the BAK molecularity and size of the apoptotic pore structure, we reasoned that pore expansion is not solely driven by BAK oligomerization but may be promoted by mechanical forces exerted by the extruding MIM. Since unfolding of the mitochondrial *cristae* and osmotic swelling of the mitochondrial matrix are well-established mitochondrial alterations downstream of MOMP (Cipolat et al., 2004; Frezza et al., 2006; Ricci et al., 2004; Scorrano et al., 2003), we hypothesized that these processes could contribute to MIM extrusion. To test this, we chemically induced osmotic swelling of the mitochondrial matrix using the ionophores valinomycin and nigericin (Val/Nig). Confocal imaging confirmed robust mitochondrial swelling in healthy cells (Appendix 2.1 Figure 4E). In apoptotic cells, Val/Nig-treatment significantly increased the fraction of mitochondria with MIM extrusion compared to untreated apoptotic controls (Appendix 2.1 Figure 4F-H), indicating that elevated matrix pressure promotes MIM extrusion. These findings highlight the contribution of biophysical forces in driving this process.

Of note, using the CLOSE microscopy approach, we also observed instances of MIMP occurring directly beneath apoptotic pores in the MOM (Appendix 2.1 Figures 1 and S3). Although the limited number of events obtained by CLOSE microscopy precludes reliable quantification, their occurrence suggests potentially significant mechanistic implications. Such defects in the MIM permit exchange of molecules between the cytosol and the mitochondrial matrix, thereby amplifying osmotic matrix swelling under physiological apoptotic conditions. This is consistent with a previous cryo-electron microscopy study demonstrating occasional cases of MIMP, the influx of cytosolic content, and mitochondrial matrix content dilution at apoptotic MOM pores formed by BAX (Ader et al., 2019). However, the molecular mechanism driving MIMP remains elusive. Based on our observation that BAK localizes exclusively to MOM pores, we

propose that MIMP is not directly mediated by BAX or BAK, but instead arises through an alternative, yet unidentified mechanism. In line with this, recent studies have suggested that caspase-activated gasdermin E (GSDME) may contribute to mitochondrial pore formation during apoptosis ((Luo et al., 2024; Miao et al., 2023; Neel et al., 2023; Rogers et al., 2019; Wang et al., 2017; Zhang et al., 2022), see Functional implications for apoptosis execution).

Interestingly, MIM extrusions through restricted MOM openings appeared constricted at the site of the MOM pore, adopting a characteristic hourglass morphology (Appendix 2.1 Figure 4I). This deformation of the membrane from a minimal-energy spherical shape implies that the MOM exerts a closing force on the extruding MIM, reflecting line tension at the pore edge. The persistence of MIM extrusion despite this constriction indicates that the MIM generates an opposing outward pressure sufficient to stabilize the open pore configuration and potentially promote pore expansion. To validate this hypothesis, we applied a modified version of the quantitative "neck model" developed by Baumgart and colleagues (Baumgart et al., 2003) to analyze the geometry of the hourglass-shaped MIM extrusions. This model is based on the minimization of the energy contributions associated with membrane curvatures and tensions, transmembrane pressure, and line tension, consistent with the measured membrane geometry based on the conservation of a zero-value Hamiltonian. Fitting the experimental data obtained by the geometry of the MIM while adjusting membrane bending modulus, membrane tension, and excess pressure yielded an estimated line tension of $\gamma = 7 \pm 6$ pN at apoptotic MOM pore edges (Appendix 2.1 Figure 4J-M). This value closely matches previously reported line tension estimates for pores formed by the α-helix 5 of BAX in model membranes (García-Sáez et al., 2007), supporting a similar underlying biophysical mechanism of pore stabilization.

Together, the observation of hourglass-shaped MIM extrusions through apoptotic pores demonstrates that the MOM exerts a constrictive force generated by line tension at the pore rim. Conversely, the unfolding and extrusion of the MIM exerts a counterbalancing outward force that promotes or stabilizes pore opening. These findings suggest that, following the onset of MIM extrusion, pore widening occurs

independently of BAK oligomerization and is instead driven, at least in part, by biophysical forces arising from MIM remodeling. This reasoning is further reinforced by the lack of correlation between BAK molecularity and pore size, and in agreement with the toroidal nature of the pore.

To further quantify the mechanical forces associated with MIM extrusion, we performed membrane dynamics simulations. For this, we modeled the MIM as a triangulated fluid-elastic membrane containing densely packed *cristae* structures enclosed within a pill-shaped container mimicking the MOM. To simulate the MOM pores, we introduced a circular opening of fixed size on one side of the MOM container (Appendix 2.1 Figure 5A and S5). Our simulations revealed spontaneous extrusion of the MIM through MOM pores once the pore radius exceeded approximately half of the mitochondrial diameter (Appendix 2.1 Figure 5A and S4A). This extrusion was accompanied by remodeling and rounding of the *cristae*, which appeared to push the MIM through the MOM opening and reduce the overall membrane bending energy, thereby driving extrusion. Over time, the *cristae* opened or merged, and the extruding MIM exerted an expansive force on the pore rim, which we quantified as an effective line tension. For pores with a size corresponding to ~70% of the mitochondrial diameter, the simulations yielded line tensions of approximately γ = 3 - 5 pN for a low membrane bending rigidity (κ_B = 10 k_BT) and γ = 10 - 15 pN for stiffer membranes (κ_B = 60 k_BT, Appendix 2.1 Figures 5A and S4B). These values are in good agreement with the experimentally estimated line tension of γ = 7 ± 6 pN derived from the MIM hourglass geometries (Appendix 2.1 Figure 4M). Larger pores exhibited lower effective line tension, consistent with the mechanical relaxation of the system following pore expansion (Appendix 2.1 Figure S4C). During the early stages of MIM extrusion, the mitochondrial matrix volume initially decreased, associated with *cristae* rounding, but subsequently increased as extrusion progressed (Appendix 2.1 Figure 5A). Stiffer membranes with larger pores (comparable in size to the mitochondrial diameter) exhibited even more dramatic matrix volume expansion as the MIM extrusion was more pronounced and the *cristae* structures unfolded outside the MOM (Appendix 2.1 Figure S4D).

To further examine the contribution of osmotic swelling to MIM extrusion and apoptotic pore expansion, we mimicked the conditions of MIMP during apoptosis (McArthur et al., 2018; Riley et al., 2018), by simulating osmotic matrix swelling. These simulations revealed accelerated MIM extrusion in the absence of simulated osmotic swelling and an increase in line tension (γ > 10 pN) at the apoptotic pore rim (Appendix 2.1 Figure 5B). However, even strong osmotic forces failed to induce extrusion through small (< 50% of mitochondrial diameter) and static MOM openings (Appendix 2.1 Figure S4E), suggesting that the observed increase in line tension may progressively enlarge the apoptotic pore over time. Consistent with this prediction, quantification of the size of individual MOM discontinuities in our EM datasets revealed that pores associated with MIM extrusion were significantly wider than those without extrusion at mitochondrial tips or sides (Appendix 2.1 Figure 5C–G). These data indicate that MIM extrusion preferentially occurs through large apoptotic pores and mechanically contributes to their expansion, thereby shaping the structural organization of the apoptotic pore.

Together, our findings suggested a multimodal mechanism of apoptotic pore formation and expansion, in which BAX and BAK mediate initial pore opening and oligomerization-dependent pore growth until a critical pore diameter is reached that allows MIM extrusion. From this point onward, the mechanical forces associated with MIM extrusion and matrix swelling dominate to progressively promote pore expansion by counterbalancing the line tension at the pore rim. As this tension is progressively reduced by the forces of the extruding MIM, additional recruitment of BAX and BAK to the pore edge might shield exposed hydrophobic membrane regions and further stabilize the pore. Continued pore expansion would thus establish a positive feedback loop, in which larger pores substantially accelerate MIM extrusion and further promote apoptotic pore growth. This model is consistent with a previous study that combined correlative cryo-microscopy and electron cryo-tomography to directly visualize BAX-associated MOM ruptures of variable sizes (Ader et al., 2019). In line with our observations, this study demonstrated that apoptotic pore formation correlated with extensive remodeling of the MIM, including *cristae* unfolding and the disassembly of ATP synthase dimers, particularly in regions of the MIM exposed to the cytosol.

Additionally, the study revealed that MOM disruption was accompanied by the influx of cytosolic content into the intermembrane space, dilution of matrix content, and potential swelling of the MIM, which in some cases extruded through MOM pores. Notably, the extent of cytosolic exposure of the MIM varied substantially and scaled with pore size. Based on these observations, the authors suggested that MIM reorganization, osmotic imbalance, and membrane tension may act synergistically with BAX accumulation to drive pore formation and expansion. This is consistent with our observation that, in pores larger than a critical diameter, osmotic matrix swelling, *cristae* remodeling, and MIM extrusion mechanically drive pore expansion. Together, these findings independently support a model in which apoptotic pore growth is not solely protein-driven but is amplified by mechanically coupled dynamics of the inner and outer mitochondrial membranes.

3. Functional implications for apoptosis execution

Our findings that BAX and BAK exhibit distinct assembly kinetics and size of supramolecular apoptotic pore structures raised the question whether these mechanistic differences have functional consequences for regulatory events in apoptosis downstream of MOMP. We hypothesized that differences might influence the dynamics of mitochondrial content release, particularly for large mitochondrial macromolecules such as the mtDNA.

To test this, we performed correlative live-cell confocal and fixed-cell Airyscan super-resolution microscopy to monitor mtDNA release relative to MOMP, marked by the efflux of fluorescently labeled SMAC into the cytosol, in single cells expressing either only BAX or BAK (U2OS BAK KO, or BAX KO, respectively), compared to WT cells (Appendix 1.2 Figure 7A-B). In untreated cells, mtDNA localized entirely within mitochondria. Following MOMP, mtDNA release was detected in all three cell lines, demonstrating that either BAX or BAK alone can form pores large enough to permit mtDNA efflux. However, quantitative temporal analysis revealed that mtDNA release occurred significantly faster in cells expressing only BAK than in those expressing only BAX. While in cells expressing only BAK, all analyzed cells released the mtDNA within 30 minutes of SMAC release, while 25% of the cells expressing only BAX retained the

mtDNA even 60 minutes after SMAC release (Appendix 1.2 Figure 7B-C). WT cells exhibited kinetics similar to BAX-only cells, indicating that BAK accelerates mtDNA release. These results are consistent with the faster assembly kinetics of BAK compared to BAX (Appendix 1.2 Figure 5E-G). To further confirm this link, we analyzed a BAX mutant with reduced oligomerization capacity, BAX(T182I) (Kuwana et al., 2020; Zhang et al., 2016), which we validated at the single molecule level by stoichiometry quantification in living BAX/BAK DKO cells during apoptosis (Appendix 1.2 Figure 7D-F). We found that cells expressing BAX(T182I) exhibited delayed mtDNA release compared to those expressing WT BAX (Appendix 1.2 Figure 7G-H). These findings hence provide direct evidence that the assembly kinetics of BAX and BAK determine the kinetics of mtDNA release, independent of the cellular genetic background.

Since mtDNA release has been shown to activate the cGAS–STING signaling pathway and modulate the inflammatory outcome of apoptosis when caspase activity is inhibited (Giampazolias et al., 2017; Rongvaux et al., 2014; White et al., 2014), we next examined the consequences of inducing apoptotic pore formation solely by BAX or BAK, or both, on innate immune signaling. We monitored hallmarks of cGAS-STING pathway activation, such as STING degradation and TANK-binding kinase 1 (TBK1) phosphorylation, in apoptotic SVEC cells expressing only BAK (SVEC BAX KO), only BAX (SVEC BAK KO), or both (SVEC WT) under conditions of caspase inhibition. In line with the accelerated mtDNA release, BAK-driven MOMP triggered more rapid cGAS–STING activation compared with cells expressing only BAX or WT cells (Appendix 1.2 Figure 7I-J). We further explored whether BAX- versus BAK-mediated MOMP differentially affects adaptive immune activation in immune cells. For this, we co-cultured WT, BAK KO, and BAX KO SVEC cells (Appendix 1.2 Figure S8A), pretreated to induce apoptotic pore formation (and mtDNA release) under conditions of caspase inhibition, with primary murine splenocytes and assessed their activation markers. Notably, compared to WT or BAK KO SVEC cells, splenocytes exposed to apoptotic BAX KO cells exhibited a significantly higher fraction of $CD45^+$ hematopoietic cells showing T-cell activation markers (i.e., loss of CD62L and upregulation of CD44)

with the strongest response among $CD4^+$ T helper cells (Appendix 1.2 Figures 7K and S8B-D).

Together, these findings uncover a previously unrecognized function of BAX and BAK in controlling the timing of mtDNA release and, consequently, modulating mtDNA-driven inflammatory signaling during apoptosis. The coordinated assembly of BAX and BAK determines both the growth rate and permeability of apoptotic pores to mitochondrial macromolecules, thereby shaping downstream immune responses. Mechanistically, this function is regulated by the balance of BAX- versus BAK-mediated MOMP and arises from their distinct yet cooperative assembly dynamics into apoptotic pores. The reciprocal interplay between BAX and BAK defines the relative kinetics of the apoptotic release of mitochondrial content, such as cyt *c*, SMAC, and mtDNA, upon MOMP. Specifically, the post-MOMP oligomerization kinetics of BAX and BAK into apoptotic macropores critically determine the timing of mtDNA release with functional consequences for the magnitude of cGAS–STING pathway activation, linking mitochondrial apoptosis to immunogenic signaling and T cell activation. Recent studies have reported that mtDNA can drive interferon responses and immunogenic cell death in a model of radiation-treated breast cancer cells, where caspase activation fails to suppress innate immune signaling (McArthur and Kile, 2020; Yamazaki et al., 2020). In this context, our findings suggest that the dynamic regulation of apoptotic pore growth by BAX and BAK fine-tunes the temporal relationship between caspase activation and cGAS–STING signaling. Through this mechanism, the interplay of BAX and BAK enables tuning of the timing and extent of inflammatory responses downstream of apoptosis.

Adding further complexity, our CLOSE microscopy data and biophysical modeling of MIM extrusion reveal an additional layer of regulation in apoptotic pore formation. We demonstrate that once the apoptotic pore reaches a critical diameter, the mechanical forces generated by mitochondrial matrix swelling and MIM extrusion through the MOM become dominant drivers of pore expansion, extending beyond the BAX- and BAK-dependent mechanism. Functionally, this transition may determine the irreversibility of MOMP and the onset of MIMP, influencing downstream inflammatory signaling initiated

by mitochondrial content release. While anti-apoptotic BCL-2 family members can disassemble BAX oligomers and thereby inhibit pore formation or at least limit pore growth (Subburaj et al., 2015), extrusion of the MIM involves extensive remodeling of the mitochondrial membranes, rendering MOMP energetically irreversible. Consequently, the removal of permeabilized mitochondria, for example, through extensive cellular mitophagy (Saunders et al., 2024), emerges as the only currently recognized means to mitigate the cellular consequences of apoptotic pore formation in this context, with implications for the transition from sublethal to lethal MOMP.

Moreover, the exposure of the MIM to the cytosolic environment, either through the apoptotic pore or upon MIM extrusion, renders it accessible to potential mediators of MIMP. Recent studies implicate pore-forming gasdermins (GSDMs), such as GSDMD, in cardiolipin-dependent mitochondrial permeabilization (Luo et al., 2024; Miao et al., 2023; Zhang et al., 2022). In particular, GSDME, which is cleaved and activated by caspase-3 during apoptosis, has been shown to induce permeabilization of both the plasma membrane and mitochondria, amplifying MOMP in a positive feedback loop (Neel et al., 2023; Rogers et al., 2019; Wang et al., 2017). Given its activation downstream of caspase-3 and potential CL-dependence, GSDME represents a plausible mediator of MIMP. However, further studies are required to define its involvement and regulatory interplay with apoptotic pore formation and MIM extrusion. Additionally, once exposed to the cytosol, the extruded MIM becomes mechanically fragile and prone to rupture under mechanical stress, providing an alternative, non-protein-mediated route to MIMP.

Collectively, these findings reveal a previously unrecognized mechanistic interplay between the MOM and MIM, in which biophysical forces govern apoptotic pore dynamics, determining both the irreversibility of MOMP and the downstream inflammatory response.

Concluding remarks

Our study delineates a cohesive mechanistic framework for mitochondrial apoptotic pore formation that integrates the function of apoptotic executioner and mitochondrial dynamics proteins with mitochondrial membrane mechanics. First, we establish that BAX and DRP1 engage in a direct, membrane-dependent interaction that is strongly enhanced during apoptosis and temporally coincides with MOMP. This interaction requires the N-terminal region of BAX rather than the canonical BH3 groove, and it reciprocally augments membrane activities: DRP1 increases BAX-mediated pore formation, while BAX enhances DRP1-mediated membrane tethering. Forced BAX-DRP1 dimerization is sufficient to drive mitochondrial apoptosis in the absence of canonical apoptotic triggers, revealing DRP1 as a previously unrecognized, non-canonical activator of BAX.

Second, we uncover intrinsic differences in the assembly properties of BAX and BAK into apoptotic pore complexes despite their homology and functional redundancy. Using super-resolution imaging, AFM, and single-molecule stoichiometry quantification, we show that both proteins form line, arc, and ring structures and that both arcs and rings can form toroidal pores, yet BAK pores are smaller and more uniform than those formed by BAX. BAK oligomers stabilize rapidly after MOMP, while BAX assemblies grow continuously to higher molecularity. Dual-color STED nanoscopy and complementary proximity assays demonstrate that BAX and BAK co-assemble within the same macromolecular pore complexes and reciprocally influence each other’s assembly: BAK accelerates BAX oligomerization, whereas BAX increases the size of BAK structures. Optogenetic and reconstitution experiments indicate that BAK oligomers can nucleate, recruit, and activate cytosolic BAX, consistent with a cooperative amplification mechanism of apoptotic pore assembly.

Third, by developing CLOSE microscopy and combining it with quantitative modeling, we demonstrate that mitochondrial membrane mechanics are active determinants of pore architecture and growth. Apoptotic pores preferentially form at mitochondrial tips and frequently correlate with MIM extrusion through the MOM opening. The resulting hourglass geometries report a line tension at the pore rim that is counterbalanced by

outward forces generated by *cristae* remodeling, matrix swelling, and MIM extrusion. Simulations recapitulate the measured line tensions and predict that large pores are further expanded by MIM extrusion, establishing a positive feedback between pore widening and MIM extrusion. This mechanical regime renders MOMP irreversible and provides routes to MIMP, either through mechanical rupture in the cytosol or by exposing the MIM to additional permeabilizing factors.

Finally, these mechanistic insights have important immunological consequences in the cellular context. Differences in the post-MOMP assembly kinetics of BAX and BAK translate into distinct dynamics of mtDNA release: BAK-driven pores promote faster mtDNA efflux, earlier cGAS–STING activation, and elevated T-cell activation under caspase-inhibited conditions. Thus, the balance and cooperation between BAX and BAK define the kinetics of mitochondrial content release and tune the inflammatory output of apoptosis. Together, our data support a multimodal model in which BAX/BAK oligomerization nucleates apoptotic pore opening and early growth, after which membrane mechanics dominate to drive pore expansion, link MOMP to MIMP, and shape downstream immune signaling.

Looking ahead, delineating the dynamics of MIM extrusion and MIMP associated with apoptotic BAX/BAK macropores will be essential for identifying context-specific regulatory control points within the cellular environment. Moreover, dissecting the crosstalk between biochemical and mechanical regulation of this process, particularly clarifying the mechanism of MIMP, including the potential involvement of GSDMs or other modulators, may open avenues to therapeutically modulate the consequences of mitochondrial apoptotic pore formation, with implications for cancer immunogenicity, inflammatory disease, and tissue homeostasis.

References

Adams, J.M., Cory, S., 2007. The Bcl-2 apoptotic switch in cancer development and therapy. Oncogene 2007 269 26, 1324–1337. https://doi.org/10.1038/sj.onc.1210220

Ader, N.R., Hoffmann, P.C., Ganeva, I., Borgeaud, A.C., Wang, C., Youle, R.J., Kukulski, W., 2019. Molecular and topological reorganizations in mitochondrial architecture interplay during Bax-mediated steps of apoptosis. Elife 8. https://doi.org/10.7554/eLife.40712

Alsop, A.E., Fennell, S.C., Bartolo, R.C., Tan, I.K.L., Dewson, G., Kluck, R.M., 2015. Dissociation of Bak α1 helix from the core and latch domains is required for apoptosis. Nat. Commun. 6, 6841. https://doi.org/10.1038/ncomms7841

Aouacheria, A., Rech de Laval, V., Combet, C., Hardwick, J.M., 2013. Evolution of Bcl-2 homology motifs: homology versus homoplasy. Trends Cell Biol. 23, 103–111. https://doi.org/10.1016/j.tcb.2012.10.010

Ardail, D., Privat, J.P., Egret-Charlier, M., Levrat, C., Lerme, F., Louisot, P., 1990. Mitochondrial contact sites: Lipid composition and dynamics. J. Biol. Chem. 265, 18797–18802. https://doi.org/10.1016/s0021-9258(17)30583-5

Arnoult, D., 2007. Mitochondrial fragmentation in apoptosis. Trends Cell Biol. 17, 6–12. https://doi.org/10.1016/J.TCB.2006.11.001/ASSET/CA3BC554-EBCA-4E9C-9222-0BDFB424D3C6/MAIN.ASSETS/GR1.JPG

Basanez, G., Nechushtan, A., Drozhinin, O., Tutt, S., Wood, K.A., Hsu, Y.T., Youle, R.J., Zimmerberg, J., 1999. Studying the mechanism of Bax induced membrane destabilization: does Bax promote lipidic pore formation?, in: FASEB JOURNAL. pp. A1436--A1436.

Basañez, G., Sharpe, J.C., Galanis, J., Brandt, T.B., Hardwick, J.M., Zimmerberg, J., 2002. Bax-type apoptotic proteins porate pure lipid bilayers through a mechanism sensitive to intrinsic monolayer curvature. J. Biol. Chem. 277, 49360–5. https://doi.org/10.1074/jbc.M206069200

Baumgart, T., Hess, S.T., Webb, W.W., 2003. Imaging coexisting fluid domains in biomembrane models coupling curvature and line tension. Nat. 2003 4256960 425, 821–824. https://doi.org/10.1038/nature02013

Bender, C.E., Fitzgerald, P., Tait, S.W.G., Llambi, F., McStay, G.P., Tupper, D.O., Pellettieri, J., Alvarado, A.S., Salvesen, G.S., Green, D.R., 2012. Mitochondrial pathway of apoptosis is ancestral in metazoans. Proc. Natl. Acad. Sci. U. S. A. 109, 4904–4909. https://doi.org/10.1073/PNAS.1120680109/SUPPL_FILE/PNAS.201120680SI.PDF

Billen, L.P., Kokoski, C.L., Lovell, J.F., Leber, B., Andrews, D.W., 2008. Bcl-XL inhibits membrane permeabilization by competing with Bax. PLoS Biol. 6, e147.

https://doi.org/10.1371/journal.pbio.0060147

Birkinshaw, R.W., Iyer, S., Lio, D., Luo, C.S., Brouwer, J.M., Miller, M.S., Robin, A.Y., Uren, R.T., Dewson, G., Kluck, R.M., Colman, P.M., Czabotar, P.E., 2021. Structure of detergent-activated BAK dimers derived from the inert monomer. Mol. Cell 81, 2123-2134.e5. https://doi.org/10.1016/j.molcel.2021.03.014

Bleicken, S., Assafa, T.E., Stegmueller, C., Wittig, A., Garcia-Saez, A.J., Bordignon, E., 2018. Topology of active, membrane-embedded Bax in the context of a toroidal pore. Cell Death Differ. 25, 1717. https://doi.org/10.1038/S41418-018-0184-6

Bleicken, S., Hantusch, A., Das, K.K., Frickey, T., Garcia-Saez, A.J., 2017. Quantitative interactome of a membrane Bcl-2 network identifies a hierarchy of complexes for apoptosis regulation. Nat. Commun. 8, 73. https://doi.org/10.1038/s41467-017-00086-6

Bleicken, S., Jeschke, G., Stegmueller, C., Salvador-Gallego, R., García-Sáez, A.J., Bordignon, E., 2014. Structural Model of Active Bax at the Membrane. Mol. Cell 56, 496–505. https://doi.org/10.1016/j.molcel.2014.09.022

Bleicken, Stephaniel, Landeta, O., Landajuela, A., Basañez, G., García-Sáez, A.J., 2013. Proapoptotic Bax and Bak Proteins Form Stable Protein-permeable Pores of Tunable Size. J. Biol. Chem. 288, 33241–33252. https://doi.org/10.1074/jbc.M113.512087

Bleicken, Stephanie, Wagner, C., García-Sáez, A.J., 2013. Mechanistic differences in the membrane activity of bax and Bcl-xL correlate with their opposing roles in apoptosis. Biophys. J. 104, 421–431. https://doi.org/10.1016/j.bpj.2012.12.010

Bock, F.J., Tait, S.W.G., 2019. Mitochondria as multifaceted regulators of cell death. Nat. Rev. Mol. Cell Biol. 21, 85–100. https://doi.org/10.1038/s41580-019-0173-8

Cantó, C., 2018. Mitochondrial Dynamics: Shaping Metabolic Adaptation. Int. Rev. Cell Mol. Biol. 340, 129–167. https://doi.org/10.1016/BS.IRCMB.2018.05.004

Cardenas-Rodriguez, M., Chatzi, A., Tokatlidis, K., 2018. Iron–sulfur clusters: from metals through mitochondria biogenesis to disease. JBIC J. Biol. Inorg. Chem. 2018 234 23, 509–520. https://doi.org/10.1007/S00775-018-1548-6

Chan, D.C., 2020. Mitochondrial Dynamics and Its Involvement in Disease. Annu. Rev. Pathol. Mech. Dis. 15, 235–259. https://doi.org/10.1146/ANNUREV-PATHMECHDIS-012419-032711/CITE/REFWORKS

Chandel, N.S., 2014. Mitochondria as signaling organelles. BMC Biol. 12, 1–7. https://doi.org/10.1186/1741-7007-12-34/FIGURES/4

Chen, H.C., Kanai, M., Inoue-Yamauchi, A., Tu, H.C., Huang, Y., Ren, D., Kim, H., Takeda, S., Reyna, D.E., Chan, P.M., Ganesan, Y.T., Liao, C.P., Gavathiotis, E., Hsieh, J.J., Cheng, E.H., 2015. An interconnected hierarchical model of cell death regulation by the BCL-2 family. Nat. Cell Biol. https://doi.org/10.1038/ncb3236

Cheng, E.H.-Y., Sheiko, T. V., Fisher, J.K., Craigen, W.J., Korsmeyer, S.J., 2003.

VDAC2 Inhibits BAK Activation and Mitochondrial Apoptosis. Science (80-.). 301, 513–517. https://doi.org/10.1126/science.1083995

Chin, H.S., Li, M.X., Tan, I.K.L., Ninnis, R.L., Reljic, B., Scicluna, K., Dagley, L.F., Sandow, J.J., Kelly, G.L., Samson, A.L., Chappaz, S., Khaw, S.L., Chang, C., Morokoff, A., Brinkmann, K., Webb, A., Hockings, C., Hall, C.M., Kueh, A.J., Ryan, M.T., Kluck, R.M., Bouillet, P., Herold, M.J., Gray, D.H.D., Huang, D.C.S., van Delft, M.F., Dewson, G., 2018. VDAC2 enables BAX to mediate apoptosis and limit tumor development. Nat. Commun. 9, 4976. https://doi.org/10.1038/s41467-018-07309-4

Chipuk, J.E., Bouchier-Hayes, L., Green, D.R., 2006. Mitochondrial outer membrane permeabilization during apoptosis: the innocent bystander scenario. Cell Death Differ. 2006 138 13, 1396–1402. https://doi.org/10.1038/sj.cdd.4401963

Chou, J.J., Li, H., Salvesen, G.S., Yuan, J., Wagner, G., 1999. Solution structure of BID, an intracellular amplifier of apoptotic signaling. Cell 96, 615–24. https://doi.org/10.1016/s0092-8674(00)80572-3

Cipolat, S., De Brito, O.M., Dal Zilio, B., Scorrano, L., 2004. OPA1 requires mitofusin 1 to promote mitochondrial fusion. Proc. Natl. Acad. Sci. U. S. A. https://doi.org/10.1073/pnas.0407043101

Cipolat, S., Rudka, T., Hartmann, D., Costa, V., Serneels, L., Craessaerts, K., Metzger, K., Frezza, C., Annaert, W., D'Adamio, L., Derks, C., Dejaegere, T., Pellegrini, L., D'Hooge, R., Scorrano, L., De Strooper, B., 2006. Mitochondrial Rhomboid PARL Regulates Cytochrome c Release during Apoptosis via OPA1-Dependent Cristae Remodeling. Cell 126, 163–175. https://doi.org/10.1016/J.CELL.2006.06.021

Colbeau, A., Nachbaur, J., Vignais, P.M., 1971. Enzymac characterization and lipid composition of rat liver subcellular membranes. Biochim. Biophys. Acta - Biomembr. 249, 462–492. https://doi.org/10.1016/0005-2736(71)90123-4

Cosentino, K., García-Sáez, A.J., 2014. Mitochondrial alterations in apoptosis. Chem. Phys. Lipids 181, 62–75. https://doi.org/10.1016/J.CHEMPHYSLIP.2014.04.001

Cowan, A.D., Smith, N.A., Sandow, J.J., Kapp, E.A., Rustam, Y.H., Murphy, J.M., Brouwer, J.M., Bernardini, J.P., Roy, M.J., Wardak, A.Z., Tan, I.K., Webb, A.I., Gulbis, J.M., Smith, B.J., Reid, G.E., Dewson, G., Colman, P.M., Czabotar, P.E., 2020. BAK core dimers bind lipids and can be bridged by them. Nat. Struct. Mol. Biol. 27, 1024–1031. https://doi.org/10.1038/s41594-020-0494-5

Cuconati, A., Degenhardt, K., Sundararajan, R., Anschel, A., White, E., 2002. Bak and Bax function to limit adenovirus replication through apoptosis induction. J. Virol. 76, 4547–58. https://doi.org/10.1128/jvi.76.9.4547-4558.2002

Czabotar, P.E., Garcia-Saez, A.J., 2023. Mechanisms of BCL-2 family proteins in mitochondrial apoptosis. Nat. Rev. Mol. Cell Biol. 24, 732–748. https://doi.org/10.1038/s41580-023-00629-4

Czabotar, P.E., Westphal, D., Dewson, G., Ma, S., Hockings, C., Fairlie, W.D., Lee,

E.F., Yao, S., Robin, A.Y., Smith, B.J., Huang, D.C.S., Kluck, R.M., Adams, J.M., Colman, P.M., 2013. Bax crystal structures reveal how BH3 domains activate Bax and nucleate its oligomerization to induce apoptosis. Cell 152, 519–31. https://doi.org/10.1016/j.cell.2012.12.031

Dai, H., Smith, A., Meng, X.W., Schneider, P.A., Pang, Y.-P., Kaufmann, S.H., 2011. Transient binding of an activator BH3 domain to the Bak BH3-binding groove initiates Bak oligomerization. J. Cell Biol. 194, 39–48. https://doi.org/10.1083/jcb.201102027

De Kroon, A.I.P.M., Dolis, D., Mayer, A., Lill, R., De Kruijff, B., 1997. Phospholipid composition of highly purified mitochondrial outer membranes of rat liver and Neurospora crassa. Is cardiolipin present in the mitochondrial outer membrane? Biochim. Biophys. Acta - Biomembr. 1325, 108–116. https://doi.org/10.1016/S0005-2736(96)00240-4

Denisov, A.Y., Madiraju, M.S.R., Chen, G., Khadir, A., Beauparlant, P., Attardo, G., Shore, G.C., Gehring, K., 2003. Solution Structure of Human BCL-w. J. Biol. Chem. 278, 21124–21128. https://doi.org/10.1074/jbc.m301798200

Dewson, G., Kratina, T., Czabotar, P., Day, C.L., Adams, J.M., Kluck, R.M., 2009. Bak Activation for Apoptosis Involves Oligomerization of Dimers via Their α6 Helices. Mol. Cell 36, 696–703. https://doi.org/10.1016/j.molcel.2009.11.008

Dewson, G., Kratina, T., Sim, H.W., Puthalakath, H., Adams, J.M., Colman, P.M., Kluck, R.M., 2008. To Trigger Apoptosis, Bak Exposes Its BH3 Domain and Homodimerizes via BH3:Groove Interactions. Mol. Cell 30, 369–380. https://doi.org/10.1016/J.MOLCEL.2008.04.005

Dewson, G., Ma, S., Frederick, P., Hockings, C., Tan, I., Kratina, T., Kluck, R.M., 2012. Bax dimerizes via a symmetric BH3:groove interface during apoptosis. Cell Death Differ. 19, 661–670. https://doi.org/10.1038/cdd.2011.138

Du, C., Fang, M., Li, Y., Li, L., Wang, X., 2000. Smac, a Mitochondrial Protein that Promotes Cytochrome c–Dependent Caspase Activation by Eliminating IAP Inhibition. Cell 102, 33–42. https://doi.org/10.1016/S0092-8674(00)00008-8

Duchen, M.R., 2004. Roles of Mitochondria in Health and Disease. Diabetes 53, S96–S102. https://doi.org/10.2337/DIABETES.53.2007.S96

Dyall, S.D., Brown, M.T., Johnson, P.J., 2004. Ancient Invasions: From Endosymbionts to Organelles. Science (80-.). 304, 253–257. https://doi.org/10.1126/SCIENCE.1094884/ASSET/16E897DC-BDD3-4755-82CC-C68154F3CA2F/ASSETS/GRAPHIC/ZSE0130424220003.JPEG

Edlich, F., Banerjee, S., Suzuki, M., Cleland, M.M., Arnoult, D., Wang, C., Neutzner, A., Tjandra, N., Youle, R.J., 2011. Bcl-x(L) retrotranslocates Bax from the mitochondria into the cytosol. Cell 145, 104–116. https://doi.org/10.1016/J.CELL.2011.02.034

Eisenberg-Bord, M., Schuldiner, M., 2017a. Ground control to major TOM:

mitochondria–nucleus communication. FEBS J. 284, 196–210. https://doi.org/10.1111/FEBS.13778

Eisenberg-Bord, M., Schuldiner, M., 2017b. Mitochatting – If only we could be a fly on the cell wall. Biochim. Biophys. Acta - Mol. Cell Res. 1864, 1469–1480. https://doi.org/10.1016/j.bbamcr.2017.04.012

Elmore, S., 2007. Apoptosis: A Review of Programmed Cell Death. Toxicol. Pathol. 35, 495–516. https://doi.org/10.1080/01926230701320337

Escobar-Henriques, M., Langer, T., 2014. Dynamic survey of mitochondria by Ubiquitin. EMBO Rep. 15, 231–243. https://doi.org/10.1002/EMBR.201338225/ASSET/A9203242-62FA-4046-827D-9B4862681226/ASSETS/GRAPHIC/EMBR201338225-FIG-0003-M.PNG

Estaquier, J., Arnoult, D., 2007. Inhibiting Drp1-mediated mitochondrial fission selectively prevents the release of cytochrome c during apoptosis. Cell Death Differ. 2007 146 14, 1086–1094. https://doi.org/10.1038/sj.cdd.4402107

Finan, K., Raulf, A., Heilemann, M., 2015. A Set of Homo-Oligomeric Standards Allows Accurate Protein Counting. Angew. Chemie Int. Ed. 54, 12049–12052. https://doi.org/10.1002/anie.201505664

Flores-Romero, H., Ros, U., Garcia-Saez, A.J., 2020. Pore formation in regulated cell death. EMBO J. 39, e105753. https://doi.org/10.15252/embj.2020105753

Flores-Romero, H., Hohorst, L., John, M., Albert, M., King, L.E., Beckmann, L., Szabo, T., Hertlein, V., Luo, X., Villunger, A., Frenzel, L.P., Kashkar, H., Garcia-Saez, A.J., 2022. BCL-2-family protein tBID can act as a BAX-like effector of apoptosis. EMBO J. 41, e108690. https://doi.org/10.15252/embj.2021108690

Frank, S., Gaume, B., Bergmann-Leitner, E.S., Leitner, W.W., Robert, E.G., Catez, F., Smith, C.L., Youle, R.J., 2001. The Role of Dynamin-Related Protein 1, a Mediator of Mitochondrial Fission, in Apoptosis. Dev. Cell 1, 515–525. https://doi.org/10.1016/S1534-5807(01)00055-7

Frey, T.G., Renken, C.W., Perkins, G.A., 2002. Insight into mitochondrial structure and function from electron tomography. Biochim. Biophys. Acta - Bioenerg. 1555, 196–203. https://doi.org/10.1016/S0005-2728(02)00278-5

Frezza, C., Cipolat, S., Martins de Brito, O., Micaroni, M., Beznoussenko, G. V., Rudka, T., Bartoli, D., Polishuck, R.S., Danial, N.N., De Strooper, B., Scorrano, L., 2006. OPA1 Controls Apoptotic Cristae Remodeling Independently from Mitochondrial Fusion. Cell 126, 177–189. https://doi.org/10.1016/j.cell.2006.06.025

Friedman, J.R., Lackner, L.L., West, M., DiBenedetto, J.R., Nunnari, J., Voeltz, G.K., 2011. ER Tubules Mark Sites of Mitochondrial Division. Science (80-.). 334, 358–362. https://doi.org/10.1126/science.1207385

Fröhlich, C., Grabiger, S., Schwefel, D., Faelber, K., Rosenbaum, E., Mears, J., Rocks, O., Daumke, O., 2013. Structural insights into oligomerization and mitochondrial

remodelling of dynamin 1-like protein. EMBO J. 32, 1280–1292. https://doi.org/10.1038/emboj.2013.74

Fuchs, Y., Steller, H., 2011. Programmed Cell Death in Animal Development and Disease. Cell 147, 742–758. https://doi.org/10.1016/J.CELL.2011.10.033

Galluzzi, L., Vitale, I., Aaronson, S.A., Abrams, J.M., Adam, D., Agostinis, P., Alnemri, E.S., Altucci, L., Amelio, I., Andrews, D.W., Annicchiarico-Petruzzelli, M., Antonov, A. V., Arama, E., Baehrecke, E.H., Barlev, N.A., Bazan, N.G., Bernassola, F., Bertrand, M.J.M., Bianchi, K., Blagosklonny, M. V., Blomgren, K., Borner, C., Boya, P., Brenner, C., Campanella, M., Candi, E., Carmona-Gutierrez, D., Cecconi, F., Chan, F.K.M., Chandel, N.S., Cheng, E.H., Chipuk, J.E., Cidlowski, J.A., Ciechanover, A., Cohen, G.M., Conrad, M., Cubillos-Ruiz, J.R., Czabotar, P.E., D'Angiolella, V., Dawson, T.M., Dawson, V.L., De Laurenzi, V., De Maria, R., Debatin, K.M., Deberardinis, R.J., Deshmukh, M., Di Daniele, N., Di Virgilio, F., Dixit, V.M., Dixon, S.J., Duckett, C.S., Dynlacht, B.D., El-Deiry, W.S., Elrod, J.W., Fimia, G.M., Fulda, S., García-Sáez, A.J., Garg, A.D., Garrido, C., Gavathiotis, E., Golstein, P., Gottlieb, E., Green, D.R., Greene, L.A., Gronemeyer, H., Gross, A., Hajnoczky, G., Hardwick, J.M., Harris, I.S., Hengartner, M.O., Hetz, C., Ichijo, H., Jäättelä, M., Joseph, B., Jost, P.J., Juin, P.P., Kaiser, W.J., Karin, M., Kaufmann, T., Kepp, O., Kimchi, A., Kitsis, R.N., Klionsky, D.J., Knight, R.A., Kumar, S., Lee, S.W., Lemasters, J.J., Levine, B., Linkermann, A., Lipton, S.A., Lockshin, R.A., López-Otín, C., Lowe, S.W., Luedde, T., Lugli, E., MacFarlane, M., Madeo, F., Malewicz, M., Malorni, W., Manic, G., Marine, J.C., Martin, S.J., Martinou, J.C., Medema, J.P., Mehlen, P., Meier, P., Melino, S., Miao, E.A., Molkentin, J.D., Moll, U.M., Muñoz-Pinedo, C., Nagata, S., Nuñez, G., Oberst, A., Oren, M., Overholtzer, M., Pagano, M., Panaretakis, T., Pasparakis, M., Penninger, J.M., Pereira, D.M., Pervaiz, S., Peter, M.E., Piacentini, M., Pinton, P., Prehn, J.H.M., Puthalakath, H., Rabinovich, G.A., Rehm, M., Rizzuto, R., Rodrigues, C.M.P., Rubinsztein, D.C., Rudel, T., Ryan, K.M., Sayan, E., Scorrano, L., Shao, F., Shi, Y., Silke, J., Simon, H.U., Sistigu, A., Stockwell, B.R., Strasser, A., Szabadkai, G., Tait, S.W.G., Tang, D., Tavernarakis, N., Thorburn, A., Tsujimoto, Y., Turk, B., Vanden Berghe, T., Vandenabeele, P., Vander Heiden, M.G., Villunger, A., Virgin, H.W., Vousden, K.H., Vucic, D., Wagner, E.F., Walczak, H., Wallach, D., Wang, Y., Wells, J.A., Wood, W., Yuan, J., Zakeri, Z., Zhivotovsky, B., Zitvogel, L., Melino, G., Kroemer, G., 2018. Molecular mechanisms of cell death: recommendations of the Nomenclature Committee on Cell Death 2018. Cell Death Differ. 25, 486–541. https://doi.org/10.1038/s41418-017-0012-4

García-Sáez, A.J., Chiantia, S., Salgado, J., Schwille, P., 2007. Pore formation by a Bax-derived peptide: effect on the line tension of the membrane probed by AFM. Biophys. J. 93, 103–12. https://doi.org/10.1529/biophysj.106.100370

García-Sáez, A.J., Coraiola, M., Dalla Serra, M., Mingarro, I., Menestrina, G., Salgado, J., 2005. Peptides derived from apoptotic Bax and Bid reproduce the poration activity of the parent full-length proteins. Biophys. J. 88, 3976–90. https://doi.org/10.1529/biophysj.104.058008

García-Sáez, A.J., Ries, J., Orzáez, M., Pérez-Payà, E., Schwille, P., 2009. Membrane

promotes tBID interaction with BCLXL. Nat. Struct. Mol. Biol. 16, 1178–1185. https://doi.org/10.1038/nsmb.1671

García-Sáez, A.J., Coraiola, M., Serra, M.D., Mingarro, I., Müller, P., Salgado, J., 2006. Peptides corresponding to helices 5 and 6 of Bax can independently form large lipid pores. FEBS J. 273, 971–981. https://doi.org/10.1111/j.1742-4658.2006.05123.x

Garcia Fernandez, M., Troiano, L., Moretti, L., Nasi, M., Pinti, M., Salvioli, S., Dobrucki, J., Cossarizza, A., 2002. Early changes in intramitochondrial cardiolipin distribution during apoptosis. Cell Growth Differ. 13, 449–55.

Garner, T.P., Reyna, D.E., Priyadarshi, A., Chen, H.-C., Li, S., Wu, Y., Ganesan, Y.T., Malashkevich, V.N., Cheng, E.H., Gavathiotis, E., 2016. An Autoinhibited Dimeric Form of BAX Regulates the BAX Activation Pathway. Mol. Cell 63, 485–97. https://doi.org/10.1016/j.molcel.2016.06.010

Gavathiotis, E., Reyna, D.E., Davis, M.L., Bird, G.H., Walensky, L.D., 2010. BH3-triggered structural reorganization drives the activation of proapoptotic BAX. Mol. Cell 40, 481–92. https://doi.org/10.1016/j.molcel.2010.10.019

Gavathiotis, E., Suzuki, M., Davis, M.L., Pitter, K., Bird, G.H., Katz, S.G., Tu, H.-C., Kim, H., Cheng, E.H.Y., Tjandra, N., Walensky, L.D., 2008. BAX activation is initiated at a novel interaction site. Nature 455, 1076–81. https://doi.org/10.1038/nature07396

Gellerich, F.N., Trumbeckaite, S., Opalka, J.R., Seppet, E., Rasmussen, H.N., Neuhoff, C., Zierz, S., 2000. Function of the mitochondrial outer membrane as a diffusion barrier in health and diseases. Biochem. Soc. Trans. 28, 164–169. https://doi.org/10.1042/BST0280164

Giacomello, M., Pyakurel, A., Glytsou, C., Scorrano, L., 2020. The cell biology of mitochondrial membrane dynamics. Nat. Rev. Mol. Cell Biol. 2020 214 21, 204–224. https://doi.org/10.1038/s41580-020-0210-7

Giampazolias, E., Zunino, B., Dhayade, S., Bock, F., Cloix, C., Cao, K., Roca, A., Lopez, J., Ichim, G., Proïcs, E., Rubio-Patiño, C., Fort, L., Yatim, N., Woodham, E., Orozco, S., Taraborrelli, L., Peltzer, N., Lecis, D., Machesky, L., Walczak, H., Albert, M.L., Milling, S., Oberst, A., Ricci, J.E., Ryan, K.M., Blyth, K., Tait, S.W.G., 2017. Mitochondrial permeabilization engages NF-κB-dependent anti-tumour activity under caspase deficiency. Nat. Cell Biol. 2017 199 19, 1116–1129. https://doi.org/10.1038/ncb3596

Gitego, N., Agianian, B., Mak, O.W., Kumar MV, V., Cheng, E.H., Gavathiotis, E., 2023. Chemical modulation of cytosolic BAX homodimer potentiates BAX activation and apoptosis. Nat. Commun. 2023 141 14, 1–20. https://doi.org/10.1038/s41467-023-44084-3

Gonzalvez, F., Pariselli, F., Dupaigne, P., Budihardjo, I., Lutter, M., Antonsson, B., Diolez, P., Manon, S., Martinou, J.C., Goubern, M., Wang, X., Bernard, S., Petit, P.X., 2005. tBid interaction with cardiolipin primarily orchestrates mitochondrial

dysfunctions and subsequently activates Bax and Bak. Cell Death Differ. 2005 126 12, 614–626. https://doi.org/10.1038/sj.cdd.4401571

Gray, M.W., 2012. Mitochondrial Evolution. Cold Spring Harb. Perspect. Biol. 4, a011403. https://doi.org/10.1101/CSHPERSPECT.A011403

Green, D.R., Kroemer, G., 2004. The pathophysiology of mitochondrial cell death. Science 305, 626–9. https://doi.org/10.1126/science.1099320

Griffiths, G.J., Dubrez, L., Morgan, C.P., Jones, N.A., Whitehouse, J., Corfe, B.M., Dive, C., Hickman, J.A., 1999. Cell Damage-induced Conformational Changes of the Pro-Apoptotic Protein Bak In Vivo Precede the Onset of Apoptosis. J. Cell Biol. 144, 903–914. https://doi.org/10.1083/JCB.144.5.903

Große, L., Wurm, C.A., Brüser, C., Neumann, D., Jans, D.C., Jakobs, S., 2016. Bax assembles into large ring-like structures remodeling the mitochondrial outer membrane in apoptosis. EMBO J. 35, 402–413. https://doi.org/10.15252/embj.201592789

Hao, Z., Mak, T.W., 2010. Type I and Type II Pathways of Fas-mediated Apoptosis Are Differentially Controlled by XIAP. J. Mol. Cell Biol. 2, 63–64. https://doi.org/10.1093/JMCB/MJP034

Hauseman, Z.J., Harvey, E.P., Newman, C.E., Wales, T.E., Bucci, J.C., Mintseris, J., Schweppe, D.K., David, L., Fan, L., Cohen, D.T., Herce, H.D., Mourtada, R., Ben-Nun, Y., Bloch, N.B., Hansen, S.B., Wu, H., Gygi, S.P., Engen, J.R., Walensky, L.D., 2020. Homogeneous Oligomers of Pro-apoptotic BAX Reveal Structural Determinants of Mitochondrial Membrane Permeabilization. Mol. Cell 79, 68-83.e7. https://doi.org/10.1016/J.MOLCEL.2020.05.029/ATTACHMENT/3B25E372-0755-4B13-9347-2A08A31B3BCD/MMC3.PDF

Heilig, R., Lee, J., Tait, S.W.G., 2023. Mitochondrial DNA in cell death and inflammation. Biochem. Soc. Trans. 51, 457–472. https://doi.org/10.1042/BST20221525

Hockings, C., Anwari, K., Ninnis, R.L., Brouwer, J., O'Hely, M., Evangelista, M., Hinds, M.G., Czabotar, P.E., Lee, E.F., Fairlie, W.D., Dewson, G., Kluck, R.M., 2015. Bid chimeras indicate that most BH3-only proteins can directly activate Bak and Bax, and show no preference for Bak versus Bax. Cell Death Dis. 2015 64 6, e1735–e1735. https://doi.org/10.1038/cddis.2015.105

Hofer, A., Wenz, T., 2014. Post-translational modification of mitochondria as a novel mode of regulation. Exp. Gerontol. 56, 202–220. https://doi.org/10.1016/J.EXGER.2014.03.006

Hoppins, S., Nunnari, J., 2012. Mitochondrial Dynamics and Apoptosis—the ER Connection. Science (80-.). 337, 1052 LP – 1054.

Hovius, R., Thijssen, J., van der Linden, P., Nicolay, K., de Kruijff, B., 1993. Phospholipid asymmetry of the outer membrane of rat liver mitochondria:

Evidence for the presence of cardiolipin on the outside of the outer membrane. FEBS Lett. 330, 71–76. https://doi.org/10.1016/0014-5793(93)80922-H

Iyer, S., Anwari, K., Alsop, A.E., Yuen, W.S., Huang, D.C.S., Carroll, J., Smith, N.A., Smith, B.J., Dewson, G., Kluck, R.M., 2016. Identification of an activation site in Bak and mitochondrial Bax triggered by antibodies. Nat. Commun. 2016 71 7, 1–10. https://doi.org/10.1038/ncomms11734

Iyer, S., Uren, R.T., Dengler, M.A., Shi, M.X., Uno, E., Adams, J.M., Dewson, G., Kluck, R.M., 2020. Robust autoactivation for apoptosis by BAK but not BAX highlights BAK as an important therapeutic target. Cell Death Dis. 11, 1–13. https://doi.org/10.1038/s41419-020-2463-7

Jacobson, M.D., Weil, M., Raff, M.C., 1997. Programmed Cell Death in Animal Development. Cell 88, 347–354. https://doi.org/10.1016/S0092-8674(00)81873-5

Jenner, A., Garcia-Saez, A.J., 2024. The regulation of the apoptotic pore—An immunological tightrope walk. Adv. Immunol. 162, 59–108. https://doi.org/10.1016/BS.AI.2024.02.004

Jenner, A., Shalaby, R., Cosentino, K., 2020. Quantitative single-molecule imaging of protein assembly in membranes, Advances in Biomembranes and Lipid Self-Assembly. Academic Press.

Joaquim, M., Escobar-Henriques, M., 2020. Role of Mitofusins and Mitophagy in Life or Death Decisions. Front. Cell Dev. Biol. 8, 572182. https://doi.org/10.3389/FCELL.2020.572182/BIBTEX

Joza, N., Susin, S.A., Daugas, E., Stanford, W.L., Cho, S.K., Li, C.Y.J., Sasaki, T., Elia, A.J., Cheng, H.Y.M., Ravagnan, L., Ferri, K.F., Zamzami, N., Wakeham, A., Hakem, R., Yoshida, H., Kong, Y.Y., Mak, T.W., Zúñiga-Pflücker, J.C., Kroemer, G., Penninger, J.M., 2001. Essential role of the mitochondrial apoptosis-inducing factor in programmed cell death. Nat. 2001 4106828 410, 549–554. https://doi.org/10.1038/35069004

Kagan, V.E., Tyurin, V.A., Jiang, J., Tyurina, Y.Y., Ritov, V.B., Amoscato, A.A., Osipov, A.N., Belikova, N.A., Kapralov, A.A., Kini, V., Vlasova, I.I., Zhao, Q., Zou, M., Di, P., Svistunenko, D.A., Kurnikov, I. V., Borisenko, G.G., 2005. Cytochrome c acts as a cardiolipin oxygenase required for release of proapoptotic factors. Nat. Chem. Biol. 1, 223–232. https://doi.org/10.1038/nchembio727

Kale, J., Osterlund, E.J., Andrews, D.W., 2018. BCL-2 family proteins: Changing partners in the dance towards death. Cell Death Differ. https://doi.org/10.1038/cdd.2017.186

Kalia, R., Wang, R.Y.-R., Yusuf, A., Thomas, P. V., Agard, D.A., Shaw, J.M., Frost, A., 2018. Structural basis of mitochondrial receptor binding and constriction by DRP1. Nature 1. https://doi.org/10.1038/s41586-018-0211-2

Karbowski, M., Lee, Y.J., Gaume, B., Jeong, S.Y., Frank, S., Nechushtan, A., Santel, A., Fuller, M., Smith, C.L., Youle, R.J., 2002. Spatial and temporal association of

Bax with mitochondrial fission sites, Drp1, and Mfn2 during apoptosis. J. Cell Biol. 159, 931–938. https://doi.org/10.1083/JCB.200209124

Kerr, J.F.R., Wyllie, A.H., Currie, A.R., 1972. Apoptosis: A Basic Biological Phenomenon with Wideranging Implications in Tissue Kinetics. Br. J. Cancer 1972 264 26, 239–257. https://doi.org/10.1038/bjc.1972.33

Kim, H., Tu, H.C., Ren, D., Takeuchi, O., Jeffers, J.R., Zambetti, G.P., Hsieh, J.J.D., Cheng, E.H.Y., 2009. Stepwise Activation of BAX and BAK by tBID, BIM, and PUMA Initiates Mitochondrial Apoptosis. Mol. Cell 36, 487–499. https://doi.org/10.1016/J.MOLCEL.2009.09.030

Kim, H.E., Du, F., Fang, M., Wang, X., 2005. Formation of apoptosome is initiated by cytochrome c-induced dATP hydrolysis and subsequent nucleotide exchange on Apaf-1. Proc. Natl. Acad. Sci. 102, 17545–17550. https://doi.org/10.1073/PNAS.0507900102

Korobova, F., Ramabhadran, V., Higgs, H.N., 2013. An actin-dependent step in mitochondrial fission mediated by the ER-associated formin INF2. Science (80-.). 339, 464–467. https://doi.org/10.1126/SCIENCE.1228360/SUPPL_FILE/1228360S6.AVI

Krasovec, G., Horkan, H.R., Quéinnec, É., Chambon, J.P., 2024. Intrinsic apoptosis is evolutionarily divergent among metazoans. Evol. Lett. 8, 267–282. https://doi.org/10.1093/EVLETT/QRAD057

Kühlbrandt, W., 2015. Structure and function of mitochondrial membrane protein complexes. BMC Biol. 13, 1–11. https://doi.org/10.1186/S12915-015-0201-X/FIGURES/9

Kuwana, T., Bouchier-Hayes, L., Chipuk, J.E., Bonzon, C., Sullivan, B.A., Green, D.R., Newmeyer, D.D., 2005. BH3 Domains of BH3-Only Proteins Differentially Regulate Bax-Mediated Mitochondrial Membrane Permeabilization Both Directly and Indirectly. Mol. Cell 17, 525–535. https://doi.org/10.1016/J.MOLCEL.2005.02.003

Kuwana, T., King, L.E., Cosentino, K., Suess, J., Garcia-Saez, A.J., Gilmore, A.P., Newmeyer, D.D., 2020. Mitochondrial residence of the apoptosis inducer BAX is more important than BAX oligomerization in promoting membrane permeabilization. J. Biol. Chem. 295, 1623–1636. https://doi.org/10.1074/jbc.RA119.011635

Kvansakul, M., Yang, H., Fairlie, W.D., Czabotar, P.E., Fischer, S.F., Perugini, M.A., Huang, D.C.S., Colman, P.M., 2008. Vaccinia virus anti-apoptotic F1L is a novel Bcl-2-like domain-swapped dimer that binds a highly selective subset of BH3-containing death ligands. Cell Death Differ. 2008 1510 15, 1564–1571. https://doi.org/10.1038/cdd.2008.83

Lazarou, M., Stojanovski, D., Frazier, A.E., Kotevski, A., Dewson, G., Craigen, W.J., Kluck, R.M., Vaux, D.L., Ryan, M.T., 2010. Inhibition of Bak Activation by VDAC2 Is Dependent on the Bak Transmembrane Anchor * □ S.

https://doi.org/10.1074/jbc.M110.159301

Lee, E.F., Clarke, O.B., Evangelista, M., Feng, Z., Speed, T.P., Tchoubrieva, E.B., Strasser, A., Kalinna, B.H., Colman, P.M., Fairlie, W.D., 2011. Discovery and molecular characterization of a Bcl-2-regulated cell death pathway in schistosomes. Proc. Natl. Acad. Sci. U. S. A. 108, 6999–7003. https://doi.org/10.1073/pnas.1100652108

Lee, J.E., Westrate, L.M., Wu, H., Page, C., Voeltz, G.K., 2016. Multiple dynamin family members collaborate to drive mitochondrial division. Nature 540, 139–143. https://doi.org/10.1038/nature20555

Lee, M.-T., Chen, F.-Y., Huang, H.W., 2004. Energetics of pore formation induced by membrane active peptides. Biochemistry 43, 3590–9. https://doi.org/10.1021/bi036153r

Letai, A., Bassik, M.C., Walensky, L.D., Sorcinelli, M.D., Weiler, S., Korsmeyer, S.J., 2002. Distinct BH3 domains either sensitize or activate mitochondrial apoptosis, serving as prototype cancer therapeutics. Cancer Cell 2, 183–192. https://doi.org/10.1016/S1535-6108(02)00127-7

Li, P., Nijhawan, D., Budihardjo, I., Srinivasula, S.M., Ahmad, M., Alnemri, E.S., Wang, X., 1997. Cytochrome c and dATP-Dependent Formation of Apaf-1/Caspase-9 Complex Initiates an Apoptotic Protease Cascade. Cell 91, 479–489. https://doi.org/10.1016/S0092-8674(00)80434-1

Lill, R., Lill, R., 2020. From the discovery to molecular understanding of cellular iron-sulfur protein biogenesis. Biol. Chem. 401, 855–876. https://doi.org/10.1515/HSZ-2020-0117/ASSET/GRAPHIC/J_HSZ-2020-0117_FIG_004.JPG

Lindsten, T., Ross, A.J., King, A., Zong, W.X., Rathmell, J.C., Shiels, H.A., Ulrich, E., Waymire, K.G., Mahar, P., Frauwirth, K., Chen, Y., Wei, M., Eng, V.M., Adelman, D.M., Simon, M.C., Ma, A., Golden, J.A., Evan, G., Korsmeyer, S.J., MacGregor, G.R., Thompson, C.B., 2000. The Combined Functions of Proapoptotic Bcl-2 Family Members Bak and Bax Are Essential for Normal Development of Multiple Tissues. Mol. Cell 6, 1389–1399. https://doi.org/10.1016/S1097-2765(00)00136-2

Losó n, O.C., Song, Z., Chen, H., Chan, D.C., 2013. Fis1, Mff, MiD49, and MiD51 mediate Drp1 recruitment in mitochondrial fission. Mol. Biol. Cell 24, 659–667. https://doi.org/10.1091/MBC.E12-10-0721/ASSET/IMAGES/LARGE/659FIG6.JPEG

Lossi, L., 2022. The concept of intrinsic versus extrinsic apoptosis. Biochem. J. 479, 357–384. https://doi.org/10.1042/BCJ20210854

Luo, X., Zhao, Y., Luo, Y., Lai, J., Ji, J., Huang, J., Chen, Y., Liu, Z., Liu, J., 2024. Cytosolic mtDNA–cGAS–STING axis contributes to sepsis-induced acute kidney injury via activating the NLRP3 inflammasome. Clin. Exp. Nephrol. 28, 375–390. https://doi.org/10.1007/s10157-023-02448-5

Lutter, M., Perkins, G.A., Wang, X., 2001. The pro-apoptotic Bcl-2 family member tBid

localizes to mitochondrial contact sites. BMC Cell Biol. 2, 1–9. https://doi.org/10.1186/1471-2121-2-22/TABLES/1

Lv, F., Qi, F., Zhang, Z., Wen, M., Kale, J., Piai, A., Du, L., Wang, S., Zhou, L., Yang, Y., Wu, B., Liu, Z., del Rosario, J., Pogmore, J., Chou, J.J., Andrews, D.W., Lin, J., OuYang, B., 2021. An amphipathic Bax core dimer forms part of the apoptotic pore wall in the mitochondrial membrane. EMBO J. 40. https://doi.org/10.15252/EMBJ.2020106438/SUPPL_FILE/EMBJ2020106438-SUP-0005-SDATAEV.ZIP

Ma, S.B., Nguyen, T.N., Tan, I., Ninnis, R., Iyer, S., Stroud, D.A., Menard, M., Kluck, R.M., Ryan, M.T., Dewson, G., 2014. Bax targets mitochondria by distinct mechanisms before or during apoptotic cell death: a requirement for VDAC2 or Bak for efficient Bax apoptotic function. Cell Death Differ. 21, 1925–1935. https://doi.org/10.1038/cdd.2014.119

MacVicar, T., Langer, T., 2016. OPA1 processing in cell death and disease - the long and short of it. J. Cell Sci. 129, 2297–2306. https://doi.org/10.1242/JCS.159186/259160/AM/OPA1-PROCESSING-IN-CELL-DEATH-AND-DISEASE-THE-LONG

Mahecic, D., Carlini, L., Kleele, T., Colom, A., Goujon, A., Matile, S., Roux, A., Manley, S., 2021. Mitochondrial membrane tension governs fission. Cell Rep. 35, 108947. https://doi.org/10.1016/J.CELREP.2021.108947

Mailloux, R.J., Bériault, R., Lemire, J., Singh, R., Chénier, D.R., Hamel, R.D., Appanna, V.D., 2007. The Tricarboxylic Acid Cycle, an Ancient Metabolic Network with a Novel Twist. PLoS One 2, e690. https://doi.org/10.1371/JOURNAL.PONE.0000690

Mandal, T., Shin, S., Aluvila, S., Chen, H.C., Grieve, C., Choe, J.Y., Cheng, E.H., Hustedt, E.J., Oh, K.J., 2016. Assembly of Bak homodimers into higher order homooligomers in the mitochondrial apoptotic pore. Sci. Reports 2016 61 6, 1–14. https://doi.org/10.1038/srep30763

Marchi, S., Bittremieux, M., Missiroli, S., Morganti, C., Patergnani, S., Sbano, L., Rimessi, A., Kerkhofs, M., Parys, J.B., Bultynck, G., Giorgi, C., Pinton, P., 2017. Endoplasmic reticulum-mitochondria communication through Ca2+ signaling: The importance of mitochondria-associated membranes (MAMs). Adv. Exp. Med. Biol. 997, 49–67. https://doi.org/10.1007/978-981-10-4567-7_4/FIGURES/3

Martínez-Reyes, I., Chandel, N.S., 2020. Mitochondrial TCA cycle metabolites control physiology and disease. Nat. Commun. 2020 111 11, 1–11. https://doi.org/10.1038/s41467-019-13668-3

Mattson, M.P., 2000. Apoptosis in neurodegenerative disorders. Nat. Rev. Mol. Cell Biol. 2000 12 1, 120–130. https://doi.org/10.1038/35040009

Mazunin, I.O., Levitskii, S.A., Patrushev, M. V., Kamenski, P.A., 2015. Mitochondrial matrix processes. Biochem. 2015 8011 80, 1418–1428. https://doi.org/10.1134/S0006297915110036

McArthur, K., Kile, B.T., 2020. Apoptotic mitochondria prime anti-tumour immunity. Cell Death Discov. 6, 98. https://doi.org/10.1038/s41420-020-00335-6

McArthur, K., Whitehead, L.W., Heddleston, J.M., Li, L., Padman, B.S., Oorschot, V., Geoghegan, N.D., Chappaz, S., Davidson, S., San Chin, H., Lane, R.M., Dramicanin, M., Saunders, T.L., Sugiana, C., Lessene, R., Osellame, L.D., Chew, T.-L.L., Dewson, G., Lazarou, M., Ramm, G., Lessene, G., Ryan, M.T., Rogers, K.L., Van Delft, M.F., Kile, B.T., Chin, H.S., Lane, R.M., Dramicanin, M., Saunders, T.L., Sugiana, C., Lessene, R., Osellame, L.D., Chew, T.-L.L., Dewson, G., Lazarou, M., Ramm, G., Lessene, G., Ryan, M.T., Rogers, K.L., Van Delft, M.F., Kile, B.T., 2018. BAK/BAX macropores facilitate mitochondrial herniation and mtDNA efflux during apoptosis. Science (80-.). 359, eaao6047. https://doi.org/10.1126/science.aao6047

McDonnell, J.M., Fushman, D., Milliman, C.L., Korsmeyer, S.J., Cowburn, D., 1999. Solution Structure of the Proapoptotic Molecule BID: A Structural Basis for Apoptotic Agonists and Antagonists. Cell 96, 625–634. https://doi.org/10.1016/S0092-8674(00)80573-5

Metzstein, M.M., Stanfield, G.M., Horvitz, H.R., 1998. Genetics of programmed cell death in C. elegans: past, present and future. Trends Genet. 14, 410–416. https://doi.org/10.1016/S0168-9525(98)01573-X

Miao, R., Jiang, C., Chang, W.Y., Zhang, H.H.H.H., An, J., Ho, F., Chen, P., Zhang, H.H.H.H., Junqueira, C., Amgalan, D., Liang, F.G., Zhang, J., Evavold, C.L., Hafner-Bratkovič, I., Zhang, Z., Fontana, P., Xia, S., Waldeck-Weiermair, M., Pan, Y., Michel, T., Bar-Peled, L., Wu, H., Kagan, J.C., Kitsis, R.N., Zhang, P., Liu, X., Lieberman, J., 2023. Gasdermin D permeabilization of mitochondrial inner and outer membranes accelerates and enhances pyroptosis. Immunity 56, 2523-2541.e8. https://doi.org/10.1016/j.immuni.2023.10.004

Mishra, P., Chan, D.C., 2016. Metabolic regulation of mitochondrial dynamics. J. Cell Biol. 212, 379–387. https://doi.org/10.1083/JCB.201511036

Montessuit, S., Somasekharan, S.P., Terrones, O., Lucken-Ardjomande, S., Herzig, S., Schwarzenbacher, R., Manstein, D.J., Bossy-Wetzel, E., Basañez, G., Meda, P., Martinou, J.-C., 2010. Membrane Remodeling Induced by the Dynamin-Related Protein Drp1 Stimulates Bax Oligomerization. Cell 142, 889–901. https://doi.org/10.1016/J.CELL.2010.08.017

Moujalled, D., Strasser, A., Liddell, J.R., 2021. Molecular mechanisms of cell death in neurological diseases. Cell Death Differ. 2021 287 28, 2029–2044. https://doi.org/10.1038/s41418-021-00814-y

Muchmore, S.W., Sattler, M., Liang, H., Meadows, R.P., Harlan, J.E., Yoon, H.S., Nettesheim, D., Chang, B.S., Thompson, C.B., Wong, S.L., Ng, S.C., Fesik, S.W., 1996. X-ray and NMR structure of human Bcl-xL, an inhibitor of programmed cell death. Nat. 1996 3816580 381, 335–341. https://doi.org/10.1038/381335a0

Nagata, S., Tanaka, M., 2017. Programmed cell death and the immune system. Nat.

Rev. Immunol. 2017 175 17, 333–340. https://doi.org/10.1038/nri.2016.153

Nechushtan, A., Smith, C.L., Hsu, Y.-T., Youle, R.J., 1999. Conformation of the Bax C-terminus regulates subcellular location and cell death. EMBO J. 18, 2330–2341. https://doi.org/10.1093/emboj/18.9.2330

Neel, D. V., Basu, H., Gunner, G., Bergstresser, M.D., Giadone, R.M., Chung, H., Miao, R., Chou, V., Brody, E., Jiang, X., Lee, E., Watts, M.E., Marques, C., Held, A., Wainger, B., Lagier-Tourenne, C., Zhang, Y.-J., Petrucelli, L., Young-Pearse, T.L., Chen-Plotkin, A.S., Rubin, L.L., Lieberman, J., Chiu, I.M., 2023. Gasdermin-E mediates mitochondrial damage in axons and neurodegeneration. Neuron 111, 1222-1240.e9. https://doi.org/10.1016/j.neuron.2023.02.019

Nicholson, D.W., 1999. Caspase structure, proteolytic substrates, and function during apoptotic cell death. Cell Death Differ. 1999 611 6, 1028–1042. https://doi.org/10.1038/sj.cdd.4400598

Osellame, L.D., Singh, A.P., Stroud, D.A., Palmer, C.S., Stojanovski, D., Ramachandran, R., Ryan, M.T., 2016. Cooperative and independent roles of the Drp1 adaptors Mff, MiD49 and MiD51 in mitochondrial fission. J. Cell Sci. 129, 2170–2181. https://doi.org/10.1242/JCS.185165/260155/AM/COOPERATIVE-AND-INDEPENDENT-ROLES-OF-DRP1-ADAPTORS

Otera, H., Miyata, N., Kuge, O., Mihara, K., 2016. Drp1-dependent mitochondrial fission via MiD49/51 is essential for apoptotic cristae remodeling. J. Cell Biol. 212, 531–544. https://doi.org/10.1083/JCB.201508099

Palade, G.E., 1953. An electron microscope study of the mitochondrial structure. J. Histochem. Cytochem. 1, 188–211. https://doi.org/10.1177/1.4.188

Palmer, C.S., Elgass, K.D., Parton, R.G., Osellame, L.D., Stojanovski, D., Ryan, M.T., 2013. Adaptor Proteins MiD49 and MiD51 Can Act Independently of Mff and Fis1 in Drp1 Recruitment and Are Specific for Mitochondrial Fission. J. Biol. Chem. 288, 27584–27593. https://doi.org/10.1074/JBC.M113.479873

Parone, P.A., James, D.I., Cruz, S. Da, Mattenberger, Y., Donzé, O., Barja, F., Martinou, J.-C., 2006. Inhibiting the Mitochondrial Fission Machinery Does Not Prevent Bax/Bak-Dependent Apoptosis. Mol. Cell. Biol. 26, 7397–7408. https://doi.org/10.1128/MCB.02282-05

Peña-Blanco, A., García-Sáez, A.J., 2018. Bax, Bak and beyond — mitochondrial performance in apoptosis. FEBS J. 285, 416–431. https://doi.org/10.1111/FEBS.14186

Petros, A.M., Medek, A., Nettesheim, D.G., Kim, D.H., Yoon, H.S., Swift, K., Matayoshi, E.D., Oltersdorf, T., Fesik, S.W., 2001. Solution structure of the antiapoptotic protein bcl-2. Proc. Natl. Acad. Sci. U. S. A. 98, 3012–3017. https://doi.org/10.1073/PNAS.041619798/ASSET/CD77F35D-0698-49BE-8688-AAB4047E77D2/ASSETS/GRAPHIC/PQ0416197006.JPEG

Petros, A.M., Olejniczak, E.T., Fesik, S.W., 2004. Structural biology of the Bcl-2 family

of proteins. Biochim. Biophys. Acta 1644, 83–94. https://doi.org/10.1016/j.bbamcr.2003.08.012

Popgeorgiev, N., Sa, J.D., Jabbour, L., Banjara, S., Nguyen, T.T.M., Akhavan-E-Sabet, A., Gadet, R., Ralchev, N., Manon, S., Hinds, M.G., Osigus, H.-J., Schierwater, B., Humbert, P.O., Rimokh, R., Gillet, G., Kvansakul, M., 2020. Ancient and conserved functional interplay between Bcl-2 family proteins in the mitochondrial pathway of apoptosis. Sci. Adv. 6, 4149. https://doi.org/10.1126/sciadv.abc4149

Prudent, J., Zunino, R., Sugiura, A., Mattie, S., Shore, G.C.C., McBride, H.M.M., 2015. MAPL SUMOylation of Drp1 Stabilizes an ER/Mitochondrial Platform Required for Cell Death. Mol. Cell 59, 941–955. https://doi.org/10.1016/J.MOLCEL.2015.08.001

Qian, S., Wang, W., Yang, L., Huang, H.W., 2008. Structure of transmembrane pore induced by Bax-derived peptide: evidence for lipidic pores. Proc. Natl. Acad. Sci. U. S. A. 105, 17379–83. https://doi.org/10.1073/pnas.0807764105

Reed, J.C., 1999. Dysregulation of apoptosis in cancer. J. Clin. Oncol. 17, 2941–2953. https://doi.org/10.1200/JCO.1999.17.9.2941/ASSET/7EF325A9-6ED4-4DAC-9540-6EB24FF7EAC5/ASSETS/GRAPHIC/2941F005Z.JPEG

Reynwar, B.J., Illya, G., Harmandaris, V.A., Müller, M.M., Kremer, K., Deserno, M., 2007. Aggregation and vesiculation of membrane proteins by curvature-mediated interactions. Nat. 2007 4477143 447, 461–464. https://doi.org/10.1038/nature05840

Ricci, J.E., Muñoz-Pinedo, C., Fitzgerald, P., Bailly-Maitre, B., Perkins, G.A., Yadava, N., Scheffler, I.E., Ellisman, M.H., Green, D.R., 2004. Disruption of Mitochondrial Function during Apoptosis Is Mediated by Caspase Cleavage of the p75 Subunit of Complex I of the Electron Transport Chain. Cell 117, 773–786. https://doi.org/10.1016/J.CELL.2004.05.008

Riedl, S.J., Salvesen, G.S., 2007. The apoptosome: signalling platform of cell death. Nat. Rev. Mol. Cell Biol. 2007 85 8, 405–413. https://doi.org/10.1038/nrm2153

Riley, J.S., Quarato, G., Cloix, C., Lopez, J., O'Prey, J., Pearson, M., Chapman, J., Sesaki, H., Carlin, L.M., Passos, J.F., Wheeler, A.P., Oberst, A., Ryan, K.M., Tait, S.W., 2018. Mitochondrial inner membrane permeabilisation enables mt DNA release during apoptosis . EMBO J. 37. https://doi.org/10.15252/embj.201899238

Robin, A.Y., Iyer, S., Birkinshaw, R.W., Sandow, J., Wardak, A., Luo, C.S., Shi, M., Webb, A.I., Czabotar, P.E., Kluck, R.M., Colman, P.M., 2018. Ensemble Properties of Bax Determine Its Function. Structure 26, 1346-1359.e5. https://doi.org/10.1016/j.str.2018.07.006

Roger, A.J., Muñoz-Gómez, S.A., Kamikawa, R., 2017. The Origin and Diversification of Mitochondria. Curr. Biol. 27, R1177–R1192. https://doi.org/10.1016/J.CUB.2017.09.015

Rogers, C., Erkes, D.A., Nardone, A., Aplin, A.E., Fernandes-Alnemri, T., Alnemri, E.S.,

2019. Gasdermin pores permeabilize mitochondria to augment caspase-3 activation during apoptosis and inflammasome activation 10. https://doi.org/10.1038/s41467-019-09397-2

Rongvaux, A., Jackson, R., Harman, C.C.D., Li, T., West, A.P., De Zoete, M.R., Wu, Y., Yordy, B., Lakhani, S.A., Kuan, C.Y., Taniguchi, T., Shadel, G.S., Chen, Z.J., Iwasaki, A., Flavell, R.A., 2014. Apoptotic Caspases Prevent the Induction of Type I Interferons by Mitochondrial DNA. Cell 159, 1563–1577. https://doi.org/10.1016/J.CELL.2014.11.037

Sabouny, R., Shutt, T.E., 2021. The role of mitochondrial dynamics in mtDNA maintenance. J. Cell Sci. 134. https://doi.org/10.1242/JCS.258944/273731

Sagan, L., 1967. On the origin of mitosing cells. J. Theor. Biol. 14. https://doi.org/10.1016/0022-5193(67)90079-3

Salvador-Gallego, R., Mund, M., Cosentino, K., Schneider, J., Unsay, J., Schraermeyer, U., Engelhardt, J., Ries, J., García-Sáez, A.J., Salvador-Gallego, R., Mund, M., Cosentino, K., Schneider, J., Unsay, J., Schraermeyer, U., Engelhardt, J., Ries, J., García-Sáez, A.J., 2016. Bax assembly into rings and arcs in apoptotic mitochondria is linked to membrane pores. EMBO J. 35, 389–401. https://doi.org/10.15252/embj.201593384

Sandow, J.J., Tan, I.K., Huang, A.S., Masaldan, S., Bernardini, J.P., Wardak, A.Z., Birkinshaw, R.W., Ninnis, R.L., Liu, Z., Dalseno, D., Lio, D., Infusini, G., Czabotar, P.E., Webb, A.I., Dewson, G., 2021. Dynamic reconfiguration of pro-apoptotic BAK on membranes. EMBO J. 40, e107237. https://doi.org/10.15252/embj.2020107237

Sarosiek, K.A., Chi, X., Bachman, J.A., Sims, J.J., Montero, J., Patel, L., Flanagan, A., Andrews, D.W., Sorger, P., Letai, A., 2013. BID Preferentially Activates BAK while BIM Preferentially Activates BAX, Affecting Chemotherapy Response. Mol. Cell 51, 751–765. https://doi.org/10.1016/J.MOLCEL.2013.08.048

Saunders, T.L., Windley, S.P., Gervinskas, G., Balka, K.R., Rowe, C., Lane, R., Tailler, M., Nguyen, T.N., Ramm, G., Lazarou, M., De Nardo, D., Kile, B.T., McArthur, K., 2024. Exposure of the inner mitochondrial membrane triggers apoptotic mitophagy. Cell Death Differ. 2024 313 31, 335–347. https://doi.org/10.1038/s41418-024-01260-2

Schweighofer, S. V., Jans, D.C., Keller-Findeisen, J., Folmeg, A., Ilgen, P., Bates, M., Jakobs, S., 2024. Endogenous BAX and BAK form mosaic rings of variable size and composition on apoptotic mitochondria. Cell Death Differ. 2024 314 31, 469–478. https://doi.org/10.1038/s41418-024-01273-x

Scorrano, L., Ashiya, M., Buttle, K., Weiler, S., Oakes, S.A., Mannella, C.A., Korsmeyer, S.J., 2002. A Distinct Pathway Remodels Mitochondrial Cristae and Mobilizes Cytochrome c during Apoptosis. Dev. Cell 2, 55–67. https://doi.org/10.1016/S1534-5807(01)00116-2

Scorrano, L., Oakes, S.A., Opferman, J.T., Cheng, E.H., Sorcinelli, M.D., Pozzan, T.,

Korsmeyer, S.J., 2003. BAX and BAK regulation of endoplasmic reticulum Ca2+: A control point for apoptosis. Science (80-.). 300, 135–139. https://doi.org/10.1126/SCIENCE.1081208/SUPPL_FILE/SCORRANO.SOM.PDF

Shalaby, R., Flores-romero, H., García-Sáez, A.J., 2020. The Mysteries around the BCL-2 Family Member BOK. Biomol. 2020, Vol. 10, Page 1638 10, 1638. https://doi.org/10.3390/BIOM10121638

Sheridan, C., Delivani, P., Cullen, S.P., Martin, S.J., 2008. Bax- or Bak-Induced Mitochondrial Fission Can Be Uncoupled from Cytochrome c Release. Mol. Cell 31, 570–585. https://doi.org/10.1016/J.MOLCEL.2008.08.002

Sicheritz-Pontén, T., Kurland, C.G., Andersson, S.G.E., 1998. A phylogenetic analysis of the cytochrome b and cytochrome c oxidase I genes supports an origin of mitochondria from within the Rickettsiaceae. Biochim. Biophys. Acta - Bioenerg. 1365, 545–551. https://doi.org/10.1016/S0005-2728(98)00099-1

Singh, G., Guibao, C.D., Seetharaman, J., Aggarwal, A., Grace, C.R., McNamara, D.E., Vaithiyalingam, S., Waddell, M.B., Moldoveanu, T., 2022. Structural basis of BAK activation in mitochondrial apoptosis initiation. Nat. Commun. 2022 131 13, 1–15. https://doi.org/10.1038/s41467-021-27851-y

Singh, R., Letai, A., Sarosiek, K., 2019. Regulation of apoptosis in health and disease: the balancing act of BCL-2 family proteins 20.

Sjöstrand, F.S., 1953. Electron Microscopy of Mitochondria and Cytoplasmic Double Membranes: Ultra-Structure of Rod-shaped Mitochondria. Nat. 1953 1714340 171, 30–31. https://doi.org/10.1038/171030a0

Subburaj, Y., Cosentino, K., Axmann, M., Pedrueza-Villalmanzo, E., Hermann, E., Bleicken, S., Spatz, J., García-Sáez, A.J., 2015. Bax monomers form dimer units in the membrane that further self-assemble into multiple oligomeric species. Nat. Commun. 6, 1–11. https://doi.org/10.1038/ncomms9042

Suzuki, M., Youle, R.J., Tjandra, N., 2000. Structure of Bax: Coregulation of Dimer Formation and Intracellular Localization. Cell 103, 645–654. https://doi.org/10.1016/S0092-8674(00)00167-7

Suzuki, Y., Imai, Y., Nakayama, H., Takahashi, K., Takio, K., Takahashi, R., 2001. A Serine Protease, HtrA2, Is Released from the Mitochondria and Interacts with XIAP, Inducing Cell Death. Mol. Cell 8, 613–621. https://doi.org/10.1016/S1097-2765(01)00341-0

Tábara, L.C., Segawa, M., Prudent, J., 2024. Molecular mechanisms of mitochondrial dynamics. Nat. Rev. Mol. Cell Biol. 2024 262 26, 123–146. https://doi.org/10.1038/s41580-024-00785-1

Tait, S.W.G., Green, D.R., 2010. Mitochondria and cell death: outer membrane permeabilization and beyond. Nat. Rev. Mol. Cell Biol. 2010 119 11, 621–632. https://doi.org/10.1038/nrm2952

Tait, S.W.G., Green, D.R., 2008. Caspase-independent cell death: leaving the set without the final cut. Oncogene 2008 2750 27, 6452–6461. https://doi.org/10.1038/onc.2008.311

Tatsuta, T., Langer, T., 2017. Intramitochondrial phospholipid trafficking. Biochim. Biophys. Acta - Mol. Cell Biol. Lipids 1862, 81–89. https://doi.org/10.1016/J.BBALIP.2016.08.006

Taylor, R.C., Cullen, S.P., Martin, S.J., 2008. Apoptosis: controlled demolition at the cellular level. Nat. Rev. Mol. Cell Biol. 2008 93 9, 231–241. https://doi.org/10.1038/nrm2312

Terrones, O., Antonsson, B., Yamaguchi, H., Wang, H.G., Liu, J., Lee, R.M., Herrmann, A., Basañez, G., 2004. Lipidic pore formation by the concerted action of proapoptotic BAX and tBID. J. Biol. Chem. 279, 30081–30091. https://doi.org/10.1074/JBC.M313420200

Unsay, J.D., Cosentino, K., Sporbeck, K., García-Sáez, A.J., 2017. Pro-apoptotic cBid and Bax exhibit distinct membrane remodeling activities: An AFM study. Biochim. Biophys. Acta - Biomembr. 1859, 17–27. https://doi.org/10.1016/J.BBAMEM.2016.10.007

Unsay, J.D., Cosentino, K., Subburaj, Y., García-Sáez, A.J., 2013. Cardiolipin effects on membrane structure and dynamics. Langmuir 29, 15878–15887. https://doi.org/10.1021/LA402669Z/ASSET/IMAGES/LARGE/LA-2013-02669Z_0007.JPEG

Uren, R.T., O'Hely, M., Iyer, S., Bartolo, R., Shi, M.X., Brouwer, J.M., Alsop, A.E., Dewson, G., Kluck, R.M., 2017. Disordered clusters of bak dimers rupture mitochondria during apoptosis. Elife 6. https://doi.org/10.7554/ELIFE.19944

van Delft, M.F., Chappaz, S., Khakham, Y., Bui, C.T., Debrincat, M.A., Lowes, K.N., Brouwer, J.M., Grohmann, C., Sharp, P.P., Dagley, L.F., Li, L., McArthur, K., Luo, M.X., Chin, H.S., Fairlie, W.D., Lee, E.F., Segal, D., Duflocq, S., Lessene, R., Bernard, S., Peilleron, L., Nguyen, T., Miles, C., Wan, S.S., Lane, R.M., Wardak, A., Lackovic, K., Colman, P.M., Sandow, J.J., Webb, A.I., Czabotar, P.E., Dewson, G., Watson, K.G., Huang, D.C.S., Lessene, G., Kile, B.T., 2019. A small molecule interacts with VDAC2 to block mouse BAK-driven apoptosis. Nat. Chem. Biol. https://doi.org/10.1038/s41589-019-0365-8

Van Loo, G., Schotte, P., Van Gurp, M., Demol, H., Hoorelbeke, B., Gevaert, K., Rodriguez, I., Ruiz-Carrillo, A., Vandekerckhove, J., Declercq, W., Beyaert, R., Vandenabeele, P., 2001. Endonuclease G: a mitochondrial protein released in apoptosis and involved in caspase-independent DNA degradation. Cell Death Differ. 2001 812 8, 1136–1142. https://doi.org/10.1038/sj.cdd.4400944

Vander Heiden, M.G., Chandel, N.S., Schumacker, P.T., Thompson, C.B., 1999. Bcl-xL Prevents Cell Death following Growth Factor Withdrawal by Facilitating Mitochondrial ATP/ADP Exchange. Mol. Cell 3, 159–167. https://doi.org/10.1016/S1097-2765(00)80307-X

Verdaasdonk, J.S., Lawrimore, J., Bloom, K., 2014. Determining absolute protein numbers by quantitative fluorescence microscopy. Methods Cell Biol. 123, 347–365. https://doi.org/10.1016/B978-0-12-420138-5.00019-7

Verhagen, A.M., Ekert, P.G., Pakusch, M., Silke, J., Connolly, L.M., Reid, G.E., Moritz, R.L., Simpson, R.J., Vaux, D.L., 2000. Identification of DIABLO, a Mammalian Protein that Promotes Apoptosis by Binding to and Antagonizing IAP Proteins. Cell 102, 43–53. https://doi.org/10.1016/S0092-8674(00)00009-X

Victorelli, S., Salmonowicz, H., Chapman, J., Martini, H., Vizioli, M.G., Riley, J.S., Cloix, C., Hall-Younger, E., Machado Espindola-Netto, J., Jurk, D., Lagnado, A.B., Sales Gomez, L., Farr, J.N., Saul, D., Reed, R., Kelly, G., Eppard, M., Greaves, L.C., Dou, Z., Pirius, N., Szczepanowska, K., Porritt, R.A., Huang, H., Huang, T.Y., Mann, D.A., Masuda, C.A., Khosla, S., Dai, H., Kaufmann, S.H., Zacharioudakis, E., Gavathiotis, E., LeBrasseur, N.K., Lei, X., Sainz, A.G., Korolchuk, V.I., Adams, P.D., Shadel, G.S., Tait, S.W.G., Passos, J.F., 2023. Apoptotic stress causes mtDNA release during senescence and drives the SASP. Nat. 2023 6227983 622, 627–636. https://doi.org/10.1038/s41586-023-06621-4

Wai, T., Langer, T., 2016. Mitochondrial Dynamics and Metabolic Regulation. Trends Endocrinol. Metab. 27, 105–117. https://doi.org/10.1016/J.TEM.2015.12.001/ASSET/F120020C-C805-41A8-92AA-A8AA99437A6F/MAIN.ASSETS/GR3.JPG

Wang, K., Gross, A., Waksman, G., Korsmeyer, S.J., 1998. Mutagenesis of the BH3 Domain of BAX Identifies Residues Critical for Dimerization and Killing. Mol. Cell. Biol. 18, 6083–6089. https://doi.org/10.1128/MCB.18.10.6083

Wang, X., 2001. The expanding role of mitochondria in apoptosis. Genes Dev. 15, 2922–33.

Wang, Y., Gao, W., Shi, X., Ding, J., Liu, W., He, H., Wang, K., Shao, F., 2017. Chemotherapy drugs induce pyroptosis through caspase-3 cleavage of a gasdermin. Nature 547, 99–103. https://doi.org/10.1038/nature22393

Weber, K., Harper, N., Schwabe, J., Cohen, G.M., 2013. BIM-Mediated Membrane Insertion of the BAK Pore Domain Is an Essential Requirement for Apoptosis. Cell Rep. 5, 409. https://doi.org/10.1016/J.CELREP.2013.09.010

Wei, M.C., Lindsten, T., Mootha, V.K., Weiler, S., Gross, A., Ashiya, M., Thompson, C.B., Korsmeyer, S.J., 2000. tBID, a membrane-targeted death ligand, oligomerizes BAK to release cytochrome c. Genes Dev. 14, 2060–71. https://doi.org/10.1101/GAD.14.16.2060

Westphal, D., Kluck, R.M., Dewson, G., 2014. Building blocks of the apoptotic pore: How Bax and Bak are activated and oligomerize during apoptosis. Cell Death Differ. https://doi.org/10.1038/cdd.2013.139

White, M.J., McArthur, K., Metcalf, D., Lane, R.M., Cambier, J.C., Herold, M.J., Van Delft, M.F., Bedoui, S., Lessene, G., Ritchie, M.E., Huang, D.C.S., Kile, B.T., 2014. Apoptotic Caspases Suppress mtDNA-Induced STING-Mediated Type I IFN

Production. Cell 159, 1549–1562. https://doi.org/10.1016/J.CELL.2014.11.036

Wiedemann, N., Pfanner, N., 2017. Mitochondrial machineries for protein import and assembly. Annu. Rev. Biochem. 86, 685–714. https://doi.org/10.1146/ANNUREV-BIOCHEM-060815-014352/CITE/REFWORKS

Yamazaki, T., Kirchmair, A., Sato, A., Buqué, A., Rybstein, M., Petroni, G., Bloy, N., Finotello, F., Stafford, L., Navarro Manzano, E., Ayala de la Peña, F., García-Martínez, E., Formenti, S.C., Trajanoski, Z., Galluzzi, L., 2020. Mitochondrial DNA drives abscopal responses to radiation that are inhibited by autophagy. Nat. Immunol. 21, 1160–1171. https://doi.org/10.1038/s41590-020-0751-0

Youle, R.J., Karbowski, M., 2005. Mitochondrial fission in apoptosis. Nat. Rev. Mol. Cell Biol. 2005 68 6, 657–663. https://doi.org/10.1038/nrm1697

Youle, R.J., Strasser, A., 2008. The BCL-2 protein family: opposing activities that mediate cell death. Nat. Rev. Mol. Cell Biol. 2008 91 9, 47–59. https://doi.org/10.1038/nrm2308

Youle, R.J., Van Der Bliek, A.M., 2012. Mitochondrial fission, fusion, and stress. Science 337, 1062–5. https://doi.org/10.1126/science.1219855

Zhang, W., Li, G., Luo, R., Lei, J., Song, Y., Wang, B., Ma, L., Liao, Z., Ke, W., Liu, H., Hua, W., Zhao, K., Feng, X., Wu, X., Zhang, Y., Wang, K., Yang, C., 2022. Cytosolic escape of mitochondrial DNA triggers cGAS-STING-NLRP3 axis-dependent nucleus pulposus cell pyroptosis. Exp. Mol. Med. 54, 129–142. https://doi.org/10.1038/s12276-022-00729-9

Zhang, Y., Tian, L., Huang, G., Ge, X., Kong, F., Wang, P., Xu, Y., Shi, Y., 2025. Structural basis of BAX pore formation. Science (80-.). 388. https://doi.org/10.1126/SCIENCE.ADV4314/SUPPL_FILE/SCIENCE.ADV4314_MDAR_REPRODUCIBILITY_CHECKLIST.PDF

Zhang, Z., Subramaniam, S., Kale, J., Liao, C., Huang, B., Brahmbhatt, H., Condon, S.G., Lapolla, S.M., Hays, F.A., Ding, J., He, F., Zhang, X.C., Li, J., Senes, A., Andrews, D.W., Lin, J., 2016. BH3-in-groove dimerization initiates and helix 9 dimerization expands Bax pore assembly in membranes. EMBO J. https://doi.org/10.15252/embj.201591552

Zhao, R.Z., Jiang, S., Zhang, L., Yu, Z. Bin, 2019. Mitochondrial electron transport chain, ROS generation and uncoupling (Review). Int. J. Mol. Med. 44, 3–15. https://doi.org/10.3892/IJMM.2019.4188/HTML

Zhou, L., Chang, D.C., 2008. Dynamics and structure of the Bax-Bak complex responsible for releasing mitochondrial proteins during apoptosis. J. Cell Sci. 121, 2186–2196. https://doi.org/10.1242/JCS.024703

Zou, H., Henzel, W.J., Liu, X., Lutschg, A., Wang, X., 1997. Apaf-1, a Human Protein Homologous to C. elegans CED-4, Participates in Cytochrome c–Dependent Activation of Caspase-3. Cell 90, 405–413. https://doi.org/10.1016/S0092-8674(00)80501-2

Declaration of generative AI tools and AI-assisted technologies in the writing process

During the preparation of this thesis, the author used DeepL Write (DeepL SE) and ChatGPT (OpenAI) to improve the readability, language, and stylistic flow of the text. These tools were employed solely for linguistic refinement and text optimization. The scientific concepts, hypotheses, interpretations, and conclusions presented in this work are entirely the author's own intellectual contributions.

All AI-generated suggestions were critically reviewed and edited by the author as necessary. The author takes full responsibility for the content of this thesis.

Appendix

1. Published Articles

1.1 DRP1 interacts directly with BAX to induce its activation and apoptosis

Article

SOURCE DATA | TRANSPARENT PROCESS | OPEN ACCESS

THE EMBO JOURNAL

DRP1 interacts directly with BAX to induce its activation and apoptosis

Andreas Jenner[1,2], Aida Peña-Blanco[2,†], Raquel Salvador-Gallego[2,†], Begoña Ugarte-Uribe[2,†], Cristiana Zollo[1,†], Tariq Ganief[3], Jan Bierlmeier[2], Markus Mund[4], Jason E Lee[5], Jonas Ries[4], Dirk Schwarzer[2], Boris Macek[3] & Ana J Garcia-Saez[1,2,*]

Abstract

The apoptotic executioner protein BAX and the dynamin-like protein DRP1 co-localize at mitochondria during apoptosis to mediate mitochondrial permeabilization and fragmentation. However, the molecular basis and functional consequences of this interplay remain unknown. Here, we show that BAX and DRP1 physically interact, and that this interaction is enhanced during apoptosis. Complex formation between BAX and DRP1 occurs exclusively in the membrane environment and requires the BAX N-terminal region, but also involves several other BAX surfaces. Furthermore, the association between BAX and DRP1 enhances the membrane activity of both proteins. Forced dimerization of BAX and DRP1 triggers their activation and translocation to mitochondria, where they induce mitochondrial remodeling and permeabilization to cause apoptosis even in the absence of apoptotic triggers. Based on this, we propose that DRP1 can promote apoptosis by acting as noncanonical direct activator of BAX through physical contacts with its N-terminal region.

Keywords BCL-2 proteins; fluorescence correlation spectroscopy; membrane protein complex; mitochondrial division; super-resolution microscopy
Subject Categories Autophagy & Cell Death; Membranes & Trafficking; Organelles
DOI 10.15252/embj.2021108587 | Received 27 April 2021 | Revised 1 December 2021 | Accepted 3 December 2021 | Published online 13 January 2022
The EMBO Journal (2022) 41: e108587

Introduction

Apoptosis is a form of programmed cell death that plays a key role in fundamental biological processes like embryo development, tissue homeostasis, and the correct functioning of the immune system. Dysregulation of apoptosis has been related with human pathology, including neurodegenerative diseases and cancer (Strasser *et al*, 2011). Apoptosis execution is mediated by the apoptotic caspases, which accelerate cell death by cleaving a defined set of target proteins that leads to the organized dismantling of the cellular components. In most cells, activation of the caspase cascade requires mitochondrial outer membrane permeabilization (MOMP), which releases cytochrome *c* (cyt *c*) and Smac/DIABLO into the cytosol (Bock & Tait, 2020). MOMP is considered the point of no return in the cell's commitment to death, as cells where all mitochondria underwent MOMP ultimately die also in the absence of caspase activity (Tait *et al*, 2010). Besides MOMP, mitochondria undergo multiple alterations during apoptosis including cristae remodeling, extensive fragmentation, changes in lipid composition and calcium signaling, loss of mitochondrial potential, and swelling (Cosentino & Garcia-Saez, 2014). Furthermore, recent studies reported the release of mitochondrial DNA (mtDNA) into the cytosol during apoptosis, which happens via extrusion of the mitochondrial inner membrane (MIM) through the mitochondrial outer membrane (MOM) and initiates type I interferon inflammatory responses normally blocked by caspase activity (McArthur *et al*, 2018; Riley *et al*, 2018).

BAX is a pro-apoptotic member of the BCL-2 family of proteins that, together with its homolog protein BAK, is necessary for the execution of MOMP and the additional mitochondrial alterations in apoptosis (Pena-Blanco & Garcia-Saez, 2018). BAX is kept in an inactive form that constantly retrotranslocates between cytosol and mitochondria in healthy cells (Edlich *et al*, 2011; Schellenberg *et al*, 2013). Upon apoptosis induction, BAX is activated by interaction with the BH3 domain of the direct activator BH3-only proteins, like tBID and BIM, which induce BAX accumulation at discrete puncta at the MOM, called apoptotic foci (Karbowski *et al*, 2002). This is accompanied by conformational changes that allow extensive membrane interactions, dimerization, and further self-assembly of BAX into multiple oligomeric species (Subburaj *et al*, 2015). BAX oligomers form supramolecular structures shaped as lines, arcs, and rings, and both arcs and rings have been associated with growing membrane pores at the MOM that reach sizes in the order of hundreds of nanometers in diameter (Große *et al*, 2016;

1 Institute for Genetics, CECAD, University of Cologne, Cologne, Germany
2 Interfaculty Institute of Biochemistry, University of Tübingen, Tübingen, Germany
3 Interfaculty Institute of Cell Biology, University of Tübingen, Tübingen, Germany
4 Cell Biology and Biophysics Unit, European Molecular Biology Laboratory, Heidelberg, Germany
5 University of Colorado, Boulder, CO, USA
*Corresponding author. Tel: +49 221 478 84263; E-mail: ana.garcia@uni-koeln.de
†These authors contributed equally to this work

Salvador-Gallego *et al*, 2016). These pores are responsible for the release of mitochondrial contents to the cytosol, ranging from cyt *c* and Smac to mtDNA (McArthur *et al*, 2018; Riley *et al*, 2018). Despite the clear paramount role of BAX and BAK in MOMP, the contribution of additional mitochondrial proteins to this process remains an open question.

Mitochondrial fragmentation is conserved in apoptotic cell death, even in organisms that do not involve MOMP (Martinou & Youle, 2011), yet its relevance for cell death is poorly understood. The dynamin-like protein DRP1 promotes mitochondrial fission in healthy human cells to maintain cellular homeostasis, and it mediates mitochondrial fragmentation and participates in cristae remodeling in apoptotic human cells to facilitate cyt *c* release (Frank *et al*, 2001; Otera *et al*, 2016). DRP1 is SUMOylated during apoptosis, which stabilizes its oligomeric form at mitochondria to stabilize membrane contacts sites between ER and mitochondria (Prudent *et al*, 2015). DRP1 co-localizes with BAX at apoptotic foci in mitochondria (Karbowski *et al*, 2002) and several lines of evidence support an interplay between the two proteins in apoptosis. DRP1 has been shown to promote the oligomerization of BAX in *in vitro* reconstituted systems by promoting negative membrane curvature (Montessuit *et al*, 2010). However, the contribution of DRP1 to apoptosis is controversial, because mitochondrial fission can be uncoupled from cyt *c* release and cells deficient in DRP1 also undergo cell death albeit with altered kinetics (Parone *et al*, 2006; Estaquier & Arnoult, 2007; Sheridan *et al*, 2008). As a result, the molecular mechanisms and functional significance of the connection between DRP1 and BAX in apoptosis remain unclear.

Here we show that direct interaction between BAX and DRP1 is induced at apoptotic foci in correlation with MOMP and maintained until the death of the cell. The association between BAX and DRP1 requires the lipid environment and affects the membrane activity of both proteins. We identify several surfaces of BAX involved in the interaction with DRP1 and determine that the N-terminal region of the protein is required for the association with DRP1 in cells. Interestingly, forced interaction between BAX and DRP1 induces their translocation to mitochondria, accumulation in apoptotic foci, as well as their activation for MOMP, and mitochondrial remodeling leading to apoptosis. Our findings provide a molecular basis for the functional link between the machineries for apoptosis execution and for mitochondrial dynamics and reveal that DRP1 can act as a non-BH3 activator of BAX to promote apoptosis.

Results

Apoptosis induction brings BAX and DRP1 in close proximity in correlation with MOMP

While we and others have so far not been able to detect direct interaction between endogenous BAX and DRP1 (Montessuit *et al*, 2010), these two proteins clearly co-localize at discrete foci in apoptotic cells visualized with confocal microscopy (Karbowski *et al*, 2002). However, the spatial resolution limit of around 200 nm does not allow to discern whether BAX and DRP1 are connected by direct physical interactions. To gain further insight into the structural organization of BAX and DRP1 during apoptosis, we took advantage of the high spatial resolution offered by single-molecule localization microscopy (SMLM) (Salvador-Gallego *et al*, 2016). We imaged fixed HeLa cells transiently transfected with GFP-BAX 3 h after staurosporine (STS) treatment for apoptosis induction and stained them with anti-GFP nanobodies labeled with Alexa Fluor (AF)647. Endogenous DRP1 was immunostained using a secondary antibody labeled with the cyanine-based fluorescent (CF) dye CF680. Using spectral unmixing based on a ratiometric classification of the individual localizations in the individual emission channels (Winterflood *et al*, 2015), we built two-color super-resolved images that revealed a close apposition between the fluorescent signals corresponding to BAX and DRP1, which appeared in discrete foci (Fig 1A). The degree of overlap was comparable to that of the positive co-localization control based on DRP1 immunostaining with two secondary antibodies labeled with AF647 and CF680 dyes, indicating that in apoptotic cells BAX and DRP1 co-localize up to a resolution of 30 nm (Fig 1B and C). In agreement with this, quantification of the distance between BAX and DRP1 in the foci revealed that the distance between them was < 30 nm in > 80% of the cases (Fig 1D).

Since both BAX and DRP1 are known to form large oligomers with sizes in the order of the measured distances between them by SMLM, we reasoned that they were likely to interact physically at the apoptotic foci. To test this hypothesis, we used the dimerization-dependent fluorescent protein (ddFP) technique (Ding *et al*, 2015). In this method, the proteins of interest are tagged with the fusion proteins RA and GB, respectively, which emit significant measurable fluorescence only when they are part of the same complex (< 10 nm apart). Compared to similar approaches, the ddFP pair offers the advantage that it does not enhance association between the tagged proteins and can be used to follow the dynamics of reversible interactions (Ding *et al*, 2015). We transiently expressed RA-BAX and GB-DRP1 in HeLa cells and imaged cells before and after apoptosis induction with STS for 3 h (optimal treatment for BAX translocation to mitochondrial foci) (Salvador-Gallego *et al*, 2016). As shown in Fig 1E, the fluorescence of RA-BAX/GB-DRP1 complexes was negligible in untreated cells, but became apparent as discrete foci in apoptotic cells with a distribution similar to that of colocalized BAX and DRP1 in Fig 1A and B. These results were consistent when we used different cell lines (U2OS BAX/BAK DKO and MEFs DRP1 KO) or different apoptotic triggers (paclitaxel and etoposide) (Fig EV1A and B). As a positive control, RA-BAX/GB-BAX interaction signal was also induced in apoptosis (Fig 1F). In contrast, the combination of the anti-apoptotic BCL-2 protein BCL-xL tagged with RA and GB-DRP1 did not give any fluorescent signal neither in untreated nor in treated cells (Fig EV1C). Quantification of the % cells with positive RA/GB signal revealed that the interaction between BAX and DRP1 was enhanced in apoptotic cells compared to untreated cells (Fig 1G).

To examine the dynamics of association between BAX and DRP1 during apoptosis progression, we performed live cell confocal imaging of HeLa cells transiently expressing RA-BAX, GB-DRP1, and Smac-GFP following STS treatment. Smac is a mitochondrial pro-apoptotic factor that is released to the cytosol upon MOMP. As shown in Fig 2A and B, the interaction between RA-BAX and GB-DRP1 was enhanced upon apoptosis induction and correlated in time with Smac-GFP release into the cytosol, persisting until cell death. Of note, we observed a delay between the redistribution of Smac-GFP and the appearance of BAX/DRP1 complexes, which was

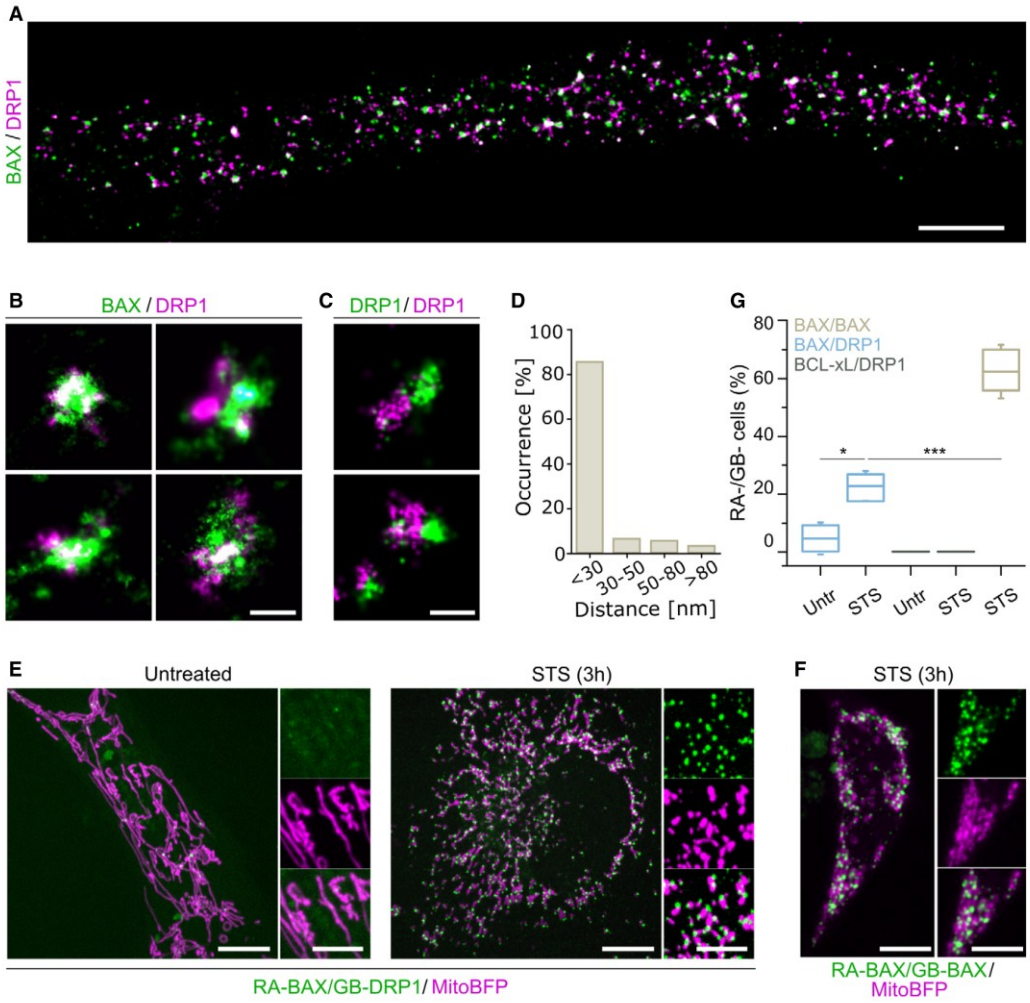

Figure 1. BAX and DRP1 specifically interact at mitochondria during apoptosis.

A–D Dual-color SMLM shows colocalization of BAX and DRP1 at the nanoscale. (A) Overview SMLM image of a HeLa cell transfected with GFP-BAX stained with anti-GFP nanobody-AF647 and anti-DRP1 antibody probed with a CF680-labeled secondary antibody, 3 h after apoptosis induction. Scale bar 2 μm. (B) Magnified SMLM images of GFP-BAX and DRP1 assemblies colocalizing up to 30 nm during apoptosis. Scale bar 100 nm. (C) Colocalization control of DRP1 immunostaining with the same primary and different secondary antibodies (labelled with AF647 and CF680) in HeLa cells. Scale bar 100 nm. (D) Quantification of the distance from GFP-BAX to DRP1 structures (distance measured at the center of each structure) from dual-color SMLM images. Data are quantified from $n = 4$ independent experiments with a total of 720 BAX structure.

E, F Representative confocal microscopy images of HeLa cells transfected with ddFP RA-BAX and GB-DRP1 (E) in untreated or apoptotic (STS) conditions, or with RA-BAX and GB-BAX during apoptosis (F). RA-BAX/GB-DRP1 and RA-BAX/GB-BAX complexes shown in green, mitochondria labeled with mito-BFP in magenta. Scale bar 10 μm. Right panels are zoomed areas representing individual and merged channels. Scale bar 5 μm.

G BAX/DRP1 interaction compared to BAX/BAX and BCL-xL/DRP1 by ddFP. % mito-BFP transfected cells that show RA/GB signal was quantified in HeLa cells untreated (untr.) and 3 h after apoptosis induction (STS). Box plots represent the interquartile (box), median (line) and SD (whiskers) of $n = 3$ independent experiments (with $n = 100$ cells each). Levels of significance were determined by paired two-tailed Student's t-test (*$P < 0.05$, ***$P < 0.001$) compared to BAX/DRP1 after apoptotic induction (STS).

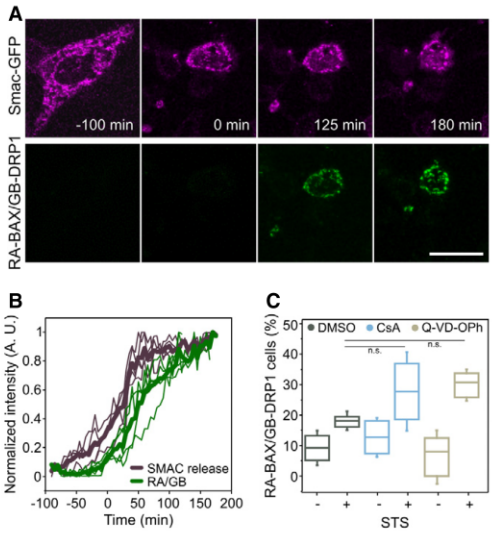

Figure 2. Dynamics of BAX and DRP1 interaction during apoptosis.

A Confocal microscopy time-series images of the increase in cytosolic Smac-GFP (magenta) in relation to the detection of RA-BAX/GB-DRP1 complexes (green) during apoptosis induction in MEF DRP1 KO cells. Scale bar 10 μm. Images are representative for $n = 3$ independent experiments.

B Normalized fluorescence intensity of Smac-GFP in a region of interest in the cytosol and of RA-BAX/GB-DRP1 foci for individual cells (thin lines) and the average of all cells (thick lines, $n = 5$). Time 0 min corresponds to the time point when RA-BAX/GB-DRP1 foci were detected.

C Quantification of BAX/DRP1 interaction (% cells with RA-BAX/GB-DRP1 foci normalized to the mito-BFP positive cells, $n = 100$ cells per experiment) during inhibition of effector caspases (Q-VD-OPh), the mitochondrial permeability transition pore (CsA) versus control (DMSO), with or without apoptosis induction (+/− STS). Box plots represent the interquartile (box), median (line) and SD (whiskers). Significance was determined from $n = 3$ independent experiments (with $n = 100$ cells each) by paired two-tailed Student's *t*-test (n.s. indicating $P > 0.05$) compared to DMSO control after apoptotic induction (STS).

of about 10 min at the 50% increase in both signals. This is comparable to that observed between the formation of GFP-BAX foci and Smac release during apoptosis (Salvador-Gallego *et al*, 2016) and likely related to their relative efficiency of detection. Due to this technical limitation, and although we observe a clear temporal correlation, we cannot exclude that one event happens before the other from these experiments.

To discard that the interaction between BAX and DRP1 was not a product of downstream caspase activity or of the permeability transition pore (PTP), we confirmed that the signal was maintained when cells were treated with a pan-caspase inhibitor (Q-VD-OPh) or with the PTP blocker cyclosporine A (CsA) (Fig 2C). Together, these findings demonstrate that, specifically during apoptosis, BAX and DRP1 associate into complexes that accumulate at discrete foci, correlate in time with MOMP, and persist until the death of the cell.

Direct interaction between BAX and DRP1 requires the membrane and affects the activity of both proteins

To investigate whether BAX and DRP1 interact directly or whether additional components are required for their association, we quantified their interaction in minimal systems of chemically controlled composition. We performed Fluorescence Cross-Correlation Spectroscopy (FCCS) measurements (Garcia-Saez *et al*, 2009; Bleicken *et al*, 2017) using recombinant, fluorescently labeled BAX (BAX-AF633) and DRP1 (DRP1-AF488) (Fig 3A–C). FCCS is a technique with single molecule sensitivity that calculates the temporal autocorrelation of diffusing BAX-AF633 and DRP1-AF488 particles, from which the diffusion coefficient is calculated (Fig EV2A and B). It also quantifies the cross-correlation (CC) signal due to the codiffusion of BAX-AF633/DRP1-AF488 complexes, which is directly proportional to the extent of association between the two proteins. As shown in Fig 3A and C, we could not detect any CC between BAX-AF633 and DRP1-AF488 in solution. In contrast, when we measured FCCS on BAX-AF633 and DRP1-AF488 bound to Giant Unilamellar Vesicles (GUVs), we clearly detected a positive CC indicative of direct interaction between the proteins (Fig 3B and C). Of note, DRP1 bound spontaneously to GUVs with a simple lipid composition containing the mitochondrial lipid cardiolipin, while association of BAX with the membrane was not induced by DRP1 and was promoted by incubation at 42°C (heat activation). As a control to confirm that the interaction between BAX and DRP1 is specific and not an artifact due to accumulation of both proteins in the membrane, an excess of unlabeled cBID (a known BAX interactor (Czabotar *et al*, 2013)) successfully competed for the association between BAX-AF633 and DRP1-AF488 and decreased the %CC (Figs 3C and EV2C). These results demonstrate that BAX and DRP1 directly interact *in vitro* and that the membrane environment is the only additional component required for such interaction.

We then took advantage of chemically controlled, *in vitro* reconstituted systems to explore whether the interaction between BAX and DRP1 affects the activities that have been reported for both proteins. First, we used assays of calcein release from large unilamellar vesicles (LUVs) (Garcia-Saez *et al*, 2005) to test the effect of DRP1 on the membrane-permeabilizing activity of BAX. As shown in Fig 3D, DRP1 enhanced the pore-formation activity of BAX activated with mild heat or with cBID. Consistent with these results, DRP1 also increased the BAX-induced permeabilization of GUVs to large molecules like cytochrome *c* and the 100 kDa protein APC (Fig 3E) in the presence of cBID. None of the individual proteins, neither BAX/DRP1 alone were able to permeabilize vesicles (Figs 3E and EV2D). These findings suggest that DRP1 can only promote BAX pore activity when it is already bound to membranes, in agreement with their interaction exclusively in the lipid environment.

Next, we studied the effect of BAX on the reported DRP1 ability to hydrolyze GTP and to tether liposomes (Ugarte-Uribe *et al*, 2014). Incubation with BAX did not alter the GTPase activity of DRP1 neither in solution nor in the presence of liposomes (Fig EV2E). Remarkably, the presence of BAX increased the density of DRP1 on the individual LUVs and its membrane-tethering activity (characterized by decrease in the shape index), both in a concentration-dependent manner (Fig 3F and G). These findings demonstrate that the direct interaction between BAX and DRP1 has functional

consequences for the membrane activities that both proteins exhibit *in vitro*.

Helices α2, α5, and α9 of BAX participate in the interaction with DRP1, although only the N-terminus is required for their association in cells

To support our data that the interaction between BAX and DRP1 is specific and functionally relevant also in cells, we sought to identify the regions in BAX that are involved in the interaction with a combination of orthogonal approaches. To this aim, we used first a peptide array covering the full sequence of BAX as in Alsop *et al*, 2015; Iyer *et al* (2016). Each peptide was 15 residues long and overlapped with the neighboring peptides by 5 amino acids in the N-terminus and 5 amino acids in the C-terminus (Fig 4A). Biotin was added at the N-terminus of each peptide. Since our FCCS data suggested that BAX and DRP1 interact only in the membrane, we implemented an assay based on GUVs with a lipid composition that does not support spontaneous binding of DRP1 and that contains biotinylated lipids and the fluorescent dye DiD. We mixed each of the biotinylated peptides of the BAX array with GUVs in presence of streptavidin to induce the association of the peptide with the membrane and added DRP1-AF488 (Fig 4B). We imaged the samples by confocal microscopy after 1 h incubation. Remarkably, some of the BAX peptides,

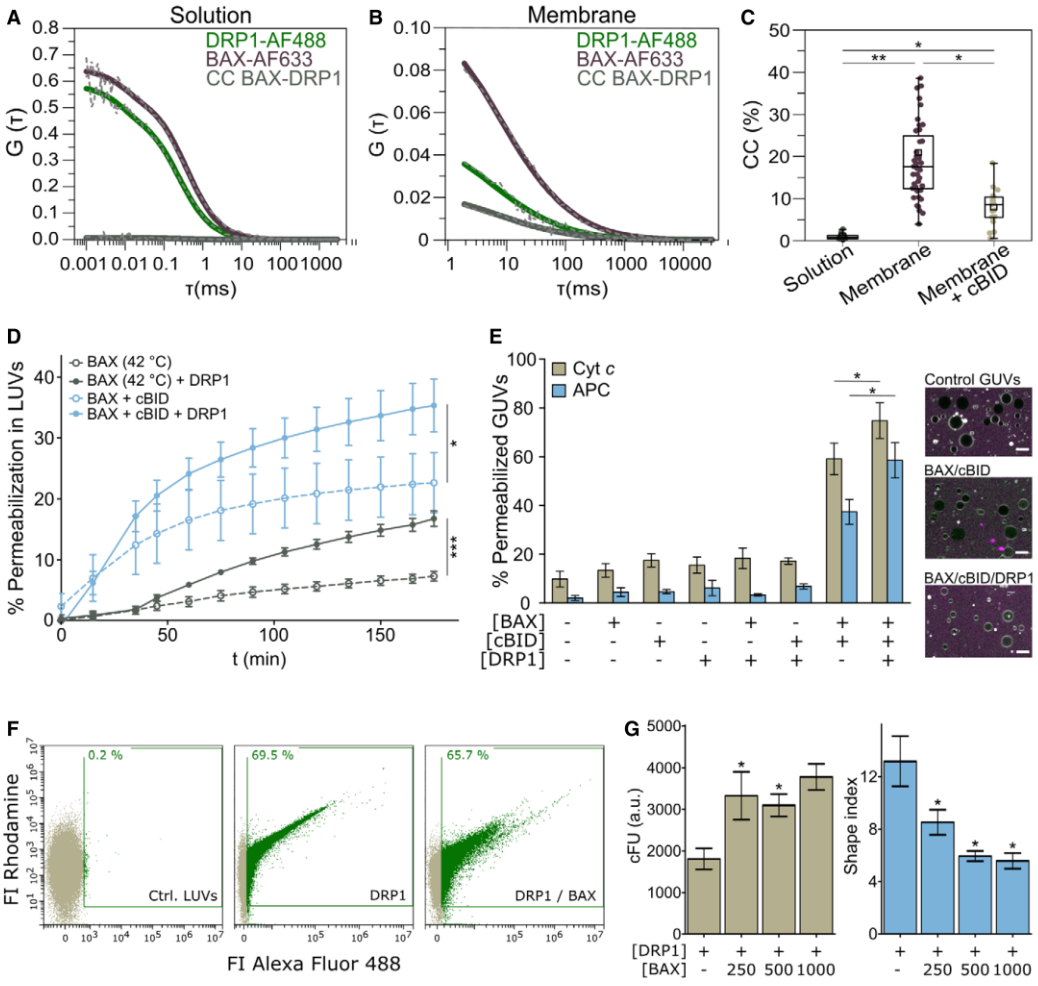

Figure 3.

Figure 3. Direct interaction of BAX and DRP1 in the membrane affects their respective activities.

A, B Representative auto- (green and violet curves) and cross-correlation (CC, BAX-DRP1, grey curves) curves of DRP1-AF488 and BAX-AF633 measured by FCCS in solution (A) and in the membrane of GUVs (B). Dash gray line depicts raw data and solid lines correspond to data fitting.

C Quantification of %CC between DRP1-AF488 and BAX-AF633 in solution (grey), in the membrane (violet), and in the membrane in presence of excess unlabeled cBID (beige). Box plots represent the interquartile (outer box), mean (inner box), median (line) and range (whiskers). Levels of significance were determined by paired two-tailed Student's *t*-test (*$P < 0.05$, **$P < 0.01$) from $n = 9$ measurements in solution, $n = 46$ individually measured GUVs in the membrane or $n = 17$ GUVs in presence of cBID.

D Effect of DRP1 on BAX-induced LUV permeabilization. BAX was activated by cBID (blue lines), or mild heat (42°C, grey lines). Data are presented as mean ± SD of $n = 3$ individual experiments. Significance was determined at the end-point of the kinetic measurement (180 min) by paired two-tailed Student's *t*-test (*$P < 0.05$, ***$P < 0.001$).

E Effect of DRP1 on BAX-induced GUV permeabilization. Left: % GUVs permeabilized to Cytochrome c_{488} (Cyt *c*, 12 kDa, beige) and allophycocianin (APC, 104 kDa, blue) in the absence or presence of cBID, BAX and DRP1 combined as indicated. Data are presented as mean ± SD of $n = 4$ independent experiments. *$P < 0.05$ (paired two-tailed Student's *t*-test). Right: representative confocal microscopy images showing GUVs (grey) in a solution of Cyt *c* (green) and APC (magenta). Scale bar 10 μm.

F, G Effect of BAX on DRP1 membrane density and DRP1-induced shape alterations of liposomes measured by flow cytometry. (F) Representative flow cytometry plots outlining DRP1 (Alexa Fluor 488 signal) binding to LUVs (Rhodamine signal) in the absence or presence of BAX. % DRP1-positive LUVs indicated in green. (G) Membrane density of DRP1 (corrected fluorescence units, cFU, left graph) and DRP1-induced membrane tethering (indicated by a shape index > 1, right graph) in LUVs in the absence or presence of different concentrations of BAX. Data are presented as mean ± SD of $n = 3$ independent experiments. *$P < 0.05$ (paired two-tailed Student's *t*-test) vs. DRP1 without BAX.

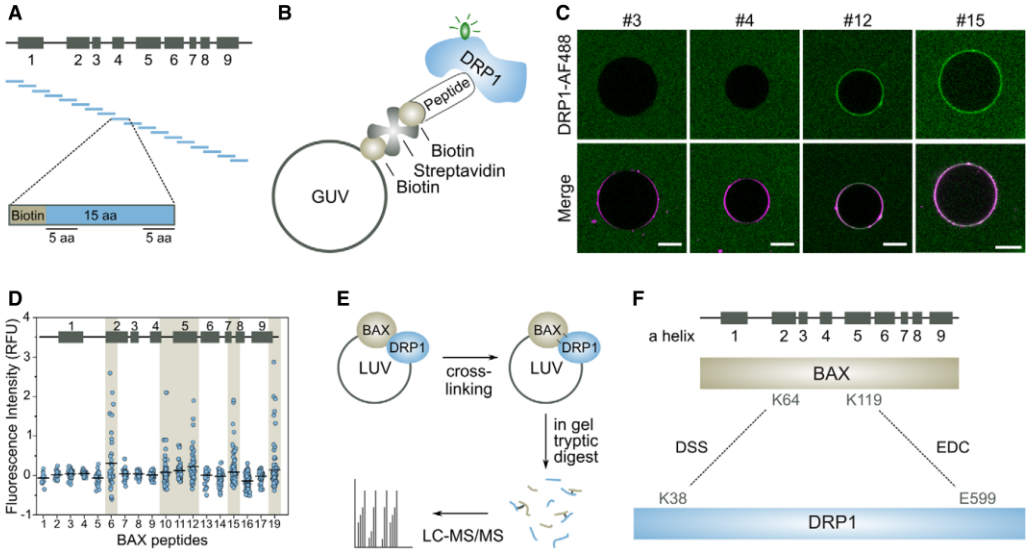

Figure 4. Interaction surfaces between BAX and DRP1.

A–D BAX peptide array to define interaction site with DRP1. (A) Schematic representation of the peptide array corresponding to BAX secondary structure with boxes indicating BAX α-helices 1-9. BAX sequence was divided in peptides of 15 amino acids (aa) preceded by a biotin head. The last 5 aa of each peptide overlapped with the first 5 aa of the next peptide. (B) Graphical representation of the DRP1 binding assay. Biotin-containing BAX peptides were attached to GUVs using biotinylated lipids and streptavidin. Binding between BAX peptides and DRP1-AF488 results in a recruitment of DRP1-AF488 to the GUV membrane indicated by AF488 fluoresce detected at the rim of the GUV. (C) Representative images of GUVs incubated with DRP1-AF488, streptavidin and the corresponding BAX peptides (#3, #4, #12, #15). Scale bar 10 μm. (D) Quantification of the relative fluorescence intensity of DRP1-AF488 at the rim of the GUVs for each BAX peptide of $n = 3$ individual experiments (with $n = 100$ vesicles each). Black lines indicate the mean value. Interacting BAX peptides are highlighted in beige.

E, F Protein crosslinking coupled with mass spectrometry of BAX and DRP1 in liposomes. (E) BAX/DRP1 crosslinking analysis workflow. After incubation with crosslinking reagents, proteins were digested using trypsin subjected to LC-MS/MS analysis. (F) Schematic representation of BAX and DRP1 with detected cross-linked residues connected by dash lines using DSS and EDC cross-linkers as indicated.

but not all of them, promoted binding of DRP1-AF488 to the membrane, which was evident by the increase in green fluorescence contrast at the vesicle rim (Fig 4C). By comparing the DRP1-AF488 fluorescence on the GUV membranes in the different peptide samples, we found that the peptides corresponding to the beginning of α2, the regions containing α5 and α7, as well as the C-terminal

anchor α9 in BAX were capable of recruiting DRP1-AF488 to the membrane (Fig 4D).

In a complementary approach, we used chemical cross-linking of BAX and DRP1 embedded in LUVs coupled with mass spectrometry analysis (Fig 4E) (O'Reilly & Rappsilber, 2018). Comparative analysis of the samples incubated with the cross-linkers EDC and DSS revealed significant cross-link sites with DRP1 at Lysines 64 and 119 of BAX, which are located at helices α2 and α5 (Figs 4F and EV3), in excellent agreement with the data obtained in the peptide array. Of note, the lack of Lysine residues after helix α5 of BAX does not allow reaction of this part of the protein with the cross-linkers used.

We then used this information to design deletion and point mutation variants of BAX that are deficient for interaction with DRP1 measured with the ddFP assay in cells (Fig 5A–E). Interestingly, deletion of the N-terminal region of BAX (amino acids 1 to 50) completely abolished the association with DRP1, which we could narrow down to deletion of residues 19–37 (Δ19–37), which includes helix α1 and the loop to helix α2 (Fig 5C). In contrast, deletion of the C-terminal helix α9 of BAX did not affect binding to DRP1, despite the ability of this region to recruit DRP1 in the assay with the peptide array (Fig 5D).

We then removed individually helices α1, α2, α4, and α5, as well as the loop between helices α1 and α2 (ΔL1–2) in BAX and analyzed the interaction with DRP1 by ddFP. Deletion of α1 or of the loop between α1 and α2 fully abrogated binding with DRP1, but not of α4 or α5, which presented reduced interaction (Fig 5D). Since the BH3 domain of BAX is located in α2, we then designed point mutations reported to block homo- and hetero-dimerization of BAX with other BCL-2 proteins. Only the exchange L63E disrupted the interaction with DRP1, but not any of the functionally relevant positions within the BH3 tested (Fig 5E), suggesting that the BH3 domain of BAX does not have the same role in the interaction with DRP1 or with other BCL-2 proteins.

When we evaluated the expression, localization, and activity of the noninteracting BAX mutants Δ19–37, ΔL1-2, and L63E (Fig EV4A–C), we found that they all could be expressed, although they seemed aggregated (BAX(Δ19–37)) or appeared constitutively mitochondrial concentrated at discrete foci (BAX(L63E) and BAX (ΔL1–2)). While they all retained their ability to induce apoptosis, BAX mutants Δ19–37 and ΔL1–2 presented an increased tendency to auto-activate, likely explaining their lower levels detected by Western Blot. In agreement with this, for these BAX mutants, mitochondria appeared stressed under resting conditions.

Following a similar rationale, we investigated whether DRP1 mutants affected in different aspects of its activity exhibited altered interaction with BAX. We tested the K38A mutation, which abolished the GTPase activity (Figueroa-Romero *et al*, 2009), the D221A mutation interfering with high order oligomerization (Kalia *et al*, 2018), the R376E mutation that blocks binding to MFF (Strack & Cribbs, 2012), the K642E mutation that renders DRP1 mostly monomeric *in vitro* and cytosolic in healthy cells (Frohlich *et al*, 2013) and the combination of K557/560/569/571R mutations that affect DRP1 SUMOylation (Figueroa-Romero *et al*, 2009) (Fig 5F). As shown in Fig 5G and H, none of these mutants clearly abolished the ddFP signal with BAX in apoptosis. Of note, unlike for wild type DRP1 and the K38A mutation, which produced ddFP signal at early stages of apoptosis induction, the ddFP signal of the rest of the mutants was observed in combination with highly damaged mitochondria typical of advanced stages of apoptosis induction. These results suggest that localization to mitochondria is the most important requirement for DRP1 interaction with BAX and that the catalytic activity is not required. However, from these experiments, we cannot discard that some of the mutants have indeed altered interaction at early time points of apoptosis.

In summary, these results suggest that the N-terminal region of BAX comprising the segments corresponding to helices α1 and the loop between α1 and α2 are required for complex formation with DRP1 in cells and that α2 seems to be sufficient to promote their association. Interestingly, this DRP1-interacting region is proximal to the rear site of BH3-domain binding in BAX, on the opposite side of the canonical hydrophobic groove involved in BID BH3 binding (Fig EV4D). In contrast, deletion of the C-terminal helix α9 or helices α4 and α5 is not sufficient to disrupt binding to DRP1, although these segments of BAX may still participate in the interaction surfaces.

Forced interaction between DRP1 and BAX induces their accumulation at apoptotic foci in mitochondria, mitochondrial remodeling, and MOMP

The association between BAX and DRP1 at apoptotic foci raised the question whether any of these proteins recruited the other to these

Figure 5. Regions required for interaction between BAX and DRP1 in apoptotic cells.

A Schematic representation of RA-BAX mutant and deletion variants analyzed for the interaction with GB-DRP1. The variants are displayed in the corresponding region of BAX secondary structure (boxes correspond to BAX helices α1-9 as indicated).

B Representative confocal microscopy images of U2OS BAX/BAK DKO cells of the interactions between RA-BAX variants and GB-DRP1, shown as green signal, 3 h after apoptosis induction. Mitochondria labeled with mito-BFP in magenta. Scale bar 10 μm.

C–E Quantification of the interaction of DRP1 with variants of BAX based on the % cells with detectable RA-BAX/GB-DRP1 fluorescence signal (interacting cells) normalized to the number of mito-BFP positive cells. Box plots represent the interquartile (box), median (line) and SD (whiskers) of $n = 3$ independent experiments (with $n = 100$ cells each). Levels of significance were determined by paired two-tailed Student's *t*-test (*$P < 0.05$, **$P < 0.01$, ***$P < 0.001$, ****$P < 0.0001$) compared to BAX wild type (WT).

F Schematic representation of GB-DRP1 mutant variants analyzed for the interaction with RA-BAX. The variants are displayed in the domain distribution of DRP1 (amino acid positions correspond to DRP1 isoform 3).

G Representative confocal microscopy images of U2OS BAX/BAK DKO cells of the interactions between RA-BAX and GB-DRP1 variants, shown as green signal, 3 h after apoptosis induction. Mitochondria labeled with mito-BFP in magenta. Scale bar 10 μm.

H Quantification of the interaction of DRP1 variants with BAX based on the % cells with detectable RA-BAX/GB-DRP1 fluorescence signal (interacting cells) normalized to the number of mito-BFP positive cells. Box plots represent the interquartile (box), median (line) and SD (whiskers) of $n = 3$ independent experiments (with $n = 100$ cells each). Significance was tested using paired two-tailed Student's *t*-test (n.s. $P > 0.05$) compared to DRP1 WT.

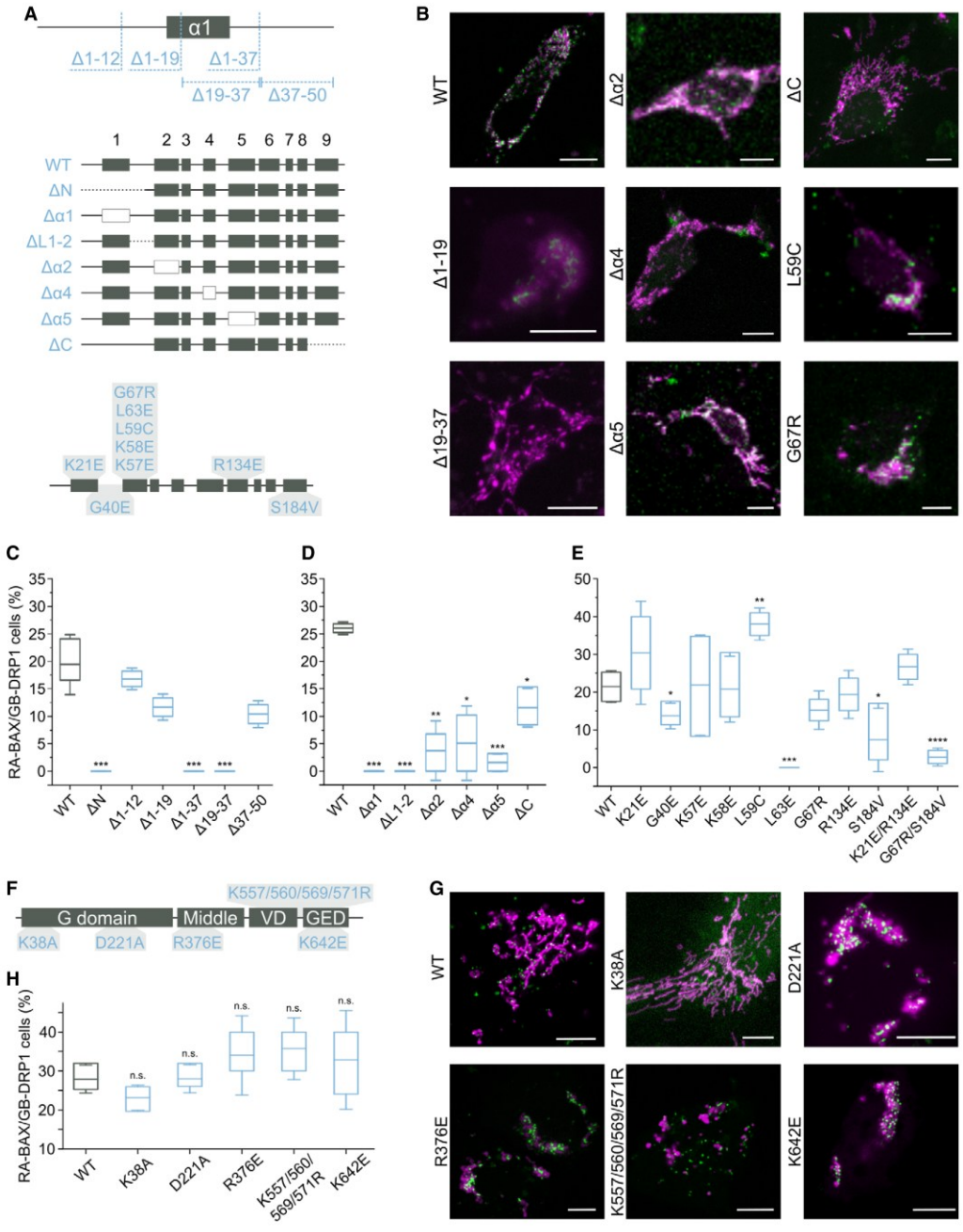

Figure 5.

sites during apoptosis. To test this possibility, we visualized the kinetics of the accumulation of mEGFP-BAX and mCherry-DRP1 at mitochondria of U2OS BAX/BAK DKO cells following apoptosis induction with BCL-2 and MCL-1 inhibitors ABT-737 and S63845. The mitochondria were labeled with the fluorescent protein mTurquoise2 targeted to mitochondria (4xmts-mTurquoise). Despite the technical difficulties to detect the proteins in the initial stages of apoptotic foci formation because of the low contrast due to high cytosolic background, mCherry-DRP1 foci repeatedly appeared at mitochondria prior to mEGFP-BAX in all cases, we could observe (Fig 6A). However, GFP-BAX also accumulated at discrete apoptotic foci in apoptotic cells depleted of DRP1 (Fig 6B). Together, these observations suggest that DRP1 is recruited to apoptotic mitochondrial foci upstream of BAX and may contribute to BAX translocation; it is not required for this process. Furthermore, knock-down of MAPL to block DRP1 SUMOylation did not disrupt the RA-BAX/GB-DRP1 complex formation in ddFP experiments, indicating that this posttranslational modification of DRP1 in apoptosis is not required for BAX/DRP1 interaction at apoptotic foci and may take place downstream (Fig EV4E–G). Altogether, these results suggest that BAX and DRP1 do not actively recruit each other to the apoptotic mitochondrial foci, but that they form a complex in their mitochondria-bound form.

Our findings indicate that interaction between BAX and DRP1 affects the membrane activities of both proteins (BAX pore formation and membrane permeabilization, and DRP1 membrane tethering activity). However, so far it has not been possible to examine the functional relevance of this interaction during apoptosis in cells due to the crucial role of DRP1 in maintaining mitochondrial dynamics and homeostasis. Alteration of DRP1 levels by depletion or overexpression modifies mitochondrial structure and function, which then indirectly affects the sensitivity of cells to apoptosis. Unfortunately, the alteration of the apoptotic activity in the noninteracting BAX mutants in Fig 5 also precluded their use to address this question (Fig EV4A–C). To overcome these limitations, we implemented a cellular inducible protein dimerization system (iDimerize™ Inducible Heterodimer System, Takara Bio). In this system, the addition of an external dimerizer (A/C Heterodimerizer) to the cells induces the artificial dimerization of two protein domains, FK506-binding protein (FKBP) and FKBP rapamycin-binding domain of mTOR (FRB), and subsequently of the proteins they are tagged to. We expressed FRB-EGFP-BAX and FKBP-mCherry-DRP1 in U2OS BAX/BAK DKO cells and added A/C heterodimerizer to induce BAX/DRP1 dimerization. Our live cell imaging experiments strikingly showed that FRB-EGFP-BAX and FKBP-mCherry-DRP1 rapidly translocated to mitochondria after the addition of the dimerizer, where both proteins accumulated together at discrete sites that resembled apoptotic foci (Fig 6C). Furthermore, FRB-EGFP-BAX/FKBP-mCherry-DRP1 translocation was accompanied by a reorganization of the mitochondrial network, which appeared to fragment and collapse at peri-nuclear regions, and by MOMP, measured as loss of mitochondrial potential (Figs 6D–F and EV5A).

As negative controls, we performed the same experiments in cells expressing FRB- and FKBP-tagged with only DRP1 or BAX and quantified their mitochondrial localization by colocalization analysis with the Pearson's coefficient (Fig EV5B–D). Addition of dimerizer to cells expressing FRB- and FKBP-tagged DRP1 led to the formation of DRP1 dots that did not colocalize with mitochondria (Figs 6G and EV5B). When dimerizer was added to cells expressing FRB- and FKBP-tagged BAX, the protein maintained its cytosolic distribution and neither MOMP nor apoptosis were induced (Figs 6H and EV5C). Of note, this is in contrast to the induced dimerization activation of BAX reported by Gross and colleagues (Gross *et al*, 1998), which could be due to the inclusion of a fluorescent protein as additional spacer between BAX and the FRB/FKBP domains in our constructs. To rule out the possibility that DRP1 activates BAX unspecifically by simply inducing its accumulation in mitochondria, we used an alternative way of targeting BAX to mitochondria by inducing the

Figure 6. Induced dimerization of BAX and DRP1 induces MOMP.

A Hierarchy of BAX and DRP1 recruitment to mitochondria in apoptotic cells. Confocal microscopy image of U2OS BAX/BAK DKO cells transfected with mCherry-DRP1 (red), mEGFP-BAX (green) and 4xmts-mTurquoise (cyan) to label mitochondria. After apoptosis induction, translocation of DRP1 to mitochondria and foci formation (set to 0 min) was observed before BAX foci formation (5 min later). Zoomed images correspond to crop regions as indicated. Arrowheads highlight co-localizing foci of DRP1 and BAX. Scale bar 20 μm, zoomed images 2 μm.

B Representative confocal microscopy image of BAX foci formation in apoptotic U2OS BAX/BAK DKO cells transfected with mEGFP-BAX (green) and 4xmts-mTurquoise (cyan) after siRNA-mediated DRP1 depletion. Scale bar 20 μm.

C Forced dimerization of BAX and DRP1 in healthy cells induces their translocation to mitochondria and foci formation. Confocal microscopy images of U2OS BAX/BAK DKO cells transfected with FKBP-mCherry-DRP1 (red) and FRB-EGFP-BAX (green) and stained with MitoTracker Deep Red FM (cyan) were acquired before (0 min) and after induction of BAX/DRP1 dimerization (5–60 min). From top to down, the individual rows correspond to fluorescence signal of BAX and DRP1 and the merge of both together with the MitoTracker signal, respectively. Scale bar 20 μm.

D Quantification of mitochondrial morphology normalized to the number of transfected cells before (Ctrl) and after induced dimerization of BAX and DRP1 (Dim). Significance was tested using paired two-tailed Student's *t*-test (**$P < 0.01$) compared to untreated control.

E Induced dimerization of BAX and DRP1 causes mitochondrial depolarization. U2OS BAX/BAK DKO cells were transfected as described in (C) and stained with the mitochondrial membrane potential-sensitive dye MitoSpy NIR (cyan). Confocal microscopy images were acquired before (0 min) and after induced dimerization of BAX and DRP1 (10 min). Scale Bar 20 μm.

F Quantification of mitochondrial depolarization normalized to the number of transfected cells before (Ctrl) and after induced dimerization of BAX and DRP1 (Dim). Significance was tested using paired two-tailed Student's *t*-test (*$P < 0.05$) compared to non-induced control.

G–K Induced dimerization of DRP1 with itself (G), BAX with itself (H), BAX with TOM20 (I) in U2OS BAX/BAK DKO cells, or BAX with DRP1 in HCT OctaKO cells (J, K), transected with FKBP- and FRB-mCherry DRP1 (G, red), FKBP- and FRB-EGFP-BAX (H, green), TOM20-mCherry-FKBP (red) and FRB-EGFP-BAX (green, I), respectively. Mitochondria were stained using MitoTracker Deep Red FM or MitoSpy NIR (cyan) as indicated. Scale bar 20 μm (G-I) and 10 μm (J, K). All images are representative of $n = 3$ independent experiments.

Data information: Values in (D and F) are presented as mean (bar, line) ± SD of $n = 3$ independent biological experiments (with $n = 100$ cells each). All images are representative of $n = 3$ independent experiments.

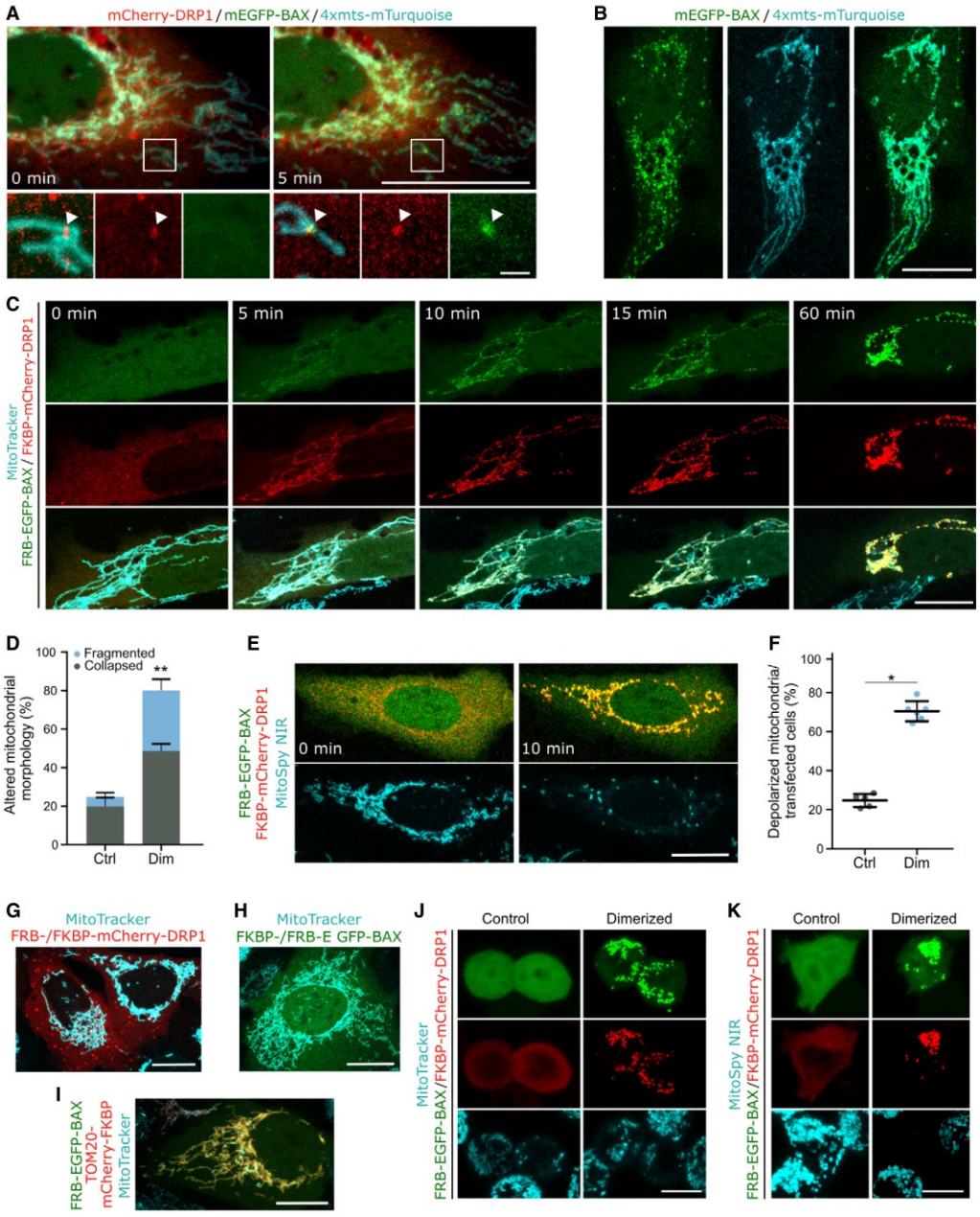

Figure 6.

binding of FRB-EGFP-BAX and FKBP-tagged TOM20 with the dimerizer. As shown in Figs 6I and EV5D, despite BAX relocalization to mitochondria, this combination also failed to induce BAX distribution into foci and MOMP, suggesting that the interaction with DRP1 specifically promotes BAX activation. In addition, when we induced the dimerization of DRP1 with the noninteracting BAX mutants Δ19–37, ΔL1–2, and L63E in living cells, we detected the recruitment of DRP1 to where BAX was initially localized thanks to the FRB/FKBP domains. However, in this case, their association did not lead to major cellular alterations beyond those already induced by the expression of the BAX mutants without dimerizer, compared to the wild type (Fig EV5E). For BAXΔL1–2, the foci-like distribution was increased in those cells that did not clearly have it before dimerization. Remarkably, chemically induced dimerization of FRB-EGFP-BAX and FKBP-mCherry-DRP1 in HCT116 OctaKO cells, which are depleted of BH3-only proteins, also led to their accumulation into mitochondrial foci, mitochondrial reorganization and depolarization (Fig 6J and K).

Finally, we established that the mitochondrial alterations promoted by the induction of BAX/DRP1 interaction were accompanied by the hallmarks of apoptosis induction (Figs 6F and EV5F–K). We confirmed that dimerizer treatment promoted FRB-EGFP-BAX and FKBP-mCherry-DRP1 accumulation in mitochondria by Western Blot. This was accompanied by BAX activation and exposure of the 6A7 epitope, loss of mitochondrial potential, cyt *c* release into the cytosol, caspase activation, PARP cleavage, and cell death.

Altogether, these findings indicate that although DRP1 and BAX are not required for each other's recruitment to apoptotic foci, their interaction promotes their accumulation at discrete sites in mitochondria as well as BAX activation independently of BH3-only proteins, which results in the induction of apoptosis.

Discussion

While a connection between BAX and DRP1 was proposed more than a decade ago based on the colocalization that both proteins exhibit during apoptosis, the underlying molecular basis and its relevance in apoptosis have remained rather obscure and a matter of debate (Karbowski *et al*, 2002; Parone *et al*, 2006; Estaquier & Arnoult, 2007; Sheridan *et al*, 2008). A thorough study previously failed to detect physical contacts between the two proteins and instead proposed that the effect of DRP1 on BAX apoptotic activity would be solely mediated by the membrane remodeling induced by DRP1, without interaction (Montessuit *et al*, 2010). Here, we used a combination of multiple orthogonal approaches both *in vitro* and in cells to challenge this notion and demonstrate the physical interaction between BAX and DRP1 under several experimental conditions.

First, BAX and DRP1 colocalize at mitochondrial apoptotic foci in SMLM images with a spatial resolution of around 30 nm. Given that both proteins are known to form supra-molecular larger structures (Frohlich *et al*, 2013; Große *et al*, 2016; Salvador-Gallego *et al*, 2016), our results are a strong indicator of molecular contact between them. Second, we resolve the spatiotemporal dynamics of the interaction between BAX and DRP1 in apoptosis by ddFP, which reveals that the two proteins form part of the same complex (< 10 nm) (Ding *et al*, 2015) in tight correlation with the loss of mitochondrial potential upon MOMP and that they stay together until the death of the cell. Although these results pinpoint the association of BAX and DRP1 in the physiological environment of the cell and specifically in the context of apoptosis induction, they cannot discern whether BAX and DRP1 binding is direct or mediated by other cellular components. This issue is solved by a third approach in which the detection of codiffusion of BAX and DRP1 by FCCS in reconstituted systems reveals that the two proteins only associate when bound to the membrane. It also shows that the affinity between them is high, as we detect significant complex formation at the low membrane densities used in FCCS, and that the interaction can be regulated, based on the competition observed by cBID. Our findings with the peptide array in GUVs and with cross-linking coupled to mass spectrometry in LUVs provide additional evidence for the direct binding between both proteins *in vitro*. Thus, our results clearly establish a direct interaction between BAX and DRP1, which may have escaped previous characterization due to the technical difficulties linked to the necessity of a lipid membrane for the interaction.

The requirement of the membrane for the interaction between BAX and DRP1 has important implications. Both proteins present distinct conformations and oligomeric states when they are soluble in the cytosol or embedded in the mitochondrial outer membrane. Our findings thereby strongly suggest that it is specifically the membrane-bound conformation of these proteins that fulfills the structural requirements for association. Although the conformation of DRP1 assemblies on constricted lipid tubes has been solved (Frohlich *et al*, 2013), we only have incomplete or low-resolution information about the structure of BAX in the membrane (Czabotar *et al*, 2013; Salvador-Gallego *et al*, 2016; Hauseman *et al*, 2020; Lv *et al*, 2021). It will be very interesting to uncover the structural details of the association between the macromolecular structures formed by both proteins in membranes.

We also show how the binding between BAX and DRP1 affects their biochemical activities on membrane model systems. The enhancement of pore formation by BAX is in line with a pro-apoptotic role of DRP1. Although our data are not at odds with an additional indirect effect of the membrane remodeling activities exerted by both proteins (Montessuit *et al*, 2010), the implication of the pore-forming regions and the C-terminal transmembrane anchor of BAX in the interaction with DRP1 suggest that DRP1 could affect BAX permeabilizing activity by directly tuning the BAX pore (Garcia-Saez *et al*, 2005; Zhang *et al*, 2016). On the other hand, the effect of BAX on the membrane tethering activity of DRP1 suggests a role on the extensive mitochondrial fragmentation mediated by DRP1 during apoptosis, which would not be at the level of its GTPase activity. We propose that the participation of these membrane-interacting regions of BAX in contact with DRP1 may impact the membrane fission process mediated by DRP1.

In cells, we find that forcing the interaction between BAX and DRP1 shifts the equilibrium toward their membrane-bound active conformations. Two main aspects underlie the difficulties so far in defining the functional role of the association between BAX and DRP1 by genetic ablation. First, the impossibility of genetic approaches to disentangle a direct effect of DRP1 on BAX activity *versus* an indirect effect on mitochondrial structure and function that ultimately impacts BAX activity and apoptosis. Second, the functional overlap of the multiple regulatory functions by BCL-2 family members, special the BH3-only proteins, which provide the

cell with multiple mechanisms for BAX activation that can replace for each other. We now solve this conundrum by using artificial dimerizers, which provide temporal control of the interaction and a direct readout of the specific consequences of bringing BAX and DRP1 together, which lead to BAX activation and apoptosis even in the absence of other BH3-only proteins. Our findings thus establish an activating role for their interaction and open up new and intriguing scenarios in which DRP1, which lacks a BH3 domain, could replace and or modulate the canonical BH3-mediated activation of BAX.

In this regard, our results that the N-terminal region of BAX restricts its activation and is also required for the interaction with DRP1 suggest a mechanism how DRP1 could promote BAX activation. Previous studies have shown that, besides the canonical hydrophobic groove of BAX involved in regulatory interactions with BH3 domains, binding to a rear site in soluble BAX can trigger its activation (Gavathiotis *et al*, 2008). Furthermore, Kluck and colleagues elegantly dissected the role of the N-terminus of BAX and BAK activation and reported that antibodies binding to the α1-α2 loop are capable of activating mitochondria-associated BAX (Westphal *et al*, 2014; Alsop *et al*, 2015; Iyer *et al*, 2016). Taking this into consideration, our data support a new mechanism by which DRP1 would activate membrane-bound BAX by binding to its N-terminal region and triggering the conformational changes leading to BAX activation and oligomerization (Fig EV6). To our best knowledge, DRP1 would represent the first cellular component using this site in membrane-bound inactive BAX to promote its activation.

In summary, here we report that BAX and DRP1 directly interact specifically during apoptosis and that their association is spatially restricted to apoptotic foci on mitochondria. We identify the domains in BAX involved in the association between these two proteins, which include the pore-forming hairpin and the transmembrane anchor, and require the N-terminal region. Our results establish the pro-death function resulting from the interplay between BAX and DRP1, which promotes the activation of BAX via a non-BH3 mechanism, leading to MOMP and apoptotic cell death. Together, our findings support a new model for how the physical contact with DRP1 promotes both the activation and pore activity of BAX, thus defining the molecular and functional interplay between these two proteins.

Materials and Methods

Plasmids and antibodies

The plasmids and antibodies used in this study are listed in Tables 1 and 2, respectively.

Table 1. Plasmids.

Name (short name)	Resistance	Promoter	Description
pEGFP-C1-BAX (GFP-BAX)	Kan	CMV	For expression of EGFP-tagged BAX (or mutant versions of BAX) in mammalian cells.
pAcGFP-C1-GB-BAX (GB-BAX)	Kan	CMV	For mammalian expression of GB-tagged BAX.
pAcGFP-C1-RA-BAX (RA-BAX)	Kan	CMV	For mammalian expression of RA-tagged BAX (or mutant versions of BAX as indicated).
pAcGFP-C1-GB-DRP1 (GB-DRP1)	Kan	CMV	For mammalian expression of GB-tagged DRP1 (or mutant versions of DRP1 as indicated).
pAcGFP-C1-mitoBFP (mitoBFP)	Kan	CMV	For expression of mitochondria-localized BFP in mammalian cells. Provided by Dr. Gia Voeltz lab.
pAcGFP-C1-RA-BCLxL (RA-BCL-xL)	Kan	CMV	For mammalian expression of RA-tagged BCL-xL.
pSmac-GFP	Kan	CMV	For expression of GFP-tagged Smac in mammalian cells. Addgene no. #40881
pAcGFP-C1-mCherry-DRP1 (mCherry-DRP1)	Kan	CMV	For mammalian expression of mCherry-tagged DRP1 isoform 3 (or mutant versions of DRP1 as indicated).
pEGFP-A206K_BAX_C1 (mEGFP-BAX)	Kan	CMV	For expression of monomeric EGFP(A206K)-tagged BAX in mammalian cells.
pEGFP-N1-4xmt-mTurquoise2 (4xmts-mTurquoise)	Kan	CMV	For visualization of mitochondria with mTurquoise2 in mammalian cells.
pFKBP-EGFP-BAX	Kan	CMV	For mammalian expression of EGFP-tagged BAX fused to the FKBP inducible dimerization domain.
pFRB-EGFP-BAX	Kan	CMV	For mammalian expression of EGFP-tagged BAX (or mutant versions of BAX) fused to the FRB inducible dimerization domain.
pFKBP-mCherry-DRP1	Kan	CMV	For mammalian expression of mCherry-tagged DRP1 fused to the FKBP inducible dimerization domain.
pFKBP-EGFP-DRP1	Kan	CMV	For mammalian expression of GFP-tagged DRP1 fused to the FKBP inducible dimerization domain.
pFRB-mCherry-DRP1	Kan	CMV	For mammalian expression of mCherry-tagged DRP1 fused to the FRB inducible dimerization domain.
pAcGFP-TOM20-mCherry-FKBP (TOM20-mCherry-FKBP)	Kan	CMV	For mammalian expression of mCherry-tagged TOM20 fused to the FKBP inducible dimerization domain.

Table 2. Antibodies.

Antibody	Dilution	Source	Application
α-BAX (6A7)	1:100	Thermo Fischer (MA5-14003)	IF
α-BAX	1:1,000	CST (#2772)	WB
α-Cytc	1:1,000	BD (556433)	WB
α-DRP1	1:30	CST (#26954)	IF
α-DRP1 (D6C7)	1:1,000	CST (#8570)	WB
α-GAPDH (D4C6R)	1:1,000	CST(#97166)	WB
α-GFP	1:1,000	Roche (11814460001)	WB
α-GFP nanobody AF647	1:2,000	Chromotek (home labeled)	IF
α-IMMT (Mitofilin)	1:1,000	10179-AP	WB
α-MAPL (MUL1)	1:1,000	Sigma (SAB2702071)	WB
α-mouse CF680	1:500	Sigma (SAB4600371)	IF
α-mouse AF647	1:500	Thermo Fischer (A28181)	IF
α-mouse IgG-HRP	1:10,000	JIR (115-035-003)	WB
α-mouse IgG-IRDye 800CW	1:10,000	Li-Cor (926-32212)	WB
α-PARP	1:1,000	CST (#9542)	WB
α-rabbit IgG-HRP	1:10,000	JIR (111-035-003)	WB
α-rabbit IgG-IRDye 680LT	1:20,000	Li-Cor (926-68023)	WB
α-Tom20 (D8T4N)	1:1,000	CST #42406	WB

IF, Application Immunofluorescence; WB, Western Blot.

Cell culture

Human osteosarcoma U2OS double *BAX*$^{-/-}$ *BAK*$^{-/-}$ (BAX/BAK DKO), MEF *DRP1*$^{-/-}$ (DRP1 KO) and HeLa cells were cultivated in DMEM, HCT116 *BAD*$^{-/-}$*BID*$^{-/-}$*BIK*$^{-/-}$*BIM*$^{-/-}$*BMF*$^{-/-}$*HRK*$^{-/-}$*NOXA*$^{-/-}$*PUMA*$^{-/-}$ (HCT OctaKO) cells in McCoy 5A medium supplemented with 10% (v/v) FBS and 1% (v/v) penicillin/streptomycin (Invitrogen, Germany) at 37°C and 5% (v/v) CO_2. Cells were transfected one day after seeding at 70–80% confluence using Lipofectamine™ (Invitrogen, Germany) and Opti-MEM™ reduced serum medium (Gibco). The HeLa cell line used in this study was authenticated confirming 100% match to the DNA profile of HeLa (ATCC® CCL-2™) and 100% match over all 15 autosomal short tandem repeats to the DNA profile of HeLa (Cellosaurus, RRID:CVCL_0030 [PubMed=25877200]). HeLa and U2OS BAX/BAK DKO cell lines were tested mycoplasma negative.

siRNA-mediated knock-down

The expression of the MAPL or DRP1 was downregulated using siRNA-mediated knock-down. Cells were cultivated in 6-well plates to 70–80% confluence and transfected with 5 nM siRNA against MAPL (siMUL1, L-007062-00-0005), DRP1 (5′-GGAGCCAGCTAG ATATTAA-3′) or a control scramble siRNA (D-001810-01-05, all siRNAs were purchased from Dharmacon™) in 1 ml Opti-MEM reduced serum medium (Gibco) using 1 µl of Lipofectamine 2000 (Invitrogen, Germany). After 6 h, 1 ml of DMEM supplemented with 20% (v/v) FBS and 1% (v/v) penicillin/streptomycin (Invitrogen, Germany) was added. siRNA-mediated knock-down was performed 4 days before microscopy experiments. Efficient protein downregulation was verified by western blot (antibodies see Table 2).

Western blot

Cells were harvested with Trypsin-EDTA (Sigma), resuspended in culture medium, collected by centrifugation at 300–400 *g* at 4°C for 5 min, and washed twice with ice-cold PBS. For lysis, cell pellets were resuspended in RIPA lysis buffer (50 mM of Tris/HCl pH 8.0, 150 mM NaCl, 1% (v/v) Triton™ X-100, 0.5% (w/v) sodium deoxycholate, 0.1% (w/v) SDS), incubated on ice for 20 min and spun at 20,000 *g* at 4°C for 20 min to remove cellular debris.

Protein concentration was determined by Bradford protein assay (Bio-Rad) according to the manufacturer's protocol. A total amount of 50–100 µg protein was boiled in SDS-PAGE sample buffer (62.5 mM of Tris/HCl pH 6.8, 2% (w/v) SDS, 10% (v/v) glycerol, 0.005% (v/v) ß-Mercaptoethanol, 0.01% (w/v) bromophenol blue) for 5 min at 95°C prior to SDS-PAGE. Proteins were transferred to nitrocellulose membrane (Trans-Blot Turbo, BioRad) and equal sample loading was tested using Ponceau S staining. Blots were washed with TBST (50 mM of Tris/HCl pH 7.5, 150 mM of NaCl, 0.1% (v/v) Tween 20) and blocked with 5% (w/v) low-fat milk in TBST for 60 min. Primary antibodies (Table 2) were diluted in 5% (w/v) milk in TBST and incubated for 16 h at 4°C. After 3x washing with TBST for 5 min, HRP-coupled or fluorescent secondary antibodies (Table 2) were incubated for 1 h at room temperature. Blots were washed 3x with TBST and detected with SuperSignal™ West Pico PLUS chemiluminescenct substrate (Thermo Scientific) using the Fusion SL Gel Chemiluminescence Documentation System (Vilber Lourmat) or scanned using an Odyssey CLx imaging system (Li-Cor Biosciences) when fluorescent antibodies were used. Images were adjusted in brightness and contrast and cropped using Fiji/ImageJ (Schindelin *et al*, 2012).

Single-molecule localization microscopy

HeLa cells were grown on 24 mm round glass coverslips for 24 h and transfected with 200 ng pEGFP-C1-BAX (Table 1) for 12 h. Apoptosis was induced with 1 µM STS (Sigma) for 3 h and then cells were fixed in 4% (v/v) PFA in PBS for 15 min at room temperature. Coverslips were incubated for 15 min in PBS with 50 mM of NH_4Cl and permeabilized in PBS with 0.25% (v/v) Triton™ X-100 for 5 min. Cells were washed 3x for 5 min in PBS and blocked for 45 min in PBS with 1% (w/v) BSA. Labeling was done with AF647–anti-GFP nanobodies and/or anti-DRP1 primary antibodies (Table 2) in 1% (w/v) BSA for 90 min. After extensive washes with PBS, coverslips were incubated for 30 min at room temperature with CF680- or AF647-coupled secondary antibodies (Table 2). Samples were mounted and imaged in a custom-made microscope (Deschamps *et al*, 2016) and covered with 300 µl of imaging buffer (50 mM of Tris-HCl pH 8, 10 mM of NaCl, 10% (w/v) glucose, 35 mM of cysteamine (MEA), 0.5 mg/ml of glucose oxidase (Sigma) and 40 µg/ml of catalase (Sigma)). An exposure time of 15 ms for single color and 30 s for dual color measurements was used with an EM gain of 100. Imaging laser intensity at 640 nm was 2.5 kW/cm^2 and the 405 nm

activation laser intensity was automatically adjusted to keep a constant number of localizations per frame. Typically, 70,000–100,000 frames were recorded. Analysis was performed using SMAP (Ries, 2020). Localizations with uncertainties above 15 nm were discarded. Images were rendered using a Gaussian with a width according to the localization precision. Image analysis was done with Fiji/ImageJ (Schindelin *et al*, 2012). Quantification of the distance between BAX and DRP1 was done by analyzing all colocalizing BAX and DRP1 structures (maximal distance 180 nm) and measuring the distance from the center of every BAX structure to the center of the DRP1 structures. Quantification was done from $n = 4$ independent experiments (with a total of 720 BAX structures) and performed in a blinded fashion to exclude confirmation bias.

Confocal imaging

Confocal microscopy was performed using an LSM710 confocal microscope with a C-Apochromat 40X/1.2 water immersion objective (Zeiss, Jena, Germany) with laser lines to excite at 405, 488, 561, or 633 nm. Emitted fluorescence was separated using a spectral beam guide and detected on photomultiplier tube (PMT) or avalanche photodiode (APD) detectors. Confocal imaging for induced dimerization experiments was performed on a TCS SP8 (Leica Microsystems) inverse confocal laser scanning microscope equipped with a PL Apo 63×/1.40 Oil CS2 objective and a tunable white light laser (470–670 nm). Fluorescence emission was detected using HyD SMD detectors. Live cell imaging was performed under 5% (v/v) CO_2 and temperature control at 37°C. Images have been adjusted for brightness and contrast using Fiji/ImageJ (Schindelin *et al*, 2012).

Dimerization-dependent fluorescent protein (ddFP) experiments

Dimerization-dependent fluorescent protein (ddFP) was described in Ding *et al* (2015). Cells were seeded in 8-well chambered cover glass µ-slides (IBIDI) and transfected with 50 ng pAcGFP-C1-RA-BAX (or respective N-terminal truncation, deletion or point mutation variants of BAX), 100 ng pAcGFP-C1-GB-DRP1 (or mutation variants of DRP1), and 100 ng pAcGFP-C1-mitoBFP or 100 ng pSmac-GFP (Table 1) to visualize the release of Smac from mitochondria. Apoptosis was induced using 1 µM of STS (Sigma) in DMEM without phenol red and cells were imaged after 3 h of apoptosis induction. To inhibit caspase activation or block the permeability transition pore cells were treated with 20 µM of Q-VD-OPh (Hölzel Biotech) for 3 h or 50 µM CsA (Sigma) for 30 min, respectively. Interaction of BAX and DRP1 was quantified from background-corrected, maximum intensity z-projection images by normalizing the number of RA-BAX/GB-DRP1 positive cells (cells that show RA-BAX/GB-DRP1 foci at mitochondria) to mito-BFP positive cells. Interaction of BAX and DRP1 was additionally verified in apoptotic U2OS BAX/BAK DKO and MEF DRP1 KO cells transfected as described above and with apoptosis induction using 100 nM of Paclitaxel for 24 h or 10 µM of Etoposide for 6 h. Data analysis was performed form $n = 3$ independent experiments (with $n = 100$ cells each) in a blinded fashion to exclude confirmation bias. Release of Smac-GFP from mitochondria during apoptosis was quantified by measuring the background-corrected fluorescent intensity in a region of interest in the cytosol at different time points after apoptosis induction. Levels of significance were determined using Student's *t*-test.

Protein production and labeling

Full-length mouse BID, full-length human BAX, and full-length BCL-xL were expressed in *E. coli* and purified as described in (Bleicken *et al*, 2013b, 2014; Ugarte-Uribe *et al*, 2014). Cleaved BID (cBID) was obtained from BID as described in Bleicken *et al* (2014). Bovine cytochrome *c* (Cyt *c*) and allophycocyanine (APC) were purchased at Sigma-Aldrich (Munich, Germany). Protein labeling was performed at single cysteine residues as described in Bleicken *et al* (2013b). Human DRP1 (isoform 1) was cloned into pTYB2 vector, expressed in *E. coli* at 14°C for 18 h and purified using chitin resin (New England Biolabs, Inc.). Labeling of DRP1 at amine groups was performed at pH 7.4 when DRP1 was still bound to the resin as in Ugarte-Uribe *et al* (2014). The cleavage reaction proceeded at pH 8 overnight at 4°C with 30 mM of DTT, after which the protein was eluted from the column and dialyzed against 20 mM of HEPES/KOH pH 7.4, 500 mM of NaCl and 1 mM of $MgCl_2$. In some cases, an additional step of anion exchanger column (Q Sepharose) was used for purity improvement. Purified protein was stored with 50% (v/v) glycerol.

Composition of the lipid mixtures

The lipid mixture mimicking the MOM composition was prepared as in Bleicken *et al* (2016) with 49% egg l-α-phosphatidyl-choline (PC), 27% egg l-α phosphatidyl–ethanolamine (PE), 10% bovine liver l-α-phosphatidyl–inositol (PI), 10% 18:1 phosphatidyl–serine (PS) and 4% cardiolipin (CL) (all percentages represent molar ratio). In addition, a lipid composition with a high CL content was used in order to mimic the contact sites between the inner and the outer membranes of mitochondria (PC:CL:PE 54:26:20, molar ratio) (Montessuit *et al*, 2010). For the BAX peptide array, a lipid composition containing the biotinylated lipid 1,2-distearoyl-sn-glycero-3-phosphoethanolamine-N-[biotinyl(polyethyleneglycol)-2000] (DSPE-PEG(2000) Biotin) was used (DOPC:DSPE-PEG(2000) Biotin 8:2, molar ratio) to tether BAX peptides to the membrane. All lipids were purchased from Avanti polar lipids (Alabaster, AL, USA). The lipidic dye, DiD (1,1'-Dioctadecyl-3,3,3',3'-Tetramethylindodicarbocyanine perchlorate), and the lipid, L-α-phosphatidylethanolamine-N-(lissamine rhodamine B sulfonyl) (Rhod-PE), were used to visualize membranes in the confocal microscope and in the flow cytometer, respectively.

LUV and GUV preparation

Large unilamellar vesicles (LUVs) for flow cytometry were prepared as described in Ugarte-Uribe *et al* (2014). The lipid solution was passed 31 times through a membrane (200 nm pore size) using an extruder from Avestin (LiposoFast-Basic, Avestin Inc., Mannheim, Germany). Giant unilamellar vesicles (GUVs) were produced by electroformation as described in Ugarte-Uribe *et al* (2014).

Fluorescence cross-correlation spectroscopy

All experiments were performed at 22°C on an LSM710 microscope with a C-Apochromat 40×/1.2 water immersion objective (Zeiss, Oberkochen, Germany). Excitation light came from Argon (488 nm) or HeNe lasers (633 nm). FCCS and two-focus scanning FCCS

measurements were performed using a Confocor 3 module as described in Bleicken *et al* (2017) and Ugarte-Uribe *et al* (2018). Photon arrival times were recorded with a hardware correlator Flex 02-01D/C (http://correlator.com; https://www.mathworks.com/matlabcentral/fileexchange/20784-flex02-01d-correlator-interface). For solution FCS measurements, the proteins of interest were mixed with GTPase buffer (20 mM of HEPES pH 7.4, 150 mM of KCl, 1 mM of $MgCl_2$) with 0.1 mM of GTP in a total volume of 200 µl and incubated at least 30 min before measurements. Incubation and measurements were done in Nunc™ Lab-Tek™ 8-well chamber slides (Thermo Scientific) that were blocked with BSA before use. Solution FCCS analysis was carried out with Fluctuation Analyzer 4G software (http://fluctuations.de/downloads.html). For scanning FCCS on GUV membranes, recombinant proteins (20 nM of DRP1-AF488, 50 nM of BAX-AF633, and 200–300 nM of cBID) were mixed (nucleosides or M-divi1 were added if needed) in GTPase buffer to a final volume of 300 µl and added to a blocked well in a Nunc™ Lab-Tek™ 8-well chamber slide (Thermo Scientific). GUVs were added to the protein solution and incubated for 10–15 min or heated at 42°C for 30 min (for BAX activation). All analyzed GUVs had a similar size of ~ 20 µm. Photons were collected during 300 s per measurement. The detection volume with two perpendicular lines across a GUV equator was repeatedly scanned. Data analysis was performed with home-written software as in Garcia-Saez *et al* (2009). The photon stream was binned in 2 µs and arranged it as a matrix such that every row corresponded to one-line scan. Membrane movements were corrected by calculating the maximum of running average over several hundred line scans and shifting it to the same column. An average over all rows was fitted with a Gaussian and added only the elements of each row between −2.5 and 2.5σ to construct the intensity trace. Autocorrelation and spectral and spatial cross-correlation curves were computed from the intensity traces and irregular curves resulting from instability and distortion were excluded. Auto- and cross-correlation functions were fitted with a nonlinear least-squares global fitting algorithm (Garcia-Saez *et al*, 2009). In addition, values for the diffusion coefficients of BAX and DRP1 were obtained under the different experimental conditions used (Fig EV2A and B).

LUV permeabilization assay

Experiments were performed as in Bleicken *et al* (2017). Briefly, LUVs were prepared by solving 2.5 mg dried lipid mixture in 500 µl buffer (20 nM of HEPES/KOH, pH 7.4, 150 mM of NaCl, and 80 mM of Calcein [fluorescein-bis-methyl-iminodiacetic acid at pH 7.5]) using intensive vortexing paused by 4 cycles of freezing and thawing. The multilamellar vesicles were passed 31 times through an extruder (Avestin) using membranes with 400 nm of pore size (Avestin), followed by size exclusion column purification (Sephadex G-50 beads, GE Healthcare). Calcein was entrapped in the vesicles at a self-quenching concentration so that its release in external medium was accompanied by an increase of the intensity of fluorescence. 100 µM LUVs were incubated with proteins of interest (100 nM BAX, 100 nM DRP1, 10 nM cBID) in GTPase buffer (20 mM HEPES pH 7.4, 150 mM KCl, 1mM $MgCl_2$) with 1 mM GTP, at room temperature (in the presence of cBID) or at 42°C (in the absence of cBID in order to activate BAX by heat). The kinetics of calcein release were measured using a Tecan Infinite M200 microplate reader (Tecan, Männedorf, Switzerland). The percentage of release was calculated as described in (Bleicken *et al*, 2017). The experiment was performed three times in duplicate and the results are presented as mean ± SD.

GUV permeabilization assay

The experiments were performed as described in Bleicken *et al* (2013a). Cyt c_{488}, APC, and the proteins of interest (20 nM BAX, 100 nM DRP1, 20 nM cBID) were mixed in Nunc™ Lab-Tek™ 8-well chamber slides (Thermo Scientific) with GTPase buffer (20 mM of HEPES pH 7.4, 150 mM of KCl, and 1 mM of $MgCl_2$) and 0.1 mM of GTP. Afterwards, 70 µl of the GUVs suspension was added to get a final volume of 300 µl. Confocal imaging was performed after 60 min incubation at room temperature. Images were processed with a homemade analysis software (Hermann *et al*, 2014) detecting the filling and the size of each GUVs. Per sample, well 100–200 GUVs were analyzed. The experiment was performed four times and the results are presented as mean ± SD. Levels of significance were determined by paired two-tailed Student's *t*-test and a confidence level of greater than 95% ($P < 0.05$) was used to establish statistical significance.

Flow cytometry

Flow cytometry experiments were conducted using CytoFlex, and data were analyzed using the FACSDiva Software (Beckman Coulter). DRP1 binding per normalized liposome and membrane tethering was described previously (Ugarte-Uribe *et al*, 2014). Shape index values (*y* axis) above 1 are indicative of an increase (negative membrane curvature or tethering) in a rhodamine-derived signal averaged for all liposome size gates. The experiment was performed three times in duplicate and the results are presented as mean ± SD. Levels of significance were determined by paired two-tailed Student's *t*-test and a confidence level of greater than 95% ($P < 0.05$) was used to establish statistical significance.

GTPase activity assay

The GTPase activity of DRP1 was assayed using a colorimetric assay as described in Ugarte-Uribe *et al* (2014). Briefly, 0.5 µM of DRP1 was added to 1 mM of GTP in the absence or presence of BAX (0.25, 0.5, or 1 µM) and/or LUVs (150 µM) over a 20 to 180 min time course at 37°C in GTPase buffer (20 mM of HEPES/KOH pH 7.4, 150 mM of NaCl, and 1 mM of $MgCl_2$). Reactions were stopped at the indicated times by diluting 20 µl of the sample in 100 mM of EDTA (final concentration) in a microtiter plate. Samples were then incubated with 150 µl of malachite green stock solution (1 mM of malachite green and 10 mM of ammonium molybdate in 1 N HCl), and the absorbance at 620 nm was determined using an Infinite M200 microplate reader (Tecan, Mainz, Germany). The experiment was performed four times in duplicate and the results are presented as mean ± SD.

Solid-phase synthesis of BAX peptides and DRP1 binding assay in GUVs

N-terminally biotinylated BAX peptides (with SGSG linker sequence) were synthesized by Fmoc-based solid-phase peptide chemistry

using a Syro I synthesizer (MultiSynTech GmbH) as described in (Liokatis *et al*, 2012). They were 15-mers with five-residue overlap, spanning all residues of human BAX (isoform alpha, NP_620166). Biotin was coupled manually with 4-fold molar excess and Pyoxim was used as activator of the reaction. Except one peptide (peptide no. 18) for which the synthesis was not successful, all peptides were obtained with an average purity of > 90%.

GUVs (70 µl from the electroformation chamber) composed of DOPC:DSPE-PEG(2000) Biotin (8:2, molar ratio) and labeled with DiD were mixed in a Nunc™ Lab-Tek™ 8-well chamber slide (Thermo Scientific) at a final concentration of 0.65 µM streptavidin with 3 µM of the corresponding BAX peptide, 0.1 mM GTP and 0.5 µM DRP1-AF488 and incubated for 1 h. This way, the peptides were anchored via streptavidin to the GUV surface. Binding of DRP1-AF488 to the GUVs was visualized with confocal microscopy and analyzed by quantifying the radial intensity in individual GUVs using home built software (Hermann *et al*, 2014). Data analysis was performed from $n = 3$ independent experiments (with $n = 100$ vesicles each) in an automated and blinded fashion to avoid observer bias.

Protein cross-linking coupled to mass spectrometry

Crosslink sample preparation and LC-MS/MS data acquisition

Recombinant BAX and DRP1 (final concentrations of 2 µM and 0.8 µM, respectively) were mixed with 1 mM of LUVs in GTPase buffer (20 mM HEPES/KOH pH 7.4, 150 mM NaCl and 1 mM $MgCl_2$) containing 100 µM of GTP and incubated at 42°C for 30 min. Then cross-linkers EDC or DSS were added at a final concentration of 25 mM and incubated for 1h (for EDC) and 45 min (for DSS) at room temperature. Then reactions were quenched for 15 min with Tris/HCl pH8 at a concentration of 50 nM (in case of EDC) and 60 mM (in case of DSS) and β-mercaptoethanol was added at a final concentration of 20 mM. The samples were then run 1 cm into a denaturing SDS-PAGE gel before being excised and digested in-gel using trypsin and chymotrypsin as previously described (Borchert *et al*, 2010). The resultant peptides were analyzed on an EASY-nLC 1200 (Thermo Fisher Scientific) coupled to Q Exactive HF mass spectrometer (Thermo Fisher Scientific). Peptides were loaded onto a 75 µm (ID), 20 cm column packed in-house with reversed-phase ReproSil-Pur 120 C18-AQ 1.9 µm resin (Dr. Maisch GmbH). Peptides were eluted using a 43 min linear gradient of solvent B (80% ACN in 0.1% formic acid) from 10 to 33% at 200 nl/min. Full-scans were recorded between 300 and 1,650 Thompson at a resolution of 60,000 with an AGC target of 1E6. The 7 most intense ions from each full scan were selected for fragmentation (MS/MS) by higher-energy collisional dissociation (HCD) using an NCE of 27 and an AGC target of 1E5 in 110 ms at a resolution of 60,000.

XL-MS data analysis

Crosslinks were identified using pLink software (http://pfind.ict.ac.cn/software/pLink) (Fan *et al*, 2015). Mass error tolerance for precursors was set to 5 ppm for 5 isotopes including the monoisotopic mass. Minimum peptide length was set to 6 amino acids with oxidation (Met) and carbamidomethylation (Cys) set as variable and fixed modifications respectively. Both trypsin and chymotrypsin cleavage sites were defined for the digestion enzyme and 5 missed cleavages were allowed. Digestion efficiency and raw mass accuracy were determined in a dedicated processing using MaxQuant software (Cox & Mann, 2008) using default settings. Based on the MaxQuant analysis searching against the human BAX and DRP1 proteins and the complete *E. coli* uniprot database (4,313 sequences) a database containing the top 20 most abundant *E. coli* proteins as decoys and the two human proteins was constructed for the pLink search. The same approach was used to identify both EDC and DSS cross-linked peptides. The interaction maps between complex proteins were generated via xiNET-Crosslink Viewer (http://crosslinkviewer.org).

Recruitment hierarchy of BAX and DRP1 to apoptotic mitochondria

To test the hierarchy of the recruitment of BAX and DRP1 to mitochondria in apoptosis, U2OS BAX/BAK DKO cells were seeded in 8-well chambered cover glass µ-slides (IBIDI) and transfected with 50 ng pEGFP-A206K_BAX_C1, 50 ng pAcGFP-C1-mCherry-DRP1, 50 ng pEGFP-N1-4xmt-mTurquoise2 (Table 1) using 0.5 µl of Lipofectamine 2000 for 12 h. For visualizing BAX foci formation after down-regulation of DRP1, U2OS BAX/BAK DKO cells depleted for DRP1 (see section siRNA-mediated knock-down) were transfected with 50 ng pEGFP-A206K_BAX_C1 and 50 ng pEGFP-N1-4xmt-mTurquoise2 (Table 1). Before imaging the growth medium was changed to DMEM without phenol red and apoptosis was induced using 1 µM ABT-737, 1 µM S63845 and 10 µM Q-VD-OPh (Hölzel Biotech) to inhibit effector caspases. Three-dimensional time-lapse confocal microscopy of individual cells was performed with a time resolution of 1 min for a duration of 30 min or until foci formation was observed. Maximum intensity z-projection images were cropped and adjusted in brightness and contrast using Fiji/ImageJ (Schindelin *et al*, 2012).

Induced dimerization experiments

The induced dimerization system (iDimerize™ Inducible Heterodimer System, Takara Bio) is based on the dimerization of the FK506-binding protein (FKBP) and the FKBP rapamycin-binding domain of mTOR (FRB) in the presence of rapamycin analogues (Bayle *et al*, 2006). BAX (or mutation variants of BAX), DRP1, and TOM20 were fused to the dimerization domains FKBP (also called dimerization domain A, DmrA) and/or FRB (dimerization domain C, DmrC) in order to artificially induce their dimerization using A/C Heterodimerizer (AP21967, Takara Bio). U2OS BAX/BAK DKO or HCT OctaKO cells were seeded in 8-well chambered cover glass µ-slides (IBIDI) and transfected with 50 ng pFRB-EGFP-BAX (or mutation variants of BAX) and 100 ng pFKBP-mCherry-DRP1, 100 ng pFRB-mCherry-DRP1 and 100 ng pFKBP-mCherry-DRP1, 50 ng pFRB-EGFP-BAX and 50 ng pFKBP-EGFP-BAX or 100 ng pAcGFP-TOM20-mCherry-FKBP and 50 ng pFRB-EGFP-BAX (Table 1) for 16 h before imaging using 0.3 µl Lipofectamine 2000. Effects of induced dimerization were analyzed using confocal microscopy after changing the growth medium to DMEM without phenol red containing 300 nM A/C Heterodimerizer. Mitochondria were stained using 100 nM MitoTracker Deep Red TM (Invitrogen, Germany) or 10 nM MitoSpy TM NIR DiIC1(5) (BioLegend) to detect loss in mitochondrial membrane potential. Individual time-lapse z-stacks of 10–15 images with an z-interval of ~ 350 nm were acquired with a time

resolution of 5 min for 1 h. Maximum intensity z-projection images were cropped and modified in brightness and contrast using Fiji/ImageJ (Schindelin *et al*, 2012). Altered mitochondrial morphology and mitochondrial depolarization was quantified visually in cells transfected with both constructs (FRB-EGFP-BAX and FKBP-mCherry-DRP1) before and after induced dimerization form $n = 3$ independent experiments (with $n = 100$ cells each) in a blinded fashion to avoid confirmation bias. Levels of significance were determined using Student's *t*-test. Pearson's correlation coefficient was calculated between the induced dimerization signal of BAX/BAX, DRP1/DRP1 and BAX/TOM20, respectively, and mitochondria based on MitoTracker Deep Red TM signal using the JACoP plugin (Bolte & Cordelieres, 2006) (https://imagej.nih.gov/ij/plugins/track/jacop2.html) in Fiji/ImageJ (Schindelin *et al*, 2012).

Cell death analysis

U2OS BAX/BAK DKO cells were seeded in a 48-well plate and transfected with 50 ng pFRB-EGFP-BAX and 100 ng pFKBP-EGFP-DRP1 or 50 ng GFP-BAX (or mutant versions of BAX) (Table 1) for 16 h. Cells were stained with DRAQ7 (Thermo Fischer Scientific) in a 1:3,000 dilution in DMEM to stain the DNA of dead cells. Dimerization of BAX and DRP1 was induced using 300 nM A/C Heterodimerizer (AP21967, Takara Bio) and apoptosis was induced using 1 μM ABT-737 and 1 μM S63845 (Hölzel Biotech). Cell death and mitochondrial depolarization were measured using the IncuCyte bioimaging platform (Essen). Time-lapse measurements of fluorescent intensity were performed every hour in nine positions of each well, which were averaged for analysis. Number of DRAQ7 positive cells was normalized to the number of transfected cells (based on GFP signal) using the *cell-by-cell* analysis mode. Data analysis was performed from $n = 2$ independent experiments each of them in technical duplicates. Levels of significance were determined using Student's *t*-test.

Cytochrome c release assay and protein translocation to mitochondria

In order to measure release of cytochrome *c* from mitochondria or BAX/DRP1 translocation to mitochondria after forcing their dimerization, 5×10^5 U2OS BAX/BAK DKO cells were transfected with 300 ng pFRB-EGFP-BAX and 600 ng pFKBP-mCherry-DRP1 (Table 1) for 6–8 h and treated with 300 nM A/C Heterodimerizer (AP21967, Takara Bio) to induce BAX/DRP1 dimerization or 1 μM ABT-737, 1 μM S63845, and 10 μM Q-VD-OPh (Hölzel Biotech) to induce apoptosis for 2 h. For separation of mitochondria and cytosol, cells were harvested by trypsinization, washed in PBS, and permeabilized using permeabilization buffer (20 of mM HEPES/KOH pH7.5, 100 of mM sucrose, 2.5 mM of $MgCl_2$, 100 mM of KCl, freshly added 0.025% (w/v) digitonin and protease inhibitor cocktail in PBS) for 10 min on ice. Cellular membranes were pelleted by centrifugation at 15,000 *g* for 10 min at 4°C. After removing the supernatant (cytosolic fraction), the membranes were solubilized using RIPA buffer. Protein levels were analyzed using western blot.

Measurement of caspase 3/7 activation

For measurement of caspase activation after induced dimerization of BAX and DRP1, U2OS BAX/BAK DKO cells were seeded in a 48-well plate and transfected with 50 ng FRB-EGFP-BAX and 100 ng pFKBP-EGFP-DRP1 (Table 1) for 16 h. Cells were treated with 300 nM A/C Heterodimerizer (AP21967, Takara Bio) to force BAX/DRP1 dimerization or 1 μM ABT-737 and 1 μM S63845 (Hölzel Biotech) to induce apoptosis for a time-course of 90 min. Caspase activation was measured at individual time points as indicated using the Image-iT™ LIVE Red Caspase-3 and -7 Detection Kit (Thermo Fischer Scientific) according to the manufacturers protocol and detected with the IncuCyte bioimaging platform (Essen). Percentage of caspase activation was quantified by measuring the area of thresholded red fluorescence intensity normalized to the area of transfected cells (based on GFP fluorescence) of $n = 2$ independent experiments.

Detection of BAX activation (exposure of N-terminal 6A7 epitope)

For detection of BAX activation after induced dimerization of BAX and DRP1, the exposure of the N-terminal 6A7 motif of BAX was detected by immunofluorescence confocal microscopy. U2OS BAX/BAK DKO cells were seeded on round 15 mm 1.5H glass coverslips and transfected with 150 ng FRB-EGFP-BAX and 300 ng FKBP-mCherry-DRP1 (Table 1) for 16 h. Cells were treated with 300 mM A/C Heterodimerizer (AP21967, Takara Bio) to force BAX/DRP1 dimerization or 1 μM ABT-737, 1 μM S63845, and 10 μM Q-VD-OPh (Hölzel Biotech) for 40 min to induce apoptosis. Cells were fixed with prewarmed 4% (v/v) PFA in DMEM for 8 min at room temperature, washed 3x with PBS for 5 min, and permeabilized using 0.25% (v/v) Triton™ X-100 in PBS. After blocking with 3% (w/v) BSA in PBS for 45 min at room temperature, the cells were incubated with α-BAX(6A7) primary antibody (Table 1) for 16 h at 4°C, washed 3x with PBS for 5 min, and incubated with CF680-coupled secondary antibody (Table 2) for 1 h at room temperature. Coverslips were washed 3x with PBS, mounted using ProLong™ Gold antifade reagent, and imaged by confocal microscopy. Representative images were chosen from $n = 3$ independent experiments.

Data availability

This study includes no data deposited in external repositories.

Expanded View for this article is available online.

Acknowledgments

We thank Carolin Stegmüller, Sabine Schäfer, and Gudrun Zimmer for technical support, Dr. Lohans Pedrera Puentes for help with analysis of IncuCyte data; and the CECAD imaging facility for excellent assistance. This work was funded by the Deutsche Forschungsgemeinschaft (DFG, German Research Foundation) – 654651/GRK2364 MOMbrane and by the European Research Council (ERC-Co 817758). Open Access funding enabled and organized by Projekt DEAL.

Author contributions

Andreas Jenner: Formal analysis; Investigation; Visualization; Methodology; Writing—review and editing. **Aida Peña-Blanco:** Formal analysis; Investigation; Methodology; Writing—review and editing. **Raquel Salvador Gallego:** Formal analysis; Investigation; Visualization; Methodology; Writing—review and editing. **Begoña Ugarte-Uribe:** Formal analysis; Investigation;

Visualization; Methodology; Writing—review and editing. **Cristiana Zollo:** Formal analysis; Investigation; Visualization; Methodology. **Tariq Ganief:** Resources; Investigation; Visualization; Methodology. **Jan Bierlmeier:** Resources; Methodology. **Markus Mund:** Resources; Methodology; Writing—review and editing. **Jason E Lee:** Resources; Methodology. **Jonas Ries:** Resources; Supervision; Methodology; Writing—review and editing. **Dirk Schwarzer:** Resources; Supervision; Methodology; Writing—review and editing. **Boris Macek:** Resources; Supervision; Methodology; Writing—review and editing. **Ana J Garcia-Saez:** Conceptualization; Supervision; Funding acquisition; Writing—original draft; Project administration; Writing—review and editing.

In addition to the CRediT author contributions listed above, the contributions in detail are:

AJ, AP-B, BU-U, RS-G and CZ performed research and analyzed data. RS-G did SMLM, FCS and ddFP experiments. BU-U carried out *in vitro* activity experiments, peptide array and cross-linking coupled to MS, as well as FCS experiments. AP-B and CZ carried out ddFP experiments. AJ did recruitment and forced dimerization experiments. TG and BM did MS experiments and analyzed data. JEL contributed to ddFP experiments. MM and JR contributed to SMLM experiments. JB and DS prepared peptide array. AJG-S conceived the project, designed and supervised research and wrote the manuscript with the help of all other authors.

Disclosure statement and competing interests

The authors declare that they have no conflict of interest.

References

Alsop AE, Fennell SC, Bartolo RC, Tan IK, Dewson G, Kluck RM (2015) Dissociation of Bak alpha1 helix from the core and latch domains is required for apoptosis. *Nat Commun* 6: 6841

Bayle JH, Grimley JS, Stankunas K, Gestwicki JE, Wandless TJ, Crabtree GR (2006) Rapamycin analogs with differential binding specificity permit orthogonal control of protein activity. *Chem Biol* 13: 99 – 107

Bleicken S, Hantusch A, Das KK, Frickey T, Garcia-Saez AJ (2017) Quantitative interactome of a membrane Bcl-2 network identifies a hierarchy of complexes for apoptosis regulation. *Nat Commun* 8: 73

Bleicken S, Hofhaus G, Ugarte-Uribe B, Schroder R, Garcia-Saez AJ (2016) cBid, Bax and Bcl-xL exhibit opposite membrane remodeling activities. *Cell Death Dis* 7: e2121

Bleicken S, Jeschke G, Stegmueller C, Salvador-Gallego R, Garcia-Saez AJ, Bordignon E (2014) Structural model of active Bax at the membrane. *Mol Cell* 56: 496 – 505

Bleicken S, Landeta O, Landajuela A, Basanez G, Garcia-Saez AJ (2013a) Proapoptotic Bax and Bak proteins form stable protein-permeable pores of tunable size. *J Biol Chem* 288: 33241 – 33252

Bleicken S, Wagner C, Garcia-Saez AJ (2013b) Mechanistic differences in the membrane activity of Bax and Bcl-xL correlate with their opposing roles in apoptosis. *Biophys J* 104: 421 – 431

Bock FJ, Tait SWG (2020) Mitochondria as multifaceted regulators of cell death. *Nat Rev Mol Cell Biol* 21: 85 – 100

Bolte S, Cordelieres FP (2006) A guided tour into subcellular colocalization analysis in light microscopy. *J Microsc* 224: 213 – 232

Borchert N, Dieterich C, Krug K, Schutz W, Jung S, Nordheim A, Sommer RJ, Macek B (2010) Proteogenomics of Pristionchus pacificus reveals distinct proteome structure of nematode models. *Genome Res* 20: 837 – 846

Cosentino K, Garcia-Saez AJ (2014) Mitochondrial alterations in apoptosis. *Chem Phys Lipids* 181: 62 – 75

Cox J, Mann M (2008) MaxQuant enables high peptide identification rates, individualized p.p.b.-range mass accuracies and proteome-wide protein quantification. *Nat Biotechnol* 26: 1367 – 1372

Czabotar P, Westphal D, Dewson G, Ma S, Hockings C, Fairlie W, Lee E, Yao S, Robin A, Smith B *et al* (2013) Bax crystal structures reveal how BH3 domains activate Bax and nucleate its oligomerization to induce apoptosis. *Cell* 152: 519 – 531

Deschamps J, Rowald A, Ries J (2016) Efficient homogeneous illumination and optical sectioning for quantitative single-molecule localization microscopy. *Opt Express* 24: 28080 – 28090

Ding Y, Li J, Enterina JR, Shen YI, Zhang I, Tewson PH, Mo GCH, Zhang J, Quinn AM, Hughes TE *et al* (2015) Ratiometric biosensors based on dimerization-dependent fluorescent protein exchange. *Nat Methods* 12: 195 – 198

Edlich F, Banerjee S, Suzuki M, Cleland MM, Arnoult D, Wang CX, Neutzner A, Tjandra N, Youle RJ (2011) Bcl-x(L) Retrotranslocates bax from the mitochondria into the cytosol. *Cell* 145: 104 – 116

Estaquier J, Arnoult D (2007) Inhibiting Drp1-mediated mitochondrial fission selectively prevents the release of cytochrome c during apoptosis. *Cell Death Differ* 14: 1086 – 1094

Fan SB, Meng JM, Lu S, Zhang K, Yang H, Chi H, Sun RX, Dong MQ, He SM (2015) Using pLink to analyze cross-linked peptides. *Curr Protoc Bioinformatics* 49: 21 – 28

Figueroa-Romero C, Iniguez-Lluhi JA, Stadler J, Chang CR, Arnoult D, Keller PJ, Hong Y, Blackstone C, Feldman EL (2009) SUMOylation of the mitochondrial fission protein Drp1 occurs at multiple nonconsensus sites within the B domain and is linked to its activity cycle. *FASEB J* 23: 3917 – 3927

Frank S, Gaume B, Bergmann-Leitner ES, Leitner WW, Robert EG, Catez F, Smith CL, Youle RJ (2001) The role of dynamin-related protein 1, a mediator of mitochondrial fission, in apoptosis. *Dev Cell* 1: 515 – 525

Frohlich C, Grabiger S, Schwefel D, Faelber K, Rosenbaum E, Mears J, Rocks O, Daumke O (2013) Structural insights into oligomerization and mitochondrial remodelling of dynamin 1-like protein. *EMBO J* 32: 1280 – 1292

Garcia-Saez AJ, Coraiola M, Dalla Serra M, Mingarro I, Menestrina G, Salgado J (2005) Peptides derived from apoptotic Bax and Bid reproduce the poration activity of the parent full-length proteins. *Biophys J* 88: 3976 – 3990

Garcia-Saez AJ, Ries J, Orzaez M, Perez-Paya E, Schwille P (2009) Membrane promotes tBID interaction with BCL(XL). *Nat Struct Mol Biol* 16: 1178 – 1185

Gavathiotis E, Suzuki M, Davis ML, Pitter K, Bird GH, Katz SG, Tu H-C, Kim H, Cheng E-Y, Tjandra N *et al* (2008) BAX activation is initiated at a novel interaction site. *Nature* 455: 1076 – 1081

Gross A, Jockel J, Wei MC, Korsmeyer SJ (1998) Enforced dimerization of BAX results in its translocation, mitochondrial dysfunction and apoptosis. *EMBO J* 17: 3878 – 3885

Große L, Wurm CA, Brüser C, Neumann D, Jans DC, Jakobs S (2016) Bax assembles into large ring-like structures remodeling the mitochondrial outer membrane in apoptosis. *EMBO J* 35: 402 – 413

Hauseman ZJ, Harvey EP, Newman CE, Wales TE, Bucci JC, Mintseris J, Schweppe DK, David L, Fan L, Cohen DT *et al* (2020) Homogeneous oligomers of pro-apoptotic BAX reveal structural determinants of mitochondrial membrane permeabilization. *Mol Cell* 79: 68 – 83.e7

Hermann E, Bleicken S, Subburaj Y, Garcia-Saez AJ (2014) Automated analysis of giant unilamellar vesicles using circular Hough transformation. *Bioinformatics* 30: 1747 – 1754

Iyer S, Anwari K, Alsop AE, Yuen WS, Huang DC, Carroll J, Smith NA, Smith BJ, Dewson G, Kluck RM (2016) Identification of an activation site in Bak and mitochondrial Bax triggered by antibodies. *Nat Commun* 7: 11734

Kalia R, Wang RY, Yusuf A, Thomas PV, Agard DA, Shaw JM, Frost A (2018) Structural basis of mitochondrial receptor binding and constriction by DRP1. *Nature* 558: 401 – 405

Karbowski M, Lee YJ, Gaume B, Jeong SY, Frank S, Nechushtan A, Santel A, Fuller M, Smith CL, Youle RJ (2002) Spatial and temporal association of Bax with mitochondrial fission sites, Drp1, and Mfn2 during apoptosis. *J Cell Biol* 159: 931 – 938

Liokatis S, Stützer A, Elsässer SJ, Theillet F-X, Klingberg R, van Rossum B, Schwarzer D, Allis CD, Fischle W, Selenko P (2012) Phosphorylation of histone H3 Ser10 establishes a hierarchy for subsequent intramolecular modification events. *Nat Struct Mol Biol* 19: 819 – 823

Lv F, Qi F, Zhang Z, Wen M, Kale J, Piai A, Du L, Wang S, Zhou L, Yang Y *et al* (2021) An amphipathic Bax core dimer forms part of the apoptotic pore wall in the mitochondrial membrane. *EMBO J* 40: e106438

Martinou JC, Youle RJ (2011) Mitochondria in apoptosis: Bcl-2 family members and mitochondrial dynamics. *Dev Cell* 21: 92 – 101

McArthur K, Whitehead LW, Heddleston JM, Li L, Padman BS, Oorschot V, Geoghegan ND, Chappaz S, Davidson S, San Chin H *et al* (2018) BAK/BAX macropores facilitate mitochondrial herniation and mtDNA efflux during apoptosis. *Science* 359: eaao6047

Montessuit S, Somasekharan SP, Terrones O, Lucken-Ardjomande S, Herzig S, Schwarzenbacher R, Manstein DJ, Bossy-Wetzel E, Basañez G, Meda P *et al* (2010) Membrane remodeling induced by the dynamin-related protein Drp1 stimulates Bax oligomerization. *Cell* 142: 889 – 901

O'Reilly FJ, Rappsilber J (2018) Cross-linking mass spectrometry: methods and applications in structural, molecular and systems biology. *Nat Struct Mol Biol* 25: 1000 – 1008

Otera H, Miyata N, Kuge O, Mihara K (2016) Drp1-dependent mitochondrial fission via MiD49/51 is essential for apoptotic cristae remodeling. *J Cell Biol* 212: 531 – 544

Parone PA, James DI, Da Cruz S, Mattenberger Y, Donze O, Barja F, Martinou JC (2006) Inhibiting the mitochondrial fission machinery does not prevent Bax/Bak-dependent apoptosis. *Mol Cell Biol* 26: 7397 – 7408

Pena-Blanco A, Garcia-Saez AJ (2018) Bax, Bak and beyond - mitochondrial performance in apoptosis. *FEBS J* 285: 416 – 431

Prudent J, Zunino R, Sugiura A, Mattie S, Shore GC, McBride HM (2015) MAPL SUMOylation of Drp1 stabilizes an ER/mitochondrial platform required for cell death. *Mol Cell* 59: 941 – 955

Ries J (2020) SMAP: a modular super-resolution microscopy analysis platform for SMLM data. *Nat Methods* 17: 870 – 872

Riley JS, Quarato G, Cloix C, Lopez J, O'Prey J, Pearson M, Chapman J, Sesaki H, Carlin LM, Passos JF *et al* (2018) Mitochondrial inner membrane permeabilisation enables mtDNA release during apoptosis. *EMBO J* 37: e99238

Salvador-Gallego R, Mund M, Cosentino K, Schneider J, Unsay J, Schraermeyer U, Engelhardt J, Ries J, Garcia-Saez AJ (2016) Bax assembly into rings and arcs in apoptotic mitochondria is linked to membrane pores. *EMBO J* 35: 389 – 401

Schellenberg B, Wang P, Keeble J, Rodriguez-Enriquez R, Walker S, Owens TW, Foster F, Tanianis-Hughes J, Brennan K, Streuli C *et al* (2013) Bax exists in a dynamic equilibrium between the cytosol and mitochondria to control apoptotic priming. *Mol Cell* 49: 959 – 971

Schindelin J, Arganda-Carreras I, Frise E, Kaynig V, Longair M, Pietzsch T, Preibisch S, Rueden C, Saalfeld S, Schmid B *et al* (2012) Fiji: an open-source platform for biological-image analysis. *Nat Methods* 9: 676 – 682

Sheridan C, Delivani P, Cullen SP, Martin SJ (2008) Bax- or Bak-induced mitochondrial fission can be uncoupled from cytochrome C release. *Mol Cell* 31: 570 – 585

Strack S, Cribbs JT (2012) Allosteric modulation of Drp1 mechanoenzyme assembly and mitochondrial fission by the variable domain. *J Biol Chem* 287: 10990 – 11001

Strasser A, Cory S, Adams JM (2011) Deciphering the rules of programmed cell death to improve therapy of cancer and other diseases. *EMBO J* 30: 3667 – 3683

Subburaj Y, Cosentino K, Axmann M, Pedrueza-Villalmanzo E, Hermann E, Bleicken S, Spatz J, Garcia-Saez AJ (2015) Bax monomers form dimer units in the membrane that further self-assemble into multiple oligomeric species. *Nat Commun* 6: 8042

Tait SW, Parsons MJ, Llambi F, Bouchier-Hayes L, Connell S, Munoz-Pinedo C, Green DR (2010) Resistance to caspase-independent cell death requires persistence of intact mitochondria. *Dev Cell* 18: 802 – 813

Ugarte-Uribe B, Muller HM, Otsuki M, Nickel W, Garcia-Saez AJ (2014) Dynamin-related protein 1 (Drp1) promotes structural intermediates of membrane division. *J Biol Chem* 289: 30645 – 30656

Ugarte-Uribe B, Prevost C, Das KK, Bassereau P, Garcia-Saez AJ (2018) Drp1 polymerization stabilizes curved tubular membranes similar to those of constricted mitochondria. *J Cell Sci* 132: jcs208603

Westphal D, Kluck RM, Dewson G (2014) Building blocks of the apoptotic pore: how Bax and Bak are activated and oligomerize during apoptosis. *Cell Death Differ* 21: 196 – 205

Winterflood CM, Platonova E, Albrecht D, Ewers H (2015) Dual-color 3D superresolution microscopy by combined spectral-demixing and biplane imaging. *Biophys J* 109: 3 – 6

Zhang Z, Subramaniam S, Kale J, Liao C, Huang B, Brahmbhatt H, Condon SG, Lapolla SM, Hays FA, Ding J *et al* (2016) BH3-in-groove dimerization initiates and helix 9 dimerization expands Bax pore assembly in membranes. *EMBO J* 35: 208 – 236

Expanded View Figures

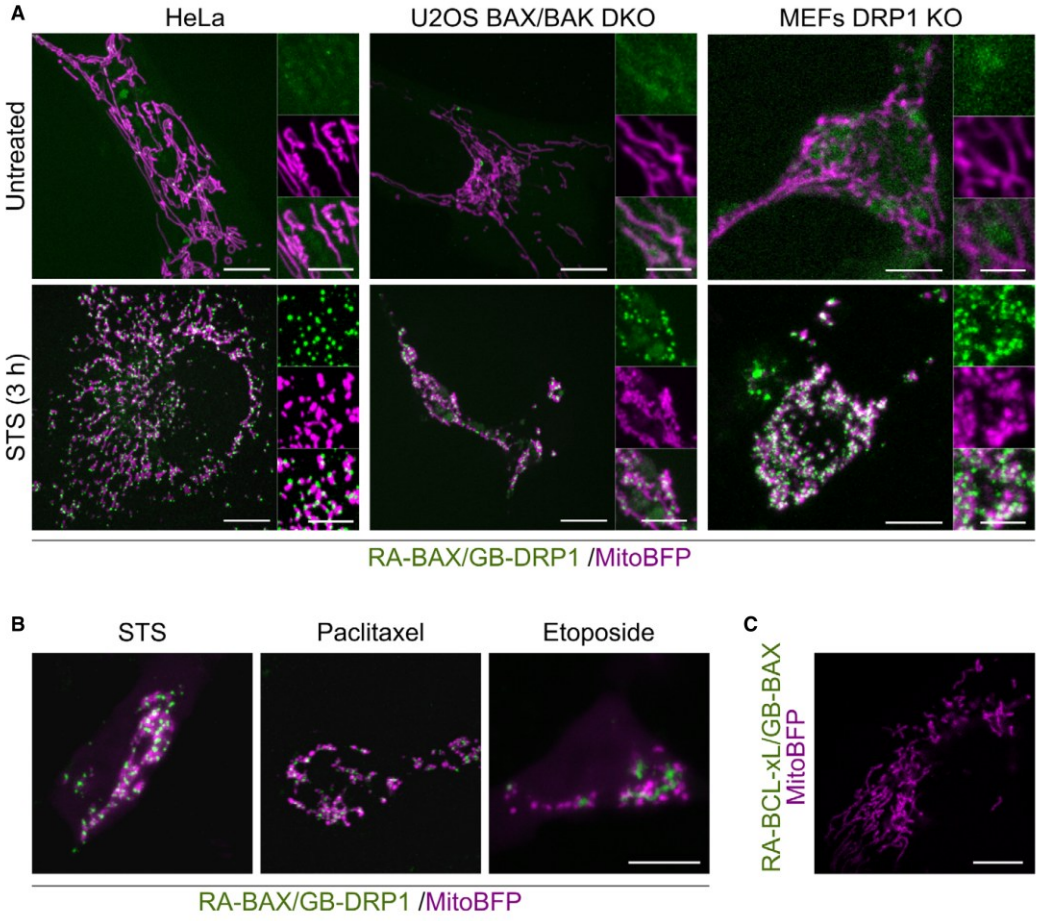

Figure EV1. Interaction of BAX and DRP1 is independent of cell type and apoptotic stimuli.

A Representative confocal microscopy images of ddFP of RA-BAX and GB-DFP1 (green) in untreated or apoptotic (STS) HeLa (same images as used in Fig 1E), U2OS BAX/BAK DKO, and MEF DRP1 KO cells. Mitochondria are visualized using mito-BFP (magenta). Scale bar 10 μm. Right panels are zoomed areas representing individual and merged channels. Scale bar 5 μm.

B Representative confocal microscopy images of RA-BAX/GB-DRP1 (green) and mito-BFP (magenta) overexpressed in U2OS BAX/BAK DKO cells after apoptosis induction using STS, Paclitaxel or Etoposide as indicated. Scale bar 10 μm.

C Representative confocal microscopy image of RA-BCL-xL/GB-DRP1 (green) and mito-BFP (magenta) overexpressed in U2OS BAX/BAK DKO cells after apoptosis induction using STS. Scale bar 10 μm. Images are representative for $n = 3$ independent experiments.

Data information: Images are representative for $n = 3$ independent experiments.

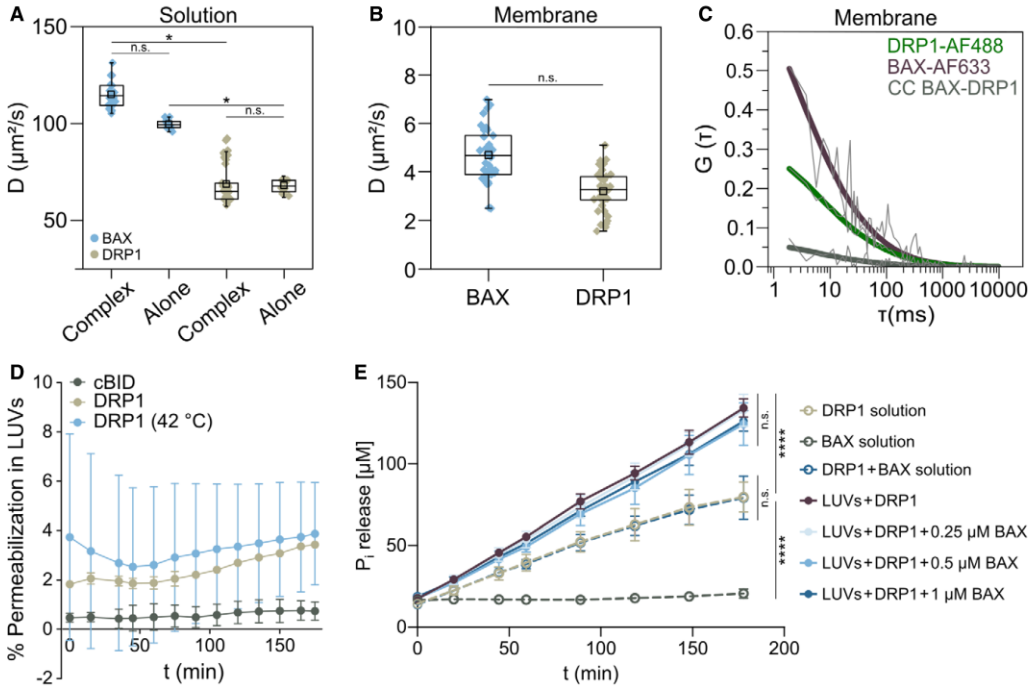

Figure EV2. Interaction between BAX and DRP1 and activity analysis *in vitro*.

A, B Diffusion coefficients derived from FCCS analysis of BAX-AF633 (blue) and DRP1-AF488 (beige) in solution in complex with each other and alone as indicated (A) or in the membrane (B). Box plots (in A and B) represent the interquartile (outer box), mean (inner box), median (line) and range (whiskers). Levels of significance were determined by paired two-tailed Student's *t*-test (n.s. $P > 0.05$, *$P < 0.05$) from $n \geq 25$ individual measurements for BAX or DRP1 in complexes and $n \geq 10$ measurements of BAX and DRP1 alone in solution (A) or $n \geq 33$ individual measurements for BAX or DRP1 in the membrane (B).

C Representative auto- (green and violet curves) and cross-correlation (CC, BAX-DRP1, grey curves) curves of DRP1-AF488 and BAX-AF633 measured in the membrane of GUVs in presence of unlabeled cBID. Thin grey lines depict raw data and thick lines correspond to data fitting.

D Negative control of LUV permeabilization by cBID and DRP1 alone. Calcein release was measured in calcein-encapsulated LUVs incubated with cBID (grey) or DRP1 at room temperature (beige) or after mild heating (42°C, blue). Data are presented as mean ± SD of $n = 3$ independent experiments.

E Effect of BAX on the GTPase activity of DRP1 in solution or in the membrane. Time course of GTP hydrolysis by DRP1 measured at 37°C in the absence or presence of LUVs and different concentrations of BAX as indicated. Data are presented as mean ± SD of $n = 4$ independent experiments. Significance was determined by paired two-tailed Student's *t*-test (n.s. $P > 0.05$, ****$P < 0.0001$).

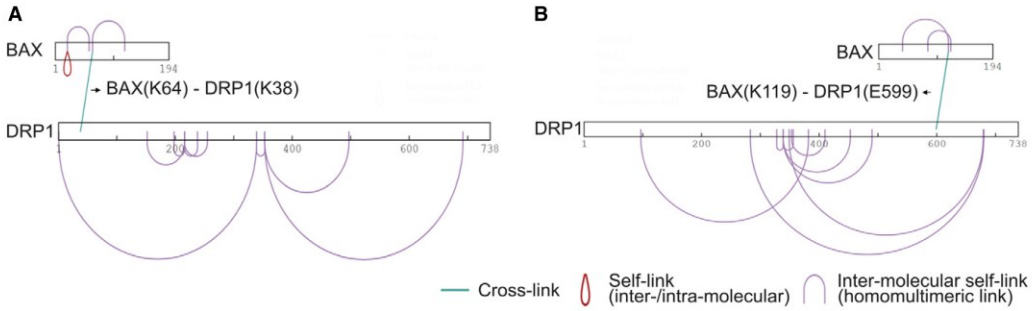

C

Peptide: SECLKRIGDELDSNMEL(5)-QSSGKSSVLESL(5)

Mod_Sites	Score	Calc_Mass	Delta_Mass	ppm	Proteins
3,C (Carbamidomethyl_C)	3,46E-03	3366,6169	-0,00071	-0,21083	BAX(64)-DRP1(38)

20170215_CO_0667AnGS_R18.14327.14327.4 File:"20170215_CO_0667AnGS_R18.raw", scan=14327"

D

Peptide: FYFASKL(6)-SKAEEL(4)

Mod_Sites	Score	Calc_Mass	Delta_Mass	ppm	Proteins
null	1,44E-03	1531,7921	-0,00447	-2,916	BAX(119)-DRP1(599)

20170215_CO_0667AnGS_R15.4135.4135.4 File:"20170215_CO_0667AnGS_R15.raw", scan=4135"

Figure EV3. pLink analysis of all crosslinks identified by XL-MS for BAX and DRP1 interaction in liposomes.

A, B Graphic representation of all positively identified crosslinks in the BAX/DRP1 complex mediated by DSS (A) and EDC (B).
C, D Excerpt from the pLink search result for the BAX(64)-DRP1(38) crosslinked by DSS (C) and BAX(K119)-DRP1(K599) crosslinked by EDC (D).

Figure EV4. Expression, localization and apoptotic activity of BAX mutants not interacting with DRP1 and effect of MAPL-mediated DRP1 SUMOylation on the interaction.

A Confocal microscopy images of U2OS BAX/BAK DKO cells transfected with GFP-BAX mutants L63E, Δ19–37 or ΔL1–2 as indicated (green) and stained with MitoTracker Deep Red FM to visualize mitochondria (magenta). Scale bar 10 μm. Images are representative for $n = 3$ independent experiments.

B Quantification of cell death induced by overexpression of GFP-BAX mutants L63E, Δ19–37 and ΔL1–2 compared to wild type (WT) in U2OS BAX/BAK DKO cells. Data are presented as fold increase of dead cells 12 h after transfection normalized to the number of dead cells at the time point of transfection. Values correspond to mean (line) ± SD of $n = 2$ independent experiments. Single data points represent individual measurements from technical and biological replicates.

C Representative western blot analysis ($n = 3$ independent experiments) of total cell lysates from U2OS BAX/BAK DKO cells overexpressing GFP-BAX mutants (as indicated) probed against GFP. Whole cell protein staining (Ponceau S) is shown to confirm equal loading.

D Structural model of BAX highlighting proposed interaction regions for DRP1 and for the BH3 domain of BID. BAX structure is based on the NMR structure of the inactive, full-length monomer, PDB 1F16. In red, the C-terminal helix of BAX occupying the hydrophobic groove, which corresponds to the binding site of the BH3 helix of BID. The regions corresponding to residues 19-37 (in helix 1, light blue), the loop between helices 1 and 2 (blue) and L63 (yellow) are required for the interaction with DRP1.

E Confocal microscopy image of apoptotic U2OS BAX/BAK DKO cells transfected with RA-BAX/GB-DRP1 (green) and mito-BFP (magenta) after siRNA-mediated depletion of MAPL (left panel, siMAPL) versus siRNA control (right panel, siControl). Scale bar 10 μm.

F Western blot analysis of total cell lysates from U2OS BAX/BAK DKO cells after siRNA-mediated depletion of MAPL (siMAPL) versus siRNA control (siControl) probed against MAPL. Whole cell protein staining (Ponceau S) is shown to confirm equal loading. Data are representative of $n = 3$ independent experiments.

G Quantification of BAX/DRP1 interaction after siRNA-mediated MAPL knock-down (siMAPL) versus knock-down control (siControl) in healthy or apoptotic conditions (+/− STS). Box plots represent the interquartile (box), median (line) and SD (whiskers) of $n = 3$ independent experiments. Significance was tested by paired two-tailed Student's t-test (n.s. indicating $P > 0.05$).

Source data are available online for this figure.

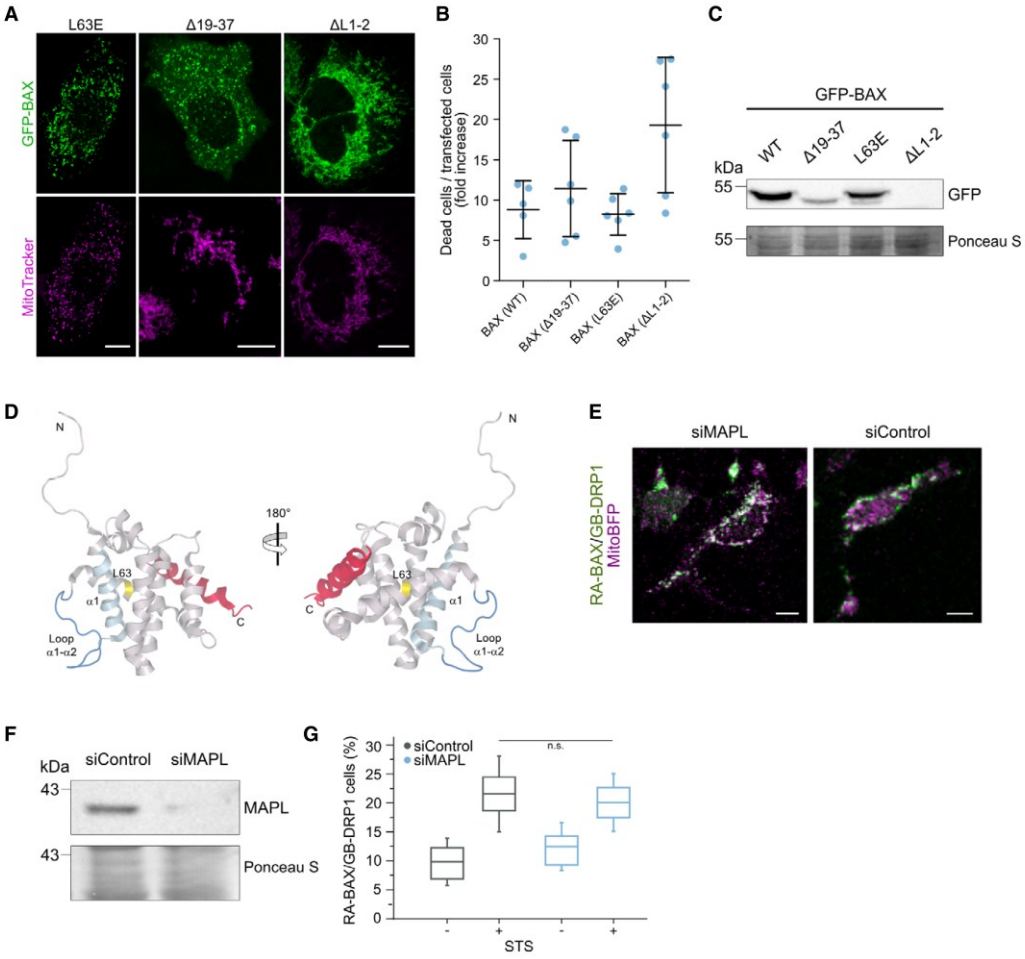

Figure EV4.

Figure EV5. Induced dimerization of BAX and DRP1 induces apoptosis.

A Confocal microscopy of U2OS BAX/BAK DKO cells transfected with FKBP-mCherry-DRP1 (red) and FRB-EGFP-BAX (green) and stained with MitoTracker Deep Red FM (cyan). Images were acquired before (0 min) and after induction of BAX/DRP1 dimerization (5, 10 min). Scale bar 20 μm.

B–D Induced dimerization of DRP1 to itself (B), BAX to itself (C) or BAX to TOM20 (D) in U2OS BAX/BAK DKO cells transected with FKBP- and FRB-mCherry DRP1 (B, red), FKBP- and FRB-EGFP-BAX (C, green) or TOM20-mCherry-FKBP (red) and FRB-EGFP-BAX (green, D) before (0 min) and after induced dimerization (10 min). Mitochondria were stained using MitoTracker Deep Red FM or MitoSpy NIR (cyan) as indicated. Scale bar 20 μm. Pearson's correlation coefficient was calculated between the induced dimerization signal of BAX/BAX, DRP1/DRP1 and BAX/TOM20, respectively, and mitochondria based on MitoTracker Deep Red TM signal as depicted below the images.

E Induced dimerization of DRP1 and BAX mutants L63E, Δ19–37 or ΔL1–2. Confocal microscopy of U2OS BAX/BAK DKO cells transfected with FKBP-mCherry-DRP1 (red) and mutant variants FRB-EGFP-BAX (green) as indicated and stained with MitoTracker Deep Red FM (cyan). Images were acquired 10 min after induction of BAX/DRP1 dimerization. Scale bar 20 μm. All images are representative of $n = 3$ independent experiments.

F–H Dimerization of BAX and DRP1 induces their translocation to mitochondria, exposure of the BAX 6A7 epitope and cytochrome *c* release. (F) Western blot analysis of cytosolic and mitochondrial fraction from U2OS BAX/BAK DKO overexpressing FKBP-mCherry-DRP1 and FRB-EGFP-BAX after induction of BAX/DRP1 dimerization (Dim) or apoptosis (Apo) compared to non-treated (Ctrl) or untransfected cells (Untr). Western blot was probed against DRP1 and BAX. Mitofilin (IMMT) was used to test for purity of cytosolic fraction. Results are representative for $n = 3$ independent experiments. (G) Representative ($n = 3$ independent experiments) confocal microscopy images of U2OS BAX/BAK DKO cells transfected with FKBP-mCherry-DRP1 (red) and FRB-EGFP-BAX (green). Cells were immunostained against the 6A7 epitope of BAX (grey) after induced dimerization of BAX and DRP1 (Dimerizer) compared to untreated (Control). Images show individual channels or overlay of FKBP-mCherry-DRP1 and BAX-(6A7) immunofluorescence signal. Scale bar 10 μm. (H) Representative ($n = 3$ independent experiments) western blot analysis of the cytosolic and mitochondrial fraction from U2OS BAX/BAK DKO treated as described in F) and probed against cytochrome *c* (Cytc). TOM20 was used to test for purity of cytosolic fraction. Protein staining (Ponceau S) is shown to confirm equal loading.

I–K Quantification of caspase activation, PARP cleavage and cell death induced by forced dimerization of BAX and DRP1. (I) U2OS BAX/BAK DKO cells were transfected with FKBP-mCherry-DRP1 and FRB-EGFP-BAX and analyzed for the percentage of cells with caspase 3/7 activation. Data are normalized to the number of transfected cells at individual time points after inducing dimerization of BAX and DRP1 (Dim, 30, 60 and 90 min) compared to apoptosis induction for 90 min (Apo, 90 min) or untreated cells (Ctrl). (J) Representative western blot analysis ($n = 3$ independent experiments) of total cell lysates from cells transfected as described in (I) after induction of BAX/DRP1 dimerization (Dim) or apoptosis (Apo) compared to non-treated (Ctrl) or untransfected cells (Untr). Blot was probed against PARP or GAPDH as a loading control. K) U2OS BAX/BAK DKO cells were transfected as described in (I) and induced for BAX/DRP1 dimerization (Dim) or apoptosis (Apo) compared to untreated (Ctrl). Data are presented as fold increase of dead cells 1 h after treatment compared to the number of dead cells before treatment and normalized to the number of transfected cells.

Data information: Values in (I) and (K) are representative of $n = 2$ independent experiments and correspond to mean (bar, line) ± SD. Single data points in (I) represent individual measurements from technical and biological replicates.
Source data are available online for this figure.

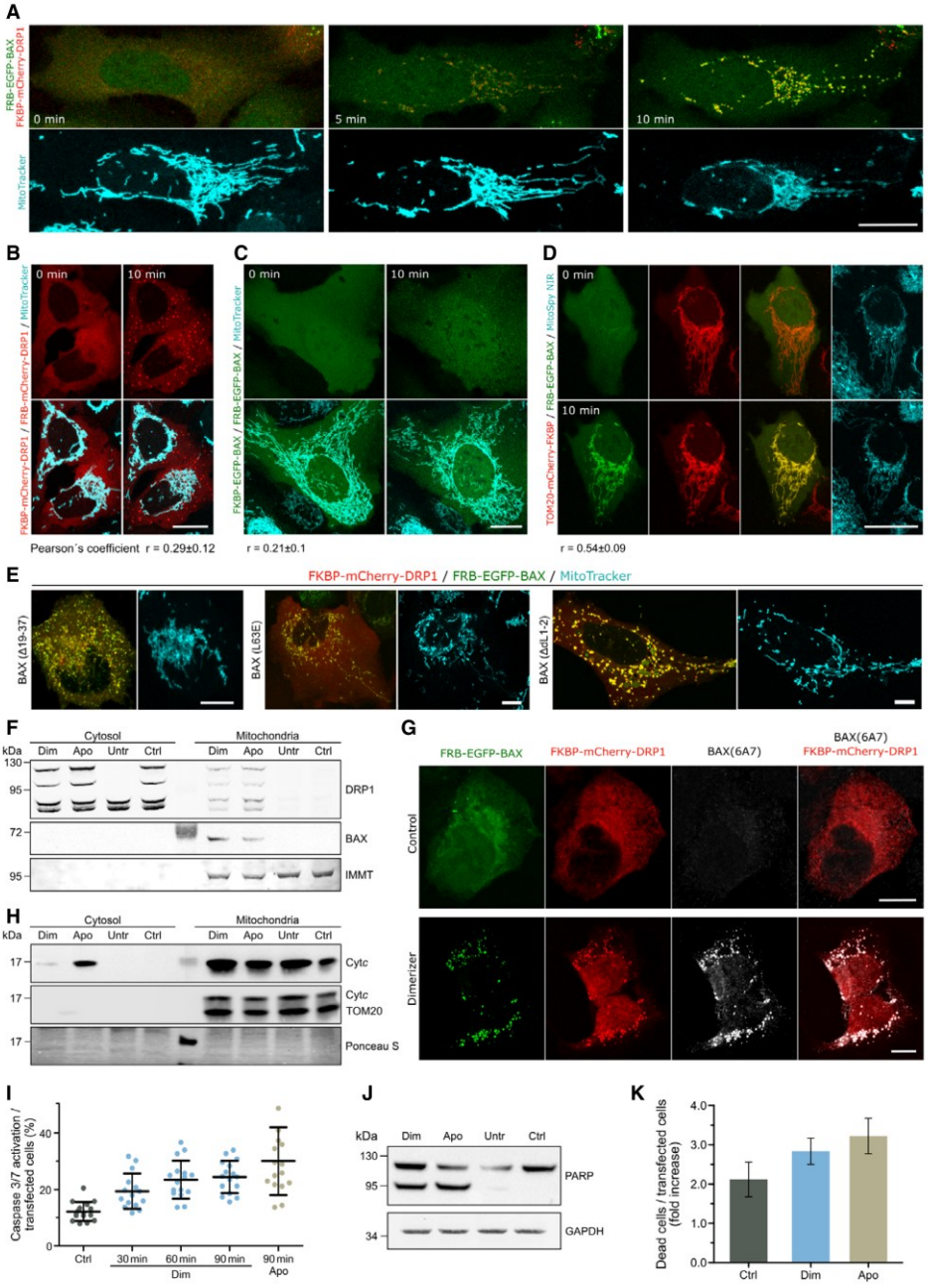

Figure EV5.

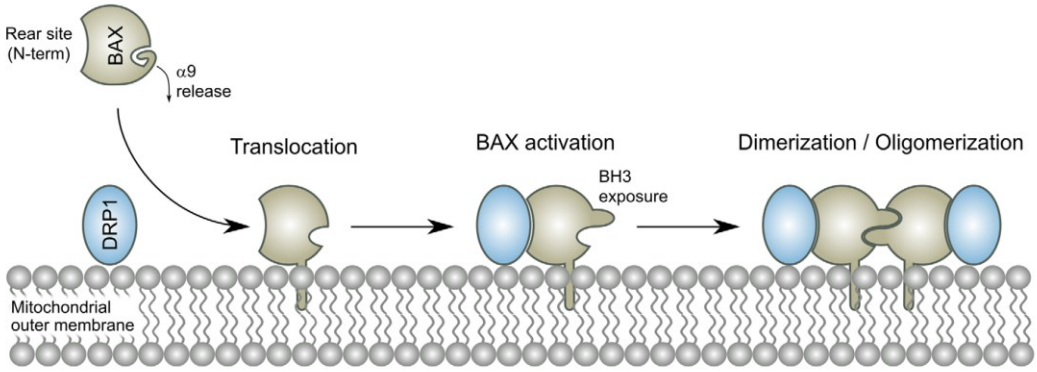

Figure EV6. Model for the interaction between BAX and DRP1 in apoptosis.

During apoptosis, DPR1 binds to mitochondrial BAX via multiple interfaces, with the N-terminus of BAX being required for the interaction. The interaction between BAX and DRP1 promotes BAX activation and apoptosis induction.

1.2 The interplay between BAX and BAK tunes apoptotic pore growth to control mitochondrial-DNA-mediated inflammation

Molecular Cell

Article

The interplay between BAX and BAK tunes apoptotic pore growth to control mitochondrial-DNA-mediated inflammation

Graphical abstract

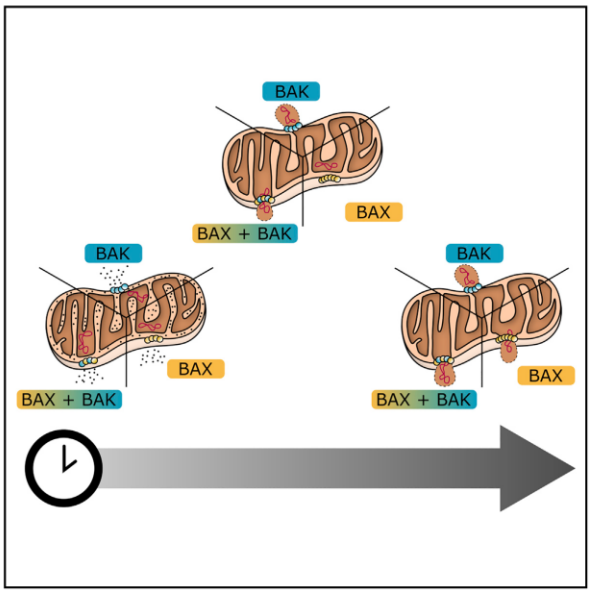

Authors

Katia Cosentino, Vanessa Hertlein, Andreas Jenner, ..., Markus Mund, Jonas Ries, Ana J. Garcia-Saez

Correspondence

ana.garcia@uni-koeln.de

In brief

BAX and BAK mediate membrane permeabilization in the mitochondrial pathway of apoptosis. Cosentino et al. show that the growth rate and permissiveness to mtDNA of the apoptotic pore can be dynamically modulated by the balance between BAX and BAK molecules, which regulate each other's assembly, thereby impacting downstream inflammatory signaling.

Highlights

- BAK oligomerizes faster into smaller lines, arcs, and rings than those formed by BAX
- BAK recruits BAX to co-assemble into the same supra-molecular apoptotic structures
- BAX and BAK reciprocal regulation defines the growth dynamics of apoptotic pores
- BAX and BAK have distinct roles in modulating the inflammatory outcome of apoptosis

Cosentino et al., 2022, Molecular Cell *82*, 933–949
March 3, 2022
https://doi.org/10.1016/j.molcel.2022.01.008

CellPress

Molecular Cell

CellPress
OPEN ACCESS

Article

The interplay between BAX and BAK tunes apoptotic pore growth to control mitochondrial-DNA-mediated inflammation

Katia Cosentino,[1,2,5] Vanessa Hertlein,[1,5] Andreas Jenner,[1,3,5] Timo Dellmann,[3] Milos Gojkovic,[3] Aida Peña-Blanco,[1] Shashank Dadsena,[3] Noel Wajngarten,[1] John S.H. Danial,[1] Jervis Vermal Thevathasan,[4] Markus Mund,[4] Jonas Ries,[4] and Ana J. Garcia-Saez[1,3,6,*]

[1]Interfaculty Institute of Biochemistry, University of Tübingen, 72076 Tübingen, Germany
[2]Department of Biology/Chemistry and Center for Cellular Nanoanalytics (CellNanOs), University of Osnabrück, 49076 Osnabrück, Germany
[3]Institute for Genetics and Cologne Excellence Cluster on Cellular Stress Responses in Aging-Associated Diseases (CECAD), University of Cologne, 50931 Cologne, Germany
[4]Cell Biology and Biophysics Unit, European Molecular Biology Laboratory (EMBL), 69117 Heidelberg, Germany
[5]These authors contributed equally
[6]Lead contact
*Correspondence: ana.garcia@uni-koeln.de
https://doi.org/10.1016/j.molcel.2022.01.008

SUMMARY

BAX and BAK are key apoptosis regulators that mediate the decisive step of mitochondrial outer membrane permeabilization. However, the mechanism by which they assemble the apoptotic pore remains obscure. Here, we report that BAX and BAK present distinct oligomerization properties, with BAK organizing into smaller structures with faster kinetics than BAX. BAK recruits and accelerates BAX assembly into oligomers that continue to grow during apoptosis. As a result, BAX and BAK regulate each other as they co-assemble into the same apoptotic pores, which we visualize. The relative availability of BAX and BAK molecules thereby determines the growth rate of the apoptotic pore and the relative kinetics by which mitochondrial contents, most notably mtDNA, are released. This feature of BAX and BAK results in distinct activation kinetics of the cGAS/STING pathway with implications for mtDNA-mediated paracrine inflammatory signaling.

INTRODUCTION

BAX and BAK are proapoptotic members of the BCL-2 family required for the permeabilization of the mitochondrial outer membrane (MOM) that during apoptosis releases apoptogenic factors such as cytochrome *c* and Smac/DIABLO into the cytosol to unleash the apoptotic cascade (Czabotar et al., 2014; Cosentino and García-Sáez, 2017). Cells from BAX and BAK double-knockout (DKO) mice are resistant to most apoptotic stimuli, and the integrity of their MOM is maintained even upon overexpression of proapoptotic BH3-only proteins (Wei et al, 2001). Furthermore, the phenotype of BAX/BAK DKO mice is perinatal lethal, and the few mice that reach adulthood present defective tissue homeostasis due to reduced apoptosis (Lindsten et al., 2000). Despite the interest in BAX and BAK as pharmaceutical targets for cancer therapy, our insufficient understanding of their molecular mechanism has so far limited the successful development of small molecule drugs.

BAX and BAK exist in an inactive form in healthy cells and shuttle between cytosol and mitochondria in a retro-translocation cycle promoted by anti-apoptotic BCL-2 proteins (Edlich et al., 2011; Schellenberg et al., 2013; Todt et al., 2015). During apoptosis, they accumulate at discrete sites at mitochondria, undergo a conformational change, and oligomerize concomitant with MOM permeabilization (MOMP) (Cosentino and García-Sáez, 2017). We previously reported that BAX oligomers exist in model membranes as multiple species, mostly based on dimer units (Subburaj et al., 2015). Super-resolution imaging revealed that BAX organizes into lines, arcs, and rings, with both arcs and rings being able to directly perforate lipid membranes (Große et al., 2016; Salvador-Gallego et al., 2016). Recent studies also showed that, after MOMP, BAX and BAK form large megapores that release big macromolecules such as mitochondrial DNA (mtDNA) (McArthur et al., 2018; Riley et al., 2018). Once in the cytosol, mtDNA triggers an inflammatory response through the cyclic GMP-AMP synthase/stimulator of interferon genes (cGAS/STING) signaling pathway that is normally dampened by caspase activity (Rongvaux et al., 2014; White et al., 2014; Giampazolias et al., 2017). These findings connect BAX and BAK to the regulation of the inflammatory outcome of apoptosis.

BAX and BAK exhibit high homology in sequence and structurally (Westphal et al., 2014; Czabotar et al., 2014), which, together with the need to knock out both proteins to block MOMP, has led to the assumption that both proteins have fully overlapping functions and share their molecular mechanism. Despite their functional redundancy, BAX and BAK differ in certain aspects. For example, their inactive forms present different steady-state cellular distribution, with BAX mainly cytosolic and BAK mainly mitochondrial. They are also usually expressed at different levels and most cell types contain higher amounts of BAX than of BAK (https://www.proteomicsdb.org/proteomicsdb; BAX ID Q07812, BAK ID Q16611). In addition, they seem to have distinct preferential binding to different BH3-only proteins and to be differentially activated by them (Kale et al., 2018; Singh et al., 2019; Sarosiek et al., 2013). Today, we still fail to understand whether these differences support a distinct molecular mechanism of action of BAX versus BAK and which biological implications this may have.

Here, we combined different single-molecule microscopy approaches to analyze the supra-molecular organization of BAX and BAK at the nanoscale. Using single-molecule localization microscopy (SMLM), we found that in the mitochondria of apoptotic cells BAK assembles into lines, arcs, and rings that are significantly smaller and more narrowly distributed compared with those of BAX. This is supported by single particle stoichiometry analysis of BAK and BAX oligomers and by atomic force microscopy (AFM) in model membranes revealing that BAK rings and arcs associate with membrane pores. Comparative analysis of the growth rate of single BAX and BAK clusters in cells undergoing apoptosis showed that distinct assembly properties underlie these differences and that BAX and BAK modulate each other's oligomerization. Mechanistically, the interplay between BAX and BAK is based on BAK promoting BAX recruitment and activation followed by their co-assembly into the same supra-molecular structures, as directly visualized by stimulated emission depletion (STED) microscopy. This has functional implications since the balance between BAX and BAK molecules regulates the dynamics of apoptotic pore growth, and thereby the relative kinetics of Smac and mtDNA release from mitochondria, which affects the downstream activation of the cGAS/STING signaling pathway and of bystander T cells. Our results support a model in which the regulation of the apoptotic pore growth by the interplay between BAX and BAK tunes the immunogenic impact of apoptosis.

RESULTS

BAK assembles into line-, arc-, and ring-like structures in apoptotic cells

To visualize the structural organization of BAK at the nanoscale, we used SMLM as previously with BAX (Salvador-Gallego et al., 2016). We first characterized the dynamics of apoptosis progression under our experimental conditions in BAX/BAK DKO HCT116 cells by live-cell confocal imaging (Figure 1A). Inactive monomeric enhanced GFP-BAK (mEGFP-BAK) appeared homogeneously distributed along the mitochondrial network of untreated cells. Upon apoptosis induction, mEGFP-BAK redistributed into discrete foci at mitochondria, in correlation with Smac-mCherry release into the cytosol as a proxy for MOMP (Figures 1A–1C). These results also confirmed that BAK tagged with mEGFP retained its apoptotic activity. Since apoptosis is a dynamic and generally irreversible process, we fixed cells for SMLM at the time point when 50% cells had undergone MOMP (3 h; Figure 1D).

SMLM of BAK in healthy cells confirmed its homogeneous distribution on the mitochondrial network, typically appearing as individual molecules lining the MOM in super-resolution images (Figure 1E). In contrast, in apoptotic cells BAK reorganized into discrete foci on fragmented mitochondria with distinct macromolecular architectures (Figure 1F), which we quantified with ASAP (automated structures analysis program [Danial and Garcia-Saez, 2019]). While most of the signal appeared as dots and aggregates, roughly 40% of BAK assemblies corresponded to lines, arcs, and rings of similar length and radius, independently of the cell line (Figures 2 and S1). These findings revealed that the architecture of BAK clusters in apoptotic cells was similar to that of BAX (Salvador-Gallego et al., 2016; Große et al., 2016), but, to our surprise, BAK formed smaller assemblies (with a mean ring radius of 18 nm compared with 34 nm of BAX [Salvador-Gallego et al., 2016]), which also were more homogeneous in size under similar conditions (Figures 2C, 2D, and S1D).

Given that 2D SMLM does not take into account the 3D nature of mitochondria and the relative orientation of the BAK structures, we cannot exclude that a fraction of the dots and aggregates correspond to unresolved distinct architectures. For example, some dots with size comparable to that of rings presented lower fluorescence in the center (Figures 2E and 2F), suggesting that they might be unresolved rings.

The finding that lines, arcs, and rings had a similar average length raised the question whether lines and arcs were intermediate structures evolving to a final ring. To study the temporal evolution of BAK structures, we established correlative live-cell confocal and SMLM microscopy (Figure S2). Using this approach, we analyzed single cells at different time points after MOMP and compared the distribution of BAK assemblies. We detected a slight decrease of linear structures accompanied by an increase in rings shortly after BAK foci formation, which then remained stable (Figure 2G). This indicated that the evolution of BAK structures occurs within the first 10 min of foci formation. The modest accumulation of rings at the expense of lines suggests that a fraction of BAK structures may develop from lines to rings. Although we cannot discard that some of the lines and arcs correspond to ring structures with tilted orientation with respect to the observation plane, the persistence of a high percentage of lines and arcs suggests that they are stable structures likely representing distinct entities.

Both arcs and rings of BAK are able to form membrane pores of a smaller size than BAX

To functionally associate the nano-assemblies of BAK detected in apoptotic cells by SMLM with their ability to form membrane pores, we used AFM. We produced recombinant full-length monomeric BAK (Figures S3A–S3D; Leshchiner et al., 2013) and prepared supported lipid bilayers (SLBs) from proteoliposomes containing activated BAK. While control membranes

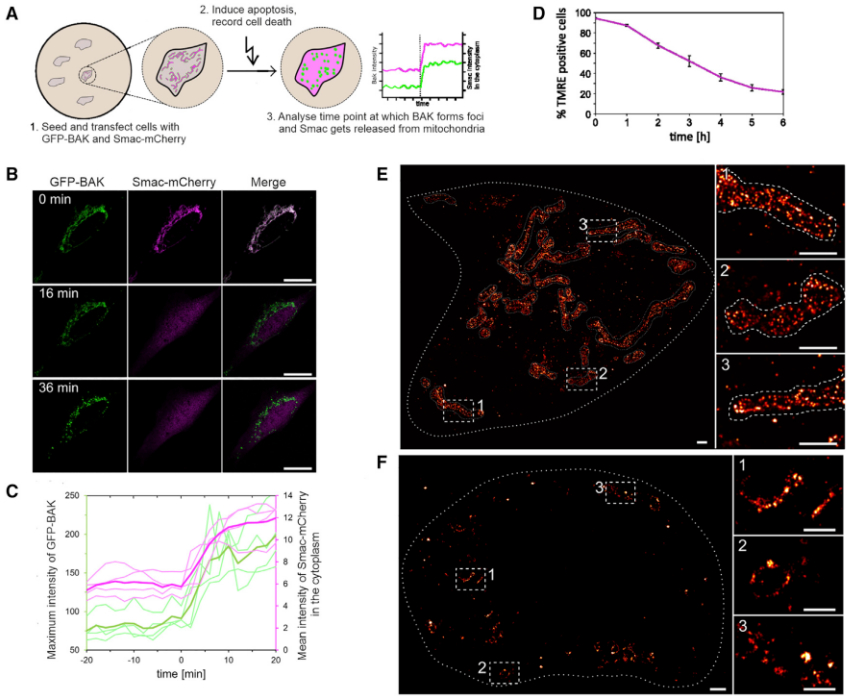

Figure 1. BAK assembly into distinct structures correlates with mitochondrial outer membrane permeabilization

(A) Scheme of the assay to monitor Smac release (magenta) from mitochondria to the cytosol due to mEGFP-BAK (green) foci formation.

(B) Representative confocal images of a BAX/BAK DKO HCT116 cell transfected with mEGFP-BAK (green) and Smac-(1-60)-mCherry (magenta) before (0 min) and 16 and 36 min after apoptosis induction with 1-μM STS. Scale bars, 10 μM.

(C) Maximum fluorescent intensity of mEGFP-BAK (green) and mean fluorescent intensity of cytosolic Smac-(1-60)-mCherry (magenta) for individual cells as in (B) (n = 4). Time point 0 min corresponds to the normalized time point of Smac-mCherry release. The release of Smac-mCherry in the cytosol correlates with an increase in the mEGFP-BAK intensity, which is indicative of foci formation. Bold lines represent the mean of individual dataset (light lines).

(D) Percentage of TMRE positive BAX/BAK DKO HCT116 cells transfected with mEGFP-BAK after treatment with 1 μM STS (n = 2). Error bars represent the SD.

(E and F) Representative SMLM images of mEGFP-BAK in BAX/BAK DKO HCT116 cells in healthy (E, mitochondria profile is defined by the dotted lines) and apoptotic conditions (F). Right panels are zoomed regions (indicated by white boxes in the main image). Scale bars: 1 μM in the main images and 500 nm in zoomed regions.

appeared flat and smooth in AFM images (Figure 3A), SLBs containing activated BAK presented structures protruding from the membrane (Figures 3B and 3C). Remarkably, besides undefined aggregates, these structures also included lines, arcs, and rings (Figures 3D and S3E). The identification of lines and arcs by AFM, in which the membrane plane has a constant orientation, supports the existence of these structures also in apoptotic cells, as suggested by the SMLM data.

Importantly, the 3D topography of the membrane surface provided by AFM allowed the visualization of membrane pores associated with both rings and arcs of BAK (Figures 3C, 3D, and S3E). Compared with BAX pores observed by AFM (Salvador-Gallego et al., 2016), BAK pores were smaller and more homogeneous, with an average pore radius of 8.12 ± 3.03 nm for the rings (Figure S3F). Due to their small size, we estimate that a fraction of them could not be resolved by our setup and appeared as aggregates on the membrane.

To estimate the size of BAK pores with an alternative method, we measured the influx of external, fluorescently labeled cytochrome *c* (12.5 kDa) and allophycocyanin (APC, 104 kDa) into giant unilamellar vesicles (GUVs) at different BAK concentrations. While cytochrome *c* was promptly internalized into GUVs in a concentration-dependent manner, we did not detect internalization of APC under our experimental conditions (Figures 3F and 3G). These results indicate that full-length BAK formed stable pores in GUVs smaller (or in the same range) than APC, in contrast to previous observations with BAX and with a truncated version of BAK

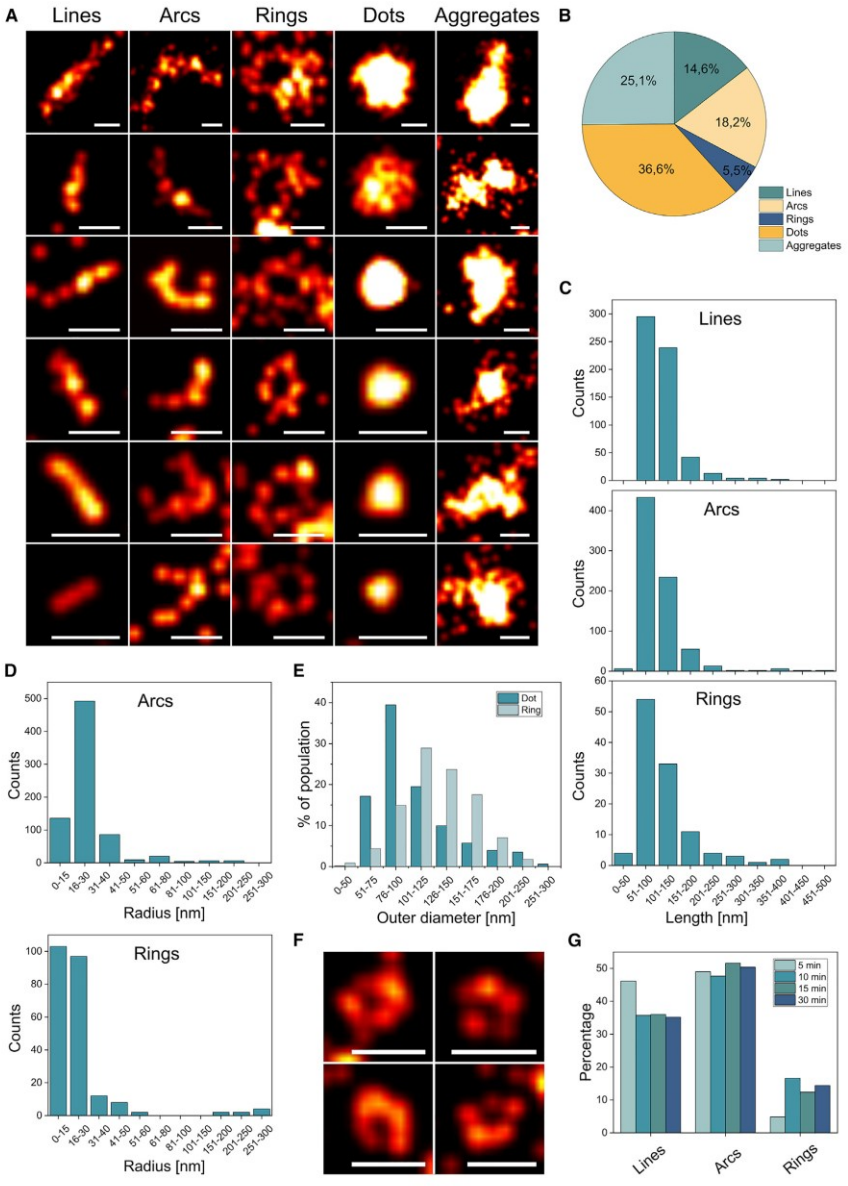

Figure 2. Super-resolution microscopy reveals nanoscopic BAK structures in apoptotic cells

(A) Gallery of BAK structures in apoptotic BAX/BAK DKO HCT116 cells transfected with mEGFP-BAK and labeled with an anti-GFP Alexa Fluor 647 nanobody. Scale bars, 100 nm.

(B) Relative distribution of the imaged BAK structure types over the total number of structures in all measured cells (n = 12).

(legend continued on next page)

(Bleicken et al., 2013a). Our findings in model membranes show the same trend as the SMLM data, collectively demonstrating that BAK forms smaller pore structures than BAX.

Oligomerization of BAX, but not BAK, is sensitive to protein density in the membrane

The distinct size of the structures formed by BAX and BAK assemblies in the membrane raised the question of whether they exhibit different oligomerization properties. To address this matter, we compared the stoichiometry *in vitro* of membrane-bound BAX and BAK oligomers at different concentrations by TIRF single-molecule imaging as in Subburaj et al. (2015) (Figures 3H–3J and S4). We produced functional mutants of BAX and BAK fluorescently labeled at single cysteines (see STAR Methods). Unexpectedly, the brightness of the individual BAX-488 particles, but not BAK-488 particles, in the population appeared as a broad distribution (Figures 3J and S4A), typical of multiple co-existing oligomeric species in the membrane. We then estimated the number of BAK and BAX molecules in the individual clusters based on the average intensity of their respective monomers. As with BAX, monomeric BAK-488 was obtained by adding it directly on an SLB (Subburaj et al., 2015) due to unspecific interactions with the glass support preventing BAK oligomerization (Figures S4C–S4E). In contrast, BAK-488 molecules pre-incubated with liposomes assembled into oligomers, predominantly dimers (Figures 3J, S4A, and S4B), independently of the activation strategy (Figures S4F and S4G). In addition, at the nanomolar range of concentrations required for TIRF single-molecule imaging, the distribution of BAX-488, but not BAK-488, oligomers increased with protein concentration. Compared with BAK, BAX-488 showed higher fluorescence intensity distributions at all tested concentrations and reached higher oligomeric states up to 10-mer (Figures 3J, S4A, and S4B). These data suggest that BAK has a lower tendency than BAX to oligomerize in the membrane, in line with the formation of smaller structures observed by AFM (Figures 3A–3E). Furthermore, BAX but not BAK oligomerization strongly depends on membrane density.

Real-time analysis of BAX and BAK assembly in the mitochondria of apoptotic cells reveals different oligomerization properties

We hypothesized that the structural differences between BAX and BAK oligomers in the membrane could be the result of mechanistic differences in their assembly. To address this question in the more physiological setting of the cell, we implemented a method to quantify the real-time kinetics of BAX and BAK oligomerization in mitochondria of apoptotic cells that allows estimating their stoichiometry over time (see STAR Methods and Figure 4). Based on photon-counting confocal microscopy in combination with ratiometric analysis (Figure S5; Jenner et al., 2020; Finan et al., 2015; Verdaasdonk et al., 2014), this approach compares the fluorescence intensity of the protein complex of interest with a standard of known stoichiometry labeled with the same fluorophore. As a standard, we used the 32-mer mEGFP-tagged nuclear pore complex component 96 (NUP96), endogenously expressed in the same U2OS cell type used for our experiments (Figure S5; Thevathasan et al., 2019).

Figure 4A shows that the assembly of transfected mEGFP-BAX into foci at mitochondria of BAX/BAK DKO U2OS cells correlated with Smac-mCherry release into the cytosol, indicative of MOMP (see also Figures S6A and S6B). We then monitored the growth of individual foci of mEGFP-BAX or mEGFP-BAK over time until the point when the mitochondrial network was too fragmented and the foci started to coalesce due to cell shrinkage (Figure 4B). Since MOMP takes place in the individual cells of the population at different time points after treatment, we synchronized the analysis of the kinetics of mEGFP-BAX and mEGFP-BAK assembly by setting Smac-mCherry release as a temporal reference. We determined the stoichiometry of the individual foci at each time point for BAX/BAK DKO cells expressing mEGFP-BAX or mEGPF-BAK at similar levels (Figure 4C). We found that the fluorescence intensities of mEFGP-BAX oligomers increased over time into a broad distribution, ranging from tens to several hundreds of units (Figure 4D). In contrast, the fluorescence intensities of mEGFP-BAK foci did not significantly change after 10 min from MOMP and displayed a more uniform oligomer distribution centered around 100–200 U (Figure 4E). This difference in the size of the BAX and BAK clusters is in good agreement with the results from SMLM and reconstituted systems.

By plotting the average foci stoichiometry over time, we observed that mEGFP-BAK oligomerized faster and reached a stable size of around 200 molecules a few minutes after MOMP (Figure 4G). In contrast, the assembly of mEGFP-BAX foci was slower, and it took around 30 min to reach the same average number of units as mEGFP-BAK under these experimental conditions (Figure 4G). Remarkably, the average stoichiometry of mEGFP-BAX continued to increase during the measurement time, resulting in a steady increase in the number of large foci (containing more than 200 or 400 U) (Figures 4H and 4I). In contrast to mEGFP-BAK, the mitochondrial density of mEGFP-BAX foci also increased with time (Figure 4J). These results were independent of the cell line and treatment (Figures S6C–S6H).

To confirm that these differences were not due to the different initial cellular localization of BAX and BAK or to slightly different expression levels, we analyzed a mutant of BAX, BAX(S184V), which retains activity but localizes constitutively at mitochondria (Verdaasdonk et al., 2014) and is expressed at similar levels as BAK (Figures 4B and 4C). mEFGP-BAX(S184V) assembled faster than mEFGP-BAX, but slower than mEGFP-BAK, and still arranged into a broad distribution of oligomers whose molecularity steadily increased similar to BAX (Figure 4F). These results indicate that the faster assembly kinetics of BAK is only partially due

(C and D) Quantification of the line and arc length and of the ring perimeter (C) and of the arc and ring radius (D) for all analyzed cells (n = 12).
(E) Quantification of the diameter of dots (blue) and outer diameter of rings (light blue) for all analyzed cells (n = 12).
(F) Exemplary images representing dots with less intensity in the center. Scale bars, 100 nm.
(G) Relative distribution of all collected line (minimum 84), arc (minimum 112), and ring (minimum 24) structures (cells n = 12) at different time points after first foci appearance. See also Figures S1 and S2.

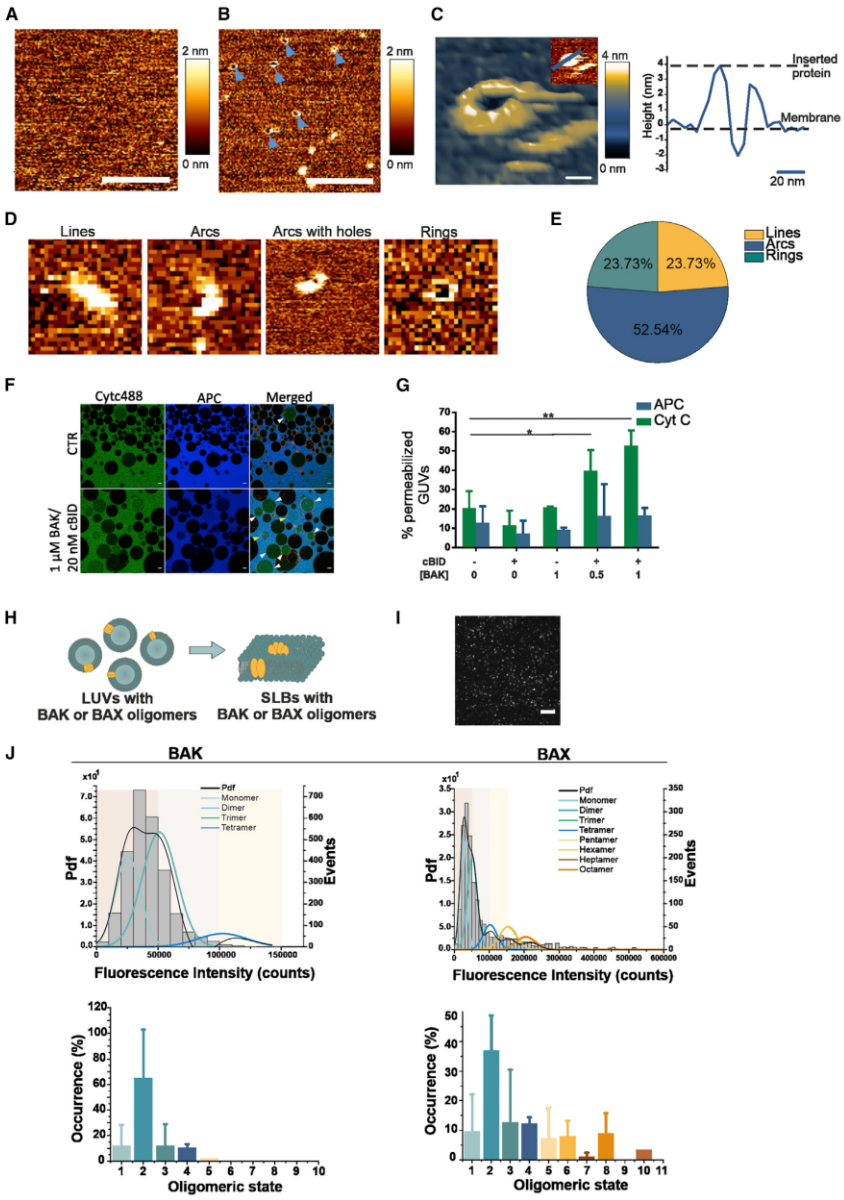

(legend on next page)

to its mitochondrial localization and that the saturation in BAK oligomers' size is not due to molecular availability. Collectively, these findings demonstrate that the assembly of BAX and BAK upon their activation in apoptosis is mechanistically different.

BAK and BAX modulate each other's oligomerization by co-assembling into the same supra-molecular structures

Since BAX and BAK co-localize into apoptotic foci (Zhou and Chang, 2008), yet they present distinct oligomerization properties, we hypothesized that BAX and BAK may influence each other's assembly. To tackle this question, we quantified the real-time foci stoichiometry of mEGFP-BAX or mEGFP-BAK in single knockout (KO) U2OS cells containing either only endogenous BAK (BAX KO) or only endogenous BAX (BAK KO) (Figures 5A–5D). Compared with the BAX/BAK DKO cells, both mEGFP-BAX and mEGFP-BAK maintained their assembly behavior in the single KO background (Figures 4G, 5E, and 5H), with the remarkable difference that mEGFP-BAX oligomerized faster and mEGFP-BAK slower (Figures 5F and 5G). A comparative analysis of super-resolved BAK structures in the presence or absence of BAX at 30 min after MOMP (Figures 5I–5M) also showed that the presence of endogenous BAX caused a significant increase in their size. The average size of transfected mEGFP-BAK nano-structures in single BAK KO cells was intermediate between that of BAK and BAX in DKO cells, while their shape and distribution was not affected. Altogether, these findings reveal that BAX and BAK reciprocally contribute to each other's assembly: BAX increases the size of BAK apoptotic structures, while BAK accelerates BAX assembly kinetics.

These results suggested that BAX and BAK may be part of the same high-order complexes. To address this question, we implemented dual-color super-resolution STED microscopy of Snap-BAX and Halo-BAK in combination with confocal microscopy of the mitochondrial network labeled with 4xmt-mTurquoise2 (Figure 6A). In living cells undergoing apoptosis, we identified individual lines, arcs, and rings formed by both proteins (Figures 6A, 6B, and S7A), revealing that BAX and BAK co-assemble into the same supra-molecular structures. Importantly, these results also provide direct visualization of the apoptotic pore formed by both BAX and BAK.

In agreement with this, the use of *in situ* proximity labeling with the engineered ascorbate peroxidase 2 (APEX2 [Lam et al., 2015]) confirmed that BAX was in direct vicinity of BAK and vice versa in the context of intact apoptotic foci, but not in healthy cells (Figure 6C). We further demonstrated the interaction between active BAX and BAK at individual apoptotic foci by dimerization-dependent fluorescent protein (ddFP) (Figure 6D), which only produces a fluorescent signal for co-expressed RA-BAX and GB-BAK proteins that are closer than 10 nm (Ding et al., 2015). Additional evidence of the association between BAX and BAK was obtained from co-immunoprecipitation (coIP) experiments using styrene maleic anhydride (SMA) co-polymers, which enable mild solubilization of mitochondria into lipid/protein nanoparticles of around 10 nm in diameter (Figure S7B) with the advantage of preserving the lipid environment (Lee et al., 2016). Following immuno-isolation of SMA lipid particles specifically containing GFP-BAK, we detected interaction with BAX exclusively under apoptotic conditions (Figures 6E–6G). Together, these results further support that BAX and BAK co-assemble into the same macromolecular complexes in apoptotic foci, whose properties depend on the ratio between BAX and BAK molecules.

The findings that BAK oligomerized faster and accelerated BAX assembly into the same supra-molecular complexes led us to speculate that BAK oligomers at mitochondria may act as seeding points for recruiting and activating cytosolic BAX. In agreement with this, we found that at early stages of apoptosis induction, mCherry-BAK clusters appeared before those of mEGFP-BAX at apoptotic foci (Figure 6H), independently of their

Figure 3. BAK assemblies are associated with stable membrane pores smaller than BAX

(A and B) Representative image of an EPC:CL (80:20 mol %) membrane without (A) and with (B) BAK pores (indicated by the blue arrows) imaged by atomic force microscopy (AFM). Scale bars, 200 nm.

(C) 3D representative image of a BAK pore (left) and its height profile (right, corresponding to the blue line in the 2D image inset). Scale bars, 20 nm.

(D) Representative BAK structures imaged by AFM. Picture size 100 nm. The full-color height range of the topographs from low (brown-orange) to high (yellow-white) is 2 nm.

(E) Percentage distribution of each BAK structure types over the total number of analyzed structures (lines = 14, arcs = 31, and rings = 14). All data (A–E) were obtained from at least four independent experiments.

(F) Representative images of giant unilamellar vesicles (GUVs, black and red membrane in the merged channel) of EPC:CL (80:20 mol %) lipid composition without (top) or with (bottom) incubation with cBid-activated BAK. After 1-h incubation, Cytc488 (green) and APC (blue) were added and images were taken 30 min later. White and yellow arrow heads indicate Cytc488 and Cytc488-APC permeabilized GUVs, respectively. Scale bars, 10 μm.

(G) Percentage of GUVs internalizing the fluorescent probes at different concentrations of BAK and 20 nM of cBid. Data (F and G) were obtained from at least three independent experiments and a minimum of 50 vesicles were analyzed per condition. Error bars represent the SD. *$p < 0.05$; **$p < 0.01$ (one-way ANOVA with Dunnett's multiple comparison test).

(H) Schematic representation of the protocol used for sample preparation of stoichiometry experiments in model membranes (BAX and BAK depicted in yellow, see STAR Methods).

(I) Representative TIRF image of an SLB containing BAK oligomers (bright spots). Scale bars, 10 μm.

(J) Upper panel: representative fluorescence intensity distribution of BAK-488 and BAX-488 oligomers (minimum 1,500 particles per condition) obtained from SLB samples with 10 nM of protein. The obtained brightness distribution was plotted as a probability density function (Pdf, black) or, alternatively, as a histogram, and fitted with a linear combination of Gaussians to estimate the percentage of occurrence of particles containing n-mer-labeled molecules (see color code in the graph). The three panels in the background indicate each a 50,000 counts range and are for a visual comparison between BAX and BAK intensity distribution graphs. Lower panel: percentage of occurrence of BAK-488 and BAX-488 different oligomeric species calculated as the average value from two different experiments. Data provided are corrected for partial labeling (see STAR Methods). The error bars correspond to the SD from the different experiments. See also Figures S3 and S4.

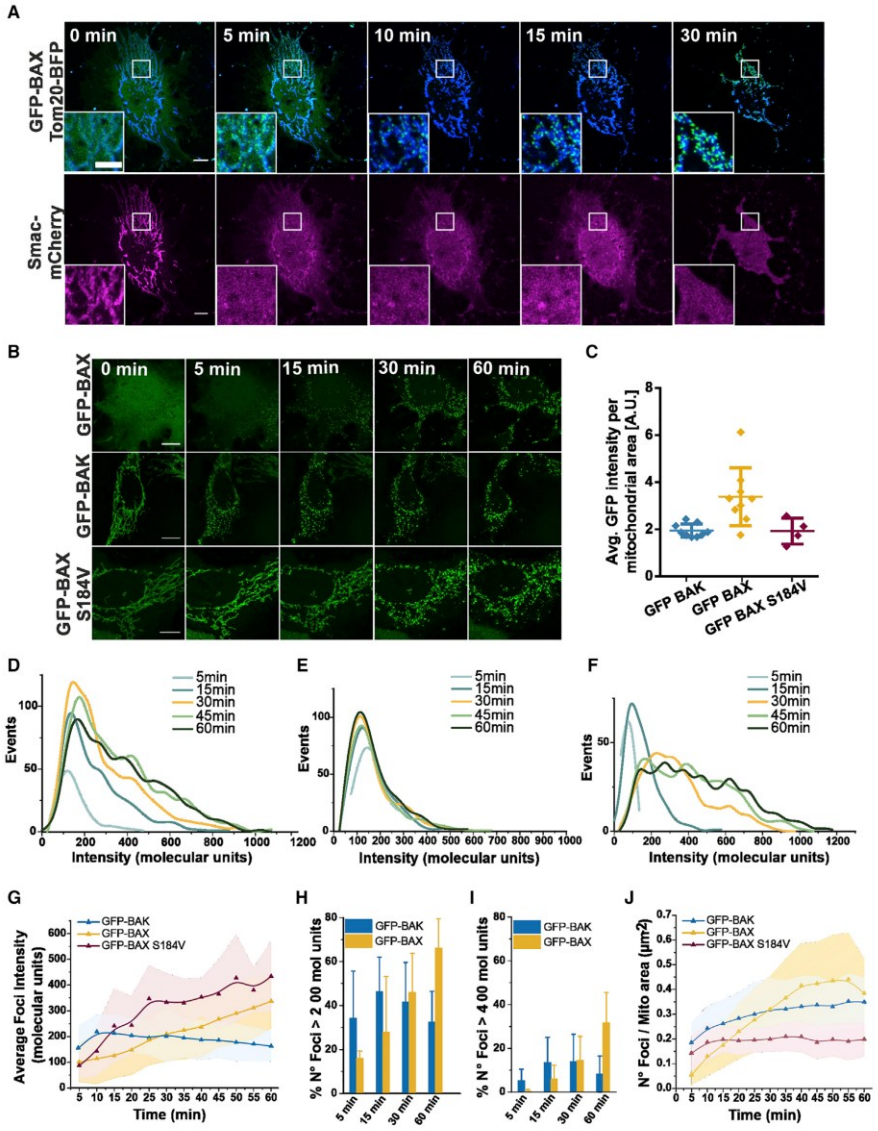

Figure 4. BAX and BAK foci assembly proceeds via a different mechanism of oligomerization

(A) Representative confocal images of a BAX/BAK DKO U2OS cell transfected with mEGFP-BAX (green), Tomm20-BFP (blue) and Smac-1-60-mCherry (magenta) and treated with ABT-737, S63845 and qVD-Oph for apoptosis induction. Time points are after Smac-1-60-mCherry release from mitochondria. Scale bars, 10 µm. Inset: apoptotic foci of mEGFP-BAX growing over time on mitochondria. Scale bars, 3 µm.

(B) Representative photon-counting confocal images of BAX/BAK DKO U2OS cells transfected with mEGFP-BAK, mEGFP-BAX, or mEGFP-BAX(S184V) and treated for apoptosis induction. Scale bars, 10 µm.

(legend continued on next page)

expression levels. Additionally, we developed an optogenetic system for the light-controlled activation of BAK. Illumination with 405 nm light induced the oligomerization and redistribution into foci of CRY2-mCherry-BAK and CIBN-mCherry-BAK in BAX/BAK DKO U2OS cells also expressing mEGFP-BAX. Interestingly, light-induced BAK oligomerization caused the recruitment and accumulation of BAX at the same foci in absence of apoptotic stimuli, which led to apoptosis induction (Figure 6I). Further demonstration was provided by experiments in chemically defined minimal systems based on GUVs. Heat-activated BAK-488 bound to and permeabilized GUVs as expected. Remarkably, membrane-bound, active BAK-488 was able to recruit inactive, soluble BAX-655 to the GUVs in absence of any other components, as shown by the red fluorescence intensity on the GUV rim (Figures 6J and 6K). These results suggest that BAK accelerates the growth of BAX foci likely by direct recruitment and activation of cytosolic BAX.

The interplay between BAX and BAK tunes the kinetics of mtDNA release and cGAS/STING-mediated inflammatory signaling

The observation that BAK has faster kinetics of assembly and different cluster size compared with BAX raised the question whether this might have functional consequences during apoptosis. We reasoned that the different high-order assembly properties of BAX and BAK might have a stronger impact on the release of large macromolecules, such as mtDNA, from mitochondria. To test this hypothesis, we performed correlative live-cell confocal and fixed-cell airyscan super-resolution microscopy to follow the kinetics of mtDNA release with respect to the initiation of MOMP, measured as Smac-mCherry release, in single cells in the presence of either only endogenous BAX (BAK KO U2OS) or BAK (BAX KO U2OS), or both (WT U2SO) (Figures 7A and S8A). While in untreated cells mtDNA completely localized within mitochondria, we could detect mtDNA release after MOMP in all three cell lines, indicating that BAX and BAK are independently capable of forming large enough pores to meditate this process (Figure 7B). To our surprise, in cells expressing only BAK, all analyzed cells released mtDNA within 30 min after Smac-mCherry release, while in cells expressing only BAX, 25% of the cells still retained mtDNA within mitochondria even 60 min after Smac-mCherry release (Figure 7C). WT cells, containing both endogenous BAK and BAX, showed a similar phenotype to cells expressing only BAK. These results indicated that the kinetics of mtDNA release relative to Smac release was accelerated by BAK, in line with its increased assembly dynamics, and thus that the assembly rate of BAX and BAK is the main determinant for the kinetics of mtDNA release (Figures 5F and 5G).

In addition, using a BAX mutant that retains activity but presents reduced oligomerization, BAX(T182I) (Kuwana et al., 2020), which we validated at the single particle level in cells (Figures 7D–7F), we detected delayed mtDNA release compared with WT GFP-BAX (Figures 7G and 7H). These results hence provide a causative link between the assembly rate of BAX and BAK and the kinetics of mtDNA release independent of the genetic background. They also suggest a correlation between the number of BAX and BAK molecules at mitochondrial foci and the size of the apoptotic pore.

Since mtDNA release has been shown to induce the cGAS/STING pathway and to affect the inflammatory outcome of apoptosis (Rongvaux et al., 2014; White et al., 2014; Giampazolias et al., 2017), we compared the consequences of inducing MOMP solely by BAX, or BAK, or both, on inflammation. Under conditions of impaired caspase activity, we found that BAK-mediated MOMP in BAX KO SVEC cells led to faster STING degradation and TANK-binding kinase 1 (TBK1) phosphorylation, compared with WT SVEC cells or cells only expressing BAX (BAK KO SVEC cells), in line with an increased activation of the pathway (Figures 7I and 7J). Finally, we also evaluated the potential differences of BAX- and BAK-mediated MOMP on immune cells. To this aim, we co-cultured WT, BAK KO, and BAX KO SVEC cells, pre-treated with a combination of BH3 mimetics and a pan-caspase inhibitor, with primary mouse splenocytes. Remarkably, we detected a significant increase in the fraction of $CD45^+$ hematopoietic cells showing hallmarks of T cell activation, i.e., loss of the L-selectin, CD62L, and increase in the cell surface protein CD44, that had been co-cultured with BAX KO SVEC cells. The $CD4^+$ T helper cell population presented the highest differences (Figures 7K and S8B–S8D).

Together, these findings demonstrate that the coordinated assembly of BAX and BAK regulates the growth rate of the apoptotic pore and its permissiveness to large macromolecules, most notably mtDNA. We also uncover a key role of post-MOMP oligomerization kinetics of BAX and BAK in mtDNA release with functional consequences for the activation of the cGAS/STING pathway and of $CD4^+$ T helper cells.

DISCUSSION

Here, we report a previously unrecognized function of BAX and BAK in timing the release of mtDNA and thereby modulating

(C) Average mEGFP expression level per mitochondrial area in individual cells (represented by individual dots in the plot) transfected with mEGFP-BAK, mEGFP-BAX, or mEGFP-BAX(S184V) detected by single-cell fluorescent intensity analysis of mEGFP signal. The error bars correspond to the SD from the different experiments.

(D–F) Representative distribution of foci intensity, in stoichiometric units, at different time points in individual apoptotic cells overexpressing mEGFP-BAX (D), mEGFP-BAK (E), or mEGFP-BAX(S184V) (F).

(G) Average foci intensity obtained from the fitting of foci distributions as in (D–F) at each time point for individual apoptotic cells expressing mEGFP-BAX (yellow, n = 9), mEGFP-BAK (blue, n = 9) or mEGFP-BAX(S184V) (purple, n = 4). Lines in the graph correspond to the average values from all measured cells and colored areas correspond to data variability from single cells (mean ± SD).

(H and I) Number of foci with molecularity higher than 200 (H) or 400 (I) normalized to the total number of foci in the cell at different time points after Smac release. Average total n° foci over analyzed cells is ranging from 67 (at 5 min) to 517 (60 min) for mEGFP-BAX (n = 9 cells) and from 250 (at 5 min) to 481 (60 min) for mEGFP-BAK (n = 9 cells). The error bars correspond to the SD from the different experiments.

(J) Number of foci per mitochondrial area over time for apoptotic cells as in (G). See also Figures S5 and S6.

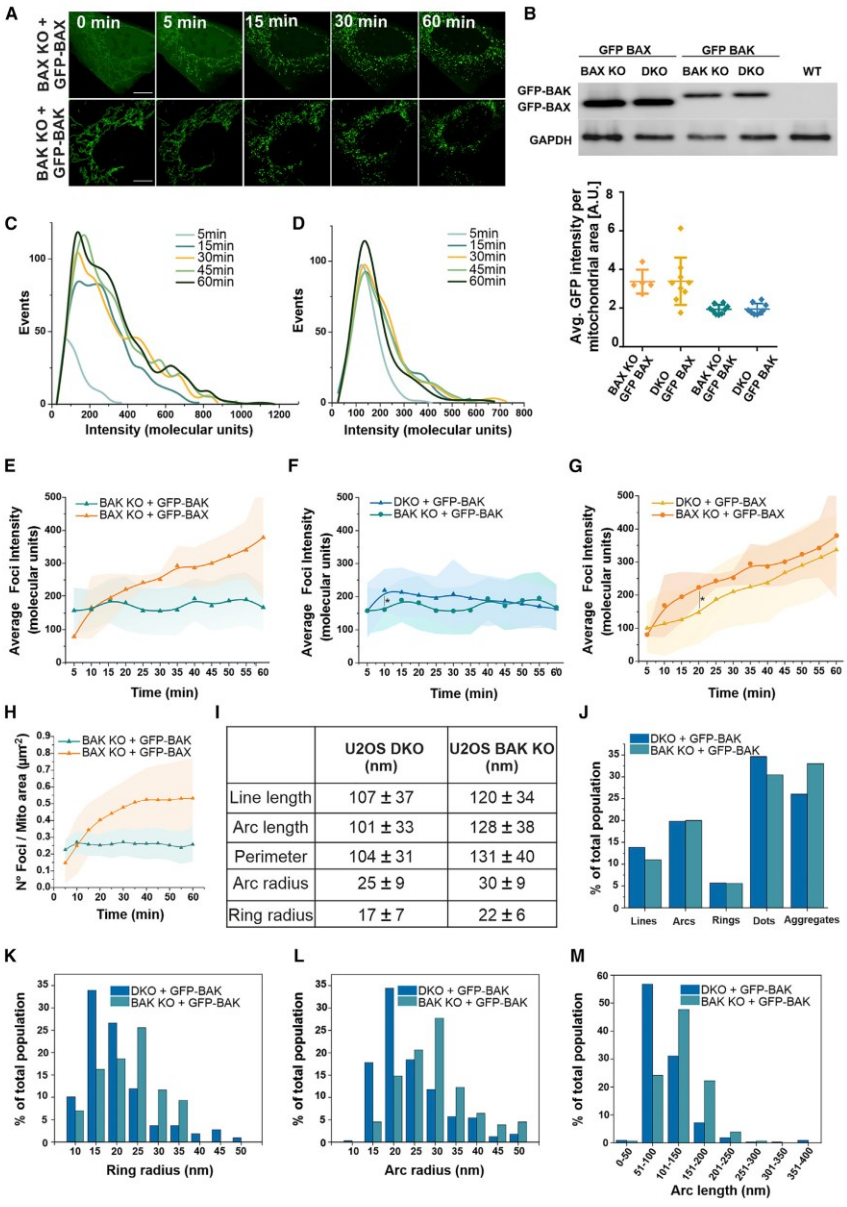

	U2OS DKO (nm)	U2OS BAK KO (nm)
Line length	107 ± 37	120 ± 34
Arc length	101 ± 33	128 ± 38
Perimeter	104 ± 31	131 ± 40
Arc radius	25 ± 9	30 ± 9
Ring radius	17 ± 7	22 ± 6

(legend on next page)

mtDNA-mediated inflammation in apoptosis. We demonstrate that the balance between BAX and BAK molecules defines the relative release kinetics of mitochondrial content, such as Smac and mtDNA, upon MOMP. The mechanistic basis for this function emerges from the distinct oligomerization dynamics of BAX and BAK and from their reciprocal regulation as they co-assemble into supra-molecular structures, which together determine the growth rate of the resulting apoptotic pore. This is important not only because it shows that the apoptotic pore size can be dynamically regulated but also because it affects downstream inflammatory signaling in apoptosis.

In this study, we provide direct structural evidence of BAK membrane pores. As previously shown for BAX, in apoptotic cells BAK assembles into heterogeneous structures that we classify as lines, arcs, and rings, with both arcs and rings being functionally able to perforate the membrane. These findings indicate a similar mechanism of membrane permeabilization for BAX and BAK based on lipidic pores, where the pore rim does not need to be fully covered by protein molecules to stabilize the open pore state. But in contrast to BAX, BAK oligomers and pores appear smaller and more homogeneous in size not only in cells but also in model membranes. This smaller size of BAK structures may be the reason why previous attempts failed to visualize BAK rings at apoptotic foci (Nasu et al., 2016).

We also show that the differences between BAX and BAK not only concern the size of the macromolecular complexes they form but also their assembly dynamics. Our quantitative analysis of individual apoptotic foci in dying cells demonstrates that BAK oligomers form faster and reach a stable average size in 5–10 min after MOMP. In contrast, BAX oligomers continue to grow almost linearly during apoptotic progression without an apparent size limit. Of note, these differences between BAX and BAK are not simply the result of different expression levels, molecular depletion or subcellular localization, as the mitochondria-resident BAX(S184V) mutant is expressed at similar levels to BAK but behaves similar to BAX WT. Together, our findings reveal underlying differences in the assembly of BAX and BAK and challenge the general assumption that these two proteins have fully overlapping mechanisms of action during apoptosis.

At the molecular level, the faster assembly and initial higher density of BAK clusters per membrane area observed could result from BAK presenting more effective intra-dimer interactions compared with BAX. In line with this hypothesis, recently, Iyer et al. showed a higher ability of BAK than BAX to activate other BAK and BAX molecules (Iyer et al., 2020). We cannot discard that other factors, including enhanced BAK accessibility to the BH3 domains of BAX and BAK (Iyer et al., 2020) or different association/dissociation kinetics with interacting partners in the cell, such as other BCL-2 proteins or VDAC2 (Ma et al., 2014; Cheng et al., 2003; Chin et al., 2018; van Delft et al., 2019), may also play a role.

Despite forming smaller structures, BAK oligomers in the cell can still reach hundreds of units and the resulting pores are big enough to release big macromolecules, such as mtDNA (Riley et al., 2018; McArthur et al., 2018; Figures 4 and 7). This raises the question about the role of persisting BAX oligomerization. It will be interesting to explore whether BAX cluster growth is a regulated process or just an uncontrolled consequence of its oligomerization and whether this has functional consequences beyond the regulation of BAK assembly shown here. In this regard, Adar et al. recently reported the presence of BAX "sponge" assemblies next to mitochondria at late stages of apoptosis (Ader et al., 2019) that may be the result of such large BAX oligomers reshaping and sequestrating outer membrane patches for membrane rupture.

Yet, unexpectedly, we found that the difference in the rate of assembly between BAX and BAK, and not their final pore size, is determinant for the timing of mtDNA release and, consequently, cGAS/STING pathway induction when caspase activity is perturbed. Another key discovery of our study is the reciprocal regulation of BAX and BAK during the growth of the apoptotic pore by co-assembly into the same supra-molecular line, arc, and ring-like structures. BAX slows down apoptotic cluster growth, yet it participates in and reshapes the architecture of BAK pores, which then reach bigger sizes at later stages of MOMP. In turn, BAK accelerates the kinetics of BAX foci assembly, likely by providing seeding points at the membrane. Although in the cellular context BAK is not essential for BAX

Figure 5. Reciprocal contribution of BAK and BAX to their assembly kinetics and molecularity

(A) Representative photon-counting confocal images of BAX/BAK KO U2OS cells transfected with mEGFP-BAX or mEGFP-BAK, respectively, after apoptosis induction by ABT-737, S63845, and qVD-OPh. Time points are after Smac-mCherry release. Scale bars, 10 μm.

(B) Comparison of the expression levels of mEGFP-BAK and mEGFP-BAX in single or double BAK/BAX KO cells detected by western blot (upper) or by single-cell (individual dots in the plot) fluorescent intensity analysis of mEGFP signal (bottom). WT, wild type.The error bars correspond to the SD from the different experiments.

(C and D) Representative foci intensity distribution, in stoichiometric units, at different time points in an apoptotic BAX (C) and BAK (D) KO cell expressing mEGFP-BAX or mEGFP-BAK, respectively.

(E) Average foci intensity obtained from the fitting of foci distributions as in (C and D) at each time point for individual apoptotic cells expressing mEGFP-BAX (orange, n = 5) or mEGFP-BAK (green, n = 9).

(F and G) Comparison between the average foci intensity of mEGFP-BAK in BAX/BAK DKO (blue, n = 9) and BAK KO (green, n = 9) cells over time (F) and of mEGFP-BAX in BAX/BAK DKO (yellow, n = 9) and BAX KO (orange, n = 5) cells over time (G). *p < 0.1 (unpaired t test with Welch's correction).

(H) Number of mEGFP-BAX (orange, n = 5) and mEGFP-BAK (green, n = 9) foci per mitochondrial area in single KO cells over time (total number of events per cell as in C and D). For (E–H), lines in the graph correspond to the average values from all measured cells and colored areas correspond to data variability from single cells (mean ± SD).

(I) Average size of the different structural parameters for mEGFP-BAK assemblies in BAX/BAK DKO (n = 7) and BAK KO (n = 6) cells measured by SMLM. Error corresponds to SD.

(J) Distribution of the different BAK structure types found in BAX/BAK DKO (n = 7) and BAK KO (n = 6) cells (minimum number of analyzed structure type = 86).

(K–M) Comparison of the quantifications of the ring radius (K), arc radius (L), and arc length (M). Number of analyzed structures in single and double KO cells, respectively: 86 and 109 (K), 310 and 363 (L), and 310 and 363 (M).

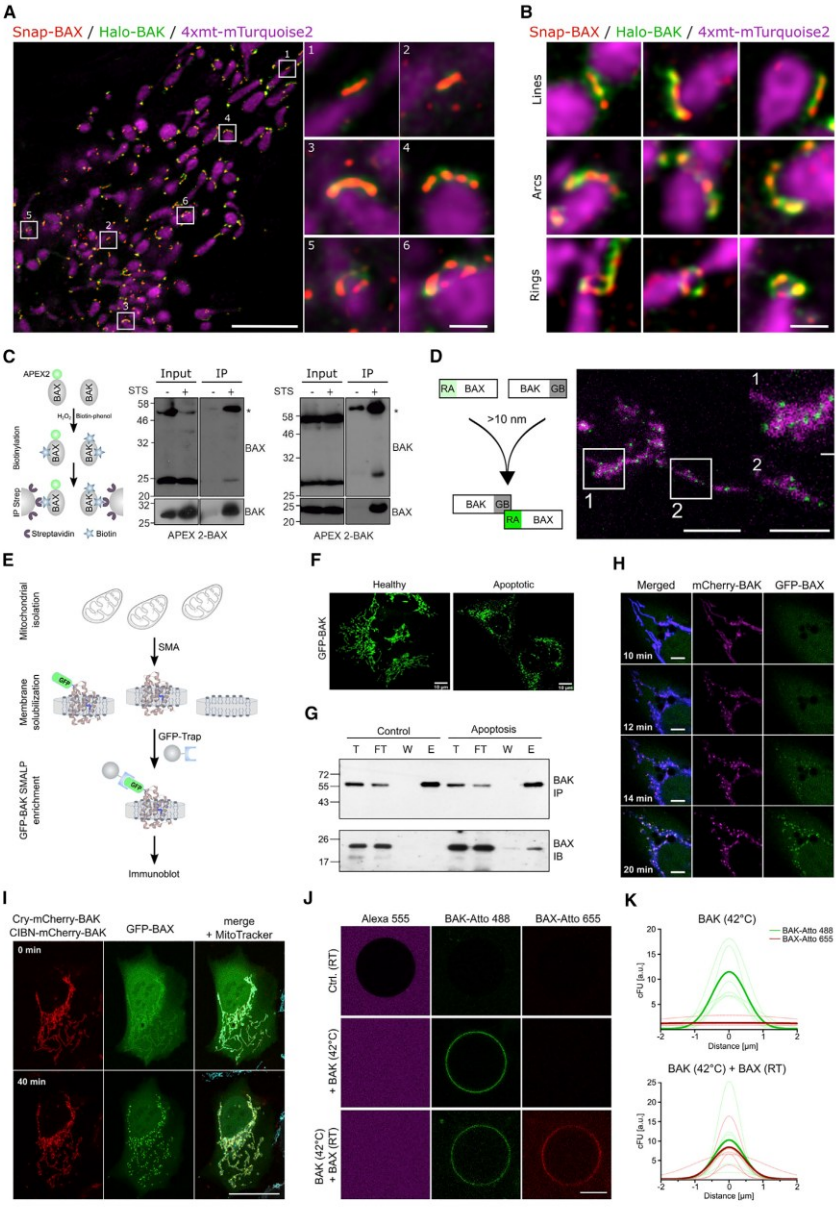

(legend on next page)

activation (Chen et al., 2015; Ma et al., 2014; Chin et al., 2018), our experiments with optogenetic control in cells and with minimal systems in GUVs demonstrate direct activation of BAX by BAK. Importantly, the two-color super-resolution imaging provides a direct visualization of individual apoptotic pores containing both BAX and BAK molecules at mitochondria.

As a result of this functional interplay between BAX and BAK, their relative expression levels control not only apoptosis sensitivity, but also the dynamics of the orderly release of mitochondrial contents during MOMP, and thereby the activation of downstream pathways. We show that the timing of mtDNA release resulting from the differential assembly rate of BAX and BAK can impact the activation of cGAS/STING signaling in a cell-autonomous manner and promotes the expression of activation markers in bystander T helper cells in a paracrine fashion. A recent study reported that mtDNA triggered IFN production in a model of radiation therapy in breast cancer cells leading to immunogenic cell death and revealed that caspase activation after MOMP does not provide sufficient proteolytic activity to dampen IFN signaling in this context (McArthur and Kile, 2020; Yamazaki et al., 2020). Considering this, our findings suggest that the regulation of apoptotic pore growth by BAX and BAK upon MOMP enables tuning the timing and extent of caspase activation with respect to cGAS/STING signaling with an impact on inflammatory responses.

In summary, here, we show that BAX and BAK present distinct oligomerization properties during apoptosis and that they regulate each other. As a result, their co-assembly into the same supra-molecular structures modulates the relative kinetics of mitochondrial content release. This dynamic interplay between BAX and BAK provides an additional level of regulation for the growth of the apoptotic pore, which, as we directly visualized here, is formed by both BAX and BAK molecules. Our findings support a model in which BAK facilitates the fast recruitment and activation of BAX in the early stages of MOMP, while, once in the membrane, BAX sustains the slower accumulation of additional BAX molecules to growing pores. As a result, the co-assembly of BAX and BAK tunes the kinetics of mtDNA release relative to Smac, which impacts the downstream cGAS/STING signaling and bystander immune cells.

Limitations of the study

Here, we show that BAX and BAK present distinct assembly properties that affect the relative timing of release of mitochondrial content. Yet, considering the overall similarity of BAX and BAK structures, the structural basis for these dynamic differences remains an open question, and it will require further structural investigation of the macromolecular complexes they form with atomic resolution. While our results with the oligomerization defective BAX mutant suggest a link between the supra-molecular assembly and permeabilization to larger content, like mtDNA, we could not find a clear-cut temporal evolution from lines, to arcs and to rings due to technical challenges. It thus remains to be determined whether the different structures detected for BAK and BAX are all relevant for MOMP and what makes the different shapes happen.

In addition, the use of overexpressed GFP-fused BAX or BAK constructs in the DKO and single KO cell lines to study the assembly of BAX/BAK on mitochondria could alter the extent of oligomerization. While overexpression of BAX and BAK is not very high because cells expressing large amounts of these proteins die, the use of genome editing to label endogenous BAX and BAK is certainly a route to address this issue. Along these

Figure 6. Recruitment of BAX by BAK and BAX-BAK co-localization

(A) Live-cell STED super-resolution microscopy in BAX/BAK DKO U2OS cell transfected with Snap-BAX (red), Halo-BAK (green) and 4xmt-mTurquoise (magenta, confocal) to stain mitochondria after apoptosis induction. Zoomed images (right) correspond to crops of the overview image (left) as indicated by numbers. Scale bars, 5 μm and 500 nm for cropped images.

(B) Gallery of BAX and BAK line, arc, and ring structures in apoptotic mitochondria by STED microscopy. Scale bars, 500 nm. Images in (A) and (B) are representative of three independent experiments.

(C) (Left) Scheme of proximity-dependent labeling with APEX2 (see STAR Methods). (Central and right) Immunoblots of streptavidin immunoprecipitation of APEX2-BAX (central) or APEX2-BAK (right) from apoptotic HeLa cells expressing FLAG-APEX2-BAX or FLAG-APEX2-BAK. Immunoblots are representative of two independent experiments. Only regions of the gel with bands of interest are shown for clarity.

(D) (Left) Principle of dimerization-dependent fluorescent protein (ddFP). RA only becomes fluorescence when it is in complex with GB. (Right) Representative confocal microscopy image of a BAX/BAK DKO U2OS cell transfected with GB-BAK, RA-BAX, and Mito-BFP (magenta) after apoptosis induction. Zoomed images correspond to cropped regions as indicated. The interaction between BAX and BAK (green dots) takes place in mitochondria upon apoptosis (negative control for collisions is not shown, it was tested in independent experiments). Scale bars, 10 μm; crop, 5 μm. Images are representative of two independent experiments.

(E) Schematic representation of sample preparation for SMALPs pull-down assay (see STAR Methods).

(F) Representative healthy (control) or apoptotic cells transfected with mEGFP-BAK (green) used in the assay.

(G) Immunoblots of SMALPs immunoprecipitation of GFP-BAK and pull-down of endogenous BAX. Immunoblots show total input (T), flow through (FT), wash (W), and elution (E) fractions of the immunoprecipitation and are representative of three independent experiments. IB, immunoblot; IP, immunoprecipitation. Only regions of the gel with bands of interest are shown for clarity.

(H) Representative confocal microscopy image of a BAX/BAK DKO U2OS cell transfected with mCherry-BAK (magenta), mEGFP-BAX (green), and Tomm20-BFP (blue) at indicated time points after apoptosis induction showing BAK foci appearing before BAX foci. Scale bars, 10 μm. Images are representative of three independent experiments.

(I) Representative confocal microscopy image of optogenetic activation of BAK and recruitment of BAX to apoptotic mitochondria (MitoTrackerTM Deep Red FM, cyan). Scale bars, 20 μm. Images are representative of 4 independent experiments.

(J) Representative images of BAK (green) activation followed by BAX (red) recruitment on a GUV (black hole). Alexa 555 (magenta) is used as a soluble dye to detect GUV permeabilization. Scale bars, 10 μm. Images are representative of 3 independent experiments.

(K) Quantification of the binding of BAK-Atto 488 (green) and BAX-Atto 655 (red) to GUVs by radial profile corrected fluorescence intensity (cFU) measurements. Thin lines indicate individual measurements and thick lines correspond to the average of n = 7 individual GUVs from n = 3 independent experiments. See also Figure S7.

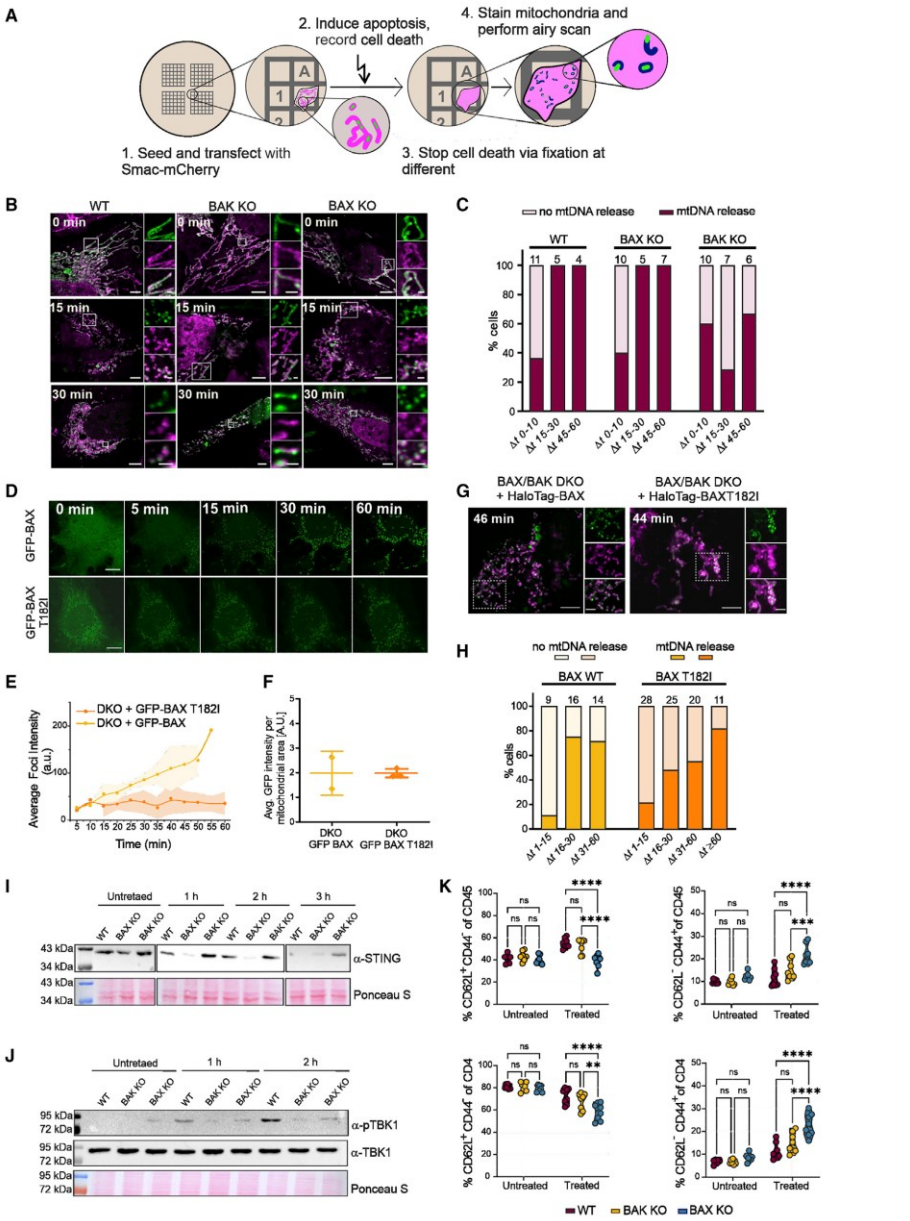

(legend on next page)

lines, although we cannot exclude that the recruitment of BAX might be amplified by BAK overexpression, this does not change our conclusion about the ability of active BAK to recruit BAX.

Finally, regarding the initial stages of BAX and BAK assembly in cells at the moment of Smac release, we could only detect the first clusters, already with several tens of units, a few minutes later. The inability to visualize BAX and BAK oligomers preceding MOMP is common to other studies (Maes et al., 2017; Riley et al., 2018; McArthur et al., 2018) and could be due to technical limitations in detecting the fluorescence signal of fast-assembling small oligomers due to low contrast with the background. Although the question about the minimal number of BAX/BAK sufficient to initiate the apoptosis cascade remains open, it is now evident that the BAX and BAK higher-order oligomers characterized here are functionally relevant for mtDNA release in apoptosis (McArthur et al., 2018; Riley et al., 2018). Further methodological developments will hopefully allow tackling these relevant questions in the future.

STAR★METHODS

Detailed methods are provided in the online version of this paper and include the following:

- KEY RESOURCES TABLE
- RESOURCE AVAILABILITY
  - Lead contact
  - Materials availability
  - Data and code availability
- EXPERIMENTAL MODEL AND SUBJECT DETAILS
  - Cell culture
  - Isolation of spleenocytes
- METHOD DETAILS
  - Plasmids and antibodies
  - Protein purification and labelling
  - Western blotting
  - Supported lipid bilayers (SLBs)
  - GUV permeabilization assay
  - Atomic force microscopy
  - TIRF microscopy
  - Stoichiometry determination
  - Analysis of BAX/BAK assembly kinetics
  - Stoichiometry analysis by ratiometric approach
  - Measurement of protein expression level
  - SMLM and Correlative fluorescence/SMLM imaging
  - Live cell STED microscopy
  - Proximity-dependent labeling with APEX2
  - Dimerization-dependent fluorescent protein
  - Immunoprecipitation of GFP-BAK-containing SMALPs
  - Confocal imaging for optogenetic measurements
  - BAX and BAK recruitment to GUVs
  - mtDNA release
  - Flow cytometry
  - Coculture experiments
- QUANTIFICATION AND STATISTICAL ANALYSIS

SUPPLEMENTAL INFORMATION

Supplemental information can be found online at https://doi.org/10.1016/j.molcel.2022.01.008.

ACKNOWLEDGMENTS

We thank Andreas Villunger for helpful discussions and Stephen Tait for providing SVEC cells. We thank Carolin Stegmüller for technical support. K.C. acknowledges the Eliteprogramme for Postdocs of the Baden-Württemberg Stiftung for financial support. This work was funded by the European Research Council (ERC-CoG 817758 to A.J.G.S. and ERC-CoG 724489 to J.R.) and partially supported by the Deutsche Forschungsgemeinschaft (CRC1403 project A02, CRC1218 project A09, and GRK2364/1 MOMbrane).

AUTHOR CONTRIBUTIONS

A.J.G.S. designed research with K.C., A.J., and V.H. V.H. performed the super-resolution microcopy experiments and analyzed the data with the help of M.M. and J.R. K.C. performed the stoichiometry and the AFM experiments and analyzed the data. K.C., A.J., A.P.-B., and N.W. performed the stoichiometry

Figure 7. BAK pores enable faster mtDNA release and downstream inflammatory responses than BAX pores

(A) Scheme of the experimental setup to investigate the kinetics of mtDNA release (green) after Smac(1-60)-mCherry (magenta) release by airy scan super-resolution microscopy.

(B) Representative airy scan microscopy images of WT, BAK KO, and BAX KO U2OS cells transfected with Smac-(1-60)-mCherry, Tfam-GFP (green) and immunostained for Tomm20 (magenta) without induction of apoptosis (0 min) and 15 and 30 min after Smac(1-60)-mCherry release. Cropped panels on the right represent zoomed region of the white box in the main image. Scale bars, 5 μm and 1 μm for the main and zoomed images, respectively.

(C) Percentage of cells with mtDNA release at different time points after Smac release. Numbers of analyzed cells (n) is on top of the bar graphs.

(D) Representative photon-counting confocal images of BAX/BAK DKO U2OS cells transfected with mEGFP-BAX or mEGFP-BAX(T182I), after apoptosis induction. Time points are after Smac-mCherry release. Scale bars, 10 μm.

(E) Average foci intensity at each time point for individual apoptotic cells expressing mEGFP-BAX (yellow, n = 2) or mEGFP-BAX(T182I) (orange, n = 3). Lines in the graph correspond to the average values from all measured cells and colored areas to data variability (mean ± SD).

(F) Average mEGFP expression level detected by single-cell fluorescent intensity analysis per mitochondrial area in the individual cells (represented by individual dots in the plot) analyzed in (E). The error bars correspond to the SD from the different experiments.

(G) Representative airy scan microscopy images of cells transfected with Smac-(1-60)-mCherry, HaloTag-BAX or HaloTag-BAX(T182I), Tfam-GFP (green) and immunostained for Tomm20 (magenta) at indicated time points after Smac release. Cropped panels on the right are zoomed region of the white box in the main image. Scale bars, 5 and 2 μm for the main and zoomed images, respectively.

(H) Percentage of cells with mtDNA release at different time points after Smac release. Numbers of analyzed cells (n) is presented on top of the bar graphs.

(I and J) STING degradation (I) and TBK1 phosphorylation (J) in WT, BAX KO, and BAK KO U2OS cells at 0 (untreated), 1, 2, and 3 h after apoptosis induction. Only regions of the gel with bands of interest are shown for clarity.

(K) Changes of CD62L and CD44 expression in spleenocytes ($CD45^+$, top row) and $CD4^+$ T cells (bottom row) with SVEC cells either untreated or pre-treated with ABT-737, S63845 and QVD for 3 h. Two-way ANOVA and Sidak multiple comparison test was used for the statistical analyses. n = 8 spleen donors. $^{**}p < 0.01$, $^{***}p < 0.001$, $^{****}p < 0.0001$. See also Figure S8.

experiments in cells and analyzed the data. A.J. performed the recruitment and STING pathway experiments. A.J. and T.D. performed the STED experiments. M.G. performed the coculture experiments and flow cytometry analysis. A.P.-B. performed the APEX2 and the ddFP experiments. S.D. performed the pull-down experiments with SMALPs. J.D. developed software for data detection and analysis. K.C., V.H., and T.D. performed the mtDNA release experiments and analyzed the data. J.V.T. and J.R. supplied materials. A.J.G.S. conceived the project and supervised research. A.J.G.S., K.C., V.H., and A.J. wrote the manuscript with the help of all other authors.

DECLARATION OF INTERESTS

The authors declare no competing interests.

Received: February 27, 2021
Revised: November 14, 2021
Accepted: January 10, 2022
Published: February 3, 2022

REFERENCES

Ader, N.R., Hoffmann, P.C., Ganeva, I., Borgeaud, A.C., Wang, C., Youle, R.J., and Kukulski, W. (2019). Molecular and topological reorganizations in mitochondrial architecture interplay during BAX-mediated steps of apoptosis. Elife *8*, e40712.

Bleicken, S., Classen, M., Padmavathi, P.V., Ishikawa, T., Zeth, K., Steinhoff, H.-J., and Bordignon, E. (2010). Molecular details of Bax activation, oligomerization, and membrane insertion. J. Biol. Chem. *285*, 6636–6647.

Bleicken, S., Landeta, O., Landajuela, A., Basañez, G., and García-Sáez, A.J. (2013a). Proapoptotic BAX and BAK proteins form stable protein-permeable pores of tunable size. J. Biol. Chem. *288*, 33241–33252.

Bleicken, S., Wagner, C., and García-Sáez, A.J. (2013b). Mechanistic differences in the membrane activity of BAX and BCL-XL correlate with their opposing roles in apoptosis. Biophys. J. *104*, 421–431.

Chen, H.C., Kanai, M., Inoue-Yamauchi, A., Tu, H.C., Huang, Y., Ren, D., Kim, H., Takeda, S., Reyna, D.E., Chan, P.M., et al. (2015). An interconnected hierarchical model of cell death regulation by the BCL-2 family. Nat. Cell Biol. *17*, 1270–1281.

Cheng, E.H., Sheiko, T.V., Fisher, J.K., Craigen, W.J., and Korsmeyer, S.J. (2003). VDAC2 inhibits BAK activation and mitochondrial apoptosis. Science *301*, 513–517.

Chin, H.S., Li, M.X., Tan, I.K.L., Ninnis, R.L., Reljic, B., Scicluna, K., Dagley, L.F., Sandow, J.J., Kelly, G.L., Samson, A.L., et al. (2018). VDAC2 enables BAX to mediate apoptosis and limit tumor development. Nat. Commun. *9*, 4976.

Cosentino, K., and García-Sáez, A.J. (2017). BAX and BAK pores: are we closing the circle? Trends Cell Biol *27*, 266–275.

Czabotar, P.E., Lessene, G., Strasser, A., and Adams, J.M. (2014). Control of apoptosis by the BCL-2 protein family: implications for physiology and therapy. Nat. Rev. Mol. Cell Biol. *15*, 49–63.

Danial, J.S.H., and Garcia-Saez, A.J. (2019). Quantitative analysis of super-resolved structures using ASAP. Nat. Methods *16*, 711–714.

Danial, J.S.H., Quintana, Y., Ros, U., Shalaby, R., Margheritis, E.G., Ramirez, S.C., Ungermann, C., Garcia-Saez, A.J., and Cosentino, K. (2022). Systematic assessment of the accuracy of subunit counting in biomolecular complexes using automated single molecule brightness analysis. J. Phys. Chem. Lett. *13*, 822–829.

Desagher, S., Osen-Sand, A., Nichols, A., Eskes, R., Montessuit, S., Lauper, S., Maundrell, K., Antonsson, B., and Martinou, J.-C. (1999). Bid-induced conformational change of Bax is responsible for mitochondrial cytochrome *c* release during apoptosis. J. Cell Biol. *144*, 891–901.

Ding, Y., Li, J., Enterina, J.R., Shen, Y., Zhang, I., Tewson, P.H., Mo, G.C., Zhang, J., Quinn, A.M., Hughes, T.E., et al. (2015). Ratiometric biosensors based on dimerization-dependent fluorescent protein exchange. Nat. Methods *12*, 195–198.

Edlich, F., Banerjee, S., Suzuki, M., Cleland, M.M., Arnoult, D., Wang, C., Neutzner, A., Tjandra, N., and Youle, R.J. (2011). BCL-X(L) retrotranslocates Bax from the mitochondria into the cytosol. Cell *145*, 104–116.

Finan, K., Raulf, A., and Heilemann, M. (2015). A set of homo-oligomeric standards allows accurate protein counting. Angew. Chem. Int. Ed. Engl. *54*, 12049–12052.

Giampazolias, E., Zunino, B., Dhayade, S., Bock, F., Cloix, C., Cao, K., Roca, A., Lopez, J., Ichim, G., Proïcs, E., et al. (2017). Mitochondrial permeabilization engages NF-κB-dependent anti-tumour activity under caspase deficiency. Nat. Cell Biol. *19*, 1116–1129.

Große, L., Wurm, C.A., Brüser, C., Neumann, D., Jans, D.C., and Jakobs, S. (2016). BAX assembles into large ring-like structures remodeling the mitochondrial outer membrane in apoptosis. EMBO J *35*, 402–413.

Hermann, E., Bleicken, S., Subburaj, Y., and García-Sáez, A.J. (2014). Automated analysis of giant unilamellar vesicles using circular Hough transformation. Bioinformatics *30*, 1747–1754.

Iyer, S., Uren, R.T., Dengler, M.A., Shi, M.X., Uno, E., Adams, J.M., Dewson, G., and Kluck, R.M. (2020). Robust autoactivation for apoptosis by BAK but not BAX highlights BAK as an important therapeutic target. Cell Death Dis *11*, 268.

Jenner, A., Shalaby, R., and Cosentino, K. (2020). Chapter 3. Quantitative single-molecule imaging of protein assembly in membranes. In Advances in Biomembranes and Lipid Self-Assembly, A. Iglič, M. Rappolt, and A.J. García-Sáez, eds. (Academic Press).

Kale, J., Osterlund, E.J., and Andrews, D.W. (2018). BCL-2 family proteins: changing partners in the dance towards death. Cell Death Differ *25*, 65–80.

Kuwana, T., King, L.E., Cosentino, K., Suess, J., García-Sáez, A.J., Gilmore, A.P., and Newmeyer, D.D. (2020). Mitochondrial residence of the apoptosis inducer BAX is more important than BAX oligomerization in promoting membrane permeabilization. J. Biol. Chem. *295*, 1623–1636.

Lam, S.S., Martell, J.D., Kamer, K.J., Deerinck, T.J., Ellisman, M.H., Mootha, V.K., and Ting, A.Y. (2015). Directed evolution of APEX2 for electron microscopy and proximity labeling. Nat. Methods *12*, 51–54.

Lee, S.C., Knowles, T.J., Postis, V.L.G., Jamshad, M., Parslow, R.A., Lin, Y.-P., Goldman, A., Sridhar, P., Overduin, M., Muench, S.P., et al. (2016). A method for detergent-free isolation of membrane proteins in their local lipid environment. Nat. Protoc. *11*, 1149–1162.

Leshchiner, E.S., Braun, C.R., Bird, G.H., and Walensky, L.D. (2013). Direct activation of full-length proapoptotic BAK. Proc. Natl. Acad. Sci. USA *110*, E986–E995.

Liße, D., Monzel, C., Vicario, C., Manzi, J., Maurin, I., Coppey, M., Piehler, J., and Dahan, M. (2017). Engineered ferritin for magnetogenetic manipulation of proteins and organelles inside living cells. Adv. Mater. *29*, 1700189.

Lindsten, T., Ross, A.J., King, A., Zong, W.X., Rathmell, J.C., Shiels, H.A., Ulrich, E., Waymire, K.G., Mahar, P., Frauwirth, K., et al. (2000). The combined functions of proapoptotic BCL-2 family members BAK and BAX are essential for normal development of multiple tissues. Mol. Cell *6*, 1389–1399.

Ma, S.B., Nguyen, T.N., Tan, I., Ninnis, R., Iyer, S., Stroud, D.A., Menard, M., Kluck, R.M., Ryan, M.T., and Dewson, G. (2014). Bax targets mitochondria by distinct mechanisms before or during apoptotic cell death: a requirement for VDAC2 or BAK for efficient BAX apoptotic function. Cell Death Differ *21*, 1925–1935.

Maes, M.E., Schlamp, C.L., and Nickells, R.W. (2017). Live-cell imaging to measure BAX recruitment kinetics to mitochondria during apoptosis. PLoS One *12*, e0184434.

Mcarthur, K., and Kile, B.T. (2020). Apoptotic mitochondria prime anti-tumour immunity. Cell Death Discov *6*, 98.

Mcarthur, K., Whitehead, L.W., Heddleston, J.M., Li, L., Padman, B.S., Oorschot, V., Geoghegan, N.D., Chappaz, S., Davidson, S., San Chin, H., et al. (2018). BAK/BAX macropores facilitate mitochondrial herniation and mtDNA efflux during apoptosis. Science *359*, eaao6047.

Nasu, Y., Benke, A., Arakawa, S., Yoshida, G.J., Kawamura, G., Manley, S., Shimizu, S., and Ozawa, T. (2016). *In situ* characterization of BAK clusters responsible for cell death using single molecule localization microscopy. Sci. Rep. *6*, 27505.

Ovesný, M., Křížek, P., Borkovec, J., Švindrych, Z., and Hagen, G.M. (2014). ThunderSTORM: a comprehensive ImageJ plug-in for PALM and STORM data analysis and super-resolution imaging. Bioinformatics *30*, 2389–2390.

Riley, J.S., Quarato, G., Cloix, C., Lopez, J., O'Prey, J., Pearson, M., Chapman, J., Sesaki, H., Carlin, L.M., Passos, J.F., et al. (2018). Mitochondrial inner membrane permeabilisation enables mtDNA release during apoptosis. EMBO J *37*, e99238.

Rongvaux, A., Jackson, R., Harman, C.C.D., Li, T., West, A.P., De Zoete, M.R., Wu, Y., Yordy, B., Lakhani, S.A., Kuan, C.-Y., et al. (2014). Apoptotic caspases prevent the induction of type I interferons by mitochondrial DNA. Cell *159*, 1563–1577.

Salvador-Gallego, R., Mund, M., Cosentino, K., Schneider, J., Unsay, J., Schraermeyer, U., Engelhardt, J., Ries, J., and García-Sáez, A.J. (2016). Bax assembly into rings and arcs in apoptotic mitochondria is linked to membrane pores. EMBO J *35*, 389–401.

Sarosiek, K.A., Chi, X., Bachman, J.A., Sims, J.J., Montero, J., Patel, L., Flanagan, A., Andrews, D.W., Sorger, P., and Letai, A. (2013). BID preferentially activates BAK while BIM preferentially activates BAX, affecting chemotherapy response. Mol. Cell *51*, 751–765.

Schellenberg, B., Wang, P., Keeble, J.A., Rodriguez-Enriquez, R., Walker, S., Owens, T.W., Foster, F., Tanianis-Hughes, J., Brennan, K., Streuli, C.H., et al. (2013). BAX exists in a dynamic equilibrium between the cytosol and mitochondria to control apoptotic priming. Mol. Cell *49*, 959–971.

Singh, R., Letai, A., and Sarosiek, K. (2019). Regulation of apoptosis in health and disease: the balancing act of BCL-2 family proteins. Nat. Rev. Mol. Cell Biol. *20*, 175–193.

Subburaj, Y., Cosentino, K., Axmann, M., Pedrueza-Villalmanzo, E., Hermann, E., Bleicken, S., Spatz, J., and García-Sáez, A.J. (2015). Bax monomers form dimer units in the membrane that further self-assemble into multiple oligomeric species. Nat. Commun. *6*, 8042.

Thevathasan, J.V., Kahnwald, M., Cieśliński, K., Hoess, P., Peneti, S.K., Reitberger, M., Heid, D., Kasuba, K.C., Hoerner, S.J., Li, Y., et al. (2019). Nuclear pores as versatile reference standards for quantitative superresolution microscopy. Nat. Methods *16*, 1045–1053.

Todt, F., Cakir, Z., Reichenbach, F., Emschermann, F., Lauterwasser, J., Kaiser, A., Ichim, G., Tait, S.W.G., Frank, S., Langer, H.F., et al. (2015). Differential retrotranslocation of mitochondrial BAX and BAK. EMBO J *34*, 67–80.

Ulbrich, M.H., and Isacoff, E.Y. (2007). Subunit counting in membrane-bound proteins. Nat. Methods *4*, 319–321.

Unsay, J.D., Cosentino, K., Sporbeck, K., and García-Sáez, A.J. (2017). Pro-apoptotic cBid and Bax exhibit distinct membrane remodeling activities: an AFM study. Biochim. Biophys. Acta Biomembr. *1859*, 17–27.

Van Delft, M.F., Chappaz, S., Khakham, Y., Bui, C.T., Debrincat, M.A., Lowes, K.N., Brouwer, J.M., Grohmann, C., Sharp, P.P., Dagley, L.F., et al. (2019). A small molecule interacts with VDAC2 to block mouse BAK-driven apoptosis. Nat. Chem. Biol. *15*, 1057–1066.

Verdaasdonk, J.S., Lawrimore, J., and Bloom, K. (2014). Determining absolute protein numbers by quantitative fluorescence microscopy. Methods Cell Biol *123*, 347–365.

Wei, M.C., Zong, W.X., Cheng, E.H., Lindsten, T., Panoutsakopoulou, V., Ross, A.J., Roth, K.A., MacGregor, G.R., Thompson, C.B., and Korsmeyer, S.J. (2001). Proapoptotic BAX and BAK: a requisite gateway to mitochondrial dysfunction and death. Science *292*, 727–730.

Westphal, D., Kluck, R.M., and Dewson, G. (2014). Building blocks of the apoptotic pore: how BAX and BAK are activated and oligomerize during apoptosis. Cell Death Differ *21*, 196–205.

White, M.J., Mcarthur, K., Metcalf, D., Lane, R.M., Cambier, J.C., Herold, M.J., Van Delft, M.F., Bedoui, S., Lessene, G., Ritchie, M.E., et al. (2014). Apoptotic caspases suppress mtDNA-induced STING-mediated type I IFN production. Cell *159*, 1549–1562.

Yamazaki, T., Kirchmair, A., Sato, A., Buqué, A., Rybstein, M., Petroni, G., Bloy, N., Finotello, F., Stafford, L., Navarro Manzano, E., et al. (2020). Mitochondrial DNA drives abscopal responses to radiation that are inhibited by autophagy. Nat. Immunol. *21*, 1160–1171.

Zhou, L., and Chang, D.C. (2008). Dynamics and structure of the BAX-BAK complex responsible for releasing mitochondrial proteins during apoptosis. J. Cell Sci. *121*, 2186–2196.

STAR★METHODS

KEY RESOURCES TABLE

REAGENT or RESOURCE	SOURCE	IDENTIFIER
Antibodies		
Alpaca anti-GFP VHH sdAb AF647 (anti-GFP nanobody-AF647) 1:2000 dilution	Chromotec (home labeled)	Cat#gt-250
Rabbit polyclonal anti-BAX 1:1000 dilution	Cell Signaling Technology	Cat#2772; RRID: AB_10695870
Rabbit monoclonal anti-BAX (D2E11) 1:1000 dilution	Cell Signaling Technology	Cat#5023; RRID: AB_10557411
Mouse monoclonal anti-GFP 1:1000 dilution	ThermoFischer	Cat#MA5-15256; RRID: AB_10979281
Rabbit polyclonal anti-GAPDH 1:2500 dilution	abcam	Cat#ab9485; RRID: AB_307275
Goat polyclonal anti-Rabbit IgG-HRP 1:10000 dilution	Jackson Immuno Research	Cat#111-035-003; RRID: AB_2313567
Goat polyclonal anti-Mouse IgG-HRP 1:10000 dilution	Jackson Immuno Research	Cat# 115-035-003; RRID: AB_10015289
Camelid sdAb anti-GFP; Clones 1H1(FluoTag-Q anti-GFP Alexa Fluor 647) 1:2000 dilution	NanoTag Biotechnologies	Cat#N0301
Goat polyclonal anti-Rabbit (AF633) 1:200 dilution	ThermoFisher	Cat#A-21070; RRID: AB_2535731
Rabbit monoclonal anti-Tom20 (D8T4N) 1:100 dilution	Cell Signaling Technology	Cat#42406; RRID: AB_2687663
Mouse anti-Cytc 1:1000 dilution	BD Biosciences	Cat#556433; RRID: AB_396417
Mouse monoclonal anti-GAPDH (D4C6R) 1:1000 dilution	Cell Signaling Technology	Cat#97166; RRID: AB_2756824
Rabbit anti-IMMT 1:1000 dilution	Proteintech	10179-AP; RRID: AB_2127193
Rabbit polyclonal anti-PARP 1:1000 dilution	Cell Signaling Technology	Cat#9542; RRID: AB_2160739
Rabbit monoclonal anti-pTBK1/NAK (Ser172) (D52C2)1:1000 dilution	Cell Signaling Technology	Cat#5483; RRID: AB_10693472
Rabbit monoclonal anti-TBK1/NAK (D1B4) 1:1000 dilution	Cell Signaling Technology	Cat#3504; RRID: AB_2255663
Rabbit monoclonal anti-STING (D2P2F) 1:1000 dilution	Cell Signaling Technology	Cat#13647; RRID: AB_2732796
PerCP/Cyanine5.5 Rat anti-mouse Ly-6C 1:200 dilution	Biolegend	Cat#128011; RRID: AB_1659242
Alexa Fluor 488 Rat anti-mouse/human CD44 1:800 dilution	Biolegend	Cat#103016; RRID: AB_493679
Alexa Fluor 647 Mouse anti-mouse NK-1.1 1:200 dilution	Biolegend	Cat#108719; RRID: AB_493186
Alexa Fluor 700 Rat anti-mouse CD4 1:100 dilution	Biolegend	Cat#100536; RRID: AB_493701
Super Bright 702 Rat monoclonal anti-CD45 (30-F11)1:200 dilution	ThermoFischer	Cat#67-0451-82; RRID: AB_2662424
Brilliant Violet 785 Rat anti-mouse CD62L 1:800 dilution	Biolegend	Cat#104440; RRID: AB_2629685

(*Continued on next page*)

Continued

REAGENT or RESOURCE	SOURCE	IDENTIFIER
Brilliant Violet 650 Armenian Hamster anti-mouse CD80 1:400 dilution	Biolegend	Cat#104732; RRID: AB_2686972
Brilliant Violet 421 Rat anti-mouse/human CD11b 1:400 dilution	Biolegend	Cat#101251; RRID: AB_2562904
Brilliant Violet 510 Rat anti-mouse CD8a 1:200 dilution	Biolegend	Cat#100752; RRID: AB_2563057
Super Bright 600 Rat monoclonal anti-CD45R (B220) (RA3-6B2) 1:200 dilution	ThermoFischer	Cat#63-0452-82; RRID: AB_2637457
PE-Cy7 Hamster anti-mouse CD11c 1:400 dilution	BD Biosciences	Cat#561022; RRID: AB_647251
PE Rat anti-mouse Ly-6G 1:800 dilution	Biolegend	Cat#127607; RRID: AB_1186104
PE/Dazzle 594 Rat anti-mouse I-A/I-E 1:800 dilution	Biolegend	Cat#107647; RRID: AB_2565978
Rat anti-mouse CD16/CD32 1:50 dilution	BD Biosciences	Cat#553142; RRID: AB_394656
Bacterial and virus strains		
BL21 (DE3) RIPL	Stratagene (available via Agilent)	Cat#230280
Chemicals, peptides, and recombinant proteins		
Egg PC	OttoNordwald (Avanti)	Cat#840051C
Cardiolipin	Sigma	Cat#C0563
DiI stain	ThermoFischer	Cat#D3911
S63845	Hölzel	Cat#HY-100741
ABT-737	Hölzel	Cat#HY-50907
Q-VD-OPh	Hölzel	Cat#HY-12305g
Staurosporine	LC laboratories (USA)	Cat#S3900
GLUCOSE OXIDASE TYPE VII	Sigma	Cat#G2133-10KU
Cysteamine-Hydrochlorid (MEA)	Sigma	Cat#95294-1L
Catalase	Merck	Cat#219261-100KU
SNAP-cell 647SiR	NEB	Cat#S9102S
Janelia Fluor® 549 HaloTag® Ligand	Promega	Cat#GA1110
Live Cell Imaging Solution	ThermoFischer	Cat#A14291DJ
Pierce™ Streptavidin Magnetic Beads	ThermoFischer	Cat#88817
GFP Trap agarose beads	Chromotek	Cat#X336.1
XIRAN® (SMA2:1)	Polyscope	Cat#SZ30010
Critical commercial assays		
Live/Dead fixable Near-IR Cell Stain Kit	ThermoFischer	Cat#L10119
Deposited data		
Raw western blot and microscopy data	Mendeley	doi: 10.17632/2gwcgpvwx5.1
Experimental models: Cell lines		
Human bone osteosarcoma cells: U2OS	Gift from S. Tait, Glasgow	https://doi.org/10.15252/embj.201899238
Human bone osteosarcoma cells: U2OS BAX $^{-/-}$ (U2OS BAX KO)	Gift from S. Tait, Glasgow	https://doi.org/10.15252/embj.201899238
Human bone osteosarcoma cells: U2OS BAK $^{-/-}$(U2OS BAK KO)	Gift from S. Tait, Glasgow	https://doi.org/10.15252/embj.201899238
Human bone osteosarcoma cells: U2OS BAX $^{-/-}$/BAK $^{-/-}$(U2OS BAX/BAK DKO)	Gift from S. Tait, Glasgow	https://doi.org/10.15252/embj.201899238

(*Continued on next page*)

Continued

REAGENT or RESOURCE	SOURCE	IDENTIFIER
Human bone osteosarcoma cells: U2OS NUP96-mEGFP	Available from CLS cell lines service GmbH	Cat#300174
Murine endothelial cells: SVEC 4–10	Gift from S. Tait, Glasgow	https://doi.org/10.15252/embj.201899238
Murine endothelial cells: SVEC 4–10 BAX -/-(SVEC BAX KO)	Gift from S. Tait, Glasgow	https://doi.org/10.15252/embj.201899238
Murine endothelial cells: SVEC 4–10 BAK -/-(SVEC BAK KO)	Gift from S. Tait, Glasgow	https://doi.org/10.15252/embj.201899238
Human colon cancer cells: HCT116 BAX ⁻/⁻/BAK ⁻/⁻(HCT116 BAX/BAK DKO)	Gift from K. Schulze-Osthoff, Tübingen	N/A
Spleenocytes extracted from female mice (C57BL/6N)	Available from The Jackson Laboratory	Cat#005304
Recombinant DNA		
pcDNA3_Smac1-60_mCherry	Gift from S. Tait, Glasgow	https://doi.org/10.15252/embj.201899238
mTagBFP2-TOMM20-N-10	Addgene	Cat#55328
pEGFP-A206K_BAX_C1 (mEGFP-BAX)	This manuscript	N/A
pEGFP-A206K_BAX(S184V) C1 (mEGFP-BAX(S184V))	This manuscript	N/A
pEGFP-A206K_BAX(T182I) C1 (mEGFP-BAX(T182I))	This manuscript	N/A
pEGFP_A206K_BAK_C1 (mEGFP-BAK)	This manuscript	N/A
pTYB21_mBAK-L192K, F193S, Y196D, C154S	This manuscript	N/A
pTYB1_hBAX-S4C,C62S, C126S	Previous study	https://doi.org/10.1038/ncomms9042
pTYB1 Bid WT	Previous study	https://doi.org/10.1038/ncomms9042
pEGFP-Tfam-GFP	This manuscript	N/A
pCRY2(1-531)-mCherry-BAK	Addgene	Cat#117238
pcDNA-CIBN-mCherry-BAK	This manuscript	N/A
pEGFP-N1-4xmt-mTurquoise2	Addgene	Cat#98819
pAcGFP-C1-SnapF-BAX	This manuscript	N/A
pAcGFP-C1-Halo7-BAK	This manuscript	N/A
pEGFP-Flag-APEX2-BAX	This manuscript	N/A
pEGFP-Flag-APEX2-BAK	This manuscript	N/A
pAcGFP-C1-RA-BAX	This manuscript	N/A
pAcGFP-C1-GB-BAK	This manuscript	N/A
Software and algorithms		
Stoichiometry Analysis Software (SAS)	https://doi.org/10.1021/acs.jpclett.1c03835	https://github.com/jdanial/SAS
GUVdetector software	https://doi.org/10.1093/bioinformatics/btu102	http://garcia-saez.cecad-labs.uni-koeln.de/GUV-software.864.0.html
ImageJ/FIJI	doi: 10.1038/nmeth.2019	https://imagej.net/software/fiji/
ThunderStorm	DOI: 10.1093/bioinformatics/btu202	https://code.google.com/p/thunder-storm/
Huygens Professional	Scientific Volume Imaging, Netherlands	http://svi.nl
Radial Profile Plot Plugin (ImageJ)	https://imagej.nih.gov/ij/plugins/radial-profile.html	N/A
GraphPad Prism 5.0	GraphPad	https://www.graphpad.com/scientific-software/prism/
Origin	OriginLab Corporation	https://www.originlab.com/
Python	https://www.python.org/	N/A

RESOURCE AVAILABILITY

Lead contact

Further information and requests for resources and reagents should be directed to and will be fulfilled by the lead contact, Ana J. García Sáez (ana.garcia@uni-koeln.de).

Materials availability

Plasmids generated in this study are available on request to the lead contact.

Data and code availability

- Original western blot images and microscopy data have been deposited as raw tiff files at Mendeley and are publicly available as of the date of publication. The DOI is listed in the key resources table. Additional data reported in this paper are available from the lead author upon request.
- The software code for the stoichiometry analysis software (SAS) (Danial et al., 2022) is available from github as indicated in the key resources table. DOIs of additional software used are listed in the key resources table.
- Any additional information required to reanalyze the data reported in this paper is available from the lead contact upon request.

EXPERIMENTAL MODEL AND SUBJECT DETAILS

Cell culture

WT, single BAX KO, single BAK KO, double BAX/BAK DKO and mEGFP-tagged NUP96 human osteosarcoma U2OS, WT, single BAX KO and BAK KO SVEC 4–10 murine endothelial and BAX/BAK DKO human colon carcinoma HCT116 cell lines were cultured at 37 °C and 5% CO_2 in DMEM (McCoy's 5A for HCT116) supplemented with 10% FBS and 1% penicillin/streptomycin (Invitrogen, Germany). BAX/BAK DKO cell lines ensured that no endogenous BAX and BAK was contributing to foci formation. Cells were transfected at 70–80% confluence. All cell lines used in this study were subjected to regular mycoplasma testing.

Isolation of spleenocytes

Spleenocytes were collected from 9-13 week old female mice (C57BL/6N). For preparation of single cell suspension, the spleens were minced through 40 μm cellstrainer using a plunger and PBS for flushing. The single cell suspension was then centrifuged at 300 x g for 5 minutes, followed by supernatant removal and treatment with 1 mL ACK buffer (A1049201, ThermoFisher) for 2 minutes at room temperature. The treatment was stopped by addition of 20 mL PBS, centrifugation for 5 minutes at 300 x g and resuspension of the single cell solution in cell media.

METHOD DETAILS

Plasmids and antibodies

The plasmids and antibodies used in this study are listed in the key resources table.

Protein purification and labelling

Full-length mouse Bid and single-cysteine, full-length human BAX mutant (S4C, C62S and C126S), were expressed in *Escherichia coli* and purified as described elsewhere (Desagher et al., 1999; Bleicken et al., 2010). Briefly, BAX and Bid were expressed in BL21 (DE3) RIPL cells from a pTYB1 and a pET15b expression vector, respectively, and isolated using chitin affinity chromatography followed by ion-exchange chromatography (BAX) and IMAC affinity chromatography (BID). Caspase-8 was used to cleave Bid (cBid). Protein quality was checked by SDS–polyacrylamide gel electrophoresis. Mouse BAK carrying a modified, more hydrophilic C-terminus (L192K, F193S, Y196D) (Leshchiner et al., 2013) and mutated to single-cysteine (C154S), was transformed into BL21 (DE3) RIPL cells (Stratagene, La Jolla, CA). Cultures were grown at 37°C in LB medium containing ampicillin (100 μg/ml) and chloramphenicol (35 μg/ml). Gene expression was induced by 1 mM IPTG (isopropyl-1-thio-β-D-galactopyranoside) at OD (600 nm) of 0.7. The temperature was lowered to 20°C, cells were harvested after an additional 16 h, frozen in liquid nitrogen and stored at -20°C. For purification, cells were resuspended in buffer A (1 M NaCl, 20 mM Tris, pH 8), ruptured by French press and separated by centrifugation. The BAK-containing supernatant was purified by incubation with chitin beads and treated for intein cleavage as described by the manufacturer (NEB) and further purified by size exclusion chromatography. Protein purity was analyzed by SDS-PAGE, LC-MS and western blot. For protein labelling, Atto 488 (Attotec, Siegen, Germany) dye was covalently attached to the single cysteine of BAX or BAK as described by the manufacturer. Excess of the label was removed by size exclusion chromatography. The activity of the unlabeled protein was tested by calcein assay as performed in Bleicken et al. (2013b). The activity of labelled proteins was controlled by giant unilamellar vesicle membrane permeabilization assay (Hermann et al., 2014). Labelling efficiency was calculated to be 75-82% for BAK and 84% for BAX by comparing protein and label concentrations with Bradford and spectrophotometer measurements.

Western blotting

Cells were lysed in RIPA buffer (150 mM NaCl, 0.5% sodium deoxycholate, 1% NP-40, 0.1% SDS, 50 mM Tris, pH 8.0) with protease and phosphatase inhibitors and pre-cleared. Protein concentration was determined by Bradford protein assay (Bio-Rad) according to the manufacturers protocol. Equal amounts of protein (30-100 μg, depending on the experiment) were loaded on a 4-12% Tris-Bis gel (Thermo Scientific) and transferred onto PVDF or nitrocellulose membrane using the Turboblot (BioRad). Blots were blocked with 5% milk in TBST and incubated overnight at 4 °C with the primary antibody (see key resources table), probed with secondary antibodies (see key resources table) and developed using ECL (BioTool).

For separation of mitochondria and cytosolic fractions, cells lysed in permeabilization buffer (20 mM HEPES/KOH pH7.5, 100 mM sucrose, 2.5 mM MgCl2, 100 mM KCl, freshly added 0.025% (w/v) digitonin and protease inhibitor cocktail in PBS) for 10 min on ice and total cellular membranes were pelleted by centrifugation at 15.000 x g for 10 min at 4°C. After removing the supernatant (cytosolic fraction), the membranes were solubilized using RIPA buffer as described above.

Supported lipid bilayers (SLBs)

All lipids were purchased from Avanti Polar Lipids. Egg phosphatidylcholine (EPC) and cardiolipin (CL) were mixed in an 8:2 ratio and dissolved in chloroform. To obtain proteoliposomes, large unilamellar vesicles (LUVs) of 100 nm were prepared as described elsewhere (Subburaj et al., 2015). Briefly, lipids were resuspended in buffer (150mM NaCl, 10mM HEPES/KOH, pH7.4) to a final concentration of 0.6 mg/ml and passed through five cycles of freezing and thawing after which they were manually extruded through a polycarbonate membrane of defined pore size (100 nm) using glass syringes. For stoichiometry measurements, LUVs were incubated with 1, 5 or 10 nM BAX-488 or BAK-488 activated by heat (43°C) or with 1 nM BAK-488 activated by 2 nM cBid. After 1 hour incubation time, BAX/BAK-containing proteoliposomes were diluted to a 1:2, 1:5 or 1:10 ratio (for 1, 5 and 10 nM protein concentration, respectively) with LUVs to be in the single-molecule regime. The resulting solution was immediately used to create SLBs on piranha-cleaned glass slides (0.13–0.16-mm thickness, Menzel; Figure 3H) (Subburaj et al., 2015). In control experiments, proteins were added after SLB formation and incubated for 30 min. Unbound proteins and non-fused vesicles were removed by careful washing with buffer and the SLBs were immediately imaged. For AFM measurements, LUVs were incubated with 200 nM heat-activated BAK for 1 hour incubation time at 43°C. Liposomes (for control measurements) or proteo-liposomes were immediately used to create SLBs on freshly-cleaved mica, like in Unsay et al. (2017). Unbound proteins and non-fused vesicles were removed by careful washing with buffer and the SLBs were immediately imaged.

GUV permeabilization assay

GUVs were produced by electro-formation and the experiments were done as described in Bleicken et al. (2013b). Briefly, 2.5 μl of a 2 mg/ml EPC:CL 80:20 lipid mixture solution, doped with the lipophilic membrane dye DiI (Thermo Fisher) and dissolved in chloroform, were spread on each platinum electrode of an electro-formation chamber and immersed in 300 mM sucrose. Electro- formation proceeded for 2 h at 10 Hz, followed by 30 min at 2 Hz. 50 μl of the GUVs suspension was added to a solution of PBS buffer mixed with the appropriate concentrations of the proteins of interest in Lab-Tek 8-well chamber slides (NUNC) to a final volume of 200 μl. To measure membrane permeabilization in steady-state conditions, a Cytc488/APC mixture solution was added after 1-hour incubation with cBid-activated BAK at reported concentrations. Images were collected 30 min later. The percentage of GUVs internalizing the fluorescent probes was determined by the *GUVdetector* software described in Hermann et al. (2014).

Atomic force microscopy

SLBs were imaged using a JPK NanoWizard II system (JPK Instruments, Berlin, Germany) mounted on an Axiovert 200 Inverted Microscope (Carl Zeiss). Intermittent contact (IC or tapping) mode images were taken using V-shaped silicon nitride cantilevers with a typical spring constant of 0.09 N/m (SNL-10 Bruker). The cantilever oscillation was tuned to a frequency between 3 and 10 kHz, and the amplitude was set between 0.2 and 1 V. The amplitude was varied during the experiment to minimize the force of the tip on the bilayer. The scan rate was set between 0.5 and 1 Hz. The height, deflection and phase-shift signals were collected, simultaneously, in both trace and retrace directions.

Roughness was measured as the average peak-to-peak distance in a cross-section of a bilayer. Images were processed by the JPK processing software, applying a smoothing function. Bilayer thickness was measured based on the height profiles from the mica (membrane defects or pores) to the membrane bulk. The height of the structures around the pores was measured based on the height profile from the membrane bulk.

TIRF microscopy

All experiments were performed using a modified Zeiss Axiovert 200M epifluorescence microscope using a 488 laser (Ichrome MLE-LFA multi-laser, Toptica) equipped with an α Plan-Fluor 100x/1.46 oil objective (Zeiss), a Laser-TIRF 3 Imaging System (Zeiss) and an EM-CCD camera (iXon 897, Andor). Sample areas of 150x150 or 200 x 200 pixels (pixel size 100 nm) were illuminated for 35 ms with a delay time between frames of 25 ms (number of frames 1200) with an intensity of $\sim$ 0.1 kW/cm^2.

Stoichiometry determination

The images acquired by TIRF microscopy were used for the stoichiometry analysis based on the fluorescence intensity of the particles (i.e. brightness analysis) using an in-house develoed Stoichiometry analysis software (SAS) (Danial et al., 2022) implemented in Matlab which is available on github (https://github.com/jdanial/SAS).

Bright spots were automatically detected using an implementation of the Difference of Gaussians method (skimage.feature.blob dog http://scikit-image.org/docs/dev/api/skimage.feature.html) and thresholding. Selected particles were defined by a region of interest (ROI) of defined pixel size (3 pixels in radius) and fitted to two-dimensional (2D) Gaussians. Background subtraction was performed by defining a ROI around the particlés ROI having a larger pixel size (4 pixels in radius). This algorithm provided the brightness value for each spot. Localized particles were filtered based on the distance between two ROIs, to avoid overlapping ROIs, and on the presence of multiple particles in the same ROI. To this aim, we implemented a method that allows detecting two or more adjacent particles in one ROI by measuring the full width at half maximum (σ) of the fitted 2D Gaussian curves (see Jenner et al., 2020; STAR Methods section "Stoichiometry analysis by ratiometric approach"). Stoichiometry counting was performed using the brightness analysis method as previously described (Subburaj et al., 2015). The obtained brightness values were plotted as a probability density function (Pdf) or as a Gaussian distribution. We calibrated the fluorescence signal of the TIRF microscope before each experiment to avoid artefacts due to small changes in the optical setup. Monomeric BAK-488 particles were obtained by adding BAK-488 directly on an SLB (in which case no oligomerization occurred due to unspecific interactions of BAK with the glass support, Figure S4) and selected by photobleaching analysis (Subburaj et al., 2015; Ulbrich and Isacoff, 2007) after smoothing of the signal with a median filter. Correction for partial labelling efficiency was performed as previously described (Subburaj et al., 2015). Only proteins having >75% labelling efficiency were considered for experiments and data collection. The graphs with the percentage of occurrence refer to the average percentage of occurrence of fluorophore units per particle obtained from at least two different experiments (minimum 1500 particles per experiment from proteoliposomes and 600 particles per experiment of protein directly added to the SLB), and the error bars correspond to the standard deviation.

Analysis of BAX/BAK assembly kinetics

The assembly kinetics of BAX and BAK were investigated using photon counting confocal microscopy. Cells were transfected with 50 ng of pEGFP-A206K-BAX-C1 or pEGFP-A206K-BAK-C1 and 100 ng pcDNA3_Smac1-60_mCherry (see key resources table), using 0.5 μl Lipofectamine 2000 per well in a glass-bottom 8-well μ-slide (IBIDI) 12 h before confocal imaging. Apoptosis was induced with 1 μM of staurosporine (Sigma, Germany) or 1 μM ABT-737, 1 μM S63845 (MedChemExpress) and 10 μM qVD-OPh (APEXBIO). Confocal microscopy was performed on an LSM 710 (Carl Zeiss Microimaging) inverted microscope equipped with a Plan-Apochromat 63x/1.4 oil immersion objective (Zeiss) and an Argon LASER (LGN 3001, Lasos Lasertechnik). Pinhole size was adjusted to yield a depth of field of 1 Airy unit ($\sim$800 nm for GFP emission). Before imaging, the growth medium was changed to 200 μl of phenol-red free DMEM and cells were maintained at 37 °C and 5% CO_2 during imaging. Cells were imaged by selecting a region of interest (ROI) and finding the focal plane of the cell using the 'fast' scanning mode of the microscope with a greatly reduced laser power. Then, z-stacks of 8 images were collected with an interval of 300 nm, which was set based on the point-spread function analysis of fluorescent beads as the maximum interval required to record at least 80% of the maximum possible intensity from any point source. Images of 44.98 x 44.98 μm (512x512 pixel) were acquired with a laser pixel dwell of 3.15 μsec and an averaging of 2 images. Single emission photons were detected on an Avalanche Photodiode (APD) detector. Kinetics analysis of mEGFP-BAX or mEGFP-BAK oligomerization was performed by photon-counting fluorescence microscopy acquiring z-stacks every 5 minutes (for a time series of 60 minutes) after MOMP. MOMP was indicated by the release of Smac-1-60-mCherry (a truncated version of Smac targeting the intermembrane space, from now on Smac-mCherry) from mitochondria to the cytosol. We verified that using these imaging parameters, we did not have significant bleaching of our samples due to laser exposure.

Stoichiometry analysis by ratiometric approach

Single-particle detection and brightness analysis were performed on maximum intensity z-projections of individual time points (Figures S5A and S5B), using an in-house python algorithm. Selected particles were defined by a region of interest (ROI) of defined pixel size (2 pixels in radius) and fitted to two-dimensional (2D) Gaussians. Background subtraction was performed by defining a ROI around the particle's ROI having a larger pixel size (3 pixels in radius). Localized particles were filtered based on the width of the 2D Gaussian, which is indicative of the presence of multiple particles in the same ROI. Specifically, we implemented a method that allows detecting two or more adjacent particles in one ROI by measuring the full width at half maximum (σ) of the fitted 2D Gaussian curves. After plotting σ values of all ROIs as a normal distribution, those ROIs whose σ fell out the 95th percentile of the distribution were excluded, as the bigger σ value is likely indicative of the presence of more particles in these ROIs (Figures S5C and S5D). Importantly, particles whose intensity was maximum in the outer frames were also discarded, as intensity information could be lost (Figure S5A). The stoichiometry (or molecularity) of mEGFP-BAX or mEGFP-BAK foci M_p were quantified by ratiometric comparison of their fluorescence intensity I_p to the fluorescence intensity of a standard I_s, of known stoichiometry M_s, tagged with the same fluorescent dye as the protein of interest, according to the formula:

$$M_p = I_p \, M_s / I_s$$

As an internal standard, we used the 32-mer mEGFP-tagged nuclear pore complex protein Nup96, endogenously expressed in the same cell line (Thevathasan et al., 2019). We additionally confirmed the validity of this standard by ratiometric comparison of the fluorescent intensity of Nup96-mEGFP complexes with the one of recombinant mEGFP-ferritin, which assembles as a 24-mer (Liße et al., 2017; Figures S5E–S5G). For each cell, the standard fluorescence intensity i_s was obtained as the mean value of the Gaussian-fitted fluorescence intensity distribution of Nup96-mEGFP oligomers within the cell. I_s represents the average value of i_s from at least 5 different imaged cells, measured on the same day of the experiment. For a given cell, at each time point, the values in molecular units for detected mEGFP-BAX or mEGFP-BAK foci were plotted as a probability density function or as cumulative counts. Exponential decay fitting of the cumulative distribution provided the average molecularity of mEGFP-BAX or mEGFP-BAK foci of individual cells at each time point.

Measurement of protein expression level

To determine the concentration of BAX and BAK in cells, we measured the expression levels of endogenous BAX and BAK or mEGFP-BAX and mEGFP-BAK in cell lysates. We used WT cells, and single $BAX^{-/-}$, $BAK^{-/-}$ or double $BAX^{-/-}$ $BAK^{-/-}$ cells transfected with mEGFP-BAX and mEGFP-BAK (see key resources table) for cell lysate production, after sorting for fluorescent cells by flow cytometry, and analysed them via Western Blotting. To measure the expression level in single living cells, the GFP intensity of each mEGFP-BAX/BAK transfected cell was imaged by confocal microscopy and measured using an in-house algorithm. The GFP intensity value of a cell was normalized to the area of its mitochondrial network, detected by measuring the number of pixels with Smac-mCherry signal before apoptosis induction. This ratio represents the expression level of mEGFP-BAX/BAK in each cell.

SMLM and Correlative fluorescence/SMLM imaging

For SMLM experiments, cells were transfected with 300 ng pEGFP-A206K-BAK (see key resources table) plasmid 16 h before the experiment. Apoptosis was induced by incubating the cells with 1 μM STS for 3 h. To determine the optimal time point for cell fixation after apoptosis induction, mEGFP-BAK transfected cells undergoing apoptosis were stained with TMRE (Life Technologies, Germany) to monitor mitochondrial depolarization. The loss of TMRE staining was analysed by flow cytometry and occurred for 50% of all mEGFP-BAK positive cells 3 hours after apoptosis induction. For correlative fluorescence/SMLM imaging, HCT116 or U2OS cells were seeded on μ-$Dish^{35\ mm,\ high}$ or μ-$Dish^{35\ mm,\ high}$ Grid-500 Glass Bottom chamber (IBIDI) . Apoptosis was induced with 1 μM ABT-737, 1 μM S63845 and 10 μM qVD-OPh. Foci formation of mEGFP-BAK was visualized in selected cells by acquiring images every 2 min using confocal microscopy performed on an LSM 710 ConfoCor3 microscope (Carl Zeiss) equipped with a Zeiss C-Apochromat 40x/1.2 water immersion objective. At individual time points after first foci appearance, cells were fixed in 4% paraformaldehyde in DMEM for 10 min, washed twice with PBS and incubated in quenching buffer (50 mM NH_4Cl in PBS) for 15 min. Cells were permeablized with 0.25% Triton-X in PBS for 8 min, washed three times for 5 min with PBS and incubated in blocking buffer (1% BSA in PBS) for 45 min. Immunostaining was performed using a FluoTag-Q anti-GFP Alexa Fluor 647 nanobody (see key resources table) in 1:2000 dilution in blocking buffer for 1.5 h followed by washing three times for 5 min with PBS. For the SMLM imaging, 1.5 ml blinking buffer (50 mM Tris/HCl pH 8, 10 mM NaCl, 10% (v/w) glucose, 35 mM cysteamine (MEA), 0.5 mg/mL glucose oxidase, 40 g/ml catalase) was added. Image acquisition was performed on an Axiovert 200 Inverted Microscope (Carl Zeiss) equipped with a 100 mW 647 nm Coherent Obis diode laser and an α Plan-Fluor 100x/1.46 oil objective. Fluorescence emission was filtered using a 700/75 nm bandpass filter and imaged on an EM-CCD camera (iXon 897, Andor). Blinking of individual fluorophores was controlled by manually tuning the power of a 405 nm laser (iChrome MLE, Toptica photonics) to achieve a constant density of fluorescent molecules throughout the acquisition period. An exposure time of 30 ms was used and 70,000-100,000 frames recorded. Frame rate was 40 ms. Imaging laser intensity at 640 nm was 2.5 kW/cm^2, and the 405-nm activation laser intensity was manually adjusted to keep a constant number of localizations per frame. The field of view varied depending on cell size or area of interest and pixel size was 100 nm. Focus was maintained to +/- 20 nm in the lateral position with the aid of a home-built autofocusing system using a back-reflected IR diode laser (LDM850,Thorlabs, 850 nm) with a Lateral effect position Sensor (PDQ80A, Thorlabs) and a piezo-stage interfaced through a PID circuit. Acquired images were analyzed using thunderSTORM (Ovesný et al., 2014). Individual fluorophore localizations were detected using a Difference of Gaussians implementation and fitted to Gaussian profiles using the Least Square method. For reconstruction of a super-resolved image the uncertainty in the fitting procedure combined with the sigma of the fitted Gaussians were used to improve the image quality and discard false localizations. Localizations with uncertainties above 20 nm were discarded.

Live cell STED microscopy

BAX/BAK DKO U2OS cells were seeded in 8-well glass bottom dishes (ibidi GmbH, Martinsried, Germany) and transfected with 50 ng pAcGFP-C1-SnapF-BAX (Snap-BAX), 50 ng pAcGFP-C1-Halo7-BAK (Halo-BAK) and 50 ng pEGFP-N1-4xmt-mTurquoise2 (mitoTruquoise, see key resources table) 16 hours prior to imaging. Cells were stained with 1 μM SNAP-Cell SiR (New England Biolabs) and 300 nM Janelia Fluor® 549 HaloTag® Ligand (Promega Corporation, 2800 Woods Hollow Road, Madison, WI 53711 USA) in DMEM for 20 min at 37 °C. After labeling, the cells were washed twice with DMEM and incubated for 15–30 min to remove unbound dye. Prior to imaging, the culture medium was changed to Live Cell Imaging Solution (Thermo Fisher Scientific) containing 1 μM ABT737, 1 μM S63845 and 10 μM and Q-VD-OPh (MedChemExpress) to induce apoptosis. Live cell STED microscopy was performed on a confocal laser scanning STED microscope (TCS SP8 STED 3x, Leica, Wetzlar) equipped

with a HL PL APO 100x/1.40 Oil STED (white) objective (Leica, Wetzlar). Imaging was performed line sequentially with a pinhole size of 1.0 Airy unit and a pixel size of 23 nm. SNAP-Cell SiR was excited at 640 nm and Janelia Fluor® 549 at 561 nm. Both dyes were depleted at 775 nm wavelength. For triple color images, a confocal image of mitoTurquoise was acquired in addition, using the line sequential mode with an excitation wavelength of 458 nm. The fluorescence signal was detected using Hybrid detectors with a gating of 0.5-8 ns, a pixel dwell-time of 2.44 μs and 8 times line averaging. Images have been adjusted for brightness and contrast and processed by one smooth step using Fiji/ImageJ. Images were deconvolved with Huygens Professional version 19.04 (Scientific Volume Imaging, The Netherlands, http://svi.nl).

Proximity-dependent labeling with APEX2

Proximity-dependent labeling with APEX2 was done as described in Lam et al. (2015). In short, the APEX2 enzyme attached to BAX (or BAK) creates a free radical from Biotin-Phenol (BPh) in presence of H_2O_2 that reacts with neighboring (~10 nm) proteins. After proximity-dependent biotinylation, cell lysates are used for immunoprecipitation with streptavidin (Figure 6C). HeLa cells were transfected with Flag-APEX2-BAX or -BAK (see key resources table) for 16h and incubated 3 h with 1 μM staurosporine at 37°C, 5% CO2 to induce apoptosis. Next, media was changed to DMEM with 500 μM biotin-phenol and cells were incubated for 30 min at 37°C, 5% CO2. Hydrogen peroxide (H2O2) was then added to a final concentration of 1 mM for 1 min at RT to initiate the biotinylation reaction. After quenching the biotinylation reaction, cells were lysed using RIPA buffer. A fraction of the whole cell lysate was stored (input) and equal amounts of whole cell lysates were incubated with 200 μl streptavidin-coated magnetic beads rotating for 1 h at 4°C. Beads were collected using a magnetic rack and were exhaustively washed on ice with RIPA buffer, 1 M potassium chloride, 0.1 M sodium carbonate, 2 M urea in 10 mM Tris-HCl pH 8.0, RIPA buffer and three times with 20 mM ammonium bicarbonate, pH 8.0, sequentially. After washing, the beads were boiled with SDS-PAGE loading buffer supplemented with 2 mM biotin for 5 min at 95°C. The supernatant fractions containing biotinylated proteins were loaded onto a polyacrylamide gel for detection of BAX (anti-BAX) and BAK (anti-BAK, see key resources table) by Western Blot.

Dimerization-dependent fluorescent protein

Dimerization-dependent fluorescent protein (ddFP) was done as described in Ding et al. (2015). HeLa cells were seeded in 8-well chambers (Ibidi) and transfected with RA-BAX, GB-BAK and mitoBFP (see key resources table). 1 μM STS was added in DMEM without phenol red media and cells were imaged after 3 h of apoptosis induction. Images were acquired using the water objective of the confocal microscope equipped with incubator at 37°C and 5% CO2.

Immunoprecipitation of GFP-BAK-containing SMALPs

SMA lipid particles (SMALPs) were generated from isolated mitochondria containing mEGFP-BAK and subjected to immuno-precipitation and immunoblotted with BAX and BAK antibodies (Figure 6E). For this, BAK KO U2OS cells transfected with mEGFP-BAK (see key resources table) were treated with 1 μM ABT737 and 1 μM S63845 to induce apoptosis and harvested 45 min post treatment. Apoptotic and control (untreated) samples were mechanically lysed using a dounce homogenizer and centrifuged at 600 x g to remove non-lysed cells and nuclei. Mitochondria were pelleted from the supernatant by centrifugation at 10,300 x g. Mitochondrial pellets were washed twice in isolation buffer (5 mM Tris/HCl pH 7.4, 250 mM sucrose, and 2 mM EDTA) and once with Tris buffer (50 mM Tris/HCl pH8.0, 200 mM NaCl). The pellet was then resuspended in the Tris buffer and equal protein content was used for the next step. The isolated mitochondria were then solubilized by addition of Styrene Malic acid (SMA 2:1; Polyscope Polymer) to a final concentration of 0.5%. The solubilized mitochondrial membranes were centrifuged at 100,000 g at 4 °C for 45 min to remove the insoluble fraction and produce a purified SMA lipid particle (SMALP). SMALPs containing GFP-BAK was subsequently enriched by GFP-Trap® magnetic beads (ChromoTek). The purified proteins were analyzed by immunoblotting.

Confocal imaging for optogenetic measurements

For measuring the recruitment of BAX after light-induced (optogenetic) BAK activation, cells were transfected with 50 ng pCRY2-mCherry-BAK, 50 ng pCIBN-mCherry-BAK and 50 ng pEGFP-A206K-BAX-C1 (see key resources table). Cells were kept in dark after transfection. The mitochondria were either visualized using MitoTracker™ Deep Red (Thermo Fisher M22426) staining (100 nM) or using transfection with 100 ng mTagBFP2-Tomm20 (see key resources table). Confocal imaging was performed on a TCS SP8 (Leica Microsystems) inverse confocal laser scanning microscope equipped with a PL Apo 63x/1.40 Oil CS2 objective, a 405 nm laser and a tunable white light laser (470 – 670 nm). Fluorescence emission was detected using HyD SMD detectors. Before imaging, the growth medium was changed to 200 μl of phenol-red free DMEM and cells were maintained in a humidified incubator chamber (Ludin IceCube) with 5% CO2. Individual z-stacks were acquired with 2.5 min interval for approx. 60 min. Maximum intensity z-projection was performed using ImageJ and individual time points before and after BAK foci formation were chosen as representative images.

BAX and BAK recruitment to GUVs

GUVs with a lipid composition of EPC:CL 7:3 (mol:mol) were prepared by electro-formation as described above. 80 μl of the GUVs suspension was added to a solution of PBS buffer mixed with Alexa 555 soluble dye and 100 nM BAK-Atto 488 in Lab-Tek 8-well chamber slides (NUNC) to a final volume of 200 μl. The samples were heated to 42 °C for 30 min to activate BAK. After cooling the samples to room temperature, 100 nM BAX-Atto 655 was added and incubated for 30 min. Binding of BAK and BAX to the

GUVs was measured at individual incubation steps using confocal microscopy. Permeabilization of the GUVs is indicated by the presence of soluble Alexa 555 inside the GUVs. Radial profiles of background-corrected normalized integrated fluorescence intensities were measured for individual GUVs using the Radial Profile Plot Plugin of ImageJ (https://imagej.nih.gov/ij/plugins/radial-profile.html). Radial profile intensities were measured and fit with a Gaussian fitting for n=7 individual GUVs from n = 3 independent experiments.

mtDNA release

To detect the release of mitochondrial DNA from mitochondria during apoptosis, WT, BAX KO and BAK KO U2OS cells were seeded in a μ-Dish$^{35\ mm,\ high}$ Grid-500 Glass Bottom chamber (IBIDI) and transfected with 100 ng pcDNA3_Smac1-60_mCherry and pEGFP-Tfam-GFP (see key resources table) 16 h before the experiment. Confocal microscopy images were acquired to identify Smac-mCherry and Tfam-GFP double transfected cells within the coordinate system (Figure 7A) using an LSM 710 microscope (Carl Zeiss) equipped with a C-Apochromat 40x/1.2 water immersion objective (Zeiss). Images were acquired every 2 minutes after apoptosis induction with 1 μM ABT-737, 1 μM S63845 and 10 μM QVD-OPh. The time point of Smac-mCherry release from mitochondria was used to set the start point for kinetic measurements. For the experiments with the BAX(T182I) mutant, BAX/BAK DKO U2OS cells were transfected with Smac-mCherry, TFAM-GFP and Halo-BAX WT or Halo-BAX(T182I) (see key resources table) and imaged the following day with an Echo Revolve fluorescence microscope (RVL-100-M). Cells were fixed by incubation with 4% paraformaldehyde in DMEM and washed three times with PBS after specific time points of Smac release (5-60 min). For the immunostaining of the mitochondria, the cells were permeabilized with 0.25% Triton-X in PBS for 8 min, washed three times for 5 min with PBS and incubated in Blocking Buffer (1% BSA in PBS) for 45 min. Immunostaining was performed with an α-Tomm20 antibody (1:100 dilution in Blocking Buffer, see key resources table) for 45 min. Cells were washed three times for 5 min with PBS and incubated with an Alexa Fluor 633-labelled anti-rabbit secondary antibody (1:200 diluted in Blocking Buffer, see key resources table) for 45 min and washed three times for 5 min with PBS. Images were acquired using an LSM 780 NLO or LSM 880 (Zeiss) equipped with a 63x/1.2 water immersion objective (Zeiss) and an Airyscan module (Zeiss). The cells chosen before by confocal microscopy were relocated using the coordinate system position (Figure 7A). Image analysis was done using ZEN software (Zeiss) and ImageJ. The percentage of cells with mtDNA release was assessed by visual inspection of non-colocalizing Tfam-GFP (green) and Tomm20 (magenta) signals.

Flow cytometry

BAX/BAK DKO HCT116 cells were seeded in a 12-well plate and transfected with 300 ng mEGFP-BAK (see key resources table) 16h before the experiment. Apoptosis was induced by incubating the cells with 1 μM STS for one to eight hours. Cells without induction of apoptosis were used as a control. Supernatant and cells were collected, washed with PBS and incubated in 100 nM TMRE in DMEM for 30 min at 37°C in the dark. Cells were pelleted, washed three times with PBS and resuspended in PBS. Cells were analyzed using a FACSCanto flow cytometer (BD Biosciences).

Coculture experiments

Single cell solutions of WT, BAK KO and BAX KO SVEC cells were prepared in complete cell media containing 106 cells/mL. While in suspension, the cells were treated with 5 μM ABT-737, 5 μM S63845 and 10 μM QVD for 3 hours. Next, the cells were washed twice by centrifugation at 300 x g for 5 minutes and resuspended in 50 mL PBS. After washing, the treated or untreated cells were plated in 6 well plate (2.5*10^5 cells/well) followed by addition of single cell suspension of spleenocytes (5*10^5 per well) and incubated for 24 hours at 37°C with 5% CO_2. The cocultured samples were then collected and stained with a viability dye for 30 minutes at room temperature. The viability staining was then followed by two washing steps with PBS and FC-receptor blocking for 10 minutes prior to antibody incubation for 30 minutes at 4°C (see key resources table). Stained cells were then washed and fixed with BD CellFIX (340181, BD Biosciences) for 30 minutes at 4°C before the samples were washed and resuspended in FACS buffer (5% FBS and 2 mM EDTA in PBS). Detailed information regarding reagents used in this procedure can be found in Table 3. All flow cytometry data was acquired using "LSR-Fortessa Analyzer" and analysed with FlowJo software.

QUANTIFICATION AND STATISTICAL ANALYSIS

Statistical details of the experiments are provided in the respective figure legends. Graphs were plotted using GraphPad Prism and Origin. Statistical significance was tested as described in the figure legends. Unless indicated differently, data are representative for three independent experiments and were analyzed in a blinded and, if applicable, automated fashion to avoid confirmation and observer bias.

Molecular Cell, Volume *82*

Supplemental information

The interplay between BAX and BAK tunes apoptotic pore growth to control mitochondrial-DNA-mediated inflammation

Katia Cosentino, Vanessa Hertlein, Andreas Jenner, Timo Dellmann, Milos Gojkovic, Aida Peña-Blanco, Shashank Dadsena, Noel Wajngarten, John S.H. Danial, Jervis Vermal Thevathasan, Markus Mund, Jonas Ries, and Ana J. Garcia-Saez

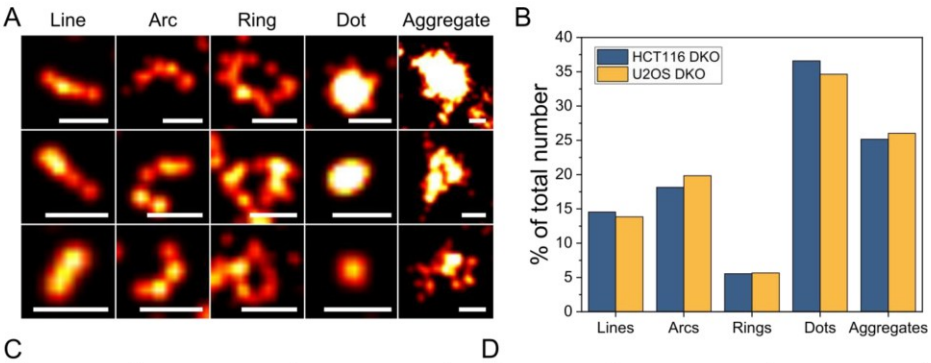

C

	HCT116 DKO	U2OS DKO
Line length	109 nm ± 32 nm	107 nm ± 37 nm
Arc length	103 nm ± 36 nm	101 nm ± 33 nm
Perimeter	106 nm ± 40 nm	104 nm ± 31 nm
Arc radius	24 nm ± 8 nm	25 nm ± 9 nm
Ring radius	18 nm ± 9 nm	17 nm ± 7 nm

D

	GFP-BAK	GFP-BAX
Line length	109 nm ± 32 nm	214 nm ± 80 nm
Arc radius	24 nm ± 8 nm	73 nm ± 30 nm
Ring radius	18 nm ± 9 nm	34 nm ± 7 nm

Figure S1: BAK structures in other cell lines have similar structure distribution and parameter sizes. Related to Fig. 2. A) Gallery of BAK structures in apoptotic BAX/BAK DKO U2OS cells. Scale bar 100 nm. B) Percentage distribution of the different BAK structure types found in BAX/BAK DKO HCT116 (n=12) and U2OS (n=7) cells. Number of lines (minimum 254), arcs (minimum 363), rings (minimum 109), dots (minimum 647) and aggregates (minimum 472). C) Comparison of the average size of mEGFP-BAK structures in BAX/BAK DKO HCT116 and U2OS cells. D) Comparison of mEGFP-BAK and mEGFP-BAX average size structures detected in mEGFP-BAX BAX/BAK DKO Hela (Salvador-Gallego et al., 2016) and mEGFP-BAK BAX/BAK DKO HCT cells.

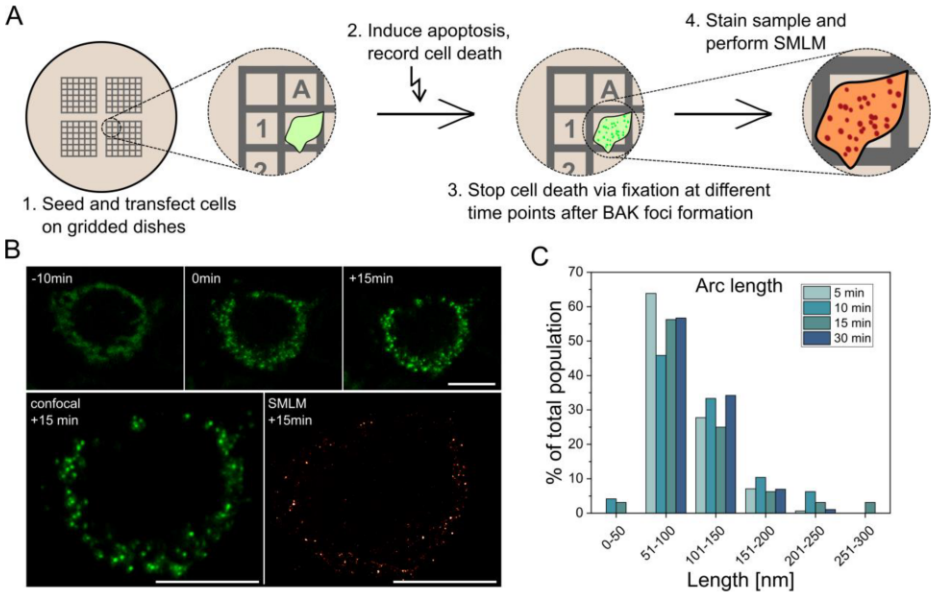

Figure S2: BAK structures evolve over time from linear to ring structures but do not show growth in size. Related to Fig. 2. A) Scheme explaining the principles of correlative fluorescence and super-resolution microscopy. Individual selected mEGFP-BAK transfected cells within the coordinate system were imaged every 2 minutes by confocal microscopy after apoptosis induction with 1 µM ABT-737, 1 µM S63845 and 10 µM qVD-Oph. The time point of first BAK foci appearance was noted and apoptosis progression was stopped by fixation. After immunostaining of mEGFP-BAK with an Alexa647 nanobody, cells were identified using the coordinate system and SMLM imaging was performed. B) Upper panel: Representative confocal fluorescence microscopy images of a BAX/BAK DKO HCT116 cell transfected with mEGFP-BAK and imaged 10 min before foci formation (-10 min), at the time point of first foci appearance (0 min) and 15 min after foci formation (+15 min). Lower panel: Comparison of the same cell imaged with confocal microscopy (left) and SMLM (right). Images are representative of at least 15 independent measurements. Scale bar 10 µm. C) Distribution of the arc length at the different time points after the first foci appearance (minimum number of analysed arcs per time point: 112).

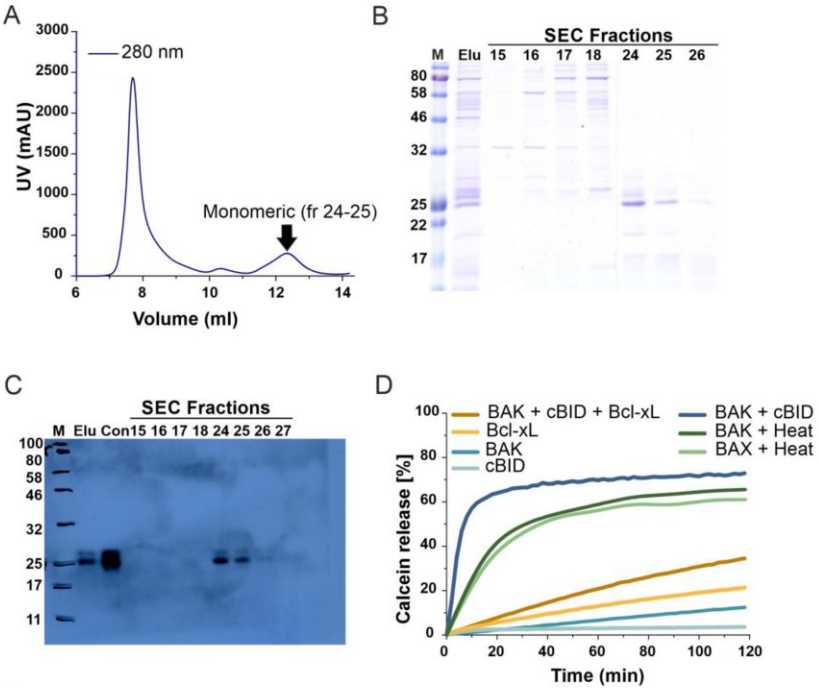

F

BAK Structure	Dimension (nm)
Line length	33.44 ± 3.76
Arc length	5.57 ± 7.481
Arc radius	5.98 ± 3.28
Ring radius	8.12 ± 3.03
Ring external radius	15.98 ± 3.78

Figure S3: Purification, activity characterization, structures and associated membrane pores of full-length BAK. Related to Fig. 3. A) Size exclusion chromatogram of recombinant full-length BAK (BAK I192K, F193S, V196D). The arrow indicates the monomeric fractions. B) SDS-PAGE gel bands (Coomassie brilliant blue staining) and C) western blot indicating the presence of pure BAK (23 kDa). D) Calcein permeabilization assay of purified BAK (200 nM) activated by cBid (20 nM) or heat and inhibited by Bcl-xL (100 nM). LUVs containing a self-quenching/highly concentrated calcein solution were incubated with activated BAK. Release of fluorescent calcein, indicating membrane permeabilization, was monitored over time. Heat-activated BAX (200 nM) was used as a positive control. All data are representative of at least 3 independent experiments. E) Gallery of BAK structures in EPC:CL (80:20 mol %) membranes imaged by atomic force microscopy (AFM). Picture size 100 nm. The full colour height range of the topographs from low (brown-orange) to high (yellow-white) is 2 nm. F) Average size and standard deviation of the different parameters for BAK structures as in E (lines =14, arcs=31 and rings=14). Data were obtained from at least four independent experiments.

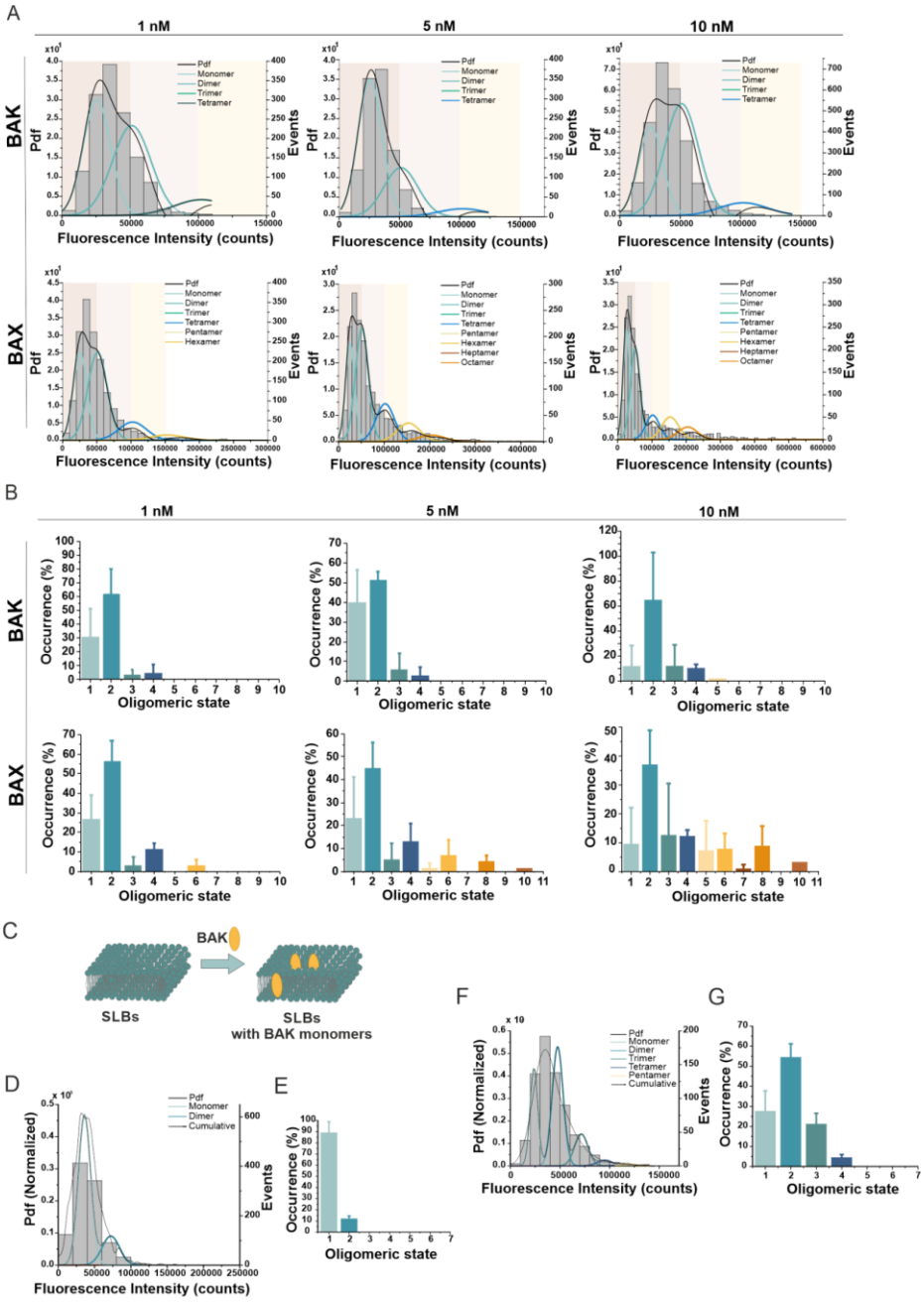

Figure S4: Stoichiometry of BAK oligomers on SLB and activation by cBid. Related to Fig. 3.
A) Representative fluorescence intensity distribution of BAK-488 (upper panel) and BAX-488

(lower panel) oligomers (minimum 1500 particles per condition, from 2 independent experiments) obtained from SLB samples with different concentrations (1, 5 and 10 nM) of protein. The obtained brightness distribution was plotted as a probability density function (Pdf, black) or, alternatively, as a histogram, and fitted with a linear combination of Gaussians to estimate, from the area under each curve, the percentage of occurrence of particles containing n-mer labelled molecules (see the colour code in the graph). The three panels in the background indicate each a 50,000 counts range and are for a visual comparison between BAX and BAK intensity distribution graphs. B) Percentage of occurrence of BAK-488 (upper panel) and BAX-488 (lower panel) different oligomeric species measured from graphs as in A) and calculated as the average value from two different experiments. Data provided are corrected for partial labeling (see STAR Methods). The error bars correspond to the standard deviation from the different experiments. C) Schematic representation of the protocol used for sample preparation in D and E. SLBs were incubated with 1 nM BAK-488 (yellow) and 2 nM cBid (not shown) for 30 minutes at room temperature, washed carefully with buffer and immediately imaged by TIRF microscopy. D) Representative intensity distribution of BAK-488 particles directly added on SLBs as in C). The obtained brightness distribution was plotted as a probability density function (Pdf, black) or, alternatively, as a histogram, and fitted with a linear combination of Gaussians to estimate, from the area under each curve, the percentage of occurrence of particles containing n-mer labelled molecules (see the color code in the graph). E) Percentage of occurrence of different BAK-488 oligomeric species measured from graphs as in D) and calculated as the average value from three different experiments. Due to unspecific interaction of BAK molecules with the SLB glass support, BAK molecules were unable to oligomerize, resulting mainly in monomers and few dimers. F) Representative intensity distribution of BAK-488 particles bound to SLBs prepared from proteoliposomes as in Figure 3, after activation of 1 nM BAK by 2 nM cBid and 1 h incubation at room temperature. G) Percentage of occurrence of different BAK-488 oligomeric species measured from graphs as in F) calculated as the average value from three different experiments. Data provided are corrected for partial labeling. The error bars correspond to the standard deviations from the different experiments.

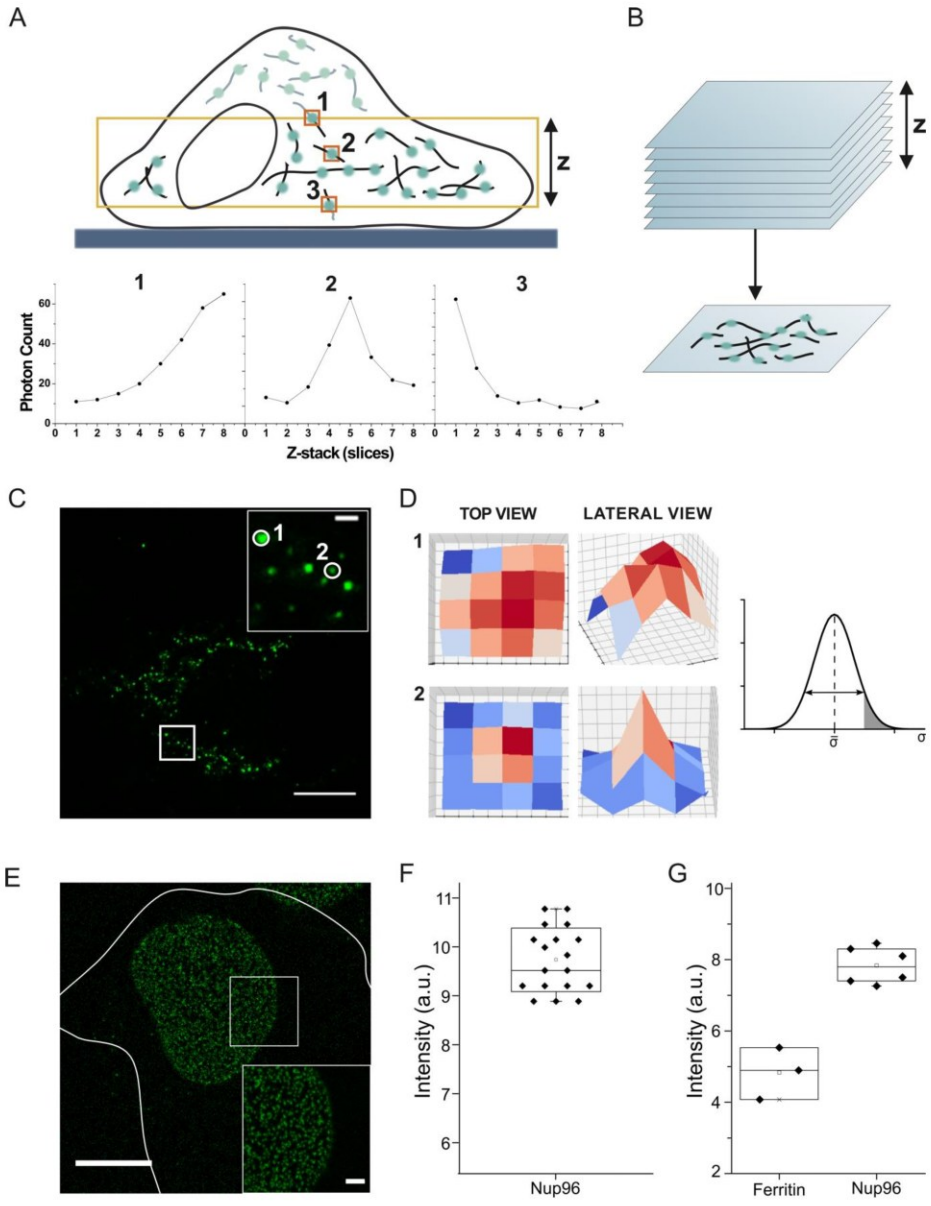

Figure S5: Ratiometric stoichiometry analysis using single-particle photon counting with confocal microscopy. Related to Fig. 4. A) Top panel: Schematic representation of a cell containing mEGFP-BAX or mEGFP-BAK foci (green dots) at mitochondria. A centered z-section of the cell was imaged (indicated by the yellow square) containing individual particles (orange boxes) located at the top z-plane (1), centered in the z-range (2) and at the bottom z-plane

(3). Bottom panel: Intensity of indicated particles 1-3 along the z-axis. Particles 1 and 3 were discarded from the analysis because we could not exclude that their maximum intensity was out of the imaged area. B) Maximum intensity projection of individual z-planes. C) Representative image of maximum intensity z-projection of mEGFP-BAX particles. Inset: Enlarged view of the indicated square with localized regions of interest (circles) containing particles 1 and 2. Scale bar 10 µm, inset scale bar 2 µm D) Left: Representative top and lateral view graphs of the detected fluorescence intensity of the individual fluorescent particles 1 and 2 of C); fluorescence intensity is colour-coded from low (blue) to high (red). Right: Normal distribution of the full width at half maximum (σ) of the fitted 2D Gaussian curves for all detected ROIs. Those ROIs whose σ fell out the 95^{th} percentile of the distribution (grey shaded area) were excluded, as the bigger σ value is likely indicative of the presence of more particles in these ROIs. E) Representative maximum intensity z-projection image of Nup96-mEGFP complexes in a U2OS cell. Inset shows an enlarged view of the indicated square. Scale bar 10 µm, inset scale bar 2 µm. F) Average intensity of Nup96-mEGFP particles obtained from individual cells (dots in box plot). G) Validation of the 32-mer Nup96-mEGFP stoichiometry by ratiometric comparison to the average fluorescence intensity of the 24-mer mEGFP-Ferritin used as an external standard and imaged under the same conditions as Nup96-mEGFP particles.

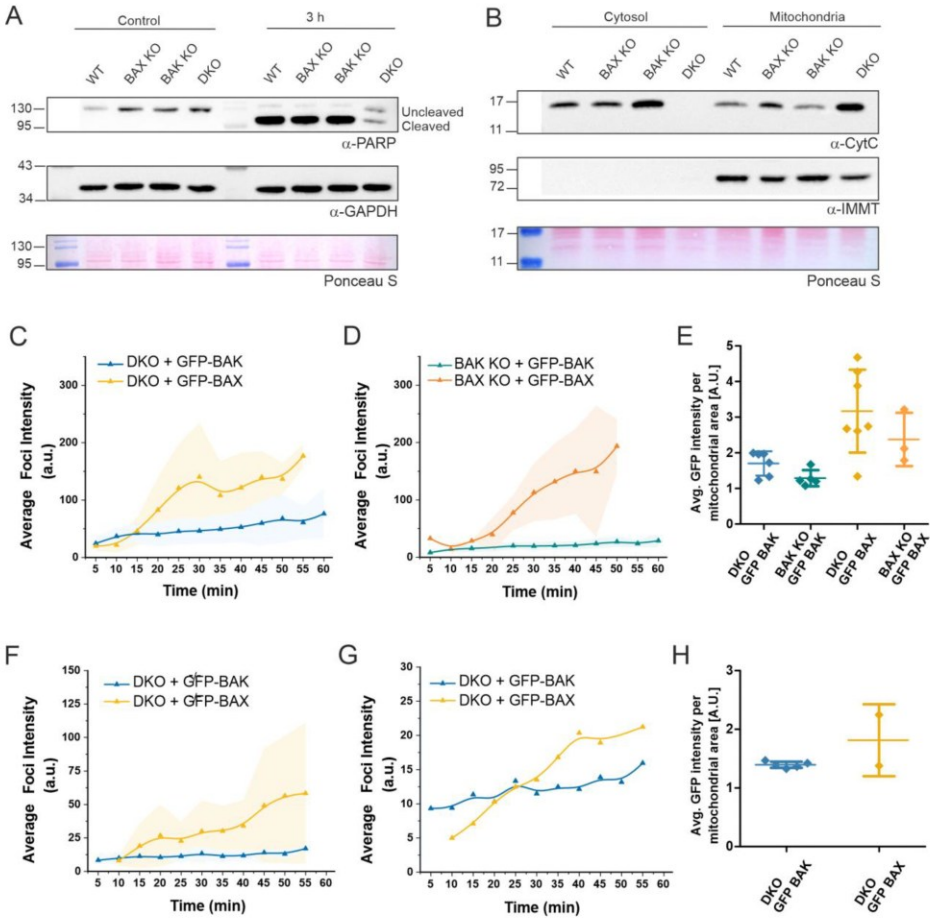

Figure S6: BAX and BAK kinetics of assembly in apoptotic cells by a different apoptosis treatment and in different cell lines. Related to Fig. 4. PARP cleavage (A) and release of cytochrome *c* to the cytosol (B) in WT, BAX KO, BAK KO and BAX/BAK DKO U2OS cells at 3 hours after apoptosis induction with ABT-737, S63845 and qVD-OPh, as typical hallmarks of apoptosis. α-GAPDH and/or Ponceau S staining is shown to control for equal sample loading; α-IMMT immunoblotting was used to control for purity of the cytosolic fraction in B). C) Average mEGFP-BAX (yellow, n° cells=7, minimum average number of foci per time point: 172) and mEGFP-BAK (blue, n° cells=6, minimum average number of foci per time point: 108) foci intensity over time in BAX/BAK DKO U2OS cells transfected with mEGFP-BAX or mEGFP-BAK after apoptosis induction by 1 µM of staurosporine (STS). D) Average mEGFP-BAX foci intensity in BAX KO U2OS cells transfected with mEGFP-BAX (orange, n° cells=3, minimum average number of foci per time point: 32) and for mEGFP-BAK in BAK KO U2OS cells transfected with mEGFP-BAK (green, n° cells=5, minimum average number of foci per time point: 124) after apoptosis induction by 1 µM STS. E) Average mEGFP expression level per mitochondrial area

detected by single-cell fluorescent intensity analysis of mEGFP signal in individual BAX KO, BAK KO or BAX/BAK DKO U2OS cells (individual dots in the plot) transfected with mEGFP-BAX or mEGFP-BAK. F) Average mEGFP-BAX (yellow, n° cells=2) and mEGFP-BAK (blue, n° cells=5) foci intensity over time in BAX/BAK DKO HCT116 cells transfected with mEGFP-BAX or mEGFP-BAK after apoptosis induction by 1 µM ABT-737, 1 µM S63845 and 10 µM qVD-OPh. G) Average foci intensity for mEGFP-BAX (yellow) and mEGFP-BAK (blue) over time in single cells extracted from F) with the same level of expression of mEGFP-BAX and mEGFP-BAK. H) Average mEGFP expression level per mitochondrial area detected by single-cell fluorescent intensity analysis of mEGFP signal in individual BAX/BAK DKO HCT116 cells (individual dots in the plot) transfected with mEGFP-BAX or mEGFP-BAK. In C, D, F, G, foci intensity is not normalized to a calibration standard, but reported in arbitrary units (a.u.). Lines in the graph correspond to the average values from all measured cells and colored areas in the graphs correspond to data variability from single cells.

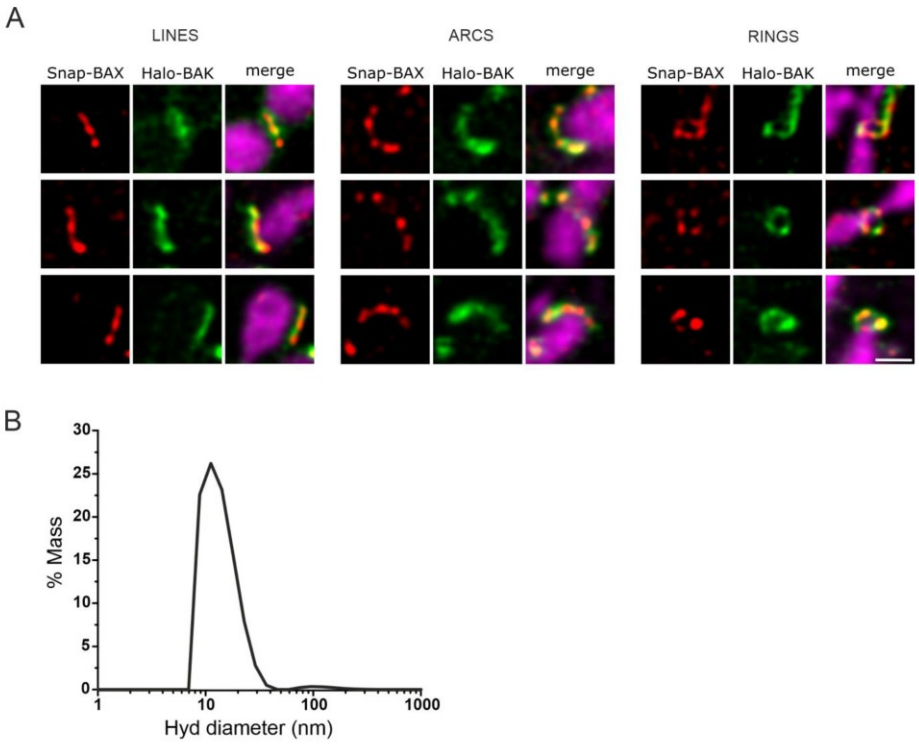

Figure S7: Visualization of BAX-BAK structures by STED microscopy. **Related to Fig. 6.** A) Gallery of line, arc and ring structures formed by BAX and BAK in apoptotic mitochondria acquired by live-cell STED microscopy in BAX/BAK DKO U2OS cell transfected with Snap-BAX (red), Halo-BAK (green) and 4xmt-mTurquoise (magenta, confocal) to stain mitochondria. Apoptosis was induced with 1µM ABT-737, 1 µM S63845 and 10 µM qVD-OPh for 30 min. Scale bar 500 nm. Images show the separated and merged channels of the same structures shown in Figure 6. Images were deconvolved using Huygens Professional and are representative of three independent experiments. B) Dynamic light scattering graph showing the size distribution (hydrodynamic diameter) of SMALPs.

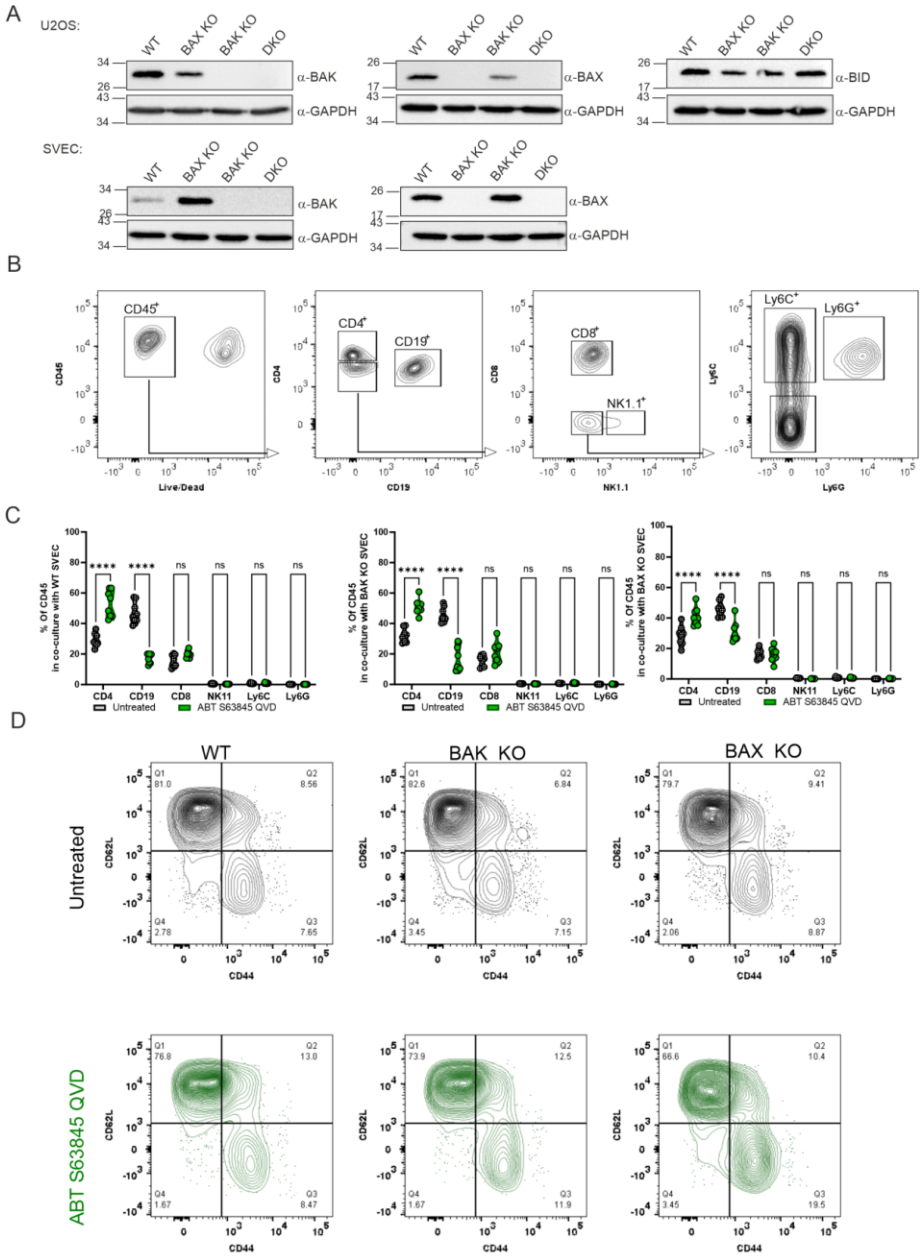

Figure S8: Apoptotic SVEC cells lead to changes in lymphocyte frequencies in a coculture system. Related to Fig. 7. A) Expression levels of endogenous BAX, BAK and BID in WT, BAK KO, and BAX KO U2OS (upper) and SVEC (lower) cells by western blot. α-GAPDH was used to control for equal sample loading. B) Examples of gating strategies used to define different cellular subtypes. C) Frequencies of different cell types in the coculture with splenocytes and

SVEC cells either untreated or pre-treated with ABT-737, S63845 and QVD for 3 hours. D) Representative flowcytometry plots demonstrating changes in CD62L and CD44 in CD4 T-cells in coculture system with either WT, BAK KO or BAX KO SVEC cells. 2way ANOVA and Sidak multiple comparison test was used for the statistical analyses. N= 8 spleen donors. *= $p< 0.05$, **= $p< 0.01$, ***= $p< 0.001$, **** = $p< 0.0001$.

2. Submitted Manuscripts

2.1 Mechanical forces drive mitochondrial matrix extrusion and apoptotic pore growth

This manuscript was submitted to Nature on May, 12, 2025, and is available on the BioRxiv preprint server at the following link: https://doi.org/10.1101/2025.05.12.653510

Mechanical forces drive mitochondrial matrix extrusion and apoptotic pore growth

Andreas Jenner[1,2], Timo Dellmann[1,2], Hyuntae Kim[3,4], David Gomez[1,2,5], Cristiana Zollo[1,2], Jürgen Köfinger[3], Katrin Seidel[2], Felix Gaedke[2], Astrid Schauss[2], Gerhard Hummer[3,6], and Ana J. Garcia-Saez[1,2,5]

[1] Institute of Genetics, University of Cologne, 50931 Cologne, Germany

[2] Cologne Excellence Cluster on Cellular Stress Responses in Aging-Associated Diseases (CECAD), University of Cologne, 50931 Cologne, Germany

[3] Department of Theoretical Biophysics, Max Planck Institute of Biophysics, 60438 Frankfurt am Main, Germany

[4] IMPRS on Cellular Biophysics, Max-von-Laue-Straße 3, 60438 Frankfurt am Main, Germany

[5] Department of Membrane Dynamics, Max Planck Institute of Biophysics, 60438 Frankfurt am Main, Germany

[6] Institute of Biophysics, Goethe University Frankfurt, 60438 Frankfurt am Main, Germany

Andreas Jenner: andreas.jenner@uni-koeln.de, https://orcid.org/0000-0002-6388-3053

Ana J. Garcia-Saez: ana.garcia@biophys.mpg.de, https://orcid.org/0000-0002-3894-5945

Tel: +49 221 478 84258

Keywords

Apoptosis, BCL-2 Proteins, BAK, MOMP, MIMP, line tension, osmotic swelling

Abstract

Apoptotic pore opening by BAX and BAK at the mitochondrial outer membrane is a key step in the cell's commitment to death. The subsequent inner membrane extrusion and permeabilization releases mitochondrial DNA into the cytosol, which can trigger inflammatory signaling. However, the underlying mechanisms have not been elucidated. Here we developed CLOSE microscopy, a multi-correlative approach that enabled the simultaneous analysis of BAK stoichiometry and nanoscale organization in individual apoptotic pore complexes in relation to mitochondrial ultrastructure. We find that the outer membrane opening at the apoptotic pore defines the spatial arrangement of BAK nanoassemblies. We identify mechanical stress as a driver of inner membrane extrusion, which can be perturbed by osmoregulation. The extruded inner membrane in turn exerts forces on the outer membrane that promote apoptotic pore growth, in line with membrane dynamics simulations. Our study reveals a tight interplay between the inner and outer membranes during mitochondrial permeabilization in apoptosis and establishes a biophysical mechanism for inner membrane extrusion that defines the structural organization of the apoptotic pore.

Introduction

BAX and BAK are proapoptotic members of the BCL-2 protein family and are critical for apoptosis execution [1,2]. They mediate mitochondrial outer membrane (MOM) permeabilization (MOMP) during apoptosis, a pivotal point in the cell's commitment to death. MOMP enables the release of apoptotic factors, including cytochrome *c* (cyt *c*) and Smac/DIABLO, from the mitochondrial intermembrane space into the cytosol, initiating the downstream apoptotic caspase cascade [3–6]. This ultimately results in the dismantling of the cell into apoptotic bodies, which are engulfed by macrophages, usually ensuring an immunologically "silent" removal of the dead cell [7,8].

The dynamic oligomerization of BAX and BAK molecules into high-order complexes of heterogeneous size and shape results in the opening of apoptotic pores at the MOM that continue to grow during apoptosis progression. At the nanoscale, these assemblies form line, arc, and ring structures, with arcs and rings capable of forming pores in the membrane [9–12]. BAX and BAK membrane pores are lined by both proteins and lipids, so that the biophysical properties of the membrane govern the pore size and stability [13–17]. *In vitro*, BAX membrane insertion has been associated with a reduction in line tension at the pore edge that stabilizes the open pore [18,19].

As apoptotic pores form in the MOM, mitochondria undergo functional and structural rearrangements [20]. The mitochondrial inner membrane (MIM) remodels, including *cristae* unfolding and reorganization [21–23]. A striking event is the permeabilization and extrusion of the MIM through BAX and BAK apoptotic pores in the MOM [24,25]. MIM permeabilization (MIMP) releases immunogenic mitochondrial factors, such as mitochondrial DNA (mtDNA), into the cytosol, which can trigger inflammatory responses under conditions of low caspase activity [26,27]. The growth rate of the apoptotic pore is tuned by the dynamic co-assembly of BAX and BAK, as well as by lipid composition, and regulates the sequential release of mitochondrial contents into the cytosol, impacting inflammatory signaling [9,12]. As a result, MIMP following MOMP can make apoptosis inflammatory, even under sublethal conditions, as recently reported in models of cellular senescence or tumor cell death [28–30].

However, the mechanisms of MIM extrusion and its connection to the nanoscale organization of BAX and BAK at the apoptotic pore in the MOM remain elusive. Addressing this question requires exploration of the discrete assemblies formed by BAX and BAK with regards to their copy number, spatial arrangement and position at organelles subdomains, which is technically challenging. To this aim, we report here a novel multi-correlative microscopy approach that allows the simultaneous investigation of the oligomeric state and supramolecular organization of BAK pores, in relation to the mitochondrial ultrastructural alterations and membrane integrity, at the single-pore level. We show that the oligomeric state is not determinant of the shape of BAK nanoassemblies, which instead delineate MOM openings. The size of MOM openings also impacts MIM extrusion, which follows mechanical forces, as supported by membrane dynamics simulations. Accordingly, MIM extrusion responds to osmotic swelling of the matrix. We find that MIM extrusion also contributes to apoptotic pore growth on the MOM, and thus to its structural arrangement, by exerting forces on its edge, which we quantify. Our findings thus uncover that MIM extrusion and the growth of the apoptotic pore at the MOM during apoptosis are tightly interconnected and establish a biophysical mechanism underlying these processes.

Results

CLOSE microscopy, a multi-correlative microscopy approach

To study how BAK oligomerization is related to the supramolecular arrangement of the apoptotic pore and how this affects mitochondrial integrity and ultrastructure, we developed a multi-correlative approach that we named CorreLative Oligomerization STED and Electron (CLOSE)

microscopy. This method enables the correlative assessment of the protein stoichiometry of single particles using photon-counting confocal microscopy and their nanoscale organization based on STED microscopy, as well as the cellular context information provided by an additional correlative step with electron tomography (ET) (Figure 1). CLOSE microscopy can be applied to discrete protein complexes in the cell, which we illustrate here by using it to dissect how BAK oligomerization and supramolecular assembly in the apoptotic pore relates to MOMP and MIM extrusion.

We seeded cells endogenously expressing HALO-BAK (Figure S1) on a coverslip coated with a coordinate system, and labeled HALO-BAK with the JFX650 HALO-tag ligand and mitochondria with MitoTracker Orange. We induced apoptosis with a combination treatment of BH3-mimetics (ABT-737 and S63845) and fixed the cells at 1 h, shortly after widespread MOMP in the cell population under our experimental conditions, which we estimated using TMRE fluorescence decline due to mitochondrial membrane potential loss as a proxy (Figure S1E-F) [9,11]. Next, the cells were subjected to photon-counting confocal imaging [11] followed by acquisition of a z-stack of the same cells with STED microscopy, to assess the stoichiometry and nanoscale structure of individual apoptotic pores, respectively. This order is important to minimize the impact of photobleaching during STED imaging for stoichiometry assessment by photon counting. The samples were then prepared for transmission ET to measure mitochondrial ultrastructure (Figure 1A). We used the cell position on the coordinate system, which was transferred to the resin like a stamp, to identify the same individual cell across the images and roughly overlay light and electron microscopy images. For fine correlation of the subcellular structures, aligning the mitochondrial network distribution across the images as an internal reference provided excellent results (Figure 1B).

We correlated distinct HALO-BAK nanoassemblies from the STED images with their fluorescence signal in photon counting confocal image. We quantified the copy number of BAK in these individual structures by ratiometric stoichiometry analysis based on the photon counting data as in [9,31–33] and using the endogenously expressed 32-mer nuclear pore complex component 96 (NUP96) tagged with HALO (NUP96-HALO) as a calibration standard [34] (Figure S2A-B). Next, we correlated the stoichiometry and supramolecular organization of single apoptotic HALO-BAK assemblies with the mitochondrial ultrastructure by overlaying the corresponding STED and ET plane images (Figure 1C). This allowed the examination of the structural integrity of mitochondrial membranes directly at the sites of apoptotic BAK assemblies measured by STED microscopy in the electron tomograms. Figure 1D exemplifies the outcome of this process by identifying a ring-

like BAK structure, which we estimated to contain about 20.8 ± 0.4 HALO-BAK molecules and which overlapped with a pore in the MOM. The fluorescence intensity of HALO-BAK along the MOM opening presented a drop inside the HALO-BAK ring, indicating an inner pore diameter of ~45 nm, which overlapped with the MOM discontinuity of ~30 nm, as measured in the EM tomogram (Figure 1E).

Interestingly, in some cases we detected MIM discontinuities indicative of MIMP directly at sites of HALO-BAK assemblies associated with MOM pores (Figures 1C and S3). Segmentation of the mitochondrial compartments in the tomogram clearly showed a pore at the MIM underneath the MOM HALO-BAK pore (Figures 1F and S3D-E; Supplementary Movie 1). The visualization of a MIM pore that correlates with apoptotic pores at the MOM with the MIM contained within the MOM reveals that MIMP can happen prior to extrusion. However, while the distribution of HALO-BAK at MOM openings suggests that it does not participate in MIMP (see below), we cannot draw definitive conclusions from our data regarding the mechanism of MIM pores.

The spatial arrangement of BAK nanoassemblies is not determined by their stoichiometry

We then performed a statistical analysis of the stoichiometry of HALO-BAK assemblies relative to their nanoscale organization. Consistent with previous studies [9], we found a broad distribution of HALO-BAK oligomeric states of individual apoptotic pores, ranging from 50 to over 500 HALO-BAK molecules per assembly (Figure S2C-G). We correlated the stoichiometry of individual HALO-BAK assemblies with their shape (classified as line, arc and ring structures) by correlating the data from photon-counting confocal and STED microscopy (Figure 2A-B). Contrary to our expectation that the HALO-BAK assembly shape would depend on oligomerization state, we did not find significant differences in BAK stoichiometry between line, arc and ring structures (Figure 2B). Despite the broad distribution, the median of BAK stoichiometry was about 100 HALO-BAK molecules in all three categories (Figure 2B and D-F). This suggests that the oligomeric state of BAK does not define the spatial arrangement of its assemblies, implying that it is likely determined by another mechanism.

HALO-BAK structures varied widely in size, ranging from less than 200 nm to over 1.4 µm in length/perimeter, with significant differences between them. With a median length of approximately 400 ± 130 nm, lines were smaller than arcs, which have a median length of approximately 500 ± 200 nm. Rings were larger than both lines and arcs, with a median perimeter of approximately 700 ± 400 nm, corresponding to a median ring diameter of approximately 200 ±

100 nm (Figure 2C). The size distributions align well with previous studies [9,12]. Yet, we found no significant correlation between the number of HALO-BAK molecules and the size of the structures (Figure 2G-J). The lack of correlation between stoichiometry and size of individual BAK assemblies found here indicates that BAK stoichiometry does not (solely) determine the supramolecular structural organization and size of BAK apoptotic pores (we cannot discard a role for BAX co-oligomerization, not quantified in our experiments).

HALO-BAK assemblies arrange along MOM openings at apoptotic pores

Given the toroidal nature of the apoptotic pore, we reasoned that other factors such as the physical properties of the membrane environment might contribute to define the pore size and shape. To explore this possibility, we correlated the shape of the supramolecular assemblies detected by STED microscopy with their mitochondrial environment visualized by ET. Generally, we found a strong correlation between the shape of the HALO-BAK nanoassembly with the position and type of MOM opening (Figure 3). We categorized MOM discontinuities (pores) in the EM images according to their appearance and location at mitochondria as i) discontinuities at the tips, ii) openings with MIM extrusion, iii) discontinuities along the lateral axes, or iv) at putative post-fission sites, where two mitochondrial fragments (and ER membranes) were in close proximity (Figure 3). MOM discontinuities appeared most frequently at mitochondrial tips (n = 39, Figures 3A and 5C) and as openings with MIM extrusion (n = 17, Figures 3B and 5D). Lateral discontinuities (n = 6, Figures 3C and 5E) and at putative post-fission sites (n = 2, Figures 3D and 5F) were comparably rare. These findings suggest that mitochondrial tips may be more favorable locations for apoptotic pore formation.

Biophysical forces promote MIM extrusion and apoptotic pore growth

CLOSE microscopy allowed us to document cases of MIM permeabilization and extrusion through MOM openings and to associate them apoptotic BAK assemblies of different shapes, although with limited statistics. To quantify the frequency MIM extrusion, we implemented an assay based on the visualization of the MOM and the mitochondrial matrix together with HALO-BAK in apoptotic cells under caspase inhibition fixed 1h after treatment, using confocal and STED microscopy (Figure 4A-B). Despite approximately 40% of mitochondria with microscopically intact MOM, MOM openings were associated with MIM extrusion in 39% of mitochondria, whereas only

21% of mitochondria showed MOM openings without MIM extrusion (Figure 4C-D), indicating the widespread nature of this event. Of note, we found BAK localized to one or both edges of the MOM opening but not to the MIM (Figure 4A-B).

Given the lack of correlation between oligomerization and pore size, we hypothesized that MIM extrusion through apoptotic MOM pores, promoted by MIMP-induced matrix swelling, might mechanically contribute to pore expansion. To test this hypothesis, we first evaluated whether matrix swelling promotes MIM extrusion. To this aim, we sought to induce osmotic swelling in the mitochondrial matrix by treatment with the ionophores valinomycin and nigericin (Val/Nig) [35], which we confirmed by confocal microscopy in healthy cells (Figure 4E). When applied to apoptotic cells, we found a significantly higher ratio of mitochondria with MIM extrusion in Val/Nig-treated cells compared to control untreated apoptotic cells (Figure 4F-H). These results indicate that increased mitochondrial matrix swelling (due to osmotic pressure) promotes MIM extrusion, uncovering a role of biophysical forces in the mechanism of MIM extrusion.

Interestingly, we observed that MIM extrusions through restricted openings of the MOM were squeezed at the site of the MOM opening adopting an hourglass shape (Figure 4B, D, G and I). This membrane deformation from the spherical shape of minimal energy reveals that the MOM opening exerts a force on the extruding MIM resulting from a line tension at the MOM edge that tends to close the pore. Such membrane arrangements also show that the MIM in turn counterbalances this force and keeps the MOM pore open.

By using an adapted version of the quantitative “neck model” geometrical analysis proposed by Baumgart et al. in [36], we estimated the line tension at the edge of the apoptotic pore directly in mitochondria of apoptotic cells. The analysis is based on the minimization of the energy contributions associated with membrane curvatures and tensions, transmembrane pressure, and line tension consistent with the measured membrane geometry based on the conservation of a zero value Hamiltonian [36,37]. For our analysis, we used images of axisymmetric hourglass-shaped MIM extrusions through MOM pores and aligned the mitochondrial longitudinal axis orthogonal to the open MOM pore axis. By tracing the MIM outline in the image, the local radius R and the local tangent angle ψ can be obtained as a function of the distance of the arc length S of the traced MIM (Figure 4J-K). Using a condition in which we minimize the energy of the Hamiltonian (by modulating the values of the membrane bending modulus, lateral tension and outer excess pressure, see Methods section) together with the experimental data obtained from the images, we estimated a line tension of $\gamma = 7 \pm 6\ \mathrm{pN}$ at the apoptotic pore edge on the MOM (Figure 4L-

M). This is in good agreement with the line tension estimated for BAX α-helix 5-mediated pores in model membranes [18].

Role of MIM confinement and permeabilization in extrusion through the MOM

We performed membrane dynamics simulations to gain further insights into the MIM extrusion process and to quantify the associated forces. We modeled the MIM as a triangulated fluid-elastic membrane with *cristae*-like structures densely packed into a pill-shaped container mimicking the MOM. To mimic MOMP, we opened a circular hole of fixed size at one end of the MOM container through which the MIM could escape.

In our simulations, we observed spontaneous MIM extrusion for apoptotic pores at the MOM whose radius exceeded 50% of the mitochondrial diameter (Figure 5A and S4A; Supplementary Movie 2). This evagination was associated with *cristae* rounding, which appeared to push the MIM through the MOM opening. Over time, we also observed *cristae* opening or merging with each other. Driving the MIM remodeling and extrusion in the simulations was a substantial reduction in the membrane bending energy.

As the MIM extrudes, it exerts an expansive force on the rim of the apoptotic pore, which we quantified in terms of an effective line tension (see Methods). For the pore in Figure 5A, with a relative diameter of $\approx 70\%$ of the mitochondrial diameter and a low membrane bending rigidity of $\kappa_B = 10\ k_BT$ [38], we obtained line tensions in the range of $\gamma_{\mathrm{tot}} \approx 3 - 5\ \mathrm{pN}$. For stiffer membranes, the line tensions were somewhat higher ($\gamma_{\mathrm{tot}} \approx 10 - 15\ \mathrm{pN}$ for $\kappa_{\mathrm{B}} = 60\ \mathrm{k_BT}$; Figure S4B). For larger pores, the effective line tension was reduced (Figure S4C). These line tensions are in quantitative agreement with the tensions of $\gamma \approx 7 \pm 4\ \mathrm{pN}$ deduced from the membrane shapes in the fluorescence microscopy images.

In the initial phase of MIM extrusion, we found that the matrix volume tended to decrease, associated with *cristae* rounding. However, as MIM extrusion progressed, we also observed volume increases (Figure 5A top panel). More dramatic volume increases were observed for the stiffer membranes with the larger pore, of diameter comparable to the mitochondrial diameter, as MIM extruded more and *cristae* opened up outside the MOM (Figure S4D).

To mimic the conditions of MIMP in apoptosis [24,25], we performed simulations with matrix osmotic swelling as a result of MIM leaks. In line with the microscopy data, we found that matrix swelling accelerated MIM extrusion (Figure 5B; Supplementary Movie 3), which also resulted in larger

effective line tensions on the apoptotic pore at the MOM, reaching values $> 10\ \mathrm{pN}$. Interestingly, even substantial osmotic forces did not result in significant MIM extrusion through a small ($< 50\%$ relative diameter) and static MOM pore (Figure S4E). However, the observed buildup in line tension would likely expand the apoptotic pore over time.

According to these results, we would expect that MIM extrusion events would be associated with larger apoptotic pores. To test this, we determined the length of individual MOM discontinuities measured as the maximum linear distance of interruption between the two ends of the MOM in the EM tomogram (Figure 5C-G). While individual examples of MOM discontinuities varied widely in length (Figure 5C-F), MOM openings associated with MIM extrusion were significantly larger than MOM discontinuities at the mitochondrial tip or side (Figure 5G), in agreement with the simulation predictions. These results indicate that MIM extrusion promotes apoptotic pore growth, impacting its structural organization.

Discussion

Here we present CLOSE microscopy, a multi-correlative approach that allows dissecting the oligomeric state of individual, discrete protein membrane complexes, based on photon-counting confocal imaging, and their supramolecular structural arrangement, imaged with STED microscopy, in relation to their cellular environment, visualized by electron tomography. It provides an easily implementable pipeline that brings together these three types of structural information and allows the study of focal protein complexes with unprecedented detail, opening new avenues for uncovering their molecular mechanisms. In future developments, it can be extended to live-cell super-resolution microscopy and combined with cryo-EM.

We apply CLOSE microscopy to study the assembly of the apoptotic pore and its relation with mitochondrial alterations in apoptotic cells (Figure 1). Our findings indicate that apoptotic pore size and shape are not determined, at least solely, by BAK oligomerization, although we cannot disentangle here the role of BAX on this process. We find that HALO-BAK oligomers delineate the apoptotic pore openings at the MOM, suggesting that it is the membrane opening that defines the spatial arrangement of BAK assemblies, which would also explain the heterogeneity in BAK nanoassemblies. The majority of MOM pores were located at tips, suggesting a preferential site for apoptotic pore assembly. Since dynamin-related protein 1 (DRP1) is functionally linked to apoptotic pore formation [39–42], it is reasonable to assume that the BAK assemblies and MOM

277 pores at mitochondrial tips may correspond to post-fission sites, as proposed in [43]. Remarkably,
278 we could visualize a few examples of pores at the MIM still contained within the MOM, which
279 raises the possibility of a kinetically regulated mechanism governing MIMP either within the
280 mitochondrion or following MIM extrusion.

281 The finding that induced osmotic mitochondrial matrix swelling promoted MIM extrusion indicates
282 that biophysical forces contribute to the MIM extrusion process. In addition, the hourglass shape
283 of the MIM extruding through the MOM pores revealed constriction by the MOM resulting from
284 line tension at the MOM opening edge. This implies that the force exerted by unfolding and
285 extrusion of the MIM through MOM openings contributes to pore widening independent of BAK
286 oligomerization, which is reasonable considering the lipid/protein nature of the apoptotic pore.
287 Accordingly, we could qualitatively and quantitatively recapitulate MIM extrusion from
288 mitochondria containing apoptotic pores at the MOM in membrane dynamic simulations. Above a
289 critical pore size, the MIM readily evaginated from the MOM in a process energetically driven by
290 a reduction in bending energy of the MIM, which is densely packed into *cristae* inside the MOM
291 in healthy cells. Remarkably, the effective line tensions on the apoptotic pore calculated directly
292 from the mechanical forces in the membrane dynamic simulations agree well with the line tensions
293 deduced from the membrane shapes seen by microscopy. In line with the wet lab experiments,
294 osmotic swelling of the matrix further accelerated the matrix extrusion in the membrane dynamic
295 simulations. It also induced a larger line tension at the apoptotic pore. While the rim was static in
296 our simulations, in apoptotic mitochondria the pore is dynamic, so that the increased line tensions
297 seen under osmotic swelling will likely further expand the pore unless balanced by contracting
298 forces, in line with the experimental data. Any pore expansion would thus result in a positive
299 feedback loop, as larger pores would substantially speed up MIM extrusion.

300 Collectively, our findings reveal that unfolding, swelling, and extrusion of the MIM mechanically
301 stabilize the apoptotic pore and promote its growth by counteracting the line tension at the edge
302 of the pore. They thus support a mechanism in which oligomerization of BAK (and BAX) at the
303 pore rim would initially open the pore and drive its expansion. Apoptotic pore growth would then
304 enable the extrusion of the MIM, further promoted by matrix swelling following MIMP. Beyond this
305 point, MIM extrusion would enhance apoptotic pore expansion at the MOM by counteracting the
306 line tension at the pore rim. If this tension is at least partially balanced by the pressure of the
307 extruding MIM, additional recruitment of BAK (and BAX) to the pore rim might shield exposed
308 hydrophobic membrane regions and further stabilize the pore. This model could explain the lack

of correlation between BAK stoichiometry and pore size, as well as why often large pores are not fully lined by BAK (and BAX) molecules.

Functionally, this may have consequences for determining the irreversibility of MOMP as well as for MIMP and the downstream inflammatory signaling triggered by mitochondrial contents release. On the one hand, while antiapoptotic BCL2 family members are capable of disassembling BAX oligomers to inhibit pore formation [44], MIM extrusion through the apoptotic pore involves reorganization of mitochondrial membranes to an extent that MOMP becomes energetically irreversible. This would likely leave the elimination of the permeabilized mitochondrion, for example by mitophagy [45], as the only mechanism to limit the cellular effects of mitochondrial permeabilization, thereby contributing to the transition from sublethal to lethal MOMP. On the other hand, exposure of the MIM to cytosolic components, both through the apoptotic pore and upon extrusion, would make it accessible to potential mediators of MIMP. The extruded MIM is no longer protected by the MOM, increasing its fragility and making it susceptible to rupture by mechanical stress, as an alternative mechanism of MIMP. Our findings uncover a previously unrecognized interplay between the MOM and the MIM that governs the dynamics of the apoptotic pore through biophysical forces, which may have consequences for MOMP irreversibility and downstream inflammatory signaling.

Materials and Methods

Cell culture. U2OS wild type, U2OS HALO-BAK, U2OS NUP96-HALO and HEK 293T cells were cultivated at 37 °C and 5% CO_2 in DMEM supplemented with 10% FBS and 1% penicillin/streptomycin (Invitrogen, Germany). The U2OS NUP96-HALO (U-2_OS-CRISPR-NUP96-Halo_clone_no252) CRISPR cell line was obtained from CLS Cell Lines Service GmbH, Eppelheim, Germany. All cell lines were tested mycoplasma negative.

The human osteosarcoma cells with BAK endogenously labeled with the HALO-Tag (U2OS HALO-BAK) were generated in this study and are available upon request.

Generation of U2OS HALO-BAK knock-in cell line using CRISPR/Cas9.

CRISPR/Cas9-mediated knock-in of HALO-Tag into the *BAK* locus directly upstream of the start codon was performed by a combinatorial approach using lentiviral transduction of the lentiCRISPR v2 (Addgene #52961, [46]) vector containing the SpCas9 enzyme and a single guide RNA (sgRNA) targeting *BAK* and transfection of a homology-directed repair (HDR) template containing 800 bp *BAK* homology arms and the HALO-Tag expression cassette into wild-type U2OS cells (Figure S1A). Genome-edited single cell clones were isolated and validated by sequencing of the *BAK* locus, immunoblotting, and fluorescence microscopy (Figure S1B-F).

sgRNA design and cloning of lentiCRISPR v2 vector. sgRNAs were designed on the human genomic *BAK* locus (*BAK1*, ENSG00000030110) near the start of the *BAK* open reading frame using the CRISPR guide RNA design tools Benchling and CRISPOR (Table 1). Suitable 20 bp sgRNAs with a NGG PAM motif were filtered based on the predicted on-target [47] and off-target [48] scores compared to the human reference genome (GRCh38 (hg38, Homo sapiens), Genome Reference Consortium) considering the described genome variants (dbSNP148, [49]). The selected sgRNA (sgRNA6: 5'-TGGAGGACGGGATCAGCCTG-3') was cloned into the lentiCRISPR v2 lentiviral transfer vector using a corresponding synthetic DNA oligonucleotide set (sgRNA6-forward: 5'-caccgTGGAGGACGGGATCAGCCTG-3' and sgRNA6-reverse: 5'-aaacCAGGCTGATCCCGTCCTCCAc-3') according to an adapted version of [50].

Design and generation of the HDR template. Homology regions to the *BAK* locus (800 bp upstream and downstream of the start codon, omitting the start codon) were amplified from genomic DNA isolated from wild-type U2OS cells and cloned into pUC19 (Addgene #50005) including a multiple cloning site between the homology regions using Gibson assembly. The HALO-Tag sequence (including the start codon and a $(GGS)_3$ linker) was amplified from pSems-HALO7-tag and cloned in between the homology regions into the pUC19-BAK-HDR vector by restriction cloning.

Virus production. To generate transgenic lentiviruses, HEK 293T cells were seeded in a 6-well plate at a density of 8 x 10^5 cells per well one day prior to transfection. The cells were transfected with 1.5 µg of the lentiCRISPR v2-BAK-gRNA6 lentiviral transfer vector, 650 ng of the psPAX2 lentiviral packaging vector (Addgene #12260), and 350 ng of the pMD2.G lentiviral envelope vector (Addgene #12259) using Lipofectamine™ 2000 (ThermoFisher). The cells were cultured for 4 days to allow virus production. On day 4, the virus-containing supernatant was collected, centrifuged at 1250 rpm for 5 minutes, and filtered through a 0.45 µm filter. Polybrene at a final concentration of 8 µg/ml was added to the viral supernatant prior to infection to increase transduction efficiency.

Cellular delivery and single cell sorting. Wild-type U2OS cells were transduced with the lentivirus containing the SpCas9-BAK-gRNA6 transfer cassette and co-transfected with 2 µg of the pUC19-BAK-HALO-HDR construct using Lipofectamine™ 2000. One week after transfection/transduction, the cells were stained with 300 nM Janelia Fluor 646 HaloTag® Ligand (Janelia Materials) for 45 minutes at 37°C. After staining, the cells were washed with DMEM and PBS to remove unbound dye. The cells were then analyzed by flow cytometry and individual cells positive for JF646 were isolated. Gating was performed to exclude dead cells using the DAPI channel to ensure that only viable cells were collected. Single-cell clones were expanded and validated by PCR genotyping of genomic DNA, immunoblotting, and fluorescence imaging.

Validation by Western blot. Cells were harvested using trypsin-EDTA (Sigma), resuspended in culture medium, and collected by centrifugation at 300 × g for 5 minutes at 4 °C. The cell pellets were washed twice with ice-cold PBS. For lysis, the pellets were resuspended in RIPA lysis buffer (50 mM Tris/HCl, pH 8.0, 150 mM NaCl, 1% (v/v) Triton™ X-100, 0.5% (w/v) sodium deoxycholate, 0.1% (w/v) SDS), incubated on ice for 20 minutes, and centrifuged at 20,000 × g for 20 minutes at 4 °C to remove cellular debris. Protein concentration was determined using the Bradford protein assay (Bio-Rad) according to the manufacturer's protocol. A total of 50–100 µg

of protein was boiled in SDS-PAGE sample buffer (62.5 mM Tris/HCl, pH 6.8, 2% (w/v) SDS, 10% (v/v) glycerol, 0.005% (v/v) β-mercaptoethanol, 0.01% (w/v) bromophenol blue) for 5 minutes at 95°C prior to SDS-PAGE. Proteins were transferred to a nitrocellulose membrane (Trans-Blot Turbo, Bio-Rad), and equal sample loading was confirmed using Ponceau S staining. The blots were washed with TBST (50 mM Tris/HCl, pH 7.5, 150 mM NaCl, 0.1% (v/v) Tween 20) and blocked with 5% (w/v) low-fat milk in TBST for 60 minutes. The membranes were incubated with a 1:1000 (v/v) dilution of rabbit α-BAK primary antibody (D4E4, CST, #12105) in 5% (w/v) milk in TBST at 4 °C for 16 hours. After three washes with TBST (5 minutes each), the membranes were incubated with a 1:10,000 (v/v) dilution of α-rabbit IgG-HRP secondary antibody (JIR, #111-035-003) in 5% (w/v) milk in TBST for 1 hour at room temperature. Blots were washed three times with TBST and developed using SuperSignal™ West Pico PLUS chemiluminescent substrate (Thermo Scientific), followed by detection on the Fusion SL Gel Chemiluminescence Documentation System (Vilber Lourmat). Images were adjusted for brightness and contrast, and cropped using Fiji/ImageJ (Table 1, [51]).

Validation by confocal microscopy and quantification of cell death kinetics. U2OS HALO-BAK cells were seeded in a glass-bottom 8-well µ-slide (IBIDI) at a density of $2x10^4$ cells per well one day prior to the experiment. Cells were stained with 300 nM Janelia Fluor X 650 HaloTag® Ligand for 1 hour at 37 °C to label BAK and with 150 nM MitoTracker™ Green FM (ThermoFisher, #M7514) to visualize mitochondria or with 150 µM tetramethylrhodamine ethyl ester (TMRE, ThermoFisher) for 20 minutes at 37 °C to measure mitochondrial depolarization. After labeling, the cells were washed twice with DMEM and incubated for 30 - 50 minutes at 37 °C to remove unbound dye. The localization of BAK in healthy conditions and the formation of BAK apoptotic foci and mitochondrial depolarization (loss in TMRE signal) during apoptosis were measured using an inverted laser scanning STED microscope (TCS SP8 STED 3x, Leica, Wetzlar) equipped with a PL Apo 100x/1.40 Oil $STED_{Ornage}$ objective (Leica, Wetzlar) and a tunable white light laser source (Leica, Wetzlar). MitoTracker™ Green FM was excited at a wavelength of 488 nm, JFX650 at 640 nm, and TMRE at a wavelength of 561 nm. The fluorescence emission signal of JFX60 and MitoTracker™ Green FM of JFX650 and TMRE was detected line sequentially on GaAsP detectors. Single confocal snapshots of individual cells were acquired to validate BAK expression and localization. To measure cell death kinetics, confocal time-lapse tile scans were acquired with a time resolution of 1 minute for a duration of 60 minutes after apoptosis induction using 10 µM ABT737 (Hölzel, #HY-50907), 10 µM S63845 (Hölzel, #HY-100741), and 10 µM Q-VD-OPh (Hölzel, #HY-12305g) in phenol red free DMEM at 37 °C and 5% CO_2. The average TMRE emission signal intensity was measured over time in individual cells using InageJ/Fiji (Table 1, [51]) and fitted with a one-phase exponential decay function to calculate the time point of 50% TMRE signal loss (t_{50}). The population distribution of the individual t_{50} values was fitted with a Gaussian function to derive the mean lag-time of 50% TMRE signal loss after apoptosis induction. For the further stoichiometry quantification, a time point 20-30 minutes after 50% TMRE signal loss (60 minutes after cell death induction) was chosen to ensure that the majority of cells underwent MOMP.

CLOSE microscopy

Sample preparation for light microscopy. U2OS HALO-BAK and U2OS NUP96-HALO cells were seeded in a glass-bottom imaging dish (MatTek, #P356-1.5-14-C) coated with a carbon finder grid using a mask (Leica, #16770162) and an ACE 200 carbon coater (Leica) at a density of 10^5 cells per dish one day before the experiment. U2OS NUP96-HALO cells are required as a calibration sample for ratiometric stoichiometry quantification and were treated in the same way as HALO-BAK cells throughout the preparation procedure unless indicated differently. The cells were stained with 300 nM Janelia Flour X 650 (JFX650) HALO-Tag ligand (Janelia Materials) for 1 hour at 37 °C to label BAK (or NUP96) followed by staining with 150 nM MitoTracker™ Orange CMTMRos (ThermoFisher, #M7510) for 30 minutes at 37 °C to visualize mitochondria. The cells were rinsed three times with DMEM and incubated for 1 hour at 37 °C to remove unbound dye. Apoptosis was induced in HALO-BAK cells with 10 µM ABT737 (Hölzel, #HY-50907), 10 µM S63845 (Hölzel, #HY-100741), and 10 µM Q-VD-OPh (Hölzel, #HY-12305g) for 50 – 60 minutes at 37 °C while the cells were monitored repeatedly at the microscope to check the progression of cell death (BAK foci formation). The cells were fixed with 2% glutaraldehyde (Sigma, #G5882) in fixation buffer (100 mM HEPES/KOH pH 7.4 (Carl Roth, #9105.1), 3 mM $CaCl_2$ (Sigma, #C7902), 2.5% (w/v) sucrose (Carl Roth, #4621.1), in HPLC water) for 30 minutes at room temperature and 30 minutes at 4 °C. The fixation reaction was quenched with 0.1 M glycine (Carl Roth, #0079.1) in cacodylate buffer (0.1 M sodium cacodylate (Applichem, #A2140.0100) in HPLC water) for 20 minutes at room temperature and the cells were washed three times with 0.1 M cacodylate buffer to remove excess quenching solution. The cells were kept in the dark at room temperature for subsequent microscopy or stored at 4 °C overnight.

Photon-counting confocal and STED microscopy. Protein stoichiometry was determined using photon-counting confocal microscopy as described in [9,31]. Briefly, confocal microscopy images were acquired with an inverted laser scanning STED microscope (TCS SP8 STED 3x, Leica, Wetzlar) equipped with a HC PL APO 100x/1.40 Oil $STED_{white}$ objective (Leica, Wetzlar) and a tunable white light laser source (Leica, Wetzlar). Z-stacks of 8 image planes were collected with an axial spacing of 300 nm, which was determined from point-spread function analysis of fluorescent beads as the maximum spacing required to record at least 80% of the maximum possible intensity from any point source. JFX650 was excited at 640 nm and MitoTracker™Orange CMTMRos at 561 nm. The excitation laser intensity and pixel dwell time were optimized to yield an emission signal detectable in the linear detector range while minimizing photobleaching during the acquisition process. Images were acquired with a pixel resolution of 1024 x 1024 pixel in a region of 46.5 x 46.5 µm (pixel size 45.45 nm) and a pixel dwell time of 2.44 µs (100 Hz scan speed) with 2-fold line averaging. Single emission photons were detected on a hybrid detector in photon counting mode. The NUP96-HALO cells were acquired with the same settings as the HALO-BAK cells for ratiometric stoichiometry analysis as described in [9,31]. Subsequently, the JFX650 and MitoTracker emission signal was acquired in the HALO-BAK cells in the same (lateral and axial) region of interest in STED (for JFX650, STED de-excitation at 775 nm) and confocal mode (for MitoTracker) with a pixel resolution of 2112 x 2112 pixel (pixel size 22.03 nm) and a pixel dwell time of 588 ns (200 Hz scan speed) with 8-fold line averaging. 2D STED z-stacks were acquired with the same axial spacing as in photon-counting mode. The fluorescence emission signal was detected line sequentially using hybrid detectors with a gating of 0.5 - 6 ns (for the STED image) and 8-fold line averaging. The localization coordinates of the acquired cells on the carbon finder grid were noted for position correlation for electron microscopy

image acquisition. Images were adjusted for brightness and contrast and smoothed using ImageJ/Fiji (Table 1, [51]). Where mentioned, images were deconvolved using Huygens Professional version 19.04 (Scientific Volume Imaging, The Netherlands, Table 1, http://svi.nl).

Stoichiometry quantification by ratiometric approach. Single particle detection and brightness analysis was performed on maximum intensity z-projections of photon-counting confocal microscopy images of HALO-BAK using an in-house Python algorithm (now available as an automated Molecularity Assessment Software (MAS, Table 1, [52]) as described in [9]. Briefly, single particles were detected in individual 5 x 5 pixel regions of interest (ROIs) based on fluorescence intensity threshold using a Difference of Gaussian detection algorithm. Particle intensities were fitted to a 2D Gaussian function and local background subtraction was performed in a slightly larger ROI around the particle ROI. Importantly, particles with their maximum intensity in the outer z-range were discarded from the analysis, as were particles with overlapping ROIs. To rule out the presence of more than one particle in a ROI, the localized particles were filtered based on the width of the 2D Gaussian. The full width at half maximum (FWHM) of all fitted particles was plotted and ROIs whose FWHM fell outside the 95th percentile of the normal distribution of the entire ROI population were excluded. Using the ratiometric approach, the stoichiometry of a particle of interest S_P was determined by ratiometric comparison of its fluorescence intensity I_P with the intensity of a reference standard I_S of known stoichiometry S_S labeled with the same fluorophore as the protein of interest according to the formula $S_P = I_P / (I_S / S_S)$. The 32-mer HALO-tagged nuclear pore complex protein NUP96, endogenously expressed in U2OS cells [34], was used as an internal calibration standard. For each cell, the intensity of the calibration standard I_S corresponds to the mean value of the Lognormal-fitted fluorescence intensity distribution individual NUP96-HALO oligomers from at least 5 imaged cells, measured on the same day and with the same parameters as the HALO-BAK samples (Figure S2A-B). For a given cell, the stoichiometry of individual HALO-BAK foci was plotted as a probability density function as well as cumulative counts. Exponential decay fitting was applied to the cumulative distribution to extract the average stoichiometry of HALO-BAK foci per cell (Figure S2C-E).

Sample preparation for electron microscopy. After light microscopy, cells were incubated with 1% osmium tetroxide (Science Services, #E19190), 1% potassium ferricyanide (Sigma, #P8131), and 1.25% sucrose (Roth, # 4621.1) in 0.1 M cacodylate buffer (Applichem, # A2140,0100) for 30 minutes at 4 °C. After washing three times with 0.1 M cacodylate buffer for 5 minutes each, samples were dehydrated in an ascending ethanol series (50%, 70%, 90%, and 100% (v/v) ethanol (VWR, #153386F) in ddH2O) for 7 minutes each at 4 °C. Cells were infiltrated with a 50% (v/v) mixture of epoxy embedding medium (Sigma, #45359-1EA-F) and ethanol for 1 hour, followed by a 66% (v/v) mixture of epoxy medium/ethanol for 2 hours, and pure epoxy medium overnight at 4 °C. Epoxy resin-filled TAAB capsules were placed upside down on the glass bottom of the imaging dish and cured at 60 °C for 48 hours. The glass bottom was removed by alternating submersion in boiling water and liquid nitrogen. The surface of the epoxy block was trimmed with a razor blade to a square at the previously noted localization coordinates of the acquired cell. Ultrathin serial sections of 300 nm for tomography were cut with an ultramicrotome (Leica Microsystems, UC6) equipped with a diamond knife (Science Services # DU3530). The ultrathin serial sections were transferred to a single slot grid (TEM, grid, 2x1 mm, slit, Cu, Science Services, #G2010-Cu) previously coated with 1% Pioloform® (Ted Pella, # 19244) in Chloroform

(VWR, # 83626.290) and incubated for 10 min with protein A gold 10 nm (CMC Utrecht, #A-1904) diluted 1:150 in ddH2O as fiducials and washed 5 times in ddH2O. Sections were stained with 1.5% uranyl acetate (Agar Scientific, #R1260A) in ddH2O for 15 minutes at 37 °C and 3% Reynold's lead citrate solution prepared from lead(II) nitrate (Roth, #HN32.1) and trisodium citrate dehydrate (Roth #4088.3) in ddH2O for 3 min. Grids were stored in grid boxes (Science Services, G71135-01) until imaging.

Electron tomography and CLEM image generation. Electron microscopy images were acquired using a JEM-2100 Plus transmission electron microscope (JEOL) operating at 200 kV for tomography equipped with a OneView 4K camera (Gatan). Transmission electron microscopy was used to identify the cells previously imaged by light microscopy based on the cell outline and shape of the mitochondrial network. Tomograms of 300 nm thick sections were then generated by tilting the sample along one axis from -60° to 60° using SerialEM (Mastronarde, 2005) and reconstructed using the Etomo plugin for IMOD (Table 1, [53]). Overlays of TEM and STED images were generated using the EC-CLEM plugin of the image analysis software ICY (Table 1, [54]). Since the 2D STED z-stacks have an axial resolution of less than 300 nm, a single z-plane of the 2D STED z-stack was aligned and overlayed with the correlating tomogram.

3D rendering of tomograms. The MOM, MIM, *cristae*, and ER membranes were traced using the Microscopy Image Browser ver. 2.83 (MIB, Table 1, http://mib.helsinki.fi) with a line width of 3 to 4 pixels. Each membrane was redrawn separately. Positions with insufficient contrast in ER and *cristae* membranes were redrawn if the z-image above and below showed a continues membrane 3D rendering and visualization of the traced membranes was performed using Imaris software version 10.0.01 (Oxford Instruments, Table 1).

Correlation of BAK stoichiometry and size of BAK structures. The length of individual BAK line and arc structures as well as the perimeter of ring structures were measured in STED images using the segmented line tracing tool in ImageJ/FiJi (Table 1, [51]). For stoichiometry/size correlation of individual BAK structures, line and arc lengths and ring perimeters were manually correlated with BAK stoichiometry derived from stoichiometric quantification of the photon-counting confocal image of the same cell. The correlation between stoichiometry and size was tested by calculating the non-parametric Spearman correlation coefficient r and the two-tailed P value at a 95% confidence interval.

Measurement of the size of MOM discontinuities. The size of MOM openings was measured using the line plot length tool in ImageJ/FiJi (Table 1, [51]). The position of BAK foci was localized in the CLEM image, and the position with the highest contrast of the MOM in the tomogram was used to define the start and end points of the line plot. The fluorescence intensity of HALO-BAK and the opening of the MOM from the EM tomogram (Figure 1D-E) was measured using a (curved) line profile along the MOM opening with a width of 5 pixels. The fluorescence intensity was plotted using the line plot tool, from which the linear distance between signal maxima (BAK fluorescence) or minima (EM signal) was measured. We cannot discard that sample preparation for EM may affect the integrity of the MOM, which we did not detect as an issue by visual inspection of our samples. Yet, we specifically focused on MOM discontinuities associated with HALO-BAK assemblies, found as few discrete foci on mitochondria, further decreasing the likelihood that the MOM discontinuities analyzed could be artifactual.

MIM extrusion measurement and mitochondrial matrix swelling. To measure the extent of MIM extrusion through apoptotic pores in the presence or absence of osmotic mitochondrial matrix swelling, U2OS HALO-BAK cells were seeded in a glass-bottom 8-well µ-slide (IBIDI) at a density of $2x10^4$ cells per well one day before the experiment. Cells were stained with 300 nM Janelia Fluor X 650 HaloTag® Ligand for 1 hour at 37 °C to label BAK and with 150 nM MitoTracker™ Orange CMTMRos for 20 minutes at 37 °C to visualize the mitochondrial matrix. After labeling, the cells were washed twice with DMEM and incubated for 15 - 30 minutes at 37 °C to remove unbound dye. Apoptosis was induced using 10 µM ABT737, 10 µM S63845, and 10 µM Q-VD-OPh for 60 minutes in phenol red free DMEM at 37 °C and 5% CO_2. For osmotic mitochondrial matrix swelling, cells were treated with 10 nM valinomycin (Sigma, #V0627) and 10 nM nigericin (Sigma, #N7143) in DMEM for 5 minutes. The cells were fixed in 4% (v/v) PFA in PBS for 10 minutes and incubated in PBS with 50 mM NH_4Cl for 15 minutes at room temperature to quench unreacted fixative. The cells were permeabilized in PBS with 0.25% (v/v) Triton™ X-100 for 5 minutes, washed three times for 5 minutes in PBS, and blocked for PBS with 2% (w/v) BSA for 60 minutes at room temperature. The MOM was labeled with a 1:200 (v/v) dilution of rabbit α-TOM20 (Sigma, #HPA011562) in 2% (w/v) BSA overnight at 4 °C. After extensive washing with PBS, the cells were incubated with a 1:150 (v/v) dilution of Abberior STAR GREEN-coupled goat α-rabbit IgG secondary antibody (Abberior, #STGREEN-1002-500UG) for 1 hour at room temperature, followed by washing with PBS.

Alternatively, cells were seeded two days prior to the experiment (as described above) and transfected one day before the experiment with 50 ng TOM20-SNAP using Lipofectamine™ 2000. The cells were stained with 300 nM Janelia Fluor X 650 SnapTag® Ligand (Janelia Materials) for 30 minutes at 37 °C to label TOM20. In parallel, the MIM was labeled with 600 nM PKFO and 10 µM verapamil at 37 °C for 2 hours. Apoptosis and osmotic swelling of the mitochondrial matrix were induced as described above. The cells were fixed with 2% glutaraldehyde (in fixation buffer (100 mM HEPES/KOH pH 7.4, 3 mM $CaCl_2$, 2.5% (w/v) sucrose, in HPLC water) for 20 minutes at room temperature and washed thoroughly with PBS.

Confocal/2D STED microscopy images of single cells were acquired using an inverted laser scanning STED microscope (TCS SP8 STED 3x, Leica, Wetzlar) equipped with a HC PL APO 100x/1.40 Oil $STED_{white}$ objective (Leica, Wetzlar) and a tunable white light laser source (Leica, Wetzlar). JFX650 was excited at a wavelength of 640 nm, MitoTracker™Orange CMTMRos and PKFO at 561 nm, and Abberior STAR GREEN at 488 nm. STED de-excitation of JFX650 and PKFO was performed at 775 nm. The fluorescence emission signal of JFX650, MitoTracker™Orange CMTMRos and Abberior STAR GREEN or JFX650 and PKFO was detected line sequentially using hybrid detectors with a gating of 0.5 - 6 ns (for the STED image) and 8-fold line averaging. Images were adjusted for brightness and contrast using InageJ/Fiji (Table 1) and, where mentioned, deconvolved using Huygens Professional version 19.04 (Scientific Volume Imaging, The Netherlands, Table 1, http://svi.nl).

MIM extrusion was quantified by eye as intact mitochondria, mitochondria with MOM discontinuity, and mitochondria with or without MIM extrusion after osmotic matrix swelling.

Line tension measurement. To measure the line tension of MIM, we adapted the protocol proposed by Baumgart et al [36] based on the theory of Jülicher and Lipowsky [55]. This protocol

consists of tracing experimental images of axisymmetric mitochondria in such a way that the equatorial plane is orthogonal to the plane defined by the mitochondrial pore. Defining this reference plane allows us to obtain the local radius R and the tangent angle ψ, as a function of the arc length S (Figure 4J-K). $R(S)$ and $\psi(S)$ allow us to calculate the Hamiltonian, H, which is conserved on every point of the system (Figure 4K-L). This Hamiltonian is defined by the bending, pressure, tension, and line energy along the arc length, and in the limit of low temperatures, the following equality holds:

$$H^{(i)} = \frac{\kappa^{(i)} R}{2}\left(\dot{\psi}^2 - \left(\frac{\sin\psi}{R}\right)^2\right) - \Sigma^{(i)} R - \frac{P}{2}R^2 \sin\psi + \lambda\cos\psi = 0$$

where $\kappa^{(i)}$, $\Sigma^{(i)}$, P, are the bending modulus, lateral tension, and outer excess pressure, respectively, of the mitochondria in the ith domain, i.e., MIM exposed to the cytosol and unperturbed MIM. The dot indicates differentiation with respect to the arc length. In this model, we do not take into account the energy contribution from the spontaneous curvature. $\lambda(S)$ is a Lagrange multiplier that enforces the spatial constraint $\dot{R} = \cos\psi$. Its derivative with respect to S satisfies[55]:

$$\dot{\lambda} = \frac{\kappa^{(i)}}{2}\left(\dot{\psi}^2\right) - \frac{\kappa^{(i)}\sin^2\psi}{2R^2} + \Sigma^{(i)} + PR\sin\psi,$$

For the MIM inside ($S < S^*$) and outside the MOM ($S > S^*$), we interpret $\lambda(S)$ as the radial force of the MOM onto the MIM, respectively. A step in $\lambda(S)$ at the MOM pore then amounts to an effective line tension on the pore,

$$\lambda(S^* - \epsilon) = \lambda(S^* + \epsilon) + \gamma$$

akin to the step in $\lambda(S)$ at the domain boundary of the phase-separated system studied by Baumgart et al [36]. The step height γ is the line tension to be determined, and ϵ an infinitesimal distance on either side of the boundary. $\lambda(S)$ was obtained by integrating along the entire arc length and using the boundary condition, and used to calculate $H(S)$ (Figure 4L).

Using R, ψ, and $\dot{\psi}$ from the experimental images, we modulate the values of $\kappa^{(2)}$, $\Sigma^{(i)}$, P, and γ to minimize the sum of $[H(S)]^2$. Here, we set $\kappa^{(1)} = 15.48\ KT$ as this value was reported for mammalian MIM in computational studies [56]. As a validation of the above ansatz, we obtained a minimized value for the MOM of $\kappa^{(2)} = 16.14\ KT \approx \kappa^{(1)}$, i.e., with the bending rigidity essentially unchanged as expected.

Modeling of MIM dynamics. The dynamics of MIM remodeling during BAX/BAK–mediated apoptosis was simulated using the TriMem code (Table 1) for a triangulated fluid-elastic model of the membrane [57]. In TriMem, the position of the vertices, the topology of the connecting edges, and in turn the membrane shape evolve in time according to the so-called Helfrich Hamiltonian. Here, the dynamics of the MIM is subject in addition to its confinement by the MOM structure.

As a minimal model of the *cristae* structures in an intact mitochondrion, we placed a stack of 6 flat disk-shaped membranes inside a tubular membrane lining the MOM container. By establishing additional edges, we created necks to fuse the disk shapes with the tubular membrane. The

resulting mesh contained 11399 vertices and 22794 triangular faces. To set up, smoothen, and subdivide the initial mesh structures, we used the Autodesk Fusion360 software (Table 1).

Modelling of MOM and its interaction with the MIM. We described the MOM of an intact mitochondrion as a rigid pill-shaped container confining the MIM (Figure S5). The container consists of a cylinder of radius $\mathbf{R_{container}} = \mathbf{0.71\ \mu m}$ and height $\mathbf{h_{container}} = \mathbf{0.74\ \mu m}$ aligned with the $\mathbf{Z}$ axis that is capped at its ends by outward-facing hemispheres of radius $\mathbf{R_{container}}$. To model the confinement of the MIM in the MOM, we added a repulsive potential on the vertices of the MIM mesh as a function of their normal distance $\mathbf{r}$ from the container,

$$\mathbf{V(r)} = \boldsymbol{\epsilon}\left[\left(\frac{\mathbf{s_0}}{\mathbf{r}}\right)^{\mathbf{12}} - \mathbf{2}\left(\frac{\mathbf{s_0}}{\mathbf{r}}\right)^{\mathbf{6}} + \mathbf{1}\right]\boldsymbol{\Theta}(\mathbf{s_0} - \mathbf{r}) \tag{1}$$

where $\boldsymbol{\Theta}$ is the Heaviside function, $\mathbf{s_0}$ is the length scale of the confining potential, and $\boldsymbol{\epsilon}$ its characteristic energy whose values, as listed in Table S1.

To describe the BAX/BAK-mediated formation of a pore in the MOM, we introduced a circular opening in the external container. Following the observations in the microscopy experiments, we placed the pore center axially at $\mathbf{z} > \mathbf{0}, \mathbf{x} = \mathbf{y} = \mathbf{0}$ at one end of the mitochondrion. With a polar angle of 'ALPHA ($\boldsymbol{\alpha}$)' on the hemispherical cap quantifying the size of the opening (SI), the radius of the pore is $\mathbf{r_{pore}} = \mathbf{R_{container}}\,\mathbf{sin}(\boldsymbol{\alpha})$. For MIM vertices $\mathbf{i}$ at Cartesian position $(\mathbf{x_i}, \mathbf{y_i}, \mathbf{z_i})$, we similarly defined a polar angle $\boldsymbol{\theta_i} = \mathbf{cos}^{-1}\left(\frac{\mathbf{z_i} - \mathbf{h_{container}}}{\sqrt{\mathbf{x_i^2} + \mathbf{y_i^2} + (\mathbf{z_i} - \mathbf{h_{container}})^2}}\right)$. For $\boldsymbol{\theta_i} \geq \boldsymbol{\alpha}$, we defined the distance $\mathbf{r}$ in Eq. (1) as the closest distance to the cylinder and the two hemispheres; for $\boldsymbol{\theta_i} < \boldsymbol{\alpha}$, we instead set $\mathbf{r}$ to the minimum distance $\boldsymbol{\Delta r_i}$ to the circular rim,

$$\boldsymbol{\Delta r_i} = \sqrt{\boldsymbol{\Delta\rho_i^2} + \boldsymbol{\Delta z_i^2}} \tag{2}$$

where $\boldsymbol{\Delta\rho_i}$ and $\boldsymbol{\Delta z_i}$ denote the shortest radial and vertical distances between the rim and the vertex $\mathbf{i}$ in cylindrical coordinates,

$$\boldsymbol{\Delta\rho_i} = \mathbf{R_{container}}\,\mathbf{sin}(\boldsymbol{\alpha}) - \sqrt{\mathbf{x_i^2} + \mathbf{y_i^2}}$$

$$\boldsymbol{\Delta z_i} = \mathbf{R_{container}}\mathbf{cos}(\boldsymbol{\alpha}) - (\mathbf{z_i} - \mathbf{h_{container}})$$

We define the contributions of the latter terms to the potential energy as the rim potential. From the associated forces exerted by the MIM on the pore rim, we deduced an effective line tension, as explained below.

Simulations. The initial MIM shape mimicking an intact mitochondrion was equilibrated with TriMem (Table 1). The hybrid Monte Carlo production runs were performed using the parameters provided in SI. The integration time step in the Hamiltonian dynamics segments of the hybrid Monte Carlo (hMC) runs was set to $\mathbf{1} \times \mathbf{10^{-4}}\boldsymbol{\tau}$, where $\boldsymbol{\tau}$ is the reduced time unit. Each segment consisted of 50 time steps, thus lasting $\mathbf{0.005}\boldsymbol{\tau}$. The simulations were run at reduced temperature

$\mathbf{T} = \mathbf{1}$ and vertex mass $\mathbf{M} = \mathbf{0.2}$ with bending rigidities $\boldsymbol{\kappa_B} = \mathbf{10\ k_BT}$ [38] and $\mathbf{60\ k_BT}$, respectively. Stiffening the membrane tended to speed up the membrane evagination. In separate runs, we examined the effect of an osmotic inflation of a leaky MIM by ramping up the matrix volume after time point $\mathbf{7500\tau}$. For this, we added a term $\boldsymbol{\kappa_V}\left(\frac{\mathbf{V(t)}}{\mathbf{10V_0}} - \mathbf{1}\right)^{\mathbf{2}}$ to the potential energy (eq 7 in [57]), where $\mathbf{V_0}$ is the initial volume of the matrix and $\mathbf{V(t)}$ the instantaneous volume. Starting from zero, we increased the coupling constant $\boldsymbol{\kappa_V}$ every $\mathbf{500\tau}$ by $\mathbf{5000 k_BT}$.

We performed simulations with varying pore opening angles of $\boldsymbol{\alpha} = \mathbf{0.25, 0.5, 0.75, 1.0}$, and $\mathbf{1.5}$ radians, which correspond to reduced pore radii of $\mathbf{r}_{\text{frac}} = \frac{\mathbf{r}_{\text{pore}}}{\mathbf{R}_{\text{container}}} = \mathbf{0.247,\ 0.479,\ 0.681, 0.841}$ and $\mathbf{0.997}$. Note that the MOM shape and pore opening are fixed in each replica run.

Pore line tension evaluation. The MIM evaginating through the pore exerts forces onto the rim of the pore in the MOM. We convert these forces into an effective line tension ($\boldsymbol{\gamma}$) decomposed into two contributions: (1) $\boldsymbol{\gamma}^{(\mathbf{1})}_{\mathbf{pore}}$ accounting for forces associated with direct vertex-rim interactions, as captured by the rim potential and (2) $\boldsymbol{\gamma_\sigma}^{(2)}$ accounting for pore expansion driven by tension in the MOM. We estimate the former as the mean outward directed force on the rim in plane with the pore,

$$\boldsymbol{\gamma}^{(\mathbf{1})}_{\text{pore}} = \frac{\oint_0^{2\pi} \tilde{\mathbf{F}}(\boldsymbol{\phi}) \cdot \hat{\boldsymbol{\rho}}\, \mathbf{d\phi}}{\oint_0^{2\pi} \mathbf{d\phi}} = \frac{\oint_0^{2\pi} \tilde{\mathbf{F}}(\boldsymbol{\phi}) \cdot \hat{\boldsymbol{\rho}}\, \mathbf{d\phi}}{\mathbf{2\pi}} \rightarrow \frac{\mathbf{1}}{\mathbf{2\pi}} \sum_{\substack{\text{Vertex i} \\ (\theta_i < \alpha)}} \mathbf{F}_{\text{pore;i}} \tag{3}$$

where $\boldsymbol{\phi}$ is the angle in the cylindrical coordinate system, $\hat{\boldsymbol{\rho}}$ is a radial unit vector normal to the $\mathbf{Z}$ axis, and $\tilde{\mathbf{F}}_{\mathbf{pore}}(\boldsymbol{\phi})$ is the force exerted on the pore rim by the MIM. In the triangulated membrane model, $\mathbf{F}_{\mathbf{pore;i}}$ denotes the radially directed component of the force a vertex $\mathbf{i}$ exerts on the pore rim, which we calculate from the gradient of the container potential $\mathbf{V(r)}$ as

$$\mathbf{F}_{\mathbf{pore;i}} = -\frac{\mathbf{dV(r)}}{\mathbf{d\rho}} = -\frac{\mathbf{dV(r)}}{\mathbf{dr}}\frac{\mathbf{dr}}{\mathbf{d\rho}} = \frac{\mathbf{12\epsilon\Delta\rho_i}}{\mathbf{\Delta r_i^2}}\left[\left(\frac{\mathbf{s_0}}{\mathbf{\Delta r_i}}\right)^{\mathbf{12}} - \left(\frac{\mathbf{s_0}}{\mathbf{\Delta r_i}}\right)^{\mathbf{6}}\right] \tag{4}$$

where $\boldsymbol{\Delta r}$ and $\boldsymbol{\Delta\rho}$ denote the closest distance and the closest lateral distance of the vertex $\mathbf{i}$ from the pore rim as defined in Eq. (2).

In addition to the direct interaction between the MIM and the pore rim inducing $\boldsymbol{\gamma}^{(\mathbf{1})}_{\mathbf{pore}}$, we account for an expansive force induced by the MIM pushing up against the MOM for $\boldsymbol{\theta_i} \geq \boldsymbol{\alpha}$. These forces normal to the MOM create an effective excess pressure ($\boldsymbol{\Delta P}$) acting on the MOM. As a curved surface, this pressure in turn induces a surface tension $\boldsymbol{\sigma}$ in the MOM. For a sphere of radius $\mathbf{R}_{\text{container}}$, this tension is given by the Laplace-Young relation, $\boldsymbol{\sigma} = \frac{\mathbf{\Delta P R}_{\text{container}}}{\mathbf{2}}$, which we use here as a rough approximation also for the model mitochondria. We calculate the average pressure gradient across the MOM as

$$\mathbf{\Delta P} = \frac{\sum_{\substack{\mathbf{Vertex\ i} \\ (\boldsymbol{\theta_i} \geq \boldsymbol{\alpha})}} \mathbf{F}_{\perp;\mathbf{i}}}{\mathbf{A_{container}}} \tag{5}$$

where $\mathbf{F_{\perp;i}} = -\frac{\mathbf{dV}}{\mathbf{dr}} = \frac{\mathbf{12\epsilon}}{\mathbf{\Delta r_i}}\left[\left(\frac{\mathbf{s_0}}{\mathbf{\Delta r_i}}\right)^{\mathbf{12}} - \left(\frac{\mathbf{s_0}}{\mathbf{\Delta r_i}}\right)^{\mathbf{6}}\right]$ is the normal force on the container exerted by vertex i for $\mathbf{r} < \mathbf{s_0}$ outside the pore angle $\boldsymbol{\alpha}$. $\mathbf{A_{container}} = \mathbf{4\pi R^2_{container}} + \mathbf{2\pi R_{container} h_{container}} - \mathbf{2\pi R^2_{container}(1 - cos(\alpha))}$ denotes the area of the container, with the spherical cap cut out by the pore subtracted.

We convert the tension $\boldsymbol{\sigma}$ in the MOM into a line tension in the pore by requiring mechanical stability,

$$\mathbf{2\pi r_{pore}} \boldsymbol{\gamma_\sigma}^{(2)} = \mathbf{\pi r^2_{pore}} \boldsymbol{\sigma} \tag{6}$$

adopting the relation for a planar membrane. The resulting effective line tension is then

$$\boldsymbol{\gamma}_{\mathrm{tot}} \approx \boldsymbol{\gamma}_{\mathrm{pore}}{}^{(1)} + \boldsymbol{\gamma_\sigma}^{(2)} \approx \frac{\mathbf{1}}{\mathbf{2\pi}} \sum_{\substack{\text{Vertex i} \\ (\theta_i < \alpha)}} \mathbf{F_{pore;i}} + \frac{\mathbf{R_{container} r_{pore}}}{\mathbf{4A_{container}}} \sum_{\substack{\text{Vertex i} \\ (\theta_i \geq \alpha)}} \mathbf{F_{\perp;i}} \tag{7}$$

We evaluate this expression for the structures saved along the TriMem simulations to obtain an effective line tension on the BAX/BAK-pore as a function of time, as the MIM evaginates through the pore. With physical units for the container dimensions and membrane bending rigidity, the effective line tensions has units of force (i.e., pN).

Data representation and statistical analysis. All correlative stoichiometry super-CLEM data are representative or individual examples of n = 8 independent experiments (Figures 1, 2, S2 and S3), except for the classification of MOM pore categories (Figures 3 and 5C-G), which represents n = 6 independent experiments. All other data are representative of at least n = 3 independent experiments (Figures 4 and S1), as indicated in the respective figure legends.

Quantitative data (in Figures 2B-C, and J, 4C, H and M, 5G, and S2F-G) were tested for normality using the Shapiro-Wilk normality test with the method of Royston using GraphPad Prism (Table 1) with a cut-off of α = 0.05 (95% confidence level). Data with a normal distribution are presented as mean ± SD, while data that do not follow a normal distribution are presented as median ± interquartile range (IQR), both together with the individual data points. Data containing at least one non-normally distributed data set along with otherwise normally distributed data sets were treated as non-normally distributed.

Significance levels of non-normally distributed data and data with more than two unpaired data sets were assessed using non-parametric one-way ANOVA (Kruskal-Wallis test) and Dunn's multiple comparison test to determine multiplicity adjusted P values (family-wise significance and confidence level set to 0.05, Figures 2B-C and J, 4C, and 5G). Normally distributed data with two unpaired data sets were tested for significance using unpaired non-parametric two-tailed Student's t-test (Mann-Whitney test, Figure 4H) at 95% confidence level. Corresponding P values are reported in the respective figures.

All datasets were analyzed using GraphPad Prism version 7.05 for Windows for data presentation and statistical analysis (Table 1).

Table 1: Software

Name	Source	Availability
GraphPad Prism version 7.05 for Windows	GraphPad Software, Boston, Massachusetts USA	www.graphpad.com
Molecularity Assessment Software (MAS)	[52] https://doi.org/10.1021/acs.jpca.3c00368	https://github.com/jdanial/MAS
ImageJ/FIJI	[51] https://doi.org/10.1038/nmeth.2019	https://imagej.net/software/fiji/
Huygens Professional	Scientific Volume Imaging, Netherlands	http://svi.nl
Microscopy Image Browser ver. 2.83	Electron Microscopy Unit, Institute of Biotechnology, University of Helsinki, Finland	http://mib.helsinki.fi
Imaris software v. 10.0.01	Oxford Instruments	https://imaris.oxinst.com/
IMOD Version 4.11.5	University of Colorado	https://bio3d.colorado.edu/imod/
Icy	[58]	https://icy.bioimageanalysis.org/
EC-CLEM plugin for Icy	[54]	https://icy.bioimageanalysis.org/plugin/ec-clem/
Benchling	Benchling	https://benchling.com
CRISPOR	[59]	http://crispor.org

TriMem		https://github.com/bio-phys/trimem
Fusion 360	Autodesk	https://github.com/AutodeskFusion360

Data availability

This study includes no data deposited in external repositories.

Code availability

Single-particle detection and brightness analysis were performed using an in-house Python algorithm, which is available upon request. This algorithm is now available as an automated molecularity assessment software (MAS; see Table 1). The original code for membrane dynamics simulation is available on GitHub (https://github.com/bio-phys/trimem/tree/external-potential). The code for the line tension calculation will be available on GitHub upon publication.

Author contributions

A.J. and T.D. implemented CLOSE microscopy and performed research, with support from F.G., K.S. and A.S. C.Z. generated and characterized the HALO-BAK cell line. D.G. perfomed line tension analysis from images. H.K. and G.H. set up and analyzed the membrane dynamics simulations with help from J.K. A.G.S. conceived the project and supervised research. A.J. and A.G.S. wrote the manuscript with the help of all other authors.

Acknowledgements

We thank the CECAD imaging facility for excellent assistance and specifically Dr. Christian Jüngst for his outstanding technical and methodological support regarding image acquisition and analysis for stoichiometry quantification and STED microscopy. We further thank Gudrun Zimmer for technical support. This work was funded by the European Research Council (ERC-Co 817758) and the Deutsche Forschungsgemeinschaft (DFG, German Research Foundation) – 654651/GRK2364 MOMbrane, DFG-INST 2016/742-1 FUGB and DFG-INST 216/793-1 FUGG, and the Max Planck Society. We thank the Max Planck Computing and Data Facility (MPCDF) for computational support and Sebastian Kehl for help with the TriMem membrane dynamics simulation code. H.K thanks International Max Planck Research Schools on cellular biophysics (IMPRS-CBP).

Declaration of AI and AI-assisted technologies in the writing process

During the preparation of this work the authors used DeepL Write (DeepL SE) in order to improve readability and language of the text. After using this tool, the authors reviewed and edited the content as needed and take full responsibility for the content of the publication.

Disclosure statement and competing interests

The authors declare that they have no conflict of interest.

References

1. Lindsten, T. *et al.* The Combined Functions of Proapoptotic Bcl-2 Family Members Bak and Bax Are Essential for Normal Development of Multiple Tissues. *Molecular Cell* **6**, 1389–1399 (2000).

2. Wei, M. C. *et al.* Proapoptotic BAX and BAK: A Requisite Gateway to Mitochondrial Dysfunction and Death. *Science* **292**, 727–730 (2001).

3. Bock, F. J. & Tait, S. W. G. Mitochondria as multifaceted regulators of cell death. *Nature Reviews Molecular Cell Biology* **21**, 85–100 (2019).

4. Goldstein, J. C. *et al.* Cytochrome c is released in a single step during apoptosis. *Cell Death & Differentiation 2005 12:5* **12**, 453–462 (2005).

5. Goldstein, J. C., Waterhouse, N. J., Juin, P., Evan, G. I. & Green, D. R. The coordinate release of cytochrome c during apoptosis is rapid, complete and kinetically invariant. *Nature Cell Biology 2000 2:3* **2**, 156–162 (2000).

6. Rehm, M., Düßgmann, H. & Prehn, J. H. M. Real-time single cell analysis of Smac/DIABLO release during apoptosis. *Journal of Cell Biology* **162**, 1031–1043 (2003).

7. Galluzzi, L. *et al.* Molecular mechanisms of cell death: recommendations of the Nomenclature Committee on Cell Death 2018. *Cell Death & Differentiation* **25**, 486–541 (2018).

8. Julien, O. & Wells, J. A. Caspases and their substrates. *Cell Death & Differentiation 2017 24:8* **24**, 1380–1389 (2017).

9. Cosentino, K. *et al.* The interplay between BAX and BAK tunes apoptotic pore growth to control mitochondrial-DNA-mediated inflammation. *Molecular cell* **82**, 933-949.e9 (2022).

10. Große, L. *et al.* Bax assembles into large ring-like structures remodeling the mitochondrial outer membrane in apoptosis. *The EMBO Journal* **35**, 402–413 (2016).

11. Salvador-Gallego, R. *et al.* Bax assembly into rings and arcs in apoptotic mitochondria is linked to membrane pores. *The EMBO Journal* **35**, 389–401 (2016).

12. Schweighofer, S. V. *et al.* Endogenous BAX and BAK form mosaic rings of variable size and composition on apoptotic mitochondria. *Cell Death & Differentiation 2024 31:4* **31**, 469–478 (2024).

13. Terrones, O. *et al.* Lipidic pore formation by the concerted action of proapoptotic BAX and tBID. *The Journal of biological chemistry* **279**, 30081–30091 (2004).

14. García-Sáez, A. J. *et al.* Peptides corresponding to helices 5 and 6 of Bax can independently form large lipid pores. *The FEBS journal* **273**, 971–81 (2006).

15. Qian, S., Wang, W., Yang, L. & Huang, H. W. Structure of transmembrane pore induced by Bax-derived peptide: evidence for lipidic pores. *Proceedings of the National Academy of Sciences of the United States of America* **105**, 17379–83 (2008).

16. Basanez, G. *et al.* Studying the mechanism of Bax induced membrane destabilization: does Bax promote lipidic pore formation? in *FASEB JOURNAL* vol. 13 A1436--A1436 (1999).

17. Basañez, G. *et al.* Bax-type apoptotic proteins porate pure lipid bilayers through a mechanism sensitive to intrinsic monolayer curvature. *The Journal of biological chemistry* **277**, 49360–5 (2002).

18. García-Sáez, A. J., Chiantia, S., Salgado, J. & Schwille, P. Pore formation by a Bax-derived peptide: effect on the line tension of the membrane probed by AFM. *Biophysical journal* **93**, 103–12 (2007).

19. Unsay, J. D., Cosentino, K., Sporbeck, K. & García-Sáez, A. J. Pro-apoptotic cBid and Bax exhibit distinct membrane remodeling activities: An AFM study. *Biochimica et Biophysica Acta (BBA) - Biomembranes* **1859**, 17–27 (2017).

20. Cosentino, K. & García-Sáez, A. J. Mitochondrial alterations in apoptosis. *Chemistry and Physics of Lipids* **181**, 62–75 (2014).

21. Frezza, C. *et al.* OPA1 Controls Apoptotic Cristae Remodeling Independently from Mitochondrial Fusion. *Cell* **126**, 177–189 (2006).

22. Scorrano, L. *et al.* A Distinct Pathway Remodels Mitochondrial Cristae and Mobilizes Cytochrome c during Apoptosis. *Developmental Cell* **2**, 55–67 (2002).

23. Scorrano, L. Cristae Remodeling and Mitochondrial Fragmentation: A Checkpoint for Cytochrome c Release and Apoptosis? *Apoptosome: An Up-and-coming Therapeutical Tool* **9789048134151**, 253–270 (2010).

24. McArthur, K. *et al.* BAK/BAX macropores facilitate mitochondrial herniation and mtDNA efflux during apoptosis. *Science* **359**, eaao6047 (2018).

25. Riley, J. S. *et al.* Mitochondrial inner membrane permeabilisation enables mt DNA release during apoptosis . *The EMBO Journal* **37**, (2018).

26. Rongvaux, A. *et al.* Apoptotic Caspases Prevent the Induction of Type I Interferons by Mitochondrial DNA. *Cell* **159**, 1563–1577 (2014).

27. White, M. J. *et al.* Apoptotic Caspases Suppress mtDNA-Induced STING-Mediated Type I IFN Production. *Cell* **159**, 1549–1562 (2014).

28. Victorelli, S. *et al.* Apoptotic stress causes mtDNA release during senescence and drives the SASP. *Nature 2023 622:7983* **622**, 627–636 (2023).

29. Yamazaki, T. *et al.* Mitochondrial DNA drives abscopal responses to radiation that are inhibited by autophagy. *Nature immunology* **21**, 1160–1171 (2020).

30. Yuan, S. *et al.* VDAC2 loss elicits tumour destruction and inflammation for cancer therapy. *Nature* **640**, 1062 (2025).

31. Jenner, A., Shalaby, R. & Cosentino, K. *Quantitative Single-Molecule Imaging of Protein Assembly in Membranes. Advances in Biomembranes and Lipid Self-Assembly* vol. 31 81–128 (Academic Press, 2020).

32. Finan, K., Raulf, A. & Heilemann, M. A Set of Homo-Oligomeric Standards Allows Accurate Protein Counting. *Angewandte Chemie International Edition* **54**, 12049–12052 (2015).

33. Verdaasdonk, J. S., Lawrimore, J. & Bloom, K. Determining absolute protein numbers by quantitative fluorescence microscopy. *Methods in Cell Biology* **123**, 347–365 (2014).

34. Thevathasan, J. V. *et al.* Nuclear pores as versatile reference standards for quantitative superresolution microscopy. *Nature Methods* **16**, 1045–1053 (2019).

35. Scorrano, L., Petronilli, V. & Bernardi, P. On the voltage dependence of the mitochondrial permeability transition pore. A critical appraisal. *Journal of Biological Chemistry* **272**, 12295–12299 (1997).

36. Baumgart, T., Hess, S. T. & Webb, W. W. Imaging coexisting fluid domains in biomembrane models coupling curvature and line tension. *Nature 2003 425:6960* **425**, 821–824 (2003).

37. Jülicher, F. & Lipowsky, R. Shape transformations of vesicles with intramembrane domains. *Physical Review E* **53**, 2670 (1996).

38. Frey, T. G., Renken, C. W. & Perkins, G. A. Insight into mitochondrial structure and function from electron tomography. *Biochimica et Biophysica Acta (BBA) - Bioenergetics* **1555**, 196–203 (2002).

39. Karbowski, M. *et al.* Spatial and temporal association of Bax with mitochondrial fission sites, Drp1, and Mfn2 during apoptosis. *Journal of Cell Biology* **159**, 931–938 (2002).

40. Montessuit, S. *et al.* Membrane Remodeling Induced by the Dynamin-Related Protein Drp1 Stimulates Bax Oligomerization. *Cell* **142**, 889–901 (2010).

41. Prudent, J. *et al.* MAPL SUMOylation of Drp1 Stabilizes an ER/Mitochondrial Platform Required for Cell Death. *Molecular Cell* **59**, 941–955 (2015).

42. Jenner, A. *et al.* DRP1 interacts directly with BAX to induce its activation and apoptosis. *The EMBO Journal* **41**, e108587 (2022).

43. Martinou, J. C. & Youle, R. J. Mitochondria in Apoptosis: Bcl-2 family Members and Mitochondrial Dynamics. *Developmental Cell* **21**, 92 (2011).

44. Subburaj, Y. *et al.* Bax monomers form dimer units in the membrane that further self-assemble into multiple oligomeric species. *Nature Communications* **6**, 1–11 (2015).

45. Saunders, T. L. *et al.* Exposure of the inner mitochondrial membrane triggers apoptotic mitophagy. *Cell Death & Differentiation 2024 31:3* **31**, 335–347 (2024).

46. Sanjana, N. E., Shalem, O. & Zhang, F. Improved vectors and genome-wide libraries for CRISPR screening. *Nature Methods 2014 11:8* **11**, 783–784 (2014).

47. Doench, J. G. *et al.* Optimized sgRNA design to maximize activity and minimize off-target effects of CRISPR-Cas9. *Nature Biotechnology 2015 34:2* **34**, 184–191 (2016).

48. Hsu, P. D. *et al.* DNA targeting specificity of RNA-guided Cas9 nucleases. *Nature Biotechnology 2013 31:9* **31**, 827–832 (2013).

49. Glusman, G., Caballero, J., Mauldin, D. E., Hood, L. & Roach, J. C. Kaviar: an accessible system for testing SNV novelty. *Bioinformatics* **27**, 3216–3217 (2011).

50. LentiCRISPRv2 and lentiGuide-Puro: lentiviral CRISPR/Cas9 and single guide RNA. doi:10.1126/science.1247005.

51. Schindelin, J. *et al.* Fiji: an open-source platform for biological-image analysis. *Nature Methods 2012 9:7* **9**, 676–682 (2012).

52. Danial, J. S. H., Jenner, A., Garcia-Saez, A. J. & Cosentino, K. Real-Time Growth Kinetics Analysis of Macromolecular Assemblies in Cells with Single Molecule Resolution. *Journal of Physical Chemistry A* **127**, 3490–3496 (2023).

53. Kremer, J. R., Mastronarde, D. N. & McIntosh, J. R. Computer Visualization of Three-Dimensional Image Data Using IMOD. *Journal of Structural Biology* **116**, 71–76 (1996).

54. Paul-Gilloteaux, P. *et al.* eC-CLEM: flexible multidimensional registration software for correlative microscopies. *Nature Methods 2017 14:2* **14**, 102–103 (2017).

883 55. Jülicher, F. & Lipowsky, R. Shape transformations of vesicles with intramembrane domains. *Phys*
884 *Rev E Stat Phys Plasmas Fluids Relat Interdiscip Topics* **53**, 2670–2683 (1996).

885 56. Konar, S., Arif, H. & Allolio, C. Mitochondrial membrane model: Lipids, elastic properties, and the
886 changing curvature of cardiolipin. *Biophysical journal* **122**, 4274–4287 (2023).

887 57. Siggel, M., Kehl, S., Reuter, K., Köfinger, J. & Hummer, G. TriMem: A parallelized hybrid Monte
888 Carlo software for efficient simulations of lipid membranes. *Journal of Chemical Physics* **157**,
889 174801 (2022).

890 58. De Chaumont, F. *et al.* Icy: an open bioimage informatics platform for extended reproducible
891 research. *Nature Methods 2012 9:7* **9**, 690–696 (2012).

892 59. Concordet, J. P. & Haeussler, M. CRISPOR: intuitive guide selection for CRISPR/Cas9 genome
893 editing experiments and screens. *Nucleic Acids Research* **46**, W242 (2018).

894

895

Figures

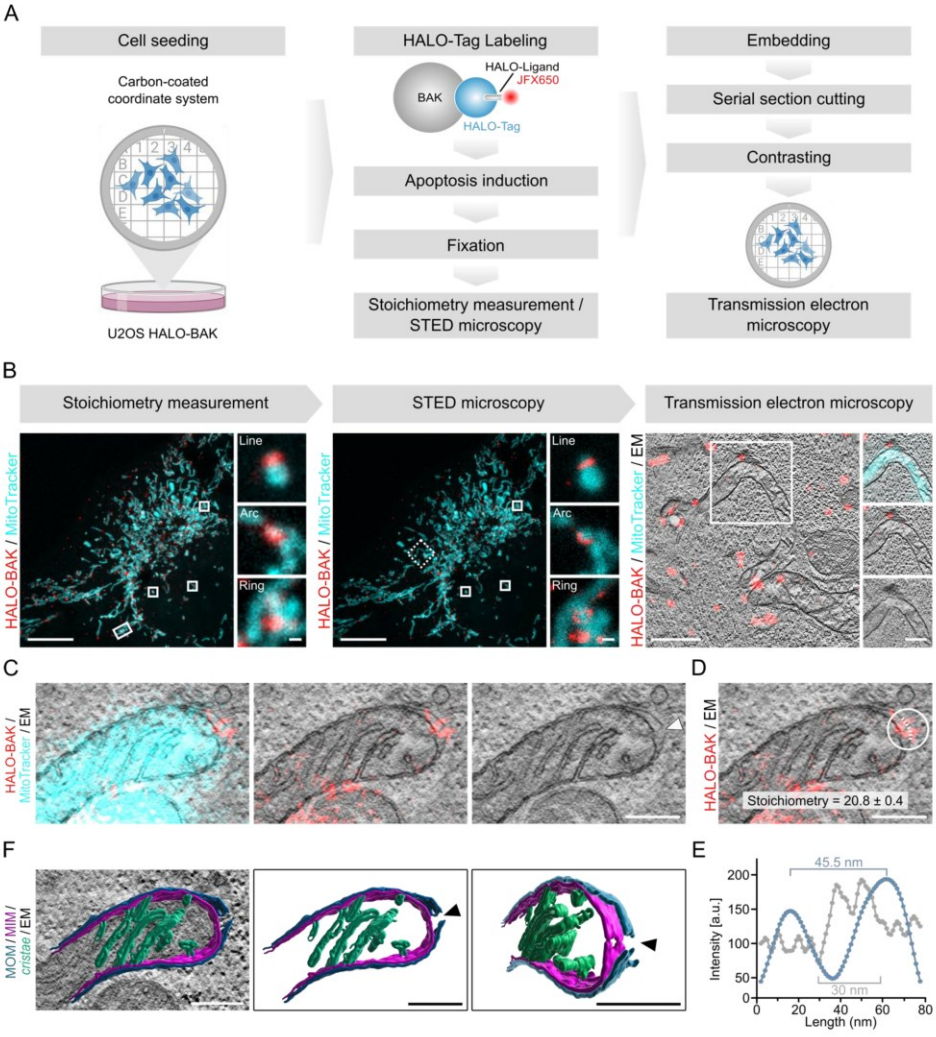

Figure 1: Development of CLOSE microscopy and application to the apoptotic pore. A) Schematic of the workflow including cell seeding on carbon-coated coordinate system gridded dishes, labeling of HALO-BAK with JFX650 HALO-Tag ligand, induction of apoptosis and cell fixation. The stoichiometry of apoptotic BAK is then measured by photon-counting confocal microscopy, followed by STED microscopy to examine the nanoscale structural organization of

BAK. Samples are resin-embedded, cut and contrasted for transmission electron microscopy to visualize mitochondrial ultrastructure. B) Representative photon-counting confocal (left), STED (middle), and transmission electron microscopy (right) images of U2OS HALO-BAK cells labeled with JFX650 HALO-Tag ligand (red) one hour after apoptosis induction. Mitochondria were visualized using MitoTracker orange (cyan). Enlarged images correspond to cropped regions of the overview image as indicated, showing representative photon-counting confocal and STED images of line, arc, and ring structures. Dashed rectangle indicates region shown in transmission electron microscopy image. Scale bar 10 µm (zoomed images 500 nm) for stoichiometry and STED images and 1 µm (zoomed images 500 nm) for transmission electron microscopy images. Data are representative of n = 8 independent experiments. C) Overlaid STED-CLEM image of a single mitochondrion showing MitoTracker (cyan, confocal) and BAK (red, STED) fluorescence signal and EM image (grayscale, left panel), BAK signal and EM image (middle panel), and single EM image (right panel). Arrowhead indicates position of MOM discontinuity. Images correspond to the magnified (rotated and flipped) region of the image in (B, left panel) as indicated by the rectangle. Scale bar 250 nm. D) STED-CLEM overlay image of BAK (red, STED) and EM signal (grayscale) of the mitochondrion shown in (C). White circle indicates region of interest for quantification of BAK stoichiometry (as indicated) from photon-counting confocal microscopy image (not shown). Dashed line indicates the region of BAK fluorescence and EM intensity measurement (shown in E) along the MOM discontinuity. Scale bar 250 nm. E) Quantification of BAK fluorescence (blue) and EM intensity (gray) at the line profile indicated by the dashed line in (D). F) 3D rendered MOM (blue), MIM (purple), and *cristae* membranes (green) overlaid with EM image (grayscale, right panel) in top view (middle panel) and tilted view (right panel) of the image shown in (C). Arrowheads indicate the position of the MOM and MIM discontinuities. Scale bar 250 nm.

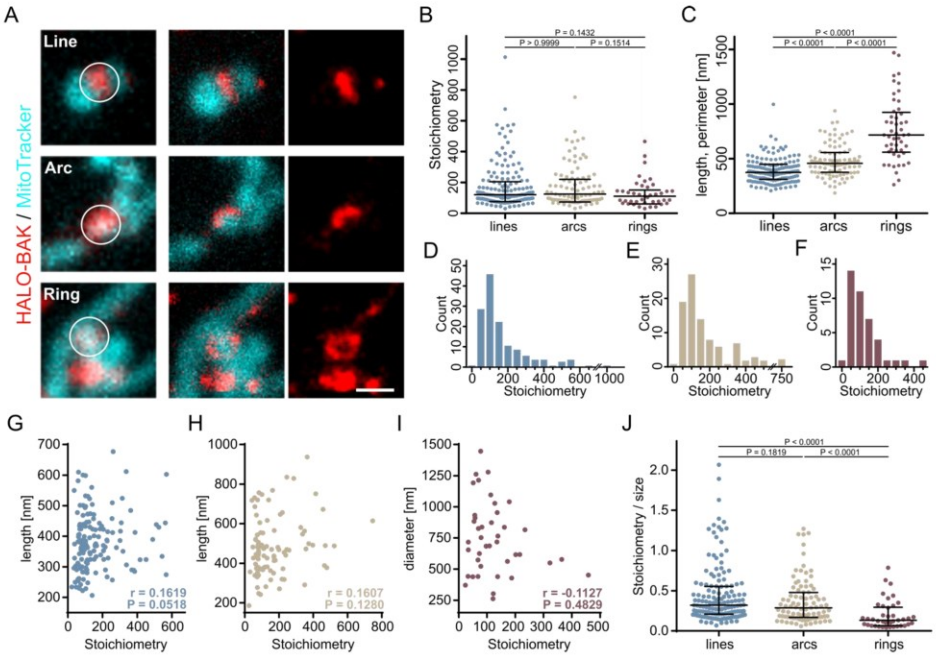

930

931 **Figure 2: Oligomerization does not determine the supramolecular arrangement of**
932 **individual BAK assemblies.** A) Gallery of representative line, arc and ring structures of BAK
933 (red) visualized using photon-counting confocal (left panel) and STED microscopy (middle and
934 right panel). Mitochondria were visualized using MitoTracker orange (cyan, confocal). Circles
935 indicate regions of interest for stoichiometry quantification. Scale bar 500 nm. B, C) Quantification
936 of the stoichiometry of line, arc, and ring structures (B) as well as the length of line and arc and
937 the perimeter of ring structures (C) formed by BAK. Values correspond to individual structures
938 (individual data points) as well as the median (line) ± interquartile range (whiskers) of n = 145
939 lines, n = 91 arcs, and n = 41 rings for stoichiometry (B) and n = 154 lines, n = 98 arcs, and n =
940 50 rings for size measurements (C). Significance levels were determined by non-parametric one-
941 way ANOVA (Kruskal-Wallis test) and Dunn's multiple comparison test. P indicates multiplicity
942 adjusted P values (family-wise significance and confidence level set to 0.05). D-F) Frequency
943 distribution of the stoichiometry of line (D), arc (E), and ring (F) structures. G-I) Correlation
944 between stoichiometry and the length of lines (blue, G), arcs (beige, H) and ring perimeter
945 (burgundy, I). Values correspond to individual structures (individual data points) of n = 145 lines,
946 n = 91 arcs, and n = 41 rings. r indicates the nonparametric Spearman correlation coefficient, P
947 indicates the two-tailed P value (95% confidence interval) for each individual category. J)
948 Stoichiometry/size-ratio of individual assemblies sown in (G-I). Values are shown for individual
949 BAK assemblies (individual data points) and the median (line) ± interquartile range (whiskers) of
950 n = 151 lines, n = 91 arcs, and n = 41 rings. Significance levels were determined by non-
951 parametric one-way ANOVA (Kruskal-Wallis test) and Dunn's multiple comparison test. P
952 indicates multiplicity adjusted P values (family-wise significance and confidence level set at 0.05).
953 All data presented are representative of n = 8 independent experiments.

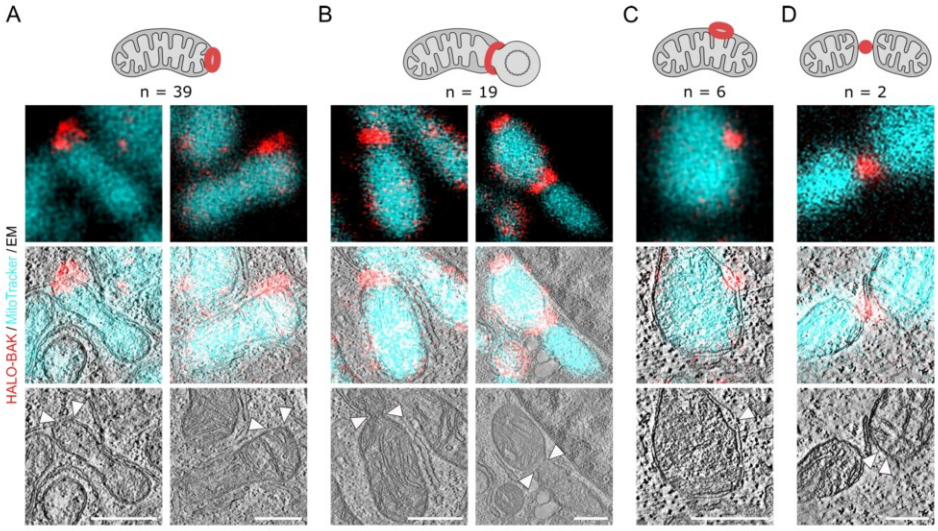

Figure 3: Organellar distribution of BAK pores at the MOM. A) MOM opening at the tip of the mitochondrion, B) MOM opening with extrusion of the MIM, C) MOM opening at the side of the mitochondrion, and D) MOM opening at a potential post-fission site, as indicated by the schematic representation (BAK shown in red). Microscopy images show representative STED microscopy (top), STED-CLEM overlay (middle) and TEM (bottom) examples of mitochondria from U2OS HALO-BAK cells one hour after apoptosis induction labeled with JFX650 Halo-Tag ligand (red, STED) for each category. Mitochondria were labeled with MitoTracker Orange (cyan, confocal). Arrowheads indicate the position of the MOM discontinuity. n indicates the number of cases assigned to the corresponding category out of a total of n = 6 independent experiments. Scale bar 500 nm.

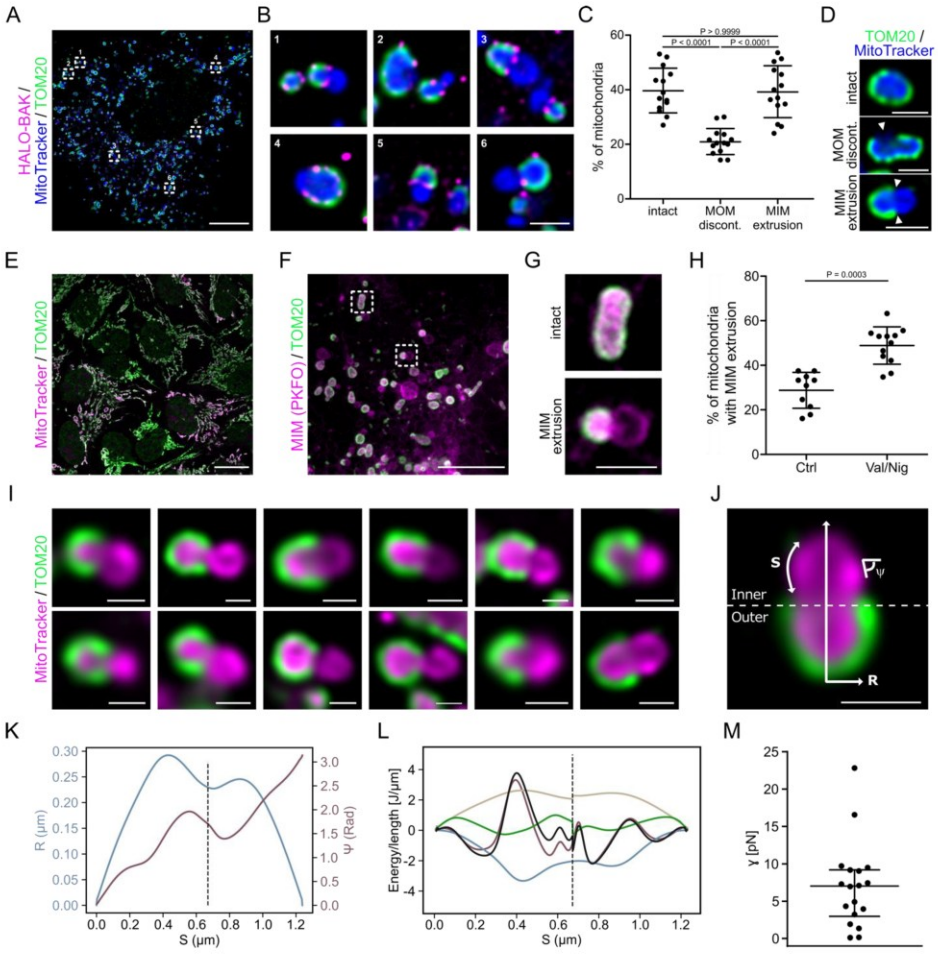

967

968

969 **Figure 4: Mechanical forces promote MIM extrusion through BAK pores in the MOM.** A)
970 Representative deconvolved confocal/STED microscopy image of U2OS HALO-BAK cells labeled
971 with JFX650 HALO-Tag ligand (magenta, STED) one hour after apoptosis induction. The MOM
972 was stained by immunolabeling against TOM20 (green, confocal) and the mitochondrial matrix
973 was visualized by MitoTracker Orange (blue, confocal). Numbered rectangles indicate cropped
974 regions in (B). Scale bar 10 µm. B) Enlarged images of cropped regions of the overview image
975 shown in (A) as indicated. Scale bar 1 µm. C) Quantification of apoptotic mitochondria with intact
976 MOM (intact) versus mitochondria with discontinuity of the MOM (MOM discont.) or mitochondria
977 with extrusion of MIM through MOM openings (MIM extrusion). Values correspond to the
978 percentage of mitochondria of individual cells (individual data points) as well as the mean (line) ±

SD (whiskers) of n = 14 cells. Significance levels were determined by non-parametric one-way ANOVA (Kruskal-Wallis test) and Dunn's multiple comparison test. P indicates multiplicity adjusted P values (family-wise significance and confidence level set to 0.05). D) Representative confocal microscopy images of the categories quantified in (C) of U2OS HALO-BAK cells prepared as described in (A). Scale bar 1 µm. E) Representative confocal microscopy overview image of valinomycin/nigericin-induced osmotic mitochondrial matrix swelling in healthy U2OS HALO-BAK cells. The MIM/mitochondrial matrix was visualized by MitoTracker Orange (magenta) and the MOM was stained by immunolabeling against TOM20 (green). Scale bar 20 µm. F) Representative confocal/STED microscopy image of U2OS HALO-BAK cells transiently transfected with TOM20-SNAP labeled with JFX650 SNAP-tag ligand (green, deconvolved confocal) one hour after apoptosis induction. The MIM was labeled with PKFO (magenta, STED). Dotted rectangles indicate cropped regions in (G). Scale bar 5 µm. G) Enlarged images of cropped regions of the image shown in (F) as indicated, showing exemplary mitochondria with intact MOM (intact) or mitochondria with MIM extrusion through MOM openings (MIM extrusion). Scale bar 1 µm. H) Quantification of mitochondria with MIM extrusion through MOM openings in apoptotic U2OS HALO-BAK control (Ctrl) cells or apoptotic U2OS HALO-BAK cells treated with valinomycin/nigericin (Val/Nig) to induce osmotic swelling of the mitochondrial matrix. Values correspond to the percentage of mitochondria of individual cells (individual data points) as well as the mean (line) ± SD (whiskers) of n = 10 (ctrl) and n = 12 (Val/Nig) cells. Significance levels were determined by unpaired nonparametric Student's t-test (Mann-Whitney test, P value as indicated). Data are representative of n = 5 (panels A-D) and n = 4 (panels F-H) independent experiments. I) Gallery of hourglass-shaped MIM extrusion examples from U2OS HALO-BAK cells one hour after apoptosis induction. The MOM was stained by immunolabeling against TOM20 (green, deconcolved) and the mitochondrial matrix was visualized by MitoTracker Orange (magenta). Scale bar 500 nm. J) Representative axisymmetric image of a MIM extrusion as described in (I). The mitochondria are aligned so that the longitudinal axis is orthogonal to the axis of the opening pore separating the regions of exposed MIM (inner) and MIM contained in MOM (outer, dashed line). The parametrization of the local radius R and the tangent angle ψ as a function of the arc length S is presented. Scale bar 500 nm. K) Local mitochondrial radius R and tangent angle ψ as a function of the arc length S, in blue and burgundy, respectively. L) Minimized energy of the experimental mitochondria presented in (J). In black, the sum of the energies is plotted as a function of the arc length S. The lateral tension, pressure, bending, and line energies are plotted as a function of S, in beige, blue, burgundy, and green, respectively. M) Pore rim line tension γ obtained from the minimization routine of n = 18 mitochondria from n = 9 individual cells. Data are presented as the line tension values for individual mitochondria (individual data points) as well as the median (line) ± interquartile range (whiskers). Data are representative of n = 3 independent experiments.

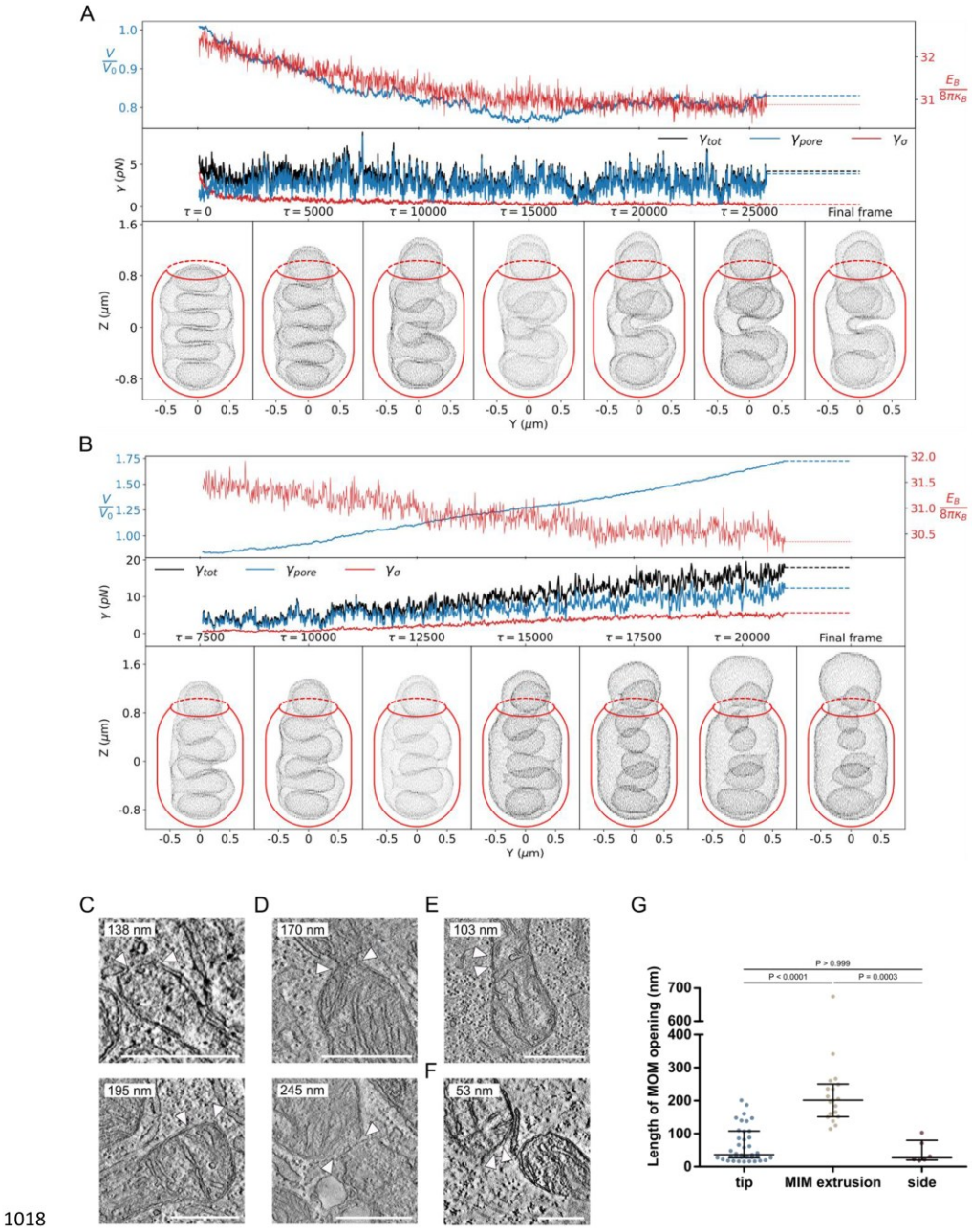
A
B
C
D
E
F
G
Y (μm)
Z (μm)
Final frame
138 nm
170 nm
103 nm
195 nm
245 nm
53 nm
Length of MOM opening (nm)
tip
MIM extrusion
side
P < 0.0001
P = 0.0003
P > 0.999

1018

Figure 5: Interplay between MIM extrusion and the apoptotic pore. A-B) Membrane dynamic simulations of MIM extrusion through the apoptotic pore at the MOM. MIM (grey in bottom panel) contained in MOM (red schematic outline) with a pore of size $\alpha = 0.75$ corresponding to a relative diameter of 0.682 and a bending rigidity of $\kappa_B = 10\ k_BT$ without (A) and with osmotic inflation after time $\tau = 7500$ (B). The bottom panels show snapshots at the indicated time points, the top panels the membrane bending energy E_B (red) and the mitochondrial matrix volume relative to that of the starting structure (blue). The center panel shows the effective line tension created by the evaginating membrane in the apoptotic pore (see Methods for components). C-G) Quantification of the size of individual MOM openings. C-F) Exemplary EM images of single mitochondria with MOM discontinuity at the tip of the mitochondrion (C), MOM opening with MIM extrusion (D), MOM discontinuity at the side of the mitochondrion (E), and at a potential post-fission site (F). Arrowheads indicate the position of the MOM discontinuity and the measurement position. The size of the measured opening is indicated in each image. Scale bar 500 nm. G) Quantification of the size of individual MOM openings according to the categories described in (C-E). Values correspond to individual measurements (individual data points) as well as the median (line) ± interquartile range (whiskers) of n = 39 MOM openings at the tip, n = 19 MOM openings with MIM extrusion, and n = 6 MOM openings at the side of the mitochondrion from n = 6 independent experiments. Significance levels were determined by non-parametric one-way ANOVA (Kruskal-Wallis test) and Dunn's multiple comparison test. P indicates multiplicity adjusted P values (family-wise significance and confidence level set to 0.05).

Supplementary Information

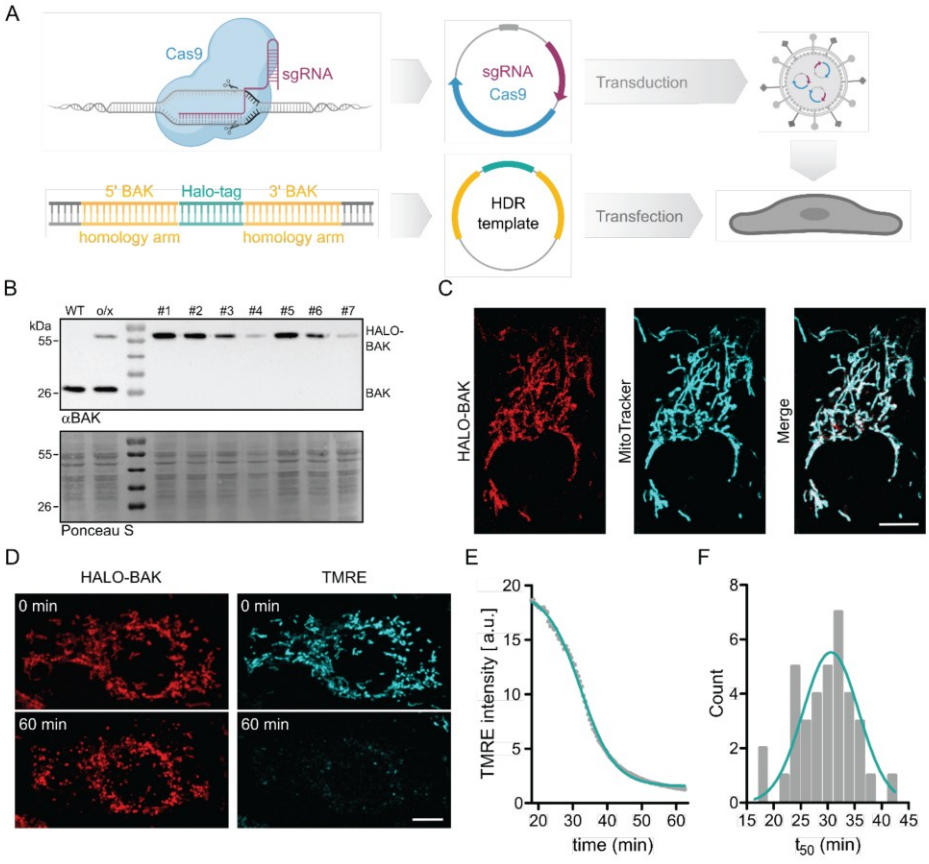

Figure S1: Generation and validation of the U2OS HALO-BAK cell line. A) We generated a U2OS cell line expressing BAK genomically tagged with HALO-tag (HALO-BAK) using CRISPR/Cas9, which allows visualization of BAK with advanced organic fluorophores at endogenous expression levels. A) shows the schematic representation of the workflow using a combined CRISPR/Cas9 approach: A synthetic guide RNA (sgRNA) specific for the endogenous locus of BAK is cloned into a lentiviral expression vector together with the coding sequence of the Cas9 enzyme (upper panel). Homology arms of 800 bp of the genomic BAK locus upstream (5' BAK homology arm) and downstream (3' BAK homology arm) of the start codon are fused to the coding sequence of the HALO tag and cloned into a homology-directed repair (HDR) template expression vector (lower panel). Both the Cas9/sgRNA and the HDR template are delivered to the target cell by lentiviral transduction or transfection, respectively. B) In addition to PCR genotyping (not shown), we performed immunoblotting of single cell clones to confirm homozygous genome editing. B) shows the expression of the HALO-BAK fusion protein in single cell clones (#1-7) by immunoblotting against BAK. Cell lysates from

wild-type U2OS cells (WT) and wild-type cells transiently overexpressing HALO-BAK (o/x) were used as controls. Whole protein staining (Ponceau S) is shown to control for equal sample loading. C-F) Live-cell confocal microscopy of HALO-BAK in healthy cells and during apoptosis demonstrates the functionality of genome-edited HALO-BAK, which presented the same subcellular localization and comparable cell death kinetics as described for wild type BAK. C) Representative confocal fluorescence microscopy image demonstrating the subcellular localization of HALO-BAK. HALO-BAK was labeled with JFX650 HALO-Tag ligand (red) and mitochondria were visualized using MitoTracker green (cyan) as a reference. Scale bar 10 µm. D) Representative confocal fluorescence microscopy images of HALO-BAK (red) before (0 min) and after induction of cell death (60 min). Mitochondria were stained with the potential-sensitive dye TMRE (cyan) to monitor the loss of mitochondrial membrane potential over time. Scale bar 10 µm. E) Representative quantification of TMRE signal intensity over time. The data were fitted with an exponential decay function (blue) to extract the time of 50% TMRE signal loss (t_{50}). F) Distribution of t_{50} values fitted with a Gaussian function (blue) to extract the mean time of 50% TMRE signal loss. Experiments are representative of n = 3 independent experiments with n = 20 cells each.

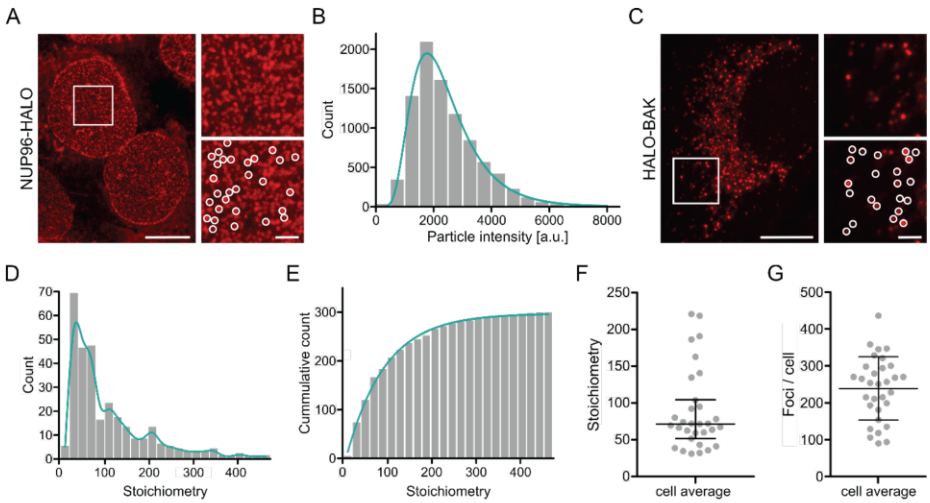

Figure S2: Stoichiometric quantification of HALO-BAK stoichiometry. We performed single particle brightness quantification of individual NUP96-HALO complexes (A-B), which allows ratiometric calculation of the theoretical brightness of a monomeric fluorescent emitter, which we used to convert the brightness of HALO-BAK apoptotic particles to HALO-BAK molecularity (C-E). A, C) Representative photon-counting confocal microscopy image of U2OS NUP96-HALO (A) and U2OS HALO-BAK (C) labeled with JFX650 HALO-Tag ligand. With the exception of apoptosis induction, U2OS NUP96-HALO cells were prepared and imaged with photon-counting confocal microscopy in the same manner as U2OS HALO-BAK samples. Right panels represent zoomed regions as indicated by the rectangle. Detected regions of interest of measured HALO-BAK and NUP96-HALO foci, respectively, are shown in the lower right panels (white circles). Scale bar 10 µm, zoomed images 2 µm. Images are representative of n = 123 NUP96-HALO and n = 31 HALO-BAK cells from n = 8 independent experiments. B) Exemplary fluorescence intensity distribution of n = 1937 individual NUP96-HALO foci measured from n = 22 individual cells of one measurement day. Lognormal fitting was applied to extract the median particle intensity of the population (blue line), which is used as the calibration standard for radiometric stoichiometry quantification. D) Population distribution (gray) and probability density function (blue line) of the stoichiometry of HALO-BAK foci detected from the cell shown in (C). E) Cumulative distribution (gray) of HALO-BAK stoichiometry in (D) fitted with an exponential decay function (blue line) to extract the average stoichiometry of HALO-BAK foci in the given cell. F, G) Quantification of median cellular BAK stoichiometry in apoptotic mitochondria (F) and number of HALO-BAK foci detected per cell (G). Values are presented for individual cells (individual data points) as well as the median (F) or mean (G, line) ± interquartile range (F) or SD (G, whiskers) of n = 31 cells from n = 8 independent experiments.

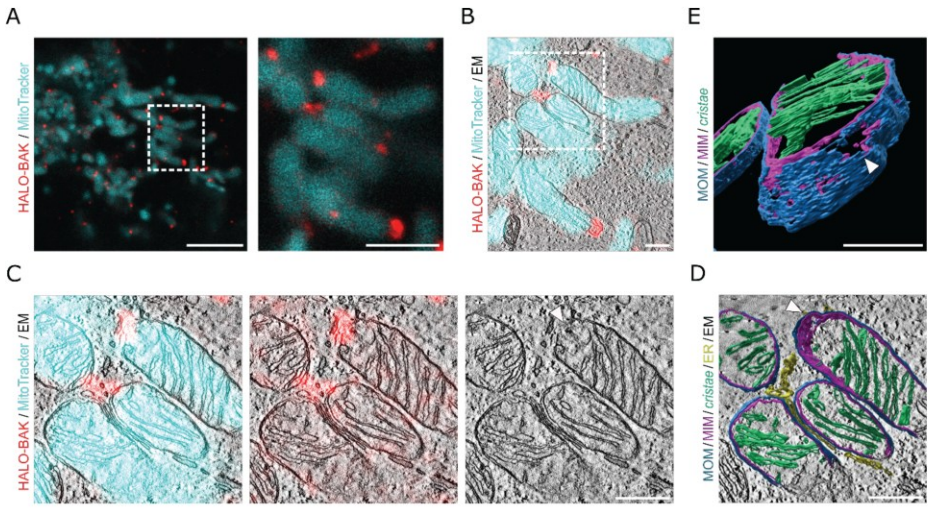

Figure S3: Correlative suplerCLEM analysis of a single mitochondrion. A) Representative STED microscopy image of U2OS HALO-BAK cells labeled with JFX650 HALO-Tag ligand (red) one hour after apoptosis induction. Mitochondria were labeled with MitoTracker orange (cyan, confocal). Enlarged image (right panel) corresponds to the cropped region as indicated. Scale bar 5 µm, magnified image 2 µm. B) Overlaid STED-CLEM image of a single mitochondrion showing MitoTracker (cyan, confocal) and BAK (red, STED) fluorescence signal and EM image (grayscale). The dashed rectangle indicates the cropped region shown in (C-D). Scale bar 500 nm. C) Enlarged image of cropped region from image in (B) showing MitoTracker (cyan, confocal) and BAK (red, STED) fluorescence signal and EM image (grayscale, left panel), BAK signal and EM image (middle panel), and single EM image (right panel). Scale bar 500 nm. D) 3D rendered MOM (blue), MIM (purple), *cristae* (green), and ER membranes (yellow) overlaid with EM image (grayscale) in top view. Scale bar 500 nm. Scale bar 500 nm. E) Tilted and magnified view of 3D rendered MOM (blue), MIM (purple), and *cristae* membranes (green). Scale bar 250 nm. Arrowheads in (C-E) indicate position of MOM and MIM discontinuities.

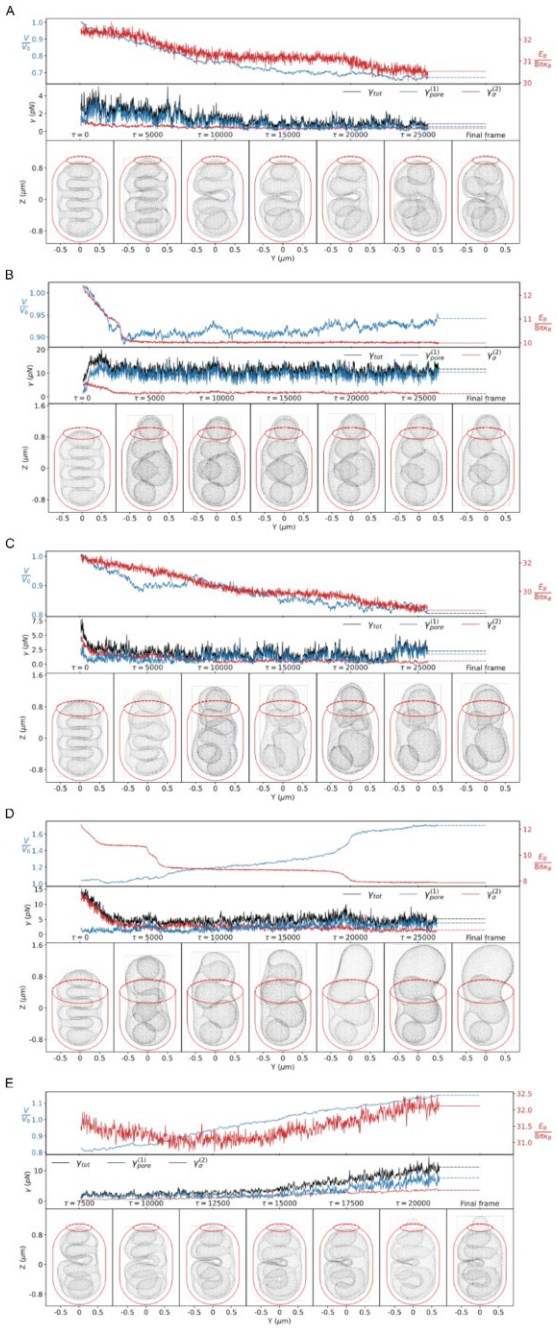

Figure S4: Membrane dynamic simulation of MIM extrusion. A-D) MIM (grey in bottom panel) contained in MOM (red schematic outline) with a pore of size $\alpha = 0.50$ corresponding to a relative diameter of $r_{\mathrm{frac}} = 0.479$ and a bending rigidity of $\kappa_B = 10\, k_B T$ (A), $\alpha =$

$0.75; r_{\mathrm{frac}} = 0.682; \kappa_B = 60 k_B T$ (B), $\alpha = 1.00; r_{\mathrm{frac}} = 0.841;\ \kappa_B = 10 k_B T$ (C), and $\alpha = 1.50; r_{\mathrm{frac}} = 0.997;\ \kappa_B = 60 k_B T$ (D) simulated without osmotic shock. E) A pore of size $\alpha = 0.50$ corresponding to a relative diameter of $r_{\mathrm{frac}} = 0.479$ and a bending rigidity of $\kappa_B = 10\ k_B T$ with osmotic inflation starting from time point $\tau = 7500$. The bottom panels show snapshots at the indicated time points, the top panels the membrane bending energy E_B (red) and the volume relative to that of the starting structure (blue). The center panel shows the effective line tension created by the evaginating membrane in the BAX/BAK-pore (see Methods for components).

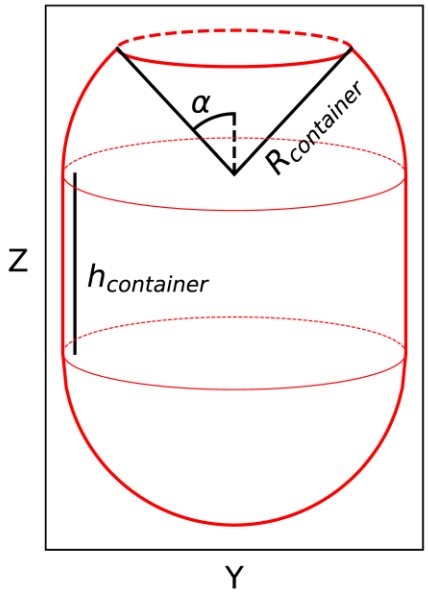

Figure S5: Schematic diagram of the rigid container mimicking the MOM. The container consists of a cylindrical central body of radius $\mathbf{R_{container}}$ and height $\mathbf{h_{container}}$ aligned with the $\mathbf{Z}$ axis that is capped at its ends by hemispheres of radius $\mathbf{R_{container}}$. The circular opening along the positive $\mathbf{Z}$ axis describes the apoptotic pore on the MOM. The size of the pore is defined by $\boldsymbol{\alpha}$, being the polar angle from the positive $\mathbf{Z}$ axis to the rim of the pore, taking the center of the intact hemispherical cap as the reference point. The pore radius is then $\mathbf{r_{pore}} = \mathbf{R_{container}}\,\mathbf{sin}(\boldsymbol{\alpha})$.

Table S1

[GENERAL]

algorithm	hmc
info	10
input	IMM.stl
output_prefix	out/out
restart_prefix	out/out
checkpoint_every	1000
output_format	vtu

[HMC]

num_steps	10000000
step_size	1e-4
traj_steps	50
momentum_variance	0.2
thin	500
flip_ratio	0.025
flip_type	parallel
initial_temperature	1
cooling_factor	0
start_cooling	10000000

[BONDS]

bond_type	Edge
r	1

[SURFACEREPULSION]

n_search	cell-list
rlist	0.5
exclusion_level	0
refresh	1
lc1	0.155

r	1

[EXTERNALPOTENTIAL]

type	porous_MITO
epsilon	1
sigma	0.5
radius	3.55
half_height	1.85
alpha	0.25/0.50/0.75/1.00/1.50

[ENERGY]

kappa_b	10/60
kappa_a	1000
kappa_v	0/$\boldsymbol{\kappa_V(\tau)}$
kappa_c	0
kappa_t	1000
kappa_r	1000
kappa_e	1
area_fraction	1.0
volume_fraction	10.0
curvature_fraction	0.01
continuation_delta	0.0
continuation_lambda	1.0

Table S1: List of parameters used in the TriMem simulations. The desired algorithm and in/output formats are defined in [GENERAL]. As listed in [HMC], the integration time step in the Hamiltonian dynamics segments of the hybrid Monte Carlo runs was set to $\mathbf{1 \times 10^{-4}\tau}$, where $\boldsymbol{\tau}$ is the reduced time unit. The duration of the each segment was 50 time steps, hence, $\mathbf{0.005\tau}$; an output vtu file is written every $\mathbf{2.5\tau}$. The simulations were run at reduced temperature $\mathbf{T = 1}$ and mass $\mathbf{M = 0.2}$. The simulations were halted soon after $\mathbf{25000\tau}$ for the replicas without the volume constraint, and around $\mathbf{20000\tau}$ for the osmotic shock cases.
[EXTERNALPOTENTIAL] defines the type and shape of the external container, where epsilon (ϵ), sigma $\left(\sigma = 2^{-\frac{1}{6}} s_0\right)$, radius $(R_{container})$, half_height $(0.5h_{container})$ and alpha (α) denote characteristic energy scale, length scale of the confining potential, radius and half the height of the cylindrical central body of the container mimicking the OMM in internal units, and the pore size, respectively. [ENERGY] defines the energy penalty constants of the Helfrich

Hamiltonian [1], and the corresponding reference properties of the IMM. Note one set of the simulations was conducted without the volume penalty ($\kappa_V = 0$), while another set of replica simulations was continued from 7500τ with the volume constraint, in which κ_V was increased by $5000 k_B T$ every 500τ with a target of $10V_0$.

1. Siggel, M., Kehl, S., Reuter, K., Köfinger, J. & Hummer, G. TriMem: A parallelized hybrid Monte Carlo software for efficient simulations of lipid membranes. *J. Chem. Phys.* **157**, 174801 (2022).